DISTINCT ELEMENT MODEL ANALYSES OF UNSTABLE FAILURES IN UNDERGROUND COAL MINES

by

Ruixiang Gu

A thesis submitted to the Faculty and the Board of Trustees of the Colorado School of Mines in partial fulfillment of the requirements for the degree of Doctor of Philosophy (Mining and Earth Systems Engineering).

Golden, Colorado

Date _____

Signed: _____
Ruixiang Gu

Signed: _____
Dr. Ugur Ozbay
Thesis Advisor

Golden, Colorado

Date _____

Signed: _____
Dr. Hugh Miller
Associate Professor and Interim Department Head
Department of Mining Engineering

ABSTRACT

Underground mining may induce shear failures along large rock discontinuities and sizable compressive failures of rock materials (e.g. coal) in sidewalls and mining faces. These failures can be in stable or unstable manner. When such failures occur in an unstable manner, they may be accompanied by a significant energy release from the surrounding rock and potentially create coal burst events. This thesis focuses on identifying failure stability in terms of their manifestation as a stable and unstable manner in underground coal mining settings using numerical modeling. Both discontinuity shear failure and material compressive failure are considered. The influence of the shear failure stability on the compressive failure stability of sidewalls and mining faces is also considered. The study uses the numerical modeling program UDEC with its optional constitutive models continuously yielding joint model and the Mohr-Coulomb strain softening model.

A laboratory scale numerical model of a double shear test setup is developed and used to assess the ability of UDEC in detecting the failure stability (i.e. stable or unstable failure) of discontinuity shear failures. The studies performed using this model confirmed that UDEC can identify the stable and unstable failures when using a previously defined failure stability criterion based on the relative stiffnesses of loading and failing systems. Using the double shear test model, methodologies are developed for identifying shear failure stability. Further and detailed analyses of failure stability are performed in in-situ scale models. The results show that the failure stability is governed by the relative stiffnesses of failing discontinuities and loading stiffness of wall rocks.

In-situ scale numerical models are also developed and used to study the failure stability in compression in coal mining settings. The results show that both stable and unstable shear failures can occur at the rock-coal interfaces depending on the post-failure characteristic of the interface and the shear loading stiffness of the interface. It is also shown that unstable

coal sidewall and mining face failures can occur when a sudden de-confinement is triggered by an unstable failure at the rock-coal interfaces or the existence of weak contact regions along the interfaces.

TABLE OF CONTENTS

LIST OF FIGURES

LIST OF TABLES

LIST OF SYMBOLS

Richter magnitude	M_L
normal stress	$\sigma_{(N)}$
strain	ε
stiffness	k
loading system stiffness	k_{ls}
post-peak stiffness	k'_p
shear stress	τ
potential (energy) function	$V(x)$
state variable	x
control variables	p_1 and p_2
coefficient of kinetic friction	μ
elastic modulus	E
Poisson's ratio	ν
shear displacement	u_s
joint normal stiffness	a_n
joint normal stiffness exponent	e_n
joint shear stiffness	a_s
joint shear stiffness exponent	e_s
joint roughness parameter	R
joint initial friction angle	$\phi_m^{(i)}$

intrinsic friction angle . . . . . ϕ

effective friction angle . . . . . ϕ_m

normal stiffness defined as a function of σ_n . . . . . k_n

shear stiffness defined as a function of σ_n . . . . . k_s

failure or "bounding" shear stress . . . . . τ_m

current shear displacement increment . . . . . $\triangle u_s$

previous shear displacement increment . . . . . $\triangle u_s^{(old)}$

accumulated plastic shear displacement . . . . . u_s^p

the stress ratio at the last reversal . . . . . r

effective dilation angle i

LIST OF ABBREVIATIONS

Universal Distinct Element Code . . . . . UDEC

Continuously yielding . . . . . CY

Double shear test . . . . . DST

Uniaxial compressive strength . . . . . UCS

Energy release rate . . . . . ERR

Finite Element Method . . . . . FEM

Boundary Element Method . . . . . BEM

Discrete Element Method . . . . . DEM

Finite Difference Method . . . . . FEM

Fast Lagrangian Analysis of Continua . . . . . FLAC

Excess shear stress . . . . . ESS

3-Dimensional Element Code 3DEC

Rock Failure Process Analysis code RFPA2D

U.S. Bureau of Mines . . . . . USBM

Canadian Rockburst Research Program . . . . . CRRP

Mining Research Directorate . . . . . MRD

Canadian Centre for Mineral and Energy Technology . . . . . CANMET

Mine Seismicity and Rockburst Risk Management . . . . . MSRRM

Australian Center for Geomechanics . . . . . ACG

National Institute for Occupational Safety and Health . . . . . NIOSH

Particle Flow Code PFC2D

Discontinuous Deformation Theory . . . . . DDA

Mohr-Coulomb . . . . . MC

Loading stiffness . . . . . LS

Mohr-Coulomb strain softening . . . . . MCSS

Unstable compressive failure . . . . . UCF

Unstable shear failure . . . . . USF

ACKNOWLEDGMENTS

Completing my PhD degree is definitely one of the most challenging and interesting things in my first 26 years of my life. The best and worst moments of my doctoral journey have been shared with many people. It has been a great privilege to spend several years in the Mining Engineering Department at Colorado School of Mines.

I would like to express my heartfelt gratitude to my advisor, Professor Ugur Ozbay who is not only a mentor but a dear friend, for his warm encouragement, endless support and insightful guidance. I really enjoyed the regular and random discussions with him for his brilliant thoughts and humor. I could not have asked for a better role model. I could not be prouder of my academic roots that has been cultivated for the past four years by him and the best university I have ever been. I hope that I could be as friendly, enthusiastic and energetic as Ugur and be able to maintain these valuable characters in my academic career.

I am also very grateful to Professor Hugh Miller, who is always very friendly and helpful, no matter how busy he is. He makes his effort to ensure that all the students in Mining Engineering Department can be educated in a great environment. I also would like to give many thanks to Professor John Grubb who dedicates himself to mining industry and education. It is great to have him around and talk to because of his tremendous experience in mining and enthusiasm about educating. I also want to give my sincere gratitude to the chairperson of my PhD committee, Professor Vaughan Griffiths, for his continuous support and valuable suggestions to my PhD study. His expertise in finite element method assures that the problems I encountered regarding numerical modeling in my PhD study can be addressed to and discussed with a professional. Another person I would talk to when I have numerical modeling issues is Professor Graham Mustoe, to whom I also want to give many appreciations. His scientific advice and knowledge and insightful discussions are very helpful.

I have to express my sincere thankfulness to my smart colleagues/dear friends, Ryan Garvey and Evan Kias, not only for their excellent comments, but also for listening to me whenever I was excited about a new idea. It was also super fun when we talked about science fictions and discussed the possibility that our universe is modeled numerically by other unknown creatures. It is a great honor for me to be one member in this research group. I hope I have chance to work with you in future (maybe not with Garvey since he will be focusing on writing science fiction books). I would also like to thank my dear friend Shannon Lamb for her warm encouragement and support and the fun parties hosted by her and her husband, Ryan Garvey.

I am also very grateful to the program assistants of Mining Engineering Department, Shannon Mann and Christine Monroe, for their help in many important administrative issues.

This thesis was funded by the National Institute for Occupational Safety and Health (NIOSH), and I would like to thank this organization for its generous support.

I would not have contemplated this road if not for my father, Jianhua Gu and mother, Qinghua Bai. I still remember when I was a little kid, my father and mother took me to school to learn interesting things. Today, I have finished my PhD thesis. It's a long journey, and you are always beside me. To my parents, thank them for their unconditional love, support, encouragement, and valuable characters they instilled within me! I know I always have my parents to count on when times are rough. I love them so much, and I would not have made it this far without them. I also want to express my heartfelt gratitude to my father-in-law, Gangye Xiao and mother-in-law, Xiaoli Ren for their love and unconditional support, both financially and emotionally throughout these years. In particular, the patience and understanding shown by them are greatly appreciated.

Last but not least, I would love to give my deepest appreciation to my dear wife and soul mate, Mengya Xiao. Without her continuous support, care, sacrifice, love and all the beautiful things she gave me, I could not have finished this thesis.

I dedicate this thesis to my father, mother, father-in-law, mother-in-law, wife, my other family members, and my beloved pets for their constant support, care and unconditional love. I love you all dearly!

非淡泊无以明志
非宁静无以致远

CHAPTER 1
INTRODUCTION

Developments of underground mines, especially deeper underground mines, are becoming more and more common in the industry due to the depletion of the shallower ore deposits. The increasing depth of underground mines results in increased in-situ stresses, which can lead to increased failures of rock discontinuities and rocks. The stability (i.e. stable or unstable) of a failure depends on the characteristic behaviors of failing materials and the stiffness of the loading system.

1.1 Problem Statement

An unstable failure refers to a failure of rock discontinuities or rock materials in a sudden and violent manner. Such unstable failures, if unplanned, can result in injuries of workers, damage to equipment and delays in production in underground mines. In this condition, these violent and sudden failures are recognized in the industry as rockburst events (also known as bumps or coal bursts in underground coal mines). Unplanned rockburst events have been a major hazard in underground mines since the earlier days of underground mining.

Generally, unstable failures can be categorized into two main types based on the mechanisms involved in the failure process: 1) *unstable shear failure* and 2) *unstable compressive failure*. An unstable shear failure is the essence of a *slip-type rockburst*, while an unstable compressive failure is the essence of a *strain-type rockburst*.

Unstable failures occur in various locations in a mine depending on the mining method adopted, the characteristics of the surrounding rocks and whether or not large geological discontinuities exist. In longwall coal mines, unstable compressive failures occur mostly at the tail-gate corners and less frequently along the sidewalls of head-gates and development entries. In room-and-pillar mining, unstable compressive failures usually occur in pillars and

entry walls. With the presence of large geological discontinuities in mining areas, unstable shear failures mostly take place along the geological discontinuities.

One of the methods of mitigating rockburst events in deep mines is improving the mine layout by taking into consideration the unstable failure potential around the work faces. The available numerical models provide reasonable estimations of stress build-up and potential failure regions around excavations, however, these models have not been used to their full potentials for failure stability analyses. There is a need for exploring the capabilities of the existing numerical modeling programs in identifying not only the failure potentials but also the stability of these failures so that design based measures can be taken against rockburst events.

1.2 Research Objective

The main objective of the research is to develop a better understanding of the mechanisms of unstable failures that lead to coal bursts in underground coal mines by studying the stability of failures using an advanced numerical analysis program. The numerical modeling program Universal Distinct Element Code (UDEC) was selected for the analyses because of its specific capabilities in modeling both rock discontinuity failures in shear and rock failures in compression. Due to the scarcity of the literature on using numerical models for failure stability analyses, the first objective was to show the capabilities of UDEC in differentiating between stable and unstable failures based on a credible failure criterion. Following the accomplishment of this objective (Chapter Three), the study focused on addressing the following questions relating to the mechanistic studies of failure stability:

- How do loading stiffness and post-peak modulus affect the failure stability in rock materials and of rock discontinuities?
- How to identify key signatures from the modeling results that can be used to clearly distinguish the failure stability?

- How do mining/excavation advances affect the failure stability of existing rock discontinuities that located nearby?
- How do the factors (e.g. the extent of excavations, the location of rock discontinuities and elastic modulus of surrounding rocks) influence the failure stability of existing rock discontinuities?
- What is the significance of roof-coal and coal-floor contact surfaces on the failure stability of coal materials?

Accomplishment of the main objective and answering the questions list above can extend our understanding of the mechanisms involved in unstable failures/rockburst events in underground mining conditions. It, hence, can help to achieve safer underground mine designs and alleviate and manage rockburst hazards.

1.3 Methodology

The first task is to validate the ability of the numerical program to simulate stable and unstable failures based on the stiffness criteria proposed by Cook (1965b), Salamon (1974) and Rice (1983). The ability of UDEC, with the application of the continuously yielding (CY) joint model, to simulate unstable shear failures of rock discontinuities is validated by performing a series of simulations with a double shear test (DST) configuration. The capability of the program to simulate stable and unstable compressive failures of rock materials is validated by conducting a series of simulations with a uniaxial compressive strength (UCS) test configuration. Signatures of unstable failures are identified in the process of the UCS and DST simulations. UDEC is then used to simulate and analyze the shear failure stability of a rock discontinuity loaded by an advancing underground excavation. Loading stiffness is considered in the model. The factors that affect the loading stiffness are studied in a series of simulations. Finally, a model consisting of a coal layer located between two rock layers (i.e. roof and floor layers) is built. The mechanical behaviors of the roof-coal and coal-floor con-

tact surfaces are taken into consideration as the possible factors that contribute to unstable compressive failures at mining faces and sidewalls in underground coal mining conditions.

1.4 Thesis Organization

This thesis is organized to address the logical and scientific approaches for achieving the research objective. The problems that need to be explained in order to better understand the mechanisms involved in unstable failures in underground coal mining conditions are described and analyzed sequentially.

Chapter One is the introduction section of the thesis. It presents the general information of unstable failures and rockbursts in underground mines, addresses the objective of the research as well as the applied methodology and it introduces the organization of the thesis.

Chapter Two is the literature survey section. It reviews the history of rockburst events in underground mines in different countries and the history of rockburst research. It then describes the important advancements in the rock mechanics field in terms of rockburst studies and discusses the relevant available theoretical analysis methods for unstable failure/rockburst problems. The important physical tests and advanced numerical studies of rockbursts are also introduced. The chapter ends with addressing the factors that contribute to rockbursts and the mechanisms involved in such violent events.

Chapter Three presents the double shear test simulations for the validation of UDEC's capability of simulating stable and unstable failures of rock discontinuities. The post-peak softening model (CY joint model) and the elastic-plastic joint model (Mohr-Coulomb joint model) are used in different simulations. The signatures of unstable shear failures are identified in the model. The behaviors of the CY joint model under different normal stresses are also investigated.

Chapter Four addresses a study on the failure stability of a geological discontinuity located in the vicinity of an advancing excavation. Stable and unstable shear failures along the rock discontinuity are identified from the model results. Loading stiffness is studied in a series of simulations with different model configurations (i.e. different extents of the

excavated area, different locations of the discontinuity and different elastic moduli of the rocks).

Chapter Five discusses the possible mechanisms of unstable compressive failures in mining faces and sidewalls in underground coal mining conditions. The mechanisms consider sudden and rapid loss of confinement to coal materials resulted from unstable shear failures and weak contact regions at roof-coal and coal-floor interfaces. A series of numerical simulations performed to study unstable compressive failures are presented and discussed in this chapter as well.

Chapter Six concludes the thesis by summarizing the key findings and introduces some possible future work.

CHAPTER 2

LITERATURE SURVEY

As one of the most important human activities since the Industrial Revolution, underground mining was extensively operated even before the existence of adequate engineering knowledge in this field. On the one hand, underground mining provided a considerable portion of natural resource that utilized in advancing every aspect of the civilization; on the other hand, underground mining resulted in serious hazards that could harm both workers in underground mines and people on the surface. Among many hazards, rockburst has been considered as the most dangerous and mysterious one for many years.

Rockburst is essentially a sudden, violent unstable failure that results in damage to equipment, delay in production, and injury or even fatality of workers. To achieve safer underground mining and tunneling operations, the understanding of rockburst mechanisms needs to be advanced. There is a large body of literature focused on rockburst studies. Some of them that related to the mechanisms or mining conditions that have been associated with rockburst and prediction of rockburst events during mining, to the best of the author's knowledge, are discussed in this chapter in a structure with the combination of thematic and chronological descriptions. In addition to presenting the current state of research related to my thesis, definitions and the classification of rockburst and historical information are presented in the beginning of this chapter. The second part of the chapter focuses on key findings, current theories and physical and numerical studies regarding rockburst problems.

2.1 Definitions of Rockburst

There are many different definitions of rockburst in rock mechanics and mining engineering fields. Based on the literature the author reviewed, the following definitions appear to be more widely used:

Coates (1965) defined rockburst as the term applied to the cases of rock failure that combine suddenness and violence accompanied by the sudden release of all the strain energy on a sufficiently large scale to endanger openings, equipment or personnel.

Cook et al. (1966) defined rockburst as damage to underground workings caused by the uncontrolled disruption of rock associated with a violent release of energy additional to that derived from falling rock fragments.

Muller (1991) described rockburst in coal mines as the spontaneous release of elastic energy, which is largely transformed into kinetic energy and leads to abrupt lateral displacements of the coal seam.

A more practical comprehension of rockburst in U.S. mines is in the regulatory definition (30 CFR 57.3000): a sudden and violent failure of overstressed rock resulting in the instantaneous release of large amounts of accumulated energy (Whyatt et al. 2002).

One of the reasons different definitions exist is because researchers tend to develop or modify an existing definition so that it better defines rockburst with respect to their research backgrounds, experiences and the unique characteristics of their research problems.

The existence of two conditions is necessary for rockburst. Firstly, the stress developed on rocks or rock discontinuities must exceed their strength. Secondly, the energy released by surrounding rocks (i.e. loading system) must be greater than the energy that can be consumed by the failure process. Essentially, a rockburst is a mode of failure – an unstable failure; however, an unstable failure may or may not be a rockburst (if an unstable failure causes no damage and injury, it is not considered as a rockburst in underground mining conditions). The terminologies "rockburst" and "unstable failure" are used interchangeably in some literatures although they are not the same concept. The term "rockburst" is often used to describe large scale unstable failures on site. Once considering the theoretical and mechanical analyses of rockburst, the term "unstable failure" is more favorable. The author also decided to use these two terms interchangeably because they describe the same problem in terms of the mechanisms. In the context of this thesis, therefore, a rockburst is

defined as an unstable failure of rocks or existing rock discontinuities (e.g. faults or bedding planes) exhibiting rapid changes in their stress states (i.e. normal stress and shear stress). The term "rockburst" will be mostly appeared in the literature survey chapter since most researchers used this term in their work. The term "unstable failure" will be mostly used in other chapters because theoretical and numerical analyses are the main components of these chapters.

2.2 Classifications of Rockburst

Ortlepp et al. (1994) suggested a classification for rockburst in underground tunneling conditions (Table 2.1) based on their essential nature and seismic magnitudes.

Table 2.1: A suggested classification of rockburst, after Ortlepp (1994).

Rockburst Type	Postulated Source Mechanism	First Motion from Seismic Records	Richter Magnitude M_L
Strain-bursting	Superficial spalling with violent ejection of fragments	Usually undetected, could be implosive	-2.0 to 0
Buckling	Outward expulsion of larger slabs pre-existing parallel to surface of opening	Probably implosive	0 to 1.5
Pillar or face crush	Sudden collapse of stope pillars, or violent expulsion of large volume of rock from tabular stope face or tunnel face	Possibly complex, implosive and shear	1.0 to 2.5
Shear rupture	Violent propagation of shear fracture through intact rockmass	Double–couple shear	2.0 to 3.5
Fault-slip	Sudden movement along existing fault	Double–couple shear	2.5 to 5.0

In underground mining conditions, rockbursts are commonly categorized into three types based on their underlying mechanisms: strain bursts, pillar bursts, and fault-slip bursts. Strain bursts usually occur at the edge of mine openings (i.e. sidewalls) due to local high stress concentrations. Pillar bursts occur when the stress on a pillar exceeds its ultimate strength in the condition that a large amount of strain energy can be released during the failure process. Fault-slip bursts take place when the strength of a geological discontinuity is exceeded by the shear stress developed on it with a release of available excess energy. Several researchers classified rockbursts into two main categories based on their spatial relationship with the working areas in underground mines (McGarr et al. 1975; Stiller et al. 1983; Gibowicz 1984): (1) events that mainly result from stress concentrations and occur near the active mine working areas, and (2) events caused by interaction between the mining-induced stresses and tectonic stress fields, which not only can occur in the vicinity of the working areas but also at a distance of hundreds of meters away.

In this thesis, rockbursts are categorized into two types: *strain-type rockburst* and *slip-type rockburst*, based on mechanisms involved in failure processes. A strain-type rockburst is an unstable failure in rock materials of underground structures (e.g. mining faces and sidewalls) due to highly concentrated stress and available excess energy. A slip-type rockburst is an unstable shear along existing geological discontinuities (e.g. faults and bedding planes) due to high shear stresses and available excess energy from the loading system (i.e. the surrounding rocks) in failure processes.

2.3 Rockburst History

A brief history of the occurrence of rockburst events is presented in this section to illustrate that rockbursts have been and are problematic and costly to mining operations throughout history, and therefore a better understanding of the underlying mechanisms of rockburst is needed.

2.3.1 Hard Rock Mining

The earliest documented rockburst event dates back to 1738, which was associated with mining in the British Derbyshire lead ore mine (Bukowska 2006). Since then, rockbursts have been recorded in many countries for underground mining operations in both hard rock mines and coal mines. Rockbursts were observed in ore mining in Czech Republic, United Kingdom, South Africa and Australia; in salt mining in Germany and France; and in stone and underground coal mining.

In South Africa, rockbursts became a major hazard in the Witwatersrand gold mines at the beginning of the 20th century (Cook et al. 1966). It was believed that the very deep and extensive tabular mining were the factors that made rockburst hazards in this region the most severe ones in the world (Ortlepp 2005). These hazards used to account for as many as 100 fatalities per year (Hagan et al. 1998). The situation has been improved considerably in recent years. However, there is no doubt that the problem has not been solved yet (Ortlepp 2005).

In Canada, the first recorded rockburst occurred in 1928 (Ortlepp 2005). In the beginning of 1980's, rockbursts became a growing problem in Northern Idaho hard rock mines. From 1984 to 1986, there were about 325 rockburst events occurred in Eastern Canada, as shown in Table 2.2 (Hedley and Udd 1989).

In Australia, rockbursts were first recognized as a major but relatively occasional problem in the Kalgoorlie district in the early 1900's (Hedley and Udd 1989). With increasing extraction ratios and depths of orebodies, an increased prevalence of rockburst problems had been experienced in the last decade of the 20th century.

In India, the occurrence of a rockburst was first reported in the Kolar Gold Field in Mysore in 1928. The Kolar Gold Field is located in southeast India, and the mining operations were at depth of 2000 meters and greater (Itasca Consulting Group 1987). As mining became deeper and more extensive, widespread damage caused by rockbursts started to affect main infrastructure (Ortlepp 2005), and resulted in many fatalities and costly damage

(Krishnamurthy and Shringarputale 1990).

In the U.S., the first rockburst was reported at the Atlantic copper mine in Michigan in 1904 (Bolstad 1990). Rockbursts started to occur in the Coeur d'Alene Mining District in Northern Idaho since the 1920's (Itasca Consulting Group 1987). By the late 1930's, rockbursts became a serious concern regarding the safety in this mining district (Bolstad 1990).

Table 2.2: Rockbursts in Ontario mines, 1984-1986, after Hedley and Udd (1989).

Mining District	1984	1985	1986
Red Lake	26	5	10
Elliot Lake	59	88	22
Sudbury	16	31	56
Kirkland Lake	5	3	4
Total	106	127	92

2.3.2 Coal Mining

In underground coal mining, rockbursts occurred mostly in Poland, Czech Republic, Germany, France, Slovenia, Russia, India, China, USA, Canada and Australia (Bukowska 2006).

In China, many deep mines have experienced rockbursts. According to the available literature, the first rockburst event in China occurred in 1933 at Shengli Coal Mine in Fushun City, Liaoning province (Pan et al. 2003). Since then, rockbursts have been reported at 102 coal mines that located in many major mining districts in China (Li et al. 2004). Among the reported rockburst events, approximately 83.6% occurred in coal mines. The coal mines with rockburst problems are mostly located in the east part of China (Li et al. 2007).

In the U.S., the first rockburst in coal mines in the U.S. occurred in 1936 based on the U.S. Bureau of Mines (USBM) Coal Bump Database. However, several documents indicated that possible rockburst problems existed in coal mines predating 1936 USBM

database (Iannacchione and Zelanko 1995a). The USBM Coal Bump Database shows that rockbursts related accidents had caused 78 fatalities between 1930 and 1995, as shown in Table 2.3. Among the 42 fatalities resulted from the rockbursts occurred between 1960 and 1995, 14 are in the Eastern U.S. and 28 are in the Western U.S..

Table 2.3: Chronological distribution of rockburst events included in the USBM Coal Bump Database.

Time Period	Number of Rockbursts	Fatalities	Injuries
1930-1939	1	1	0
1940-1949	9	7	18
1950-1959	38	28	43
1960-1969	27	13	36
1970-1979	30	10	21
1980-1989	52	19	32
1990-1995	9	0	8

2.4 A Brief History of Rockburst Research

With rockburst problems emerging in underground mines all over the world, governments and companies started funding research that focused on rockburst problems. In South Africa, the Ophirton Earth Tremors Committee started to look into rockburst problems in 1908. The committee concluded that the problems were due to the crushing of support pillars and recommended that waste packs should be used to replace the pillars. In 1915 the assignments were appointed to Witwatersrand Earth Tremors Committee, which included reporting on the origin of rockbursts and their influence on underground workings and on surface buildings. Further appointment of the Witwatersrand Earth Tremors Committee was made in 1924. The committee recommended many specific techniques to reduce the rockburst hazards, such as leaving large protective pillars and over-stoping of inclined shafts. The formal research project was conducted since 1953 with four phases to acquire empirical experience, to develop hypotheses regarding specific aspects of rockburst problems, to postulate mechanisms of rockbursts, and to design controlled experiments in underground mines sequentially (Cook et al. 1966; Ortlepp 2005).

In Canada, the first rockburst research committee was established in 1939 to look into the rockburst problems that occurred in the Kirkland Lake area of Ontario (Ortlepp 2005). In 1984, a serious episode of rockburst problems at the Falconbridge Mine resulted in four fatalities. The result of these fatalities and the Stevenson Inquiry Report led to the initiation of the Canadian Rockburst Research Program (CRRP) as a collaborative research project of the Mining Research Directorate (MRD). The program was lead by the Canadian Centre for Mineral and Energy Technology (CANMET) with funding from mining industry and both the Federal and Ontario Provincial Governments (Hedley and Udd 1989; CAMIRO Mining Division 1990).

In Australia, the Mine Seismicity and Rockburst Risk Management project (MSRRM) was initiated at the Australian Center for Geomechanics (ACG) based at the University of Western Australia in August 1999. This project is known as the only Australian based rockburst research program and it contributes to the early implementation of seismic monitoring technology in Australian. Besides the MSRRM project, the University of Queensland, the Western Australia School of Mines in Kalgoorlie, and other universities are also active in rockburst research areas (Ortlepp 2005).

According to available literature, majority of rockburst research commenced approximately in the 1960's in China. Many universities and government agencies worked with mines that experienced rockburst problems. For example, researchers from the Beijing University of Science & Technology and Fushun Municipal Seismology Bureau extensively studied the rockburst events at Laohutai Coal Mine, Liangning Province. The results of the study greatly helped in mitigating the rockburst problems in that mining region. Although major development has been made in China in the area of rockburst research, most of work has limited exposure in the English countries due to the language barrier (Li et al. 2007). The earliest research in the U.S. was initiated by the USBM in the late 1930's (Bolstad 1990). In 1941, the Denver Research Laboratory of the USBM carried out a rockburst research program, which was motivated by a major rockburst event at the Sunshine Mine that

resulted in two fatalities. At the same year, microseismic monitoring systems developed by the USBM were installed and tested at the Sunshine Mine. The Spokane Research Laboratory started to investigate rockburst at the Coeur d'Alene Mining District in Northern Idaho in 1951 (Jenkins et al. 2006). To better understand rockburst events in underground coal mines in the U.S., the USBM compiled the Coal Bump Database which contains more than 172 coal mine rockbursts that identified from various documents (Iannacchione and Zelanko 1995a). In 1995, the National Institute for Occupational Safety and Health (NIOSH) took over the responsibility of conducting rockburst research due to the closure of USBM. Many important theories, physical tests and numerical methods were developed in the researches carried out in different counties. The most important ones and those relevant to this thesis will be discussed.

2.5 Post-Peak Behavior of Rocks and Rock Discontinuities

Two basic aspects toward understanding rockburst are the capability of stress analyses of underground excavations and the grasp of the behaviors of rock materials. In 1964, Salamon (Salamon et al. 1964) applied the theory of elasticity to the problems in mining tabular deposits, and the study produced important theoretical results that were utilized as a solid component in other researchers' work. Until 1960's, only an ideally-elastic model and an ideally-plastic model were available and frequently applied in underground mining related issues to represent mathematical descriptions of the behavior of rock materials and predict deformation of underground excavations under external loads. Problems in underground mining operations, such as design of pillars and excavations, were analyzed primarily using empirical rules based on phenomenological observations obtained by experienced miners and researchers. As a major and well-known safety issue in underground mines, rockburst along with other problems in mining operations were studied qualitatively due to inadequate experimental analysis of rock materials (Linkov 1996). One important physical experiment of obtaining information about rock behaviors is uniaxial compressive strength (UCS) tests. However, researchers found that the rock specimens tested in conventional laboratory UCS

tests became unstable as soon as their strengths were exceeded, and result in inadequate information about the post-peak behavior of the rock specimens. The absence of the knowledge about the behavior of rock materials between their elastic regions before the onset of failures and their residual strengths after the failures was the major obstacle towards the understanding of characteristic behavior of rock materials, the development of quantitative analysis of rockburst, and the advancement of constitutive models for rock materials.

It was the analytical studies from South Africa that helped significantly progress rockburst research to the next level. In 1965, Cook published two very important papers with regard to the absence of laboratorial and theoretical analysis of rock instability (Cook 1965b; Cook 1965a). In the first paper titled "*A note on rockbursts considered as a problem of stability*" (Cook 1965b), he proposed a hypothetical stress–strain curve of rocks (Figure 2.1), based upon his experimental work that was published later in his second paper (Cook 1965a). He claimed that "the jack-specimen system became unstable when an increment in the specimen strain resulted in a greater loss of the specimen strength than jack stress, that is, $(d\sigma/d\varepsilon)/k > 1$" ($k$ is the stiffness of the loading system) (Cook 1965b), and based on which he made the first theoretical analysis of rockbursts in typical underground longwall mining conditions. Cook also made an important hypothesis on how you could differentiate between a stable and unstable failure. The exact words he used were "that energy, in addition to that stored as strain energy in the specimen at point a, must have been added for violent fracture of the rock to have occurred" (Cook 1965b). Note that point "a" in this quote refers to point "a" shown in Figure 2.1. This concept is the basis of the Energy Release Rate (ERR) concept, which is widely applied in designing extraction patterns of underground mining. In the second paper "*The failure of rock*" (Cook 1965a), he showed that the non-elastic behavior of hard rocks can be described by a curved Griffith locus in the strain–stress relationship based on an analysis of changes in energy associated with the extension of Griffith cracks. He also provided the experimental results that served as the experimental basis for the analytical predictions in this paper and the hypothesis in the first paper (Cook 1965b).

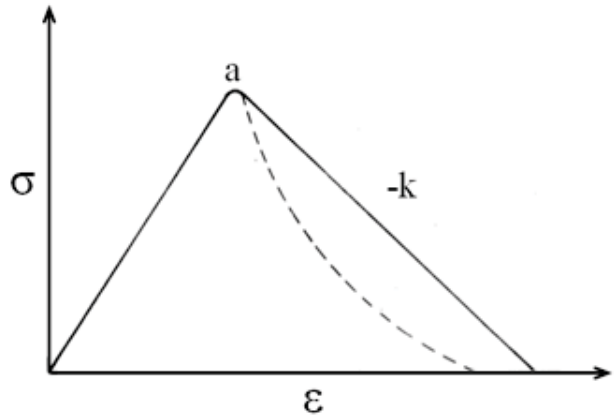

Figure 2.1: The hypothetical stress–strain curve for rock under uniaxial compression (a: point indicates maximum strength; −k: the stiffness of the loading system), after Cook (Cook 1965b).

The concepts proposed by Cook lead to many studies focused on fracture propagation and post-peak behavior of rock materials using newly designed stiff machines and servo-controlled test machines (Bieniawski 1967; Wawersik and Fairhurst 1970; Hudson et al. 1971; Hudson et al. 1972; Peng and Johnson 1972; Peng 1973). Due to the contribution from Cook and many studies that followed his work, the complete force–deformation curves for different types of rocks became available to researchers.

Existing rock discontinuities can greatly affect the mechanical properties of rock materials. Studies of the behaviors of rock discontinuities were carried out in parallel with the studies of the behaviors of rock materials. The knowledge of the behaviors of geological discontinuities (e.g. joints and faults) is crucial for understanding slip-type rockbursts. One important aspect of the behavior of joint is its deformability. The complete shear force–displacement curves of rock discontinuities were obtained in laboratory tests. Theoretical, experimental, and numerical analyses were conducted with respect to the joint behaviors (Barton 1972; Barton and Choubey 1977; Bandis et al. 1983). The shear behavior of a joint is complex and depends on many factors, such as material properties, filling material properties, boundary conditions, joint surface geometry, and size of the joint (Simon 1999). With the knowledge of the complete behavior, especially the post-peak behavior, of

rocks and rock discontinuities, theoretical studies of rockburst started to be developed and advanced.

2.6 Theoretical Analysis of Rockburst

Many theories have been developed to investigate rockburst problems. Among them, Cook's stiffness criterion (Cook 1965b) is the one with the most acceptance and widest applications. The catastrophe theory, as the newly adopted mathematical theory in rock mechanics and mining engineering, also shows its potential for analyzing rockburst problems. These two theoretical analysis methods are introduced in this section. Energy release rate and excess shear stress are also briefly discussed as important analytical methods used in rock mechanics and rock engineering.

2.6.1 Stiffness Criterion

The stiffness criterion, initially proposed by Cook (1965b), is widely accepted as the criterion for the failure stability (stable or unstable failure) of rocks in compression that may cause strain-type rockbursts in underground mining conditions. This criterion is expressed schematically in Figure 2.2. The solid line represents the characteristic stress–strain behavior of a rock specimen. The post-peak region of the specimen's stress–strain curve can only be obtained under stiff or servo-controlled loading machines. The dashed lines represent the loading system stiffness. In the case of laboratory UCS tests, the loading system stiffness is the overall stiffness of the test machine. In the case of pillars or sidewalls in underground mines, the loading system stiffness is the stiffness of roof-floor system which is also known as the mine stiffness.

When normal stress exceeds the ultimate strength of the rock specimen, failure initiates. According to the stiffness criterion, the failure is stable when the post-peak stiffness of the specimen is smaller in absolute value than the loading system stiffness, as in the case of the stiff loading system indicated by the blue line in Figure 2.2. The failure is unstable when the post-peak stiffness of the specimen is larger in absolute value than the loading

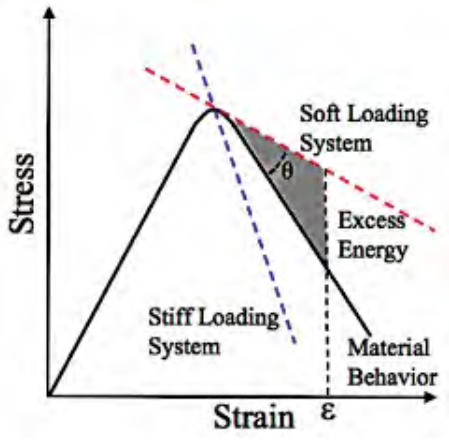

Figure 2.2: Illustration of the stiffness concept for the stability of rock materials in compression.

system stiffness shown as the soft loading system condition (the red line) in Figure 2.2. It is believed that in the process of an unstable failure, the strain energy stored in the loading system suddenly transfers into the rock specimen and contributes to the unstable failure of the rock specimen. The amount of energy represented by the grey triangle area in Figure 2.2 is the amount of available "excess energy" during an unstable failure process at a given strain ε of the specimen. The intensity of such an unstable failure is determined by the difference between the rock's post-peak stiffness and its loading system stiffness as indicated by the angle θ in Figure 2.2. As the angle θ increases the intensity of the unstable failure increases.

Salamon (1974) and Rice (1983) extended the stiffness concept to account for unstable failures of rock discontinuities that are also known as slip-type rockbursts in underground mines. The stiffness criterion for unstable failures of rock discontinuities is schematically shown in Figure 2.3. In the figure, k_{ls} represents the loading system stiffness, and k'_p represents the post-peak stiffness of the discontinuity shear stress–displacement curve. According to the stiffness criterion, unstable failures of rock discontinuities occur when the loading system stiffness is smaller in absolute value than the post-peak stiffness of discontinuity shear stress–displacement curve as shown in Figure 2.3a. The condition that the loading system stiffness is larger in absolute value than the post-peak stiffness of the discontinuities only

result in stable failures as illustrated in Figure 2.3b. In the case of unstable failures, the area between the loading system stiffness and post-peak stiffness of discontinuities' shear stress–displacement curve, as indicated by the hatched area in the figure, is considered as the amount of available excess energy that gives rise to the unstable failures. The intensity of the unstable failures increases with increase in the amount of the available excess energy.

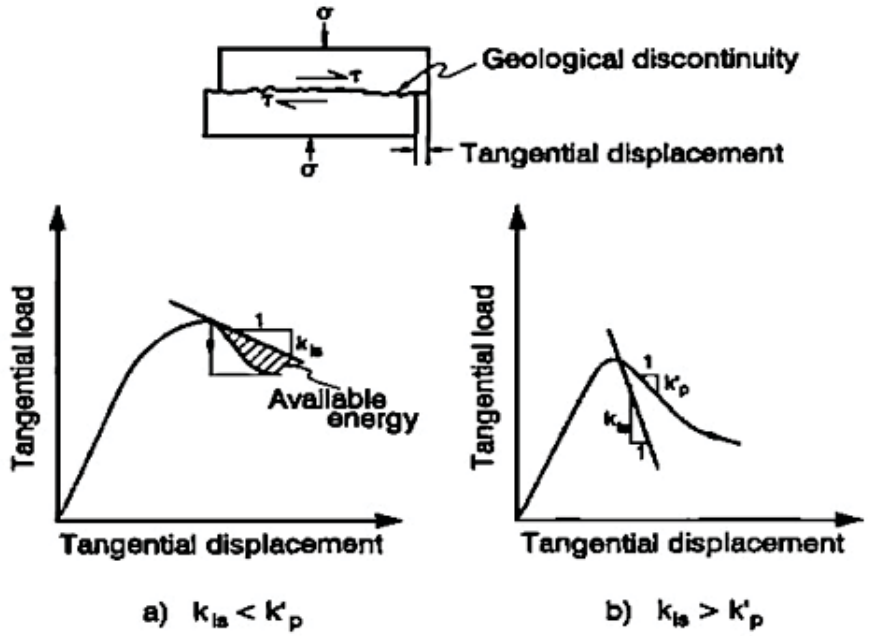

Figure 2.3: Influence of the relative stiffness of the loading system on the failure stability of discontinuities: (a) unstable failure, (b) stable failure; after Salamon (1974).

2.6.2 Catastrophe Theory

Catastrophe theory is a mathematical technique for analyzing natural phenomena that involve discontinuities or sudden changes in parameters (Henley 1976). The theory states that the behavior of a system is described by a finite set of variables (x_1, x_2,..., x_n,), and this system is controlled by another finite set of variables (p_1, p_2,..., p_m). For given values of p_i, the system has equilibrium values of x_i which correspond to stationary values of a potential (energy) function $V(x)$. Maximum $V(x)$ represents an unstable equilibrium condition, while minimum $V(x)$ represents a stable equilibrium. The p_i is referred to as

control variable, and the x_i is state variable. Limit the control space p_1, p_2,..., p_m to four dimensions (space-time model), then there are only seven elementary types of catastrophes. The simplest catastrophe, known as a cusp catastrophe, is introduced in this section. The cusp catastrophe has one state variable and two control variables. The potential function of the cusp catastrophe is

$$V(x) = \frac{1}{4}x^4 + \frac{1}{2}p_1x^2 + p_2x \tag{2.1}$$

where x is the state variable and p_1, p_2 are the control variables. The first derivative of this function with respect to x is a cubic function shown as follows

$$\frac{dV(x)}{dx} = x^3 + p_1x + p_2 \tag{2.2}$$

Figure 2.4shows the equilibrium surface $dV(x)/dx = 0$ of the system and the projection of the equilibrium surface, known as the control surface. As shown in the figure, the equilibrium surface contains a fold or pleat. The p_1-axis and p_2-axis (horizontal axis) represent the values of the control variables p_1 and p_2, and the x-axis (vertical axis) represents the values of the state variable x. The movement of the equilibrium state can be either smooth or discontinuous. For example, point B in Figure 2.4 experiences a smooth action moving towards point B'. However, point A undergoes a sudden jump to lower equilibrium surface when point A passes the edge of the fold, which implies that a small change in the control variables can trigger a catastrophe change in the state variable. Wang et al. applied the cusp catastrophe in a simple rock-rock model to investigate the mechanisms of pillar rockbursts (Wang et al. 2006). They claimed the analysis of the model with the application of the cusp catastrophe led to a conclusion that rockbursts occur when the stiffness of the loading system in absolute value is less then the stiffness of the post-peak slope of the force-deformation curve of rocks.

Besides the rockburst problems (Pan et al. 2006; Qin et al. 2006; Wang et al. 2011; Pan et al. 2009), the cusp catastrophe has been applied to deal with many other discontinuous phenomena, such as fault movement, fault earthquake and slope stability (Shi et al. 1996;

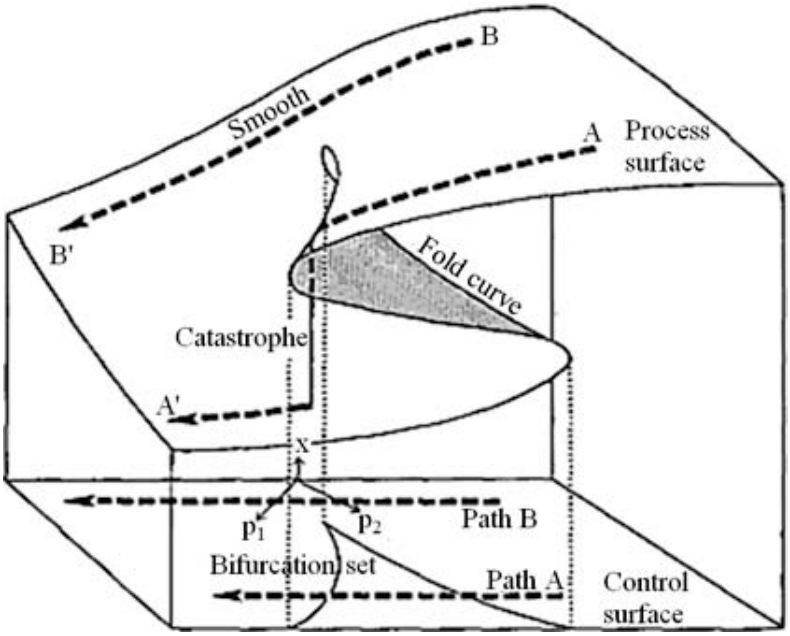

Figure 2.4: The equilibrium surface and bifurcation set of the cusp catastrophe, after (Cubitt and Shaw 1976).

Pan and Li 2010; Cubitt and Shaw 1976; Qin et al. 2001).

The criterion drawn from the cusp catastrophe analysis for rockburst is the same as Cook's stiffness criterion, which provides more confidence in utilizing the stiffness criterion. The stiffness criterion is used in this thesis for validation of the ability of the numerical program to simulate stable and unstable failures.

2.6.3 Energy Release Rate and Excess Shear Stress

Energy release rate (ERR) concept was originally developed in South Africa by Cook et al. (1966). ERR concept describes an assumption that violent failures occur only when the rate of energy release in the process of mining is larger than the rate of non-violent energy dissipation. This concept suggests a critical excavation size for a given depth, over which rockburst events are possible. Salamon (1974) expanded ERR concept by showing that the relationships among the energy components could be applied to any mining configuration for elastic conditions. ERR concept gained wide acceptance in South Africa, and it was used for stope design in deep underground mines in South Africa (Cook 1978; Spottiswoode 1990).

ERR can be applied to evaluate various mining strategies in terms of rockburst potential. However, ERR cannot indicate the locations of potential rockburst events.

Excess shear stress (ESS) concept was proposed by Ryder (1988) to assess the possible magnitude and relative likelihood of shear-type rockburst. It is defined as,

$$ESS = |\tau| - \mu\sigma_N \tag{2.3}$$

where τ is prevailing shear stress prior to the slip of a rock discontinuity, μ is coefficient of kinetic friction and σ_N is the normal stress on the discontinuity. The key parameters required in ESS analysis are the dynamic friction angle and possible maximum stress drop. Ryder claimed that the representative values of those two parameters for weakness planes may be 30° and 10 MPa respectively. ESS analysis can be used to supplement ERR analysis in the areas with geological structures. ESS does not consider the possible gradual process of shear stress drop that leads to stable failures. The study in this thesis considers the failure stability of existing geological discontinuities and the locations of the failure under the disturbance of underground mining.

2.7 Physical Tests and Numerical Techniques for Rockburst Research

Physical tests play an important role in studying rock mechanics and rock engineering problems as they can provide crucial information about rock properties. Since rockbursts are recognized as one of most complicated problems in rock mechanics and rock engineering, various types of physical tests (including laboratory and on-site tests) were designed and implemented to investigate the rockburst problems. Burgert et al. (1981) used epoxy resin Araldite B containing 3-5% hardener to model translatory rockbursts on the laboratory scale. The experiments indicated that the existence of a fracture zone and two elastic zones within rocks prior to rockburst. They also demonstrated that the materials with burst-proneness exhibit anomalous elastic-plastic coupling behavior, which means the elastic deformation superimposed on the broken plastic portion of rocks.

Rockbursts in underground mines result in ground motion that may provide useful information for rockburst studies. In most rockburst events, however, insufficient ground motion data were recorded in the vicinity of large seismic sources. New means needed to be applied to obtain important ground motion data in rockburst events. As a new method, a simulated rockburst experiment was conducted by detonating a large explosion in an unused tunnel and access crosscut with depth of 1600 m on Kopanang Mine in the Klerksdorp region (Hagan et al. 2001; Milev et al. 2001). Many findings were obtained from this experiment. Some of them are expressed as follows,

- Two damage areas were identified: (a) an area with a relatively high intensity of damage with a ground velocity of 3.3 m/s, (b) an area with a relatively low intensity of damage with a ground velocity of 1.6 m/s.

- The speed of the ejected rock fragments measured in the region of low intensity damage was in the range of 0.7 m/s to 2.5 m/s.

- The shape of rock fragments ejected from the wall was determined by the rock fractures, natural bedding planes, and the induced fractures in the process of tunnel development.

Vacek et al. (2008) used physical and mathematical modeling techniques to study rockbursts in an excavation of a horizontal coal seam. The results of the experiments showed that rockburst initiated with a small extrusion of rock mass, and followed by the main burst. Small extrusions of rock mass sometimes occurred at the end of the rockburst events. The extruded rock mass was located only on the narrow portion of the rock layer (the width of the strip was about 15-40% of the height of the rock layer) that close to the free surface of the rock. The results also suggested that the loading speed considerably affected both the number and intensity of rockburst.

To analyze strain-type rockburst in rock surfaces due to excavation, a rapid unloading of radial stress and rapid increase in tangential stress with an approximately unaltered intermediate stress needed to be modeled. To fulfill this need, a true-triaxial rock test system

was developed. This test system can provide dynamic loading and unloading independently in three principal stress directions. With the test system, many rockburst studies were conducted in laboratory conditions. Some conclusions drawn from the results are present as follows,

- Sudden unloading in one horizontal direction of a rock sample resulted in ejecting a thin layer of rock fragments, which is similar to the rockburst process observed on sites due to excavation or tunneling (He et al. 2010).

- The percentage of intra-granular cracks within fragments from rockburst tests was larger than that from uniaxial compressive tests, which implied that the stored energy in rockburst exceeded that in uniaxial compressive tests (He et al. 2010).

- Generally, fragments from rockburst tests had a much rougher surface then that from the uniaxial compression and confined compression tests (He et al. 2011).

- Mass and velocity of ejected fragments were important for identifying the energy transfer in rockburst tests. The bedding plane orientation was a main factor for assessing rockburst proneness of rock materials (He et al. 2012).

Most physical studies were related the strain-type rockburst because it is difficult to conduct physical tests for slip-type rockburst. To study slip-type rockburst, researchers typically use advanced numerical modeling programs. In this thesis, slip-type rockburst (unstable shear failure) is investigated using the distinct element code UDEC. Strain-type rockburst (unstable compressive failure) is also studied using UDEC, and some proposed mechanisms for unstable compressive failures are simulated and analyzed.

Nowadays, numerical methods and computing techniques have become readily available tools that utilized by engineers and researchers for many engineering and scientific problems that cannot be handled before. The available numerical techniques can be generally categorized as follows,

- Finite Element Method (FEM)
- Boundary Element Method (BEM)
- Discrete Element Method (DEM)
- Finite Difference Method (FDM)

An article written by Jing (2003) discussed techniques, advances, problems and future developments and applications of almost all types of available numerical methods in rock mechanics and rock engineering. Numerical methods have been applied to study fracture generation and propagation (Amitrano 2006; Feng et al. 2006; Tang and Kou 1998), inhomogeneity of rock materials (Lan et al. 2010; Ma et al. 2011), behavior of rock materials (Cho et al. 2007; Sainsbury et al. 2008; Lu et al. 2010; Shimizu et al. 2010; Park et al. 2004; Wang and Tonon 2009; Bahaaddini et al. 2011; Espinosa and Zavattieri 2003a; Espinosa and Zavattieri 2003b; Hajiabdolmajid et al. 2002; MasIvars et al. 2011), behavior of discontinuities (Cundall 2000; Lobo-Guerrero and Vallejo 2005; Yan et al. 2012; Park and Song 2009; Karami and Stead 2008), behavior and stability of pillars (Yacoub and Curran 1999; Elmo and Stead 2003; Griffiths et al. 2002; Jaiswal and Shrivastva 2009; Pietruszczak and Mroz 1980), underground mining and tunneling operations (Badr et al. 2003; Cai 2008; Golshani et al. 2007). This thesis focuses on using numerical models to analyze rockburst. Below are selected articles and papers that are relevant to this thesis.

Lemos (1987) and Cundall and Lemos (1990) described some numerical simulations with the application of the numerical program UDEC (Cundall 1971) and the continuously yielding (CY) joint model (Cundall and Hart 1984) to study the stability of an existing geological discontinuity nearby an underground excavation. The study indicated that UDEC with the application of the CY joint model could be used to simulate unstable failure of rock discontinuities in the program's dynamic mode. The work done in this thesis expands on the previous work and develops new methodologies for further and detailed studies of unstable shear failure of rock discontinuities, specifically, an existing geological discontinuities in the

vicinity of an active excavation. Failure stability, mine stiffness, various factors affecting unstable failure, and some other important aspects are discussed.

To simulate shearing process of rock discontinuities, Zou et al. (1989) used a mathematical model that describes a single block connecting to a far-field boundary by a spring. The results of the simulations showed that low elastic modulus of rocks in the vicinity of rock discontinuities, high normal stress on the rock discontinuities, high loading speed, and the initial shear stress that exceeded the shear strength of discontinuities provided a high potential of unstable failure. Bardet's (1989) study demonstrated the ability of finite element methods in detecting surface instability, and he claimed that the finite element methods could be used to analyze rockburst problems considering rockbursts as surface instability problems.

Muller (1991) compared a FEM based program ANSYS (1988) with a FDM based program Fast Lagrangian Analysis of Continua (FLAC) (Cundall 1976) in terms of their ability to model rockbursts. The results showed that FLAC is the proper numerical program for rockburst simulations. Hart et al. (1988) used the numerical program 3-Dimensional Element Code (3DEC) (Cundall 1988; Hart et al. 1988) to investigate the problem of slip-type rockburst associated with existing fault and dyke structures by comparing the slip and its radii in the model with actual seismic records. The study showed that the numerical simulations could reproduce slip locations and radii, and the study provided a basis for identifying key factors influencing slip-type rockburst problems. Bigarre et al. (1993) utilized 3DEC to quantify rockburst potential of major, existing geological structures. Their study indicated the ability of the numerical model to assess rockburst potential and investigate rockburst mechanisms. However, they assume all the slips along the geological structures were rockbursts by using non-softening joint model, which may not the fact because stable and gradual slip can also occur on the fault depending on the stiffness of rock environment. The occurrence of stable failure is considered in this thesis along with unstable failure, which provides better understanding of the mechanisms of slip-type rockbursts.

Chen et al. (1997) simulated a double rock sample model using the numerical program Rock Failure Process Analysis code (RFPA2D) (Tang 1997) to study the role of interaction between the failed rock mass and the surrounding rock mass in rockbursts. The results indicated that with increasing of the boundary displacement, microseismic events migrated from one sample to the other sample and changed from dispersive distribution to concentration on a fault plane. The results implied that a sudden decrease of microseismic rate in one zone and an increase of microseismic rate in an adjacent zone could be considered as a signature of incoming rockburst. Kaiser et al. (1998) applied the RFPA2D program to investigate unstable failures of rib pillars. The study showed that a soft loading system results in an unstable failure. Hence, it showed the ability of the program to reproduce the effects of loading system stiffness on the failure of pillars. It also demonstrated the RFPA program's potential for analysis of unstable failures/rockbursts.

Wang et al. (2006) built a rock-rock model using the RFPA2D program to study pillar rockbursts. The results of numerical simulations of the study also confirmed that a soft roof and floor resulted in an unstable failure while a stiff roof and floor only cause a stable failure. The simulations also reproduced the energy release and deformation jump in a rockburst. However, RFPA is not able to study slip-type rockburst because it cannot efficiently and effectively simulate large rock discontinuities. This characteristic of the program limits its application to rockburst researches. UDEC, instead, is capable of analyzing both strain and slip-type rockburst and is used in this thesis.

Hazzard et al. (2002) used a bonded particle program Particle Flow Code (PFC2D) (Cundall and Strack 1979) to simulate slip-type seismic events along faults caused by underground excavations. The study showed that many small tensile cracks were formed before the slip on the fault. The cracking/slip started at one point and propagated outwards to form an unstable failure along a large portion of the fault.

Sun et al. (2007) used the RFPA2D program coupled with the Discontinuous Deformation Theory (DDA) (Shi and Goodman 1984) to investigate rockburst events in a circular tunnel

in high in-situ stress conditions. The study showed that the natural bedding stratification of rock material and the stability of the surface rock were the factors that mainly affected rockbursts in underground tunnels. Li et al. (2008) used the numerical program FLAC to investigate the effect of underground coal mining on fault plane stress and slip displacement. The study showed that the slip displacement increases sharply due to an increase in shear stress and a decrease in normal stress when the working face advanced in the footwall towards the fault. When the working face advanced in the hanging wall towards the fault, however, the slip displacement of the fault was small due to an increase in normal stress and a decrease in shear stress. They claimed that a high potential of slip-type rockbursts exists when the working face moves towards the fault. Ishida et al. (2009) presented a work of simulating uniaxial compression test using a DEM program to investigate the influence of inhomogeneity on rock fracturing including rockburst. They concluded that the catastrophic fracturing was directly affected by formation of tensile cracks, and the energy released from a tensile crack was negligible comparing with that from a shear crack.

In the study conducted by Wang et al. (2011), the RFPA2D program was used to simulate the failure mechanism of serial and parallel rock pillars. The simulations of the serial rock pillars contributed to better understand rockbursts. The simulation results showed that not only the stiffness but also the uniaxial compressive strength of the rock pillar significantly affected the occurrence of rockbursts of pillars. The elastic rebound of the rock pillar with the higher strength caused a rockburst in the rock pillar with the lower strength, and the rockbursts only occurred in the pillar with the lower uniaxial compressive strength. In the rock mass around excavations in deep tunnels, the alternate occurrence of fractured and non-fractured zones was observed. This phenomenon was referred as the zonal disintegration. Qian et al. (2011) reported a numerical analysis considering the zonal disintegration under non-hydrostatic stress conditions. Based on the results they concluded that rockbursts occurred not only at the wall of the tunnel but also at the location far from the tunnel walls, and rockburst areas decreased as the post-peak modulus of rocks and the

fracture toughness increased.

The studies conducted by these and many other researchers have contributed to improve the understanding of rockburst mechanisms. However, the rockburst problems have not been completely solved yet. The existence of the problems drives more research activities in this field. These previous studies on modeling and mechanism of rockbursts were used as a starting point for my research. To expand and progress the work done by previous researchers more detailed numerical analyses of unstable failures were conducted for this thesis and details of the research are presented in future chapters.

2.8 Factors that Contribute to Rockburst in Underground Coal Mines

In addition to the general rockburst research reviewed in the previous section, numerous studies have been conducted to investigate the factors and conditions that occurred in underground mines that may have contributed to rockburst events. The results of the studies indicated that important factors influence rockbursts have both similarity and uniqueness. An analysis of 117 coal mine rockburst events showed that unfavorable mining practices in abutment areas causes stress concentrations and might be the primary cause of rockbursts (Holland and Thomas 1954). A few years later, Holland found that the cover thickness of 500 ft or more, a cover composed of strong members and lying close to or on the coal bed and a floor that does not readily heave are the factors on which rockbursts depended (Holland 1958).

USBM researchers collected and analyzed 172 coal rockbursts events that occurred in four Eastern States and three Western States between 1936 and 1993. The data and relevant results from this study were recorded into a database. A total of 87 fatalities and 163 injuries were identified in these events. Rockburst events have been recorded in a variety of mining systems and operations. Thick overburden (thicker than 500 ft), competent roof and floor, stress concentration, mining practice (mine layout and mining sequence), and geological structures were identified as the factors that favor the rockbursts (Iannacchione and Zelanko 1995a).

A longwall stability analysis was conducted on a mine located in the Upper Cretaceous Book Cliffs coalfield of north-central Utah, and the results showed that a significant overburden depth (more than 1600 feet) and a very high confinement provided by strong roof and floor strata result in a large amount of energy storage in the active mining areas. These geological conditions and improper design of yielding pillars were identified as factors contributing to rockbursts (Barron 1990).

Analysis of rockbursts in Deer Creek Mine showed that rockbursts occurred mostly in gate pillars, and to a less extent in longwall faces. High stresses associated with a deep cover, sandstone channels, competent roof and floor, and strong and brittle coal material were all considered as favorable conditions for rockbursts (Agapito et al. 1997). The roles of five stress factors (i.e. depth of cover, channels, arching of strata, faults and coal seam thickness) were studied to show the importance of these factors in causing rockbursts (Agapito and Goodrich 2000). An analysis of geological and mining conditions at 25 coal mines in U.S. identified that the most important factors contributing to rockbursts are mechanical properties of strata, gate road geometry and/or safety factors of gate road pillars, thickness of roof beam, joint spacing of roof, stiffness characteristics of roof, stress gradients associated with anomalous geological conditions and previous mining (Maleki and White 1997).

In general, the factors that tend to increase the potential for rockbursts in underground coal mining conditions are:

- Thick overburden (more than 500 ft)
- Competent roof and floor
- Geological structures (i.e. faults, dykes, sandstone channels)
- Unfavorable mining method, layout and sequence
- The properties of coal (i.e. strong and brittle)

The existence of one or more of these factors significantly increases the potential of rockbursts.

2.9 Mechanisms of Rockburst in Underground Coal Mines

Based on the research done by Cook (1965b; 1965a) and Crouch and Fairhurst (1974), it is now well believed that unstable failures/rockbursts occur when the energy can be absorb by the rock or coal is less than that is released by the surrounding rock mass during the yielding process of the rock or coal. However, various factors need to be involved when analyzing rockburst events on sites. In order to better understand mechanisms of rockbursts in underground coal mines, the influence and importance of the mining geometry, the overburden stress, the properties of the rock mass and coal, the geological structures, and many other factors need to be studied. Based on the author's survey of the research done to date, there is limited number of studies focused on rockburst in underground coal mines. Select few of the studies this author reviewed are discussed next.

Babcock et al. (1984) conducted laboratory tests to study the effect of constraint on the rockburst proneness of coal. The study showed that in the condition that the loss of constraint due to slip at the interfaces between loading steel platens resulted in rockbursts.

Iannacchione (1990) conducted a test on a 24.4 m (80 ft) square abutment pillar in a coal mine in the Southern Appalachian Basin to study the behavior of coal pillars with rockburst proneness in the process of longwall mining. Several hypotheses were made about the mechanisms of rockbursts occurred in the pillar: (1) a large amount of strain energy stored in coal materials was suddenly released and caused rockbursts, (2) the sudden release in constraint in the form of slippage along the interfaces between coal layer and roof and/or floor, (3) the stiffness of the mine was smaller than the post-peak stiffness of the pillar's load-deformation curve, and (4) a dynamic stress wave generate from other dynamic failures or rockbursts in adjacent pillars. Based on the reports of numerous rockburst-related investigations, Iannacchione et al. (1995b) proposed three possible mechanisms for rockbursts occurred in underground coal mines in the U.S.: (1) a rapid excessive pressure caused by a

sudden removal or a failure of adjacent pillars, (2) an instantaneous increase in load caused by seismic shock coming from failures along existing geological discontinuities, and (3) a loss of confinement due to slip at the roof and floor interfaces with the coal layer.

Based on the author's literature survey, unstable failures of existing rock discontinuities in underground coal mines are rarely studied. Numerical analysis of discontinuity stability conducted by the author is provided in the future chapters. The interaction between the mine stiffness and the post-peak stiffness of the discontinuity shear stress–displacement curve is discussed. The effects of various factors, such as the discontinuity locations, the extent of excavations, and the elastic modulus of rocks on mine stiffness are investigated.

There is no detailed analysis of the loss of confinement mechanism considering failure stability of the interfaces between different rock materials for strain-type rockburst. Hence, the author reports a series of numerical simulations to study de-confinement mechanisms of strain-type rockburst at mining faces and sidewalls due to rapid loss of confinements involving unstable shear failures along roof-coal and coal-floor interfaces and the existence of weak regions at the interfaces.

CHAPTER 3

NUMERICAL SIMULATIONS OF DOUBLE SHEAR TEST

The source mechanisms in many deep mine rockburst cases and earthquakes are treated as unstable shear failures along large rock discontinuities. In rock engineering applications, rock discontinuities are modeled as either an elastic-plastic or, less frequently, an elastic-softening behavior in their shear stress–shear displacement relations. The post-peak softening (elastic-softening) behavior of rock discontinuities provides a potential for unstable shear failures to occur on the discontinuities. Taking into account the post-peak softening behavior, Salamon (1974) proposed a criterion based on the relative stiffness of the loading system and post-peak softening regime to express the conditions that leads to unstable shear failures. Later, Rice (1983) illustrated the conditions for stable and unstable shear failures for a single degree-of-freedom system consisted of a slider and a spring. Both researchers suggested that an unstable shear failure of rock discontinuities occurs if the post-peak stiffness of discontinuity shear stress–displacement curve is larger than the stiffness of loading system.

In this study, the numerical modeling software UDEC (Itasca Consulting Group 2010) is used for the mechanistic analyses of unstable shear failures of rock discontinuities. This code was specifically developed for failure analysis in discontinuous rock mass. Built into the UDEC software is a "softening" constitutive model called the continuously yielding (CY) joint model. The work done by Lemos (1987) and Cundall and Lemos (1990) indicated that UDEC with the CY joint model could be used to simulate unstable failure of rock discontinuities in the program's dynamic analysis mode. In dynamic UDEC analysis, damping can significantly influence how the model behaves. Currently, determining a proper damping coefficient for a dynamic analysis can be arduous and time-consuming at best for the simulations of large underground mines. To work around the errors that can be introduced by a poorly defined damping coefficient a "quasi-static" mode is typically used. Using a

"quasi-static" mode appears feasible, however, needs to be tested and verified. To evaluate using a "quasi-static" mode, numerical simulations of laboratory scale shear test were performed. The simulations used a test geometry similar to that of a typical double shear test configuration. The stiffness of the loading system was varied by changing the elastic modulus of the rock specimen, and the CY joint model developed by Cundall and Hart (1984) was adopted as the softening constitutive model. The results verified the program's capability to simulate stable and unstable shear failures of rock discontinuities.

3.1 UDEC and Joint Models

The distinct element code UDEC and two constitutive models for rock discontinuities, the Mohr-Coulomb (MC) joint model and CY joint model, are introduced in the following sections. The calibration of the CY joint model is also presented.

3.1.1 Background on UDEC

UDEC is a two-dimensional numerical program based on the distinct element method for modeling discontinuous media, such as a jointed rockmass. The discontinuous medium is represented as an assemblage of discrete blocks separated by discontinuities. An individual discrete block can be modeled as either a rigid or deformable material for different types of analyses. A deformable block is achieved by subdividing the block into a mesh of finite-difference triangular zones. The complexity of deformation of blocks depends on the number of zones into which the blocks are divided. The vertices of the triangular zones are referred to as gridpoints. Each finite-difference zone behaves according to a prescribed linear or non-linear stress–strain law. The behavior of discontinuities in both shear and normal directions is also governed by linear or nonlinear force-displacement relationships (Itasca Consulting Group 2010). UDEC simulations can be performed under either quasi-static or dynamic loading conditions.

There are other numerical modeling programs, such as Finite Element (FEM), Boundary Element (BEM) and Finite Difference (FDM) programs that can model rock discontinu-

ities by using interface elements or specially defined forms of discontinuous elements. In most of these models, the discontinuity elements experience difficulties in modeling multiple intersecting interfaces, efficiently recognizing new contacts, or effectively modeling large displacement and rotation of blocks (Itasca Consulting Group 2010). One of the main reasons for using UDEC in this study is that it provides the capability for modeling materials with multiple intersecting discontinuities when simulating large displacement, rotation and detachment of blocks. Another main reason of adopting UDEC is that post-peak softening behaviors of discontinuities can be effectively simulated by the CY joint model in the program.

The CY joint model was originally intended to simulate internal mechanisms of progressive damage of discontinuities under shear. Compared to the MC plasticity model, the CY joint model can also account for joint shear and normal stiffness dependence of normal stress and non-linear hardening and softening behavior in the post-peak stage—as normally observed in physical discontinuity shear tests.

3.1.2 Mohr-Coulomb Plasticity Model

For most numerical simulations, discontinuities are simulated by the MC plasticity model since it fulfills the needs of most engineering problems. The MC model simulates elastic-perfectly plastic behaviors of discontinuities' (see Figure 3.1). Based on the stiffness criterion, however, the MC joint model is not suitable for unstable failure studies due to its inherent non-softening behavior in the post-peak regime. The inability to simulate unstable shear failure using the MC joint model is illustrated in the numerical simulations presented in Sections 3.3.

3.1.3 CY Joint Model

The CY joint model, proposed by Cundall and Hart (1984), was initially intended to simulate internal mechanisms of progressive damage of discontinuities under shear in a simple fashion. It is more "realistic" than the MC plasticity model as it considers joint stiffness

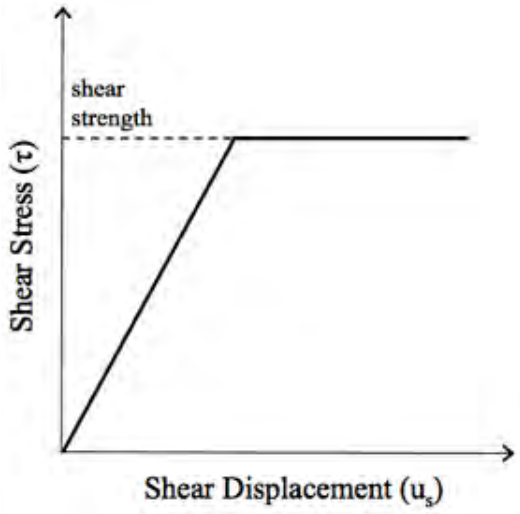

Figure 3.1: Typical shear stress–displacement curve of a MC plasticity model.

(shear stiffness and normal stiffness) dependence of normal stress and non-linear behavior of discontinuities observed in physical shear tests, such as post-peak softening. The discontinuity shear stress–displacement curve modeled by the CY joint model is designed to always approach a target shear strength τ_m by changing the instantaneous gradient of the curve based on the difference between strength and stress (see Figure 3.2). The target shear strength τ_m is a function of normal stress and accumulated plastic shear displacement of the simulated discontinuity. As normal stress increases, target shear strength increases. The increase in the target shear strength results in an increase in shear strength of the simulated discontinuity. The target shear strength continuously decreases as the accumulated plastic shear displacement increases. This results in a softening behavior in the post-peak region of the discontinuity shear stress–displacement curve. The CY model can simulate the changes in both peak shear strengths and post-peak behaviors of the simulated discontinuities caused by the changes in friction angle. The MC plasticity model only considers the peak strength variations with the changes in friction angle.

In this study, shear stiffness of discontinuity is defined as the ratio of applied shear stress to shear displacement in elastic regime and has a unit of Pa/m. The shear stiffness of the CY joint model is controlled by the factor F and the shear stiffness parameter k_s.

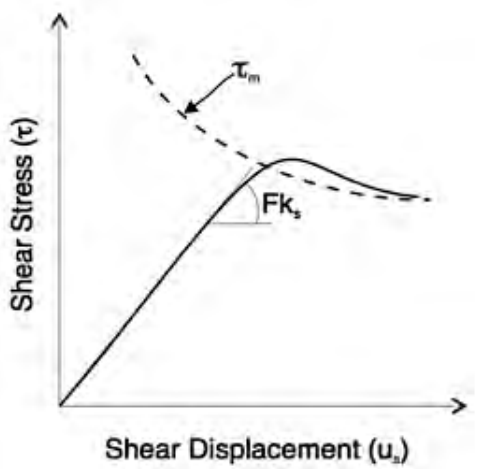

Figure 3.2: Illustration diagram of typical shear stress–displacement curve and the target shear strength τ_m of the CY joint model (after Itasca Consulting Group 2010).

Normal stiffness of discontinuity is defined as the ratio of applied normal stress to normal displacement and has the same unit as shear stiffness (Pa/m). More detailed descriptions and formulations of the CY joint model are given in the UDEC manual (Itasca Consulting Group 2010). Several equations of the model, which are important for understanding the behavior of the joint model used in this study, and a list of all parameters of the joint model (see Table A.1) are described in Appendix A.

3.1.4 Calibration of CY Joint Model

For the purpose of the study, the CY model needs to be calibrated to exhibit a specific discontinuity behavior in terms of peak shear strength, residual shear strength and post-peak stiffness. The calibration tests are conducted using the double shear test model. The shear strength and post-peak behavior of the simulated discontinuity are controlled by the target strength since the shear stress-displacement curve always tends to achieve the target strength. We can analyze the effect of different input parameters on the discontinuity behavior by knowing how the target strength behaves with utilization of different input parameters.

The target shear strength τ_m of the simulated discontinuity is a function of accumulated plastic shear displacement u_{sp}, and affected by initial friction angle ϕ_m, intrinsic friction

angle ϕ, joint roughness R, and normal stress σ_n, through the following relationship

$$\tau_m(u_{sp}) = \sigma_n \tan[(\phi_m - \phi)e^{\frac{-u_{sp}}{R}} + \phi]sgn(u_{sp}) \tag{3.1}$$

where $sgn()$ is the sign function that extracts the sign of a real number.

The effect of normal stress is not considered here because it is not significant in a calibration process. However, its influence is important when applying the CY model in relatively complex loading conditions, as will be seen in Section 3.4.

Based on Equation3.1, the parameters initial friction angle ϕ_m, intrinsic friction angle ϕ and joint roughness R govern the shear strength and post-peak behavior of the discontinuity. Since the shear strength and post-peak behavior are the main considerations in this study, the effect of ϕ_m, ϕ and R on the discontinuity behavior was analyzed. The results and conclusion from this analysis is discussed in the following sections.

3.1.4.1 Initial Friction Angle ϕ_m

The initial friction angle can be considered as the friction angle that would apply if the joint dilated at the maximum dilation angle. Using an intrinsic friction angle, ϕ_m, of 30°, a joint roughness of 0.1 mm, and a normal stress of 5 MPa, and applying five different values of initial friction angles (40°, 45°, 50°, 55° and 60°) in Equation3.1, five corresponding target shear strength curves, τ_{m1}, τ_{m2}, τ_{m3}, τ_{m4} and τ_{m5} are obtained and used to analyze the effect of the initial friction angle has on the simulated discontinuity behavior.

The target shear strength curves for the varying initial friction angles are plotted in Figure 3.3. Based on these curves, it can be deduced that the peak shear strength, residual shear strength and post-peak stiffness (brittleness) of the simulated discontinuities increase as the initial friction angle increases.

3.1.4.2 Intrinsic Friction Angle ϕ

The intrinsic friction angle represents the basic friction angle of rock surfaces. Applying an initial friction angle of 60°, a joint roughness of 0.1 mm, and a normal stress of 5 MPa,

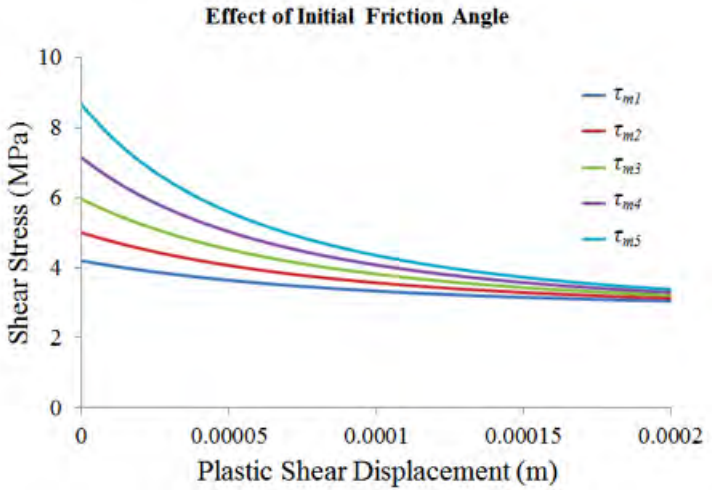

Figure 3.3: Target shear strengths of simulated discontinuities with different initial friction angles.

and using five different intrinsic friction angles, ϕ, of 10°, 15°, 20°, 25° and 30° in Equation3.1, five corresponding target shear strength curves τ_{m1}, τ_{m2}, τ_{m3}, τ_{m4} and τ_{m5} are acquired and used to investigate the effect of the intrinsic friction angle.

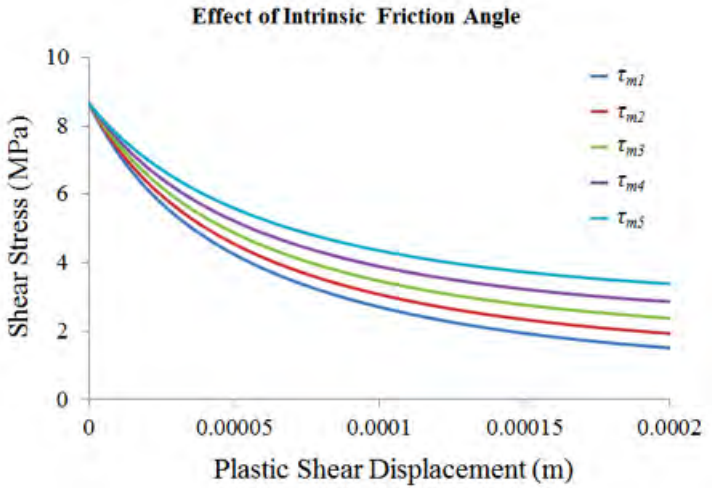

Figure 3.4: Target shear strengths of simulated discontinuities with different intrinsic friction angles.

The results of varying the intrinsic friction angles are plotted in Figure 3.4. The results shown in Figure 3.4 indicate that with the increases in the intrinsic friction angle, the peak shear strengths and residual shear strengths of the simulated discontinuity increases, and

the post-peak stiffness (brittleness) decreases. The changes in the post-peak behaviors of the simulated discontinuities resulted from the variations in the intrinsic frictional angle is achieved in the CY model, which cannot be realized in the MC plasticity model.

3.1.4.3 Joint Roughness *R*

To analyze the effect of joint roughness, R, on the simulated discontinuity behaviors the intrinsic friction angle and initial friction angle where kept constant and R was varied from 0.1 mm to 0.5 mm. An intrinsic friction angle of 30°, an initial friction angle of 60°, and a normal stress of 5 MPa was used for this analysis. The five different joint roughness values were 0.1 mm, 0.2 mm, 0.3 mm, 0.4 mm and 0.5 mm. These five R values correspond to the target shear strength curves, τ_{m1}, τ_{m2}, τ_{m3}, τ_{m4} and τ_{m5} respectively, which are shown in Figure 3.5.

In Figure 3.5, we can see that a larger value of the joint roughness R results in a slower decrease in the initial friction angle ϕ_m, therefore, causes a larger peak shear strength, a larger residual shear strength and a smaller post-peak stiffness (brittleness) of the simulated discontinuities. Results from the study conducted by Scholz et al. (1972) suggest that the larger the joint roughness is, the lesser the tendency for unstable shear failures will be. Their study implies that the post-peak stiffness of joints decreases as the joint roughness increases, which is the same trend of the changes as that simulated by the CY joint model.

3.1.4.4 Parametric Analyses Conclusions

Based on the results in Figure 3.3, Figure 3.4, and Figure 3.5, it can be concluded that the input parameters ϕ_m, ϕ, and R have significant effects on the shear strengths and post-peak behaviors (post-peak stiffnesses and residual shear strengths) of the discontinuities simulated using the CY joint model. The CY joint model is managed to simulate non-linear behavior of discontinuities in a simple manner by incorporating these parameters into the model, which cannot be achieved by other joint models (e.g. MC plasticity model). Knowing how these parameters influence discontinuity behavior, the desired discontinuity behaviors, if there is

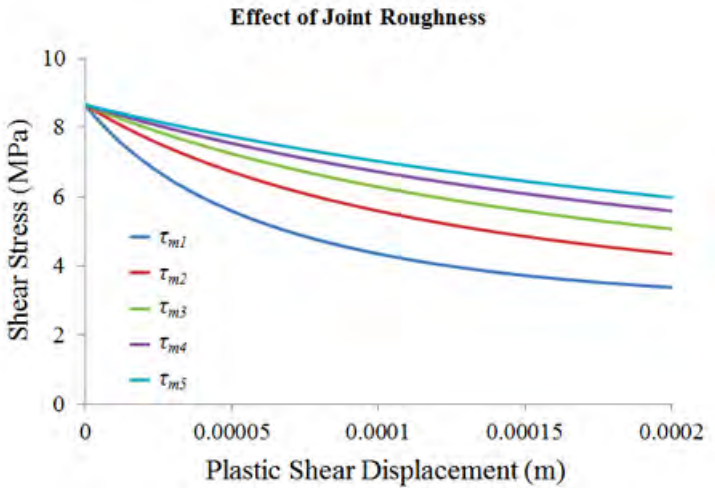

Figure 3.5: Target shear strengths of simulated discontinuities with different joint roughness values.

any, can be achieved in a series of calibration processes by adjusting these input parameters.

3.2 Double Shear Tests under Constant Normal Loading

To validate the ability of UDEC with the CY model to simulate unstable shear failures of rock discontinuities, a series of laboratorial-scale double shear tests are simulated.

3.2.1 Model Description

The double shear test model consists of three rectangular blocks as shown in Figure 3.6. Each block was made deformable by discretizing it into a mesh of finite-difference triangular zones, which are delineated by the red lines in Figure 3.6. The top and bottom blocks represent two loading platens, and the middle block represents a rock specimen. The height of each block is 0.1 m. The width of the loading platens is 0.3 m and that of the rock specimen is 0.2 m.

A constant normal stress of 10 MPa was applied at the top and bottom of the double shear model, as indicated by the vertical arrows in Figure 3.6, to simulate loading conditions of discontinuities located deep below the surface. The loading platens were fixed in the horizontal direction and free to move in the vertical direction. A constant horizontal velocity

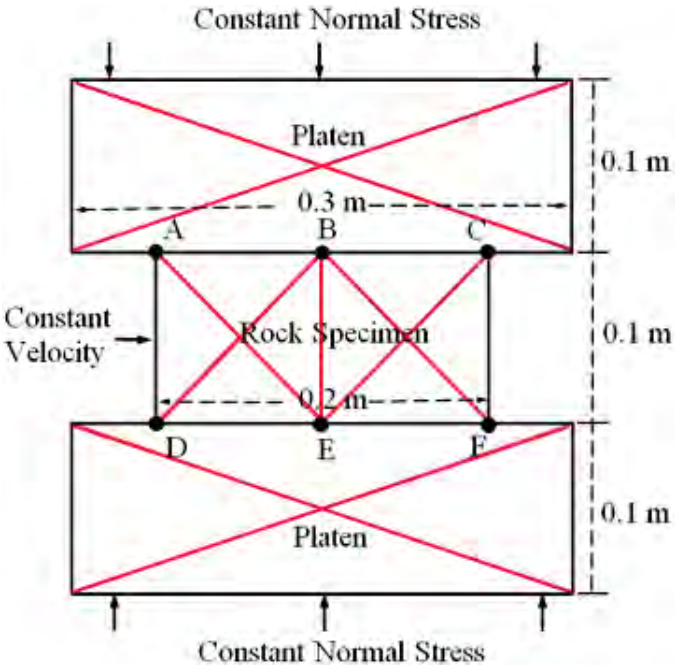

Figure 3.6: Configuration of double shear test model in UDEC.

of 0.1 mm/s was applied over the left side of the rock specimen. The loading platens are elastic materials, although with very high elastic modulus of 2000 GPa. The rock specimen was also modeled as an elastic material but with varying elastic modulus among different tests. The interfaces between the rock specimen and the loading platens were assigned the CY joint model. These interfaces represent rock discontinuities on which shear failures occur.

Energy stored in the loading platens is minimized by assigning them a very high elastic modulus (2000 GPa). As such, during shearing along the discontinuities, the loading system energy available is mainly from the elastic rock specimen. To simulate stable and unstable discontinuity shear failures, the stiffness of the loading system (i.e., the elastic modulus of the rock specimen) was varied in different tests. In this study, the loading stiffness is defined as a measure of the resistance offered by the elastic loading system to its deformation and it has a unit of Pa/m. Shear stress and shear displacement of points A, B, C, D, E and F, as indicated in Figure 3.6, were recorded in the tests. In the program, shear stress is positive for the following direction of relative movement:

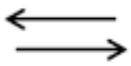

For the same direction of relative movement shown by the arrows above, shear displacement is negative. In this study, the sign of shear displacement is reversed when plotting the shear displacement records obtained from the model. The records of point B, which represent the behaviors of the middle section at the upper discontinuity, are firstly taken as examples to introduce stable and unstable shear failures. Then, behaviors of all points are presented.

For the first test, an elastic modulus of 200 GPa was assigned to the rock specimen. The first test using the high elastic modulus for the rock was done to obtain the characteristic behavior of the discontinuity. After obtaining the characteristic behavior of the discontinuity, two additional tests were done using lower elastic moduli for the rock specimen. An elastic modulus of 50 GPa and 1 Gpa were used for the two additional tests. One with an elastic modulus of 50 GPa was used to simulate the shear failure under the stiff loading system, and the other one with an elastic modulus of 1 GPa to simulate the shear failure under the soft loading system. The elastic modulus of the loading platens was kept the same in all three tests. The input parameters of the elastic model for these three tests are shown in Table 3.1. The UDEC codes for these three simulations are presented in Section D.1 in Appendix D.

Table 3.1: Input parameters of the elastic model for different double shear tests.

	Elastic Modulus (GPa)	Poisson's Ratio
Steel Platens	2000	0.2
Specimen-very stiff loading system	200	0.2
Specimen-stiff loading system	50	0.2
Specimen-soft loading system	1	0.2

The input parameters of the CY model are shown in Table 3.2. The discontinuity properties remained the same in all three tests.

Table 3.2: Input parameters of the CY model.

Parameter Symbols	Description	Value
jk_n	Joint normal stiffness	100 GPa/m
jk_s	Joint shear stiffness	100 GPa/m
je_n	Joint normal stiffness exponent	0
je_s	Joint shear stiffness exponent	0
jfric	Joint intrinsic friction angle	30°
jif	Joint initial friction angle	59.3°
jr	Joint roughness parameter	0.1 mm

3.2.2 Discontinuity Characteristic Behavior

The shear stress–displacement curve from the first test (i.e. the rock specimen with an elastic modulus of 200 GPa) is shown in Figure 3.7. The solid black line represents the characteristic behavior of the discontinuity at point B, i.e., middle length along the upper discontinuity in the double shear test (see Figure 3.6). In this study, a characteristic behavior is defined as the behavior that a discontinuity exhibits during a shear test using a very stiff loading machine. It is the discontinuity behavior when the discontinuity experiences a stable failure. Note that the characteristic curve in Figure 3.7 has a post-peak softening region. Based on the stiffness criterion, this softening behavior provides a potential for unstable shear failures. Knowing the discontinuity characteristic behavior, one test with the stiff loading system and one test with the soft loading system were then performed and are presented in Section 3.2.4.

3.2.3 Loading Stiffness Tests

The stiffnesses of the stiff and soft loading systems at point B are tested. The UDEC codes for the loading stiffness tests are shown in Section D.2 in Appendix D. Due to the symmetry condition of the double shear test, only the upper half of the rock specimen is considered in obtaining the loading stiffness of point B.

The configuration of the test is shown in Figure 3.8. The bottom of the model was fixed both in the horizontal and vertical direction. A constant horizontal displacement was applied

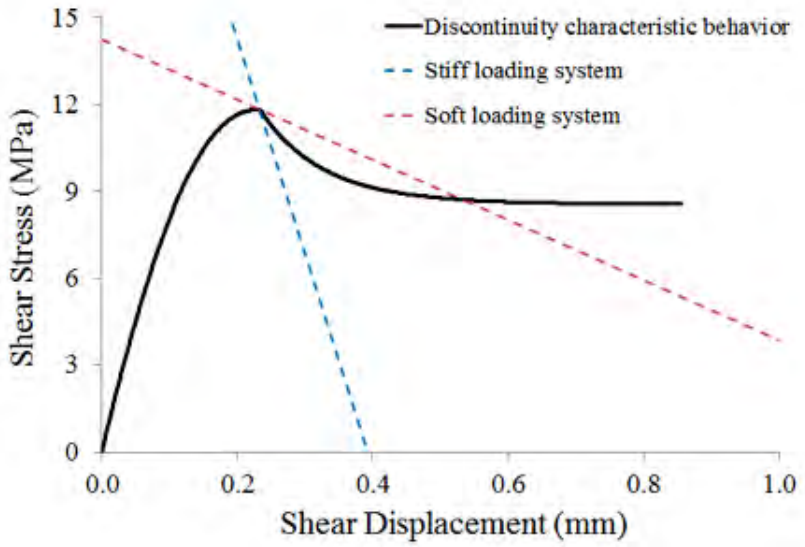

Figure 3.7: Characteristic shear stress–displacement curve of point B (the middle section at the upper discontinuity) and the stiffness of the stiff and soft loading systems.

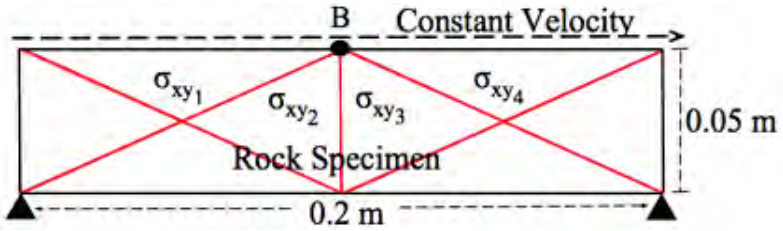

Figure 3.8: Configuration of loading stiffness test.

over the top of the model. Shear stresses within the four zones connected to point B were recorded in the tests. The horizontal displacement of point B was also monitored in the tests. According to the program's algorithm, one third of the shear stress in each adjacent zone of point B contributes to the failure of the point. Therefore, the loading stiffness (LS) can be calculated from the following equation,

$$LS = \frac{\frac{1}{3}(\sigma_{xy_1} + \sigma_{xy_2} + \sigma_{xy_3} + \sigma_{xy_4})}{d_B} \tag{3.2}$$

where σ_{xy_i} (i = 1,2,3,4) is the shear stress in zone i, d_B is the horizontal displacement of point B. The results of the tests with the rock specimen of an elastic modulus of 50 GPa (the stiff loading system) and 1 GPa (the soft loading system) are shown in Figure 3.7 as the blue and red dashed lines, respectively.

3.2.4 Shear Failure in Stiff and Soft Loading System Conditions

The results of the double shear tests under the stiff and soft loading systems are presented in Figure 3.9, Figure 3.10 and Figure 3.11 in three distinct forms: shear stress–time curve, shear displacement–time curve and shear stress–displacement curve. The time unit in the plots is a numerical time calculated through multiplying the timestep by the number of steps used in the simulations. The numerical time, based on the confirmation of this simulation, is one of the main indicators of the suddenness of the failure, which in turn relates to the failure stability of rock discontinuities.

The plots shown in Figure 3.9 are the shear displacement–time curves of point B under the stiff (the blue line) and soft (the red line) loading systems. The stiff loading system result, represented as the blue line in Figure 3.9, shows a nearly continuous change in the shear displacement of the discontinuity. This nearly linear change in shear displacement versus time indicates the discontinuity undergoes a gradual shear during the entire loading process, which implies a stable shear failure. The slight variation in the blue line at about 1.56 seconds marks the onset of the stable failure. The rate of change in the shear displacement exhibits a small increase after the stable failure takes place. The interruption in the discontinuity shear

displacement trend in the soft loading system test (red line) shows that the discontinuity goes through a sudden increase in its shear displacement. The shear displacement rapidly jumps from 0.24 mm to 0.62 mm at 2.66 seconds. This phenomenon implies a sudden shear that can be postulated as an unstable shear failure. This postulation is confirmed by interpreting Figure 3.10 and Figure 3.11, which will be discussed below. As seen in Figure 3.9, the rate of change in the shear displacement for the unstable failure undergoes a large increase in the post-failure region. The slopes of these two shear stress-displacement curves are not comparable because the time scale is determined by the timestep. The timestep is affected by the stiffness of the materials used in the model and it is different in these two tests due to different elastic moduli of the materials.

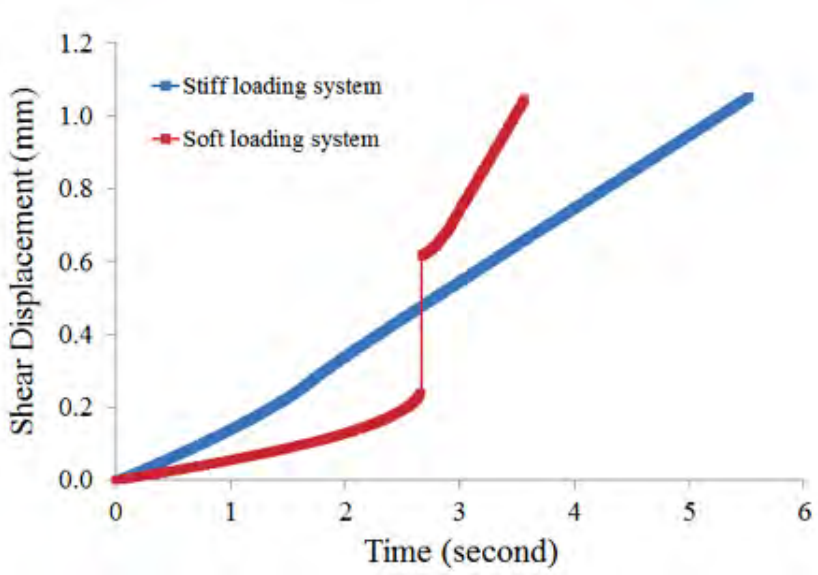

Figure 3.9: Shear displacement–time curves of point B under the stiff (the blue line) and soft (the red line) loading systems.

Behaviors similar to those in Figure 3.9 are also observed in Figure 3.10. Figure 3.10 is a plot of shear stress–time curves from the same test. The gradual decrease in the shear stress, as shown by the blue line, suggests the discontinuity undergoes a continuous shear failure process under the stiff loading system. When the failure initiates, the discontinuity is able to completely consume the energy released from the loading system. This type of failure is

recognized as a stable shear failure.

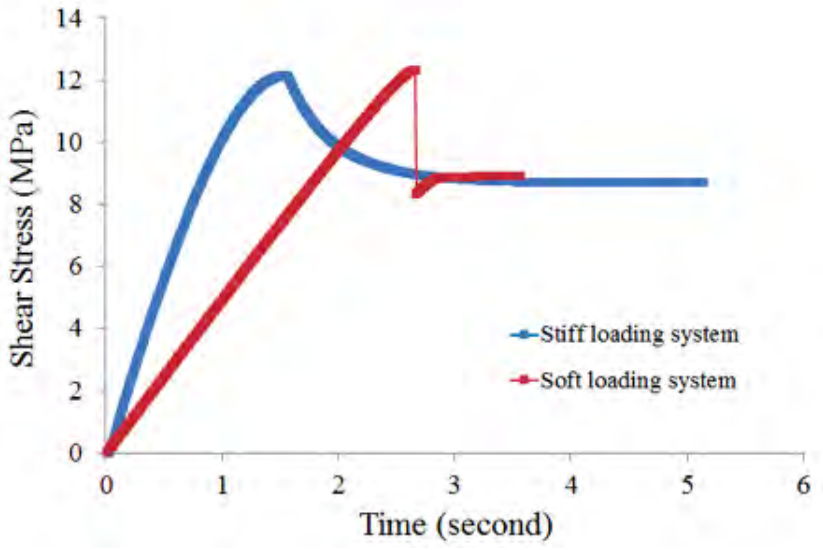

Figure 3.10: Shear stress–time curves of point B under the stiff (the blue line) and soft (the red line) loading systems.

Under the soft loading system (the red line), an abrupt drop in the shear stress from 12.3 MPa to 8.3 MPa at 2.66 seconds indicates a sudden instability. When the failure occurs in the soft loading system condition, the discontinuity can only consume a part of the energy released from the loading system, and the excess energy results in a rapid failure. This phenomenon is considered as an unstable shear failure. For the same reason discussed before, the slopes of the pre-peak regions of the curves are not directly comparable.

The results of the discontinuity shear failures under the stiff and soft loading systems are also presented in the form of the shear stress–displacement curves in Figure 3.11. The dashed lines in red and blue represent the stiffnesses of the soft and stiff loading systems, respectively. The shear stress–displacement curves of the discontinuity under the stiff and soft loading systems both undergo a gradual increase in the shear stress in their elastic regions. The blue line is not visible in its elastic region because it is completely covered by the red line. However, the post-peak regions of these two curves are dissimilar over the descending softening section.

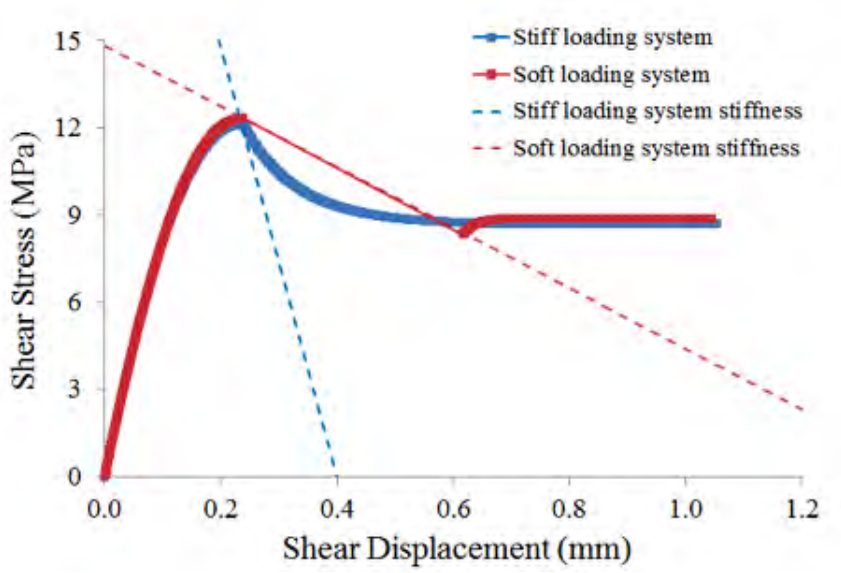

Figure 3.11: Shear stress–displacement curves of point B under the stiff (the blue curve) and soft (the red curve) loading system conditions and the stiffnesses of the stiff (the blue dashed line) and soft (the red dashed line) loading system.

The discontinuity shear stress–displacement curve obtained in the stiff loading system condition is the same as the characteristic shear stress–displacement behavior of the discontinuity, which indicates a stable failure. The change in the post-peak stiffness of the shear stress–displacement curve under the soft loading system indicates the discontinuity behavior is affected by the soft loading system. As shown in Figure 3.11, a part of the post-peak region of the shear stress–displacement curve in the soft loading system condition has no data presented. This is because the discontinuity cannot fully consume the energy released from the soft loading system, and hence it cannot resist shear rebound of the loading system. In this condition, the shear failure is dominated by the shear rebound of the soft loading system. The unstable failure process is very fast until the discontinuity achieves equilibrium again at its residual strength. The shear stress–time, shear displacement–time, and shear stress–displacement results are comparable with those obtained in the simulations of the failure stability of rocks in compression (Kias et al. 2011), which also indicate the occurrence of unstable failures.

3.2.5 Results of All Measurement Points in Double Shear Tests

The results of all the measurement points in the double shear tests are presented in Section 3.2.5.1 in the form of shear stress–time and shear displacement–time curves. As the signatures of failure stability, the results of the maximum unbalanced force and damped energy are discussed in Sections 3.2.5.2 and 3.2.5.3.

3.2.5.1 Shear Displacement and Shear Stress

Based on the analyses presented in previous sections, we know that stable and unstable failures can be distinguished by interpreting the shear displacement and shear stress records of the measurement points. There are six measurement points (i.e. A, B, C, D, E and F), as shown in Figure 3.6, located at the discontinuities in the double shear test model. However, only point B was discussed as an example to identify stable and unstable failures. Knowing the method of distinguishing the failure stability, shear displacement and shear stress records of all measurement points are analyzed in this section.

Figure 3.12 shows the shear displacement–time plots of all measurement points under the stiff loading system. The rate of change in the shear displacement of points A and D is constant since the constant horizontal velocity was directly applied on these points in the double shear tests. There are slight changes in the slopes of points B, C, E and F at approximate 1.6 seconds when these points at start to stable failures.

The shear stress-time curves for all points are shown in Figure 3.13. As seen in Figure 3.13, the changes in the shear stresses at the post-peak regions of the curves are gradual, which indicates all points undergo stable failures. Points A and D start to fail at 1.39 seconds. Points B and E fail at 1.56 seconds, and points C and F fail at 1.61 seconds. Stable shear failures occur at all points and propagate from the left end to the right end of the discontinuities when the discontinuities are loaded under the stiff loading system. Initiations of the shear failures for all points are in a relatively short period of time (between 1.39 and 1.61 seconds).

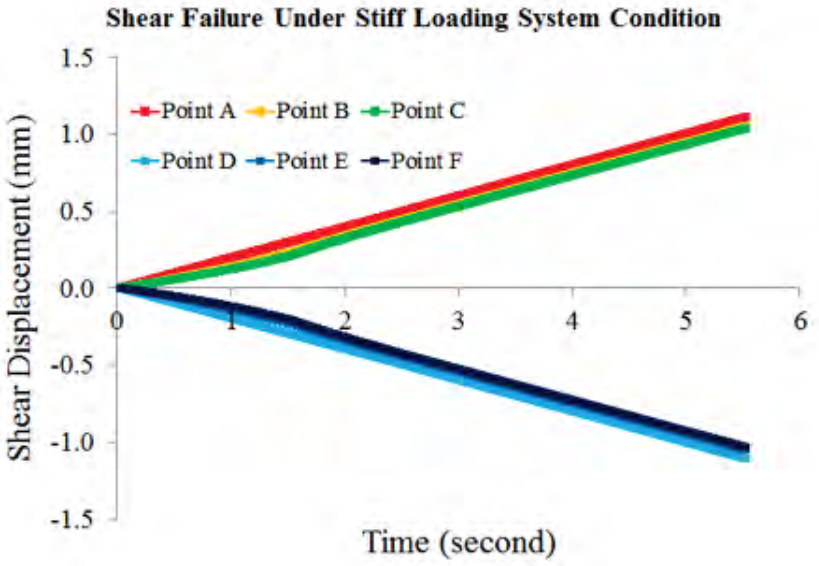

Figure 3.12: Shear displacement–time curves of all measurement points under the stiff loading system.

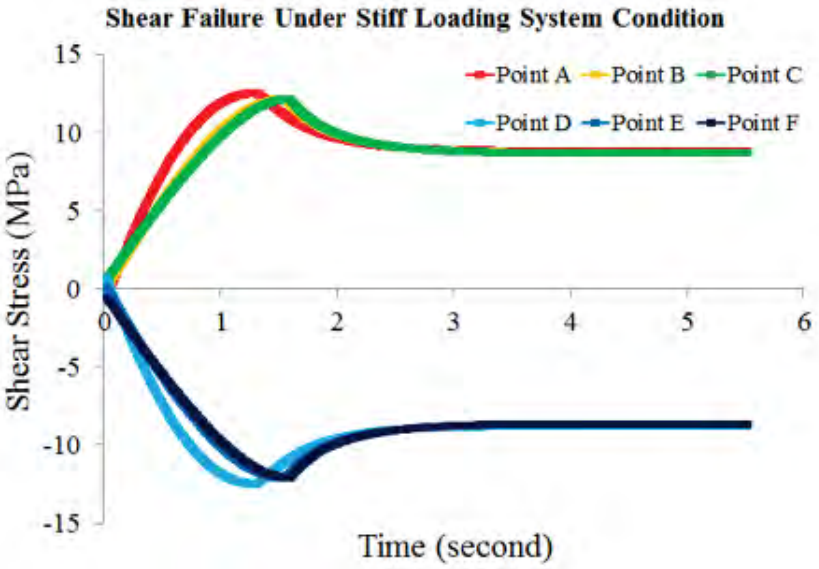

Figure 3.13: Shear stress–time curves of all measurement points under the stiff loading system.

The shear displacement–time plots of all points under the soft loading system condition are shown in Figure 3.14. For the same reason discussed before, the curves for points A and D keep the linear and continuous in the tests, which imply stable failures. For points B, C, E and F, the rapid increases in their shear displacements occur at 2.66 and 3.9 seconds. The amounts of the increases in the shear displacements of these four points are listed in Table 3.4.

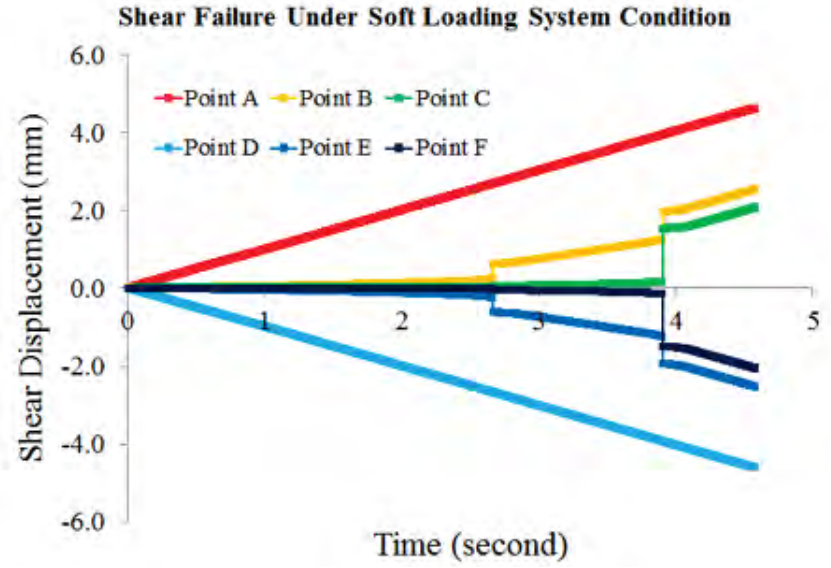

Figure 3.14: Shear displacement–time curves of all measurement points under the soft loading system.

Figure 3.14 and Table 3.3 show that the unstable failures occur at points B and E at 2.66 seconds, and then occur at points E and F at 3.9 seconds. The rapid changes in the shear displacements of points C and F are larger than that of points B and E, which implies the larger intensities of the unstable shear failure at points E and F.

Table 3.3: Rapid changes in shear displacement of points under soft loading system.

Time (second)	Rapid change in shear displacement (mm)			
	Point B	Point C	Point E	Point F
2.66	0.378	-	0.385	-
3.9	0.715	1.37	0.705	1.36

The shear stress–time plots of all points under the soft loading system are shown in Figure 3.15. Figure 3.15 shows that the changes in the shear stress in the post-peak regions of points A and D are gradual which confirm the existence of the stable failures at these points. However, points B and E exhibit sudden decreases in the shear stresses at 2.66 seconds, which are considered signatures of the unstable failures. These unstable failures affect the shear stress distribution on points C and F. As seen in Figure 3.15, the shear stresses at points C and F increase rapidly as the unstable failures at points B and E take place. This is because the shear resistance provided by points B and E decreases as the unstable failures occur, and these points cannot provide enough resistance against shearing. The non-failed points have to take over the responsibility to resist the shear movement , which leads to rapid increases in the shear stresses at the no-failed points.

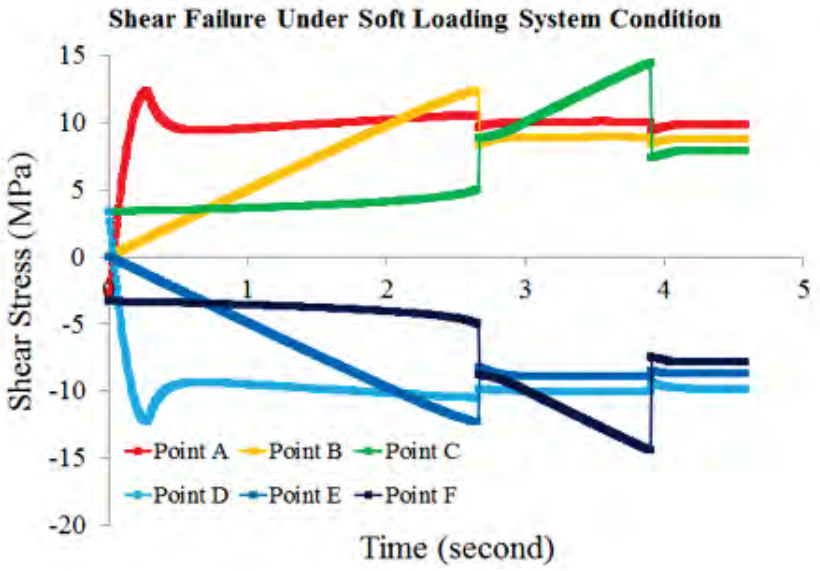

Figure 3.15: Shear stress–time curves of all measurement points under the soft loading system.

As the shearing process proceeds, points C and F exhibit rapid decreases in the shear stresses at 3.9 seconds, which indicate unstable failures at these points. The amounts of the changes in the shear stresses for points B, C, E and F are listed in Table 3.4. The rapid decreases in the shear stresses of points C and F are larger than that of points B and E,

which also implies larger intensities of the unstable failures at points C and F.

In the double shear test with the soft loading system, points A and D undergo stable shear failures because the boundary condition (i.e. the constant velocity) applied over the left side of the model results in a perfectly stiff loading system for these two points. However, points B, C, E and F all experience unstable failures under the soft loading system, and the unstable failures initiate at points B and E and then extend to points C and F with increased intensities.

Table 3.4: Rapid changes in shear stress of points under soft loading system.

Time (second)	Rapid change in shear stress (MPa)			
	Point B	Point C	Point E	Point F
2.66	Decrease 4.0	Increase 3.8	Decrease 4.1	Increase 3.8
3.9	-	Decrease 7.0	-	Decrease 6.9

3.2.5.2 Maximum Unbalanced Force

By analyzing the shear displacement and shear stress histories in the double shear tests, the failure stability of each measurement point on the discontinuities is identified. Such detailed analyses are important. It is also important to distinguish the failure stability in a relatively large scale: investigating the failure stability in the model-scale rather than gridpoint-scale or zone-scale. One of the powerful tools for model-scale analyses, in the finite-difference based numerical modeling programs, is the maximum unbalanced force. The maximum unbalanced force, as the name implies, is the largest amount of unbalanced force in a model. In UDEC, it is continuously updated in every modeling step in the process of a simulation. The maximum unbalanced force is a measure for assessing the state and stability of a model. If the maximum unbalanced force decreases by orders of magnitudes and keeps at very small values, it suggests that a model is stable and approaching equilibrium. In other words, there are no unstable failures, no disturbance in the model and all blocks are in steady states. If the maximum unbalanced force increases dramatically, it indicates

that instabilities exist in the model (e.g. sudden failures or disturbance in the model by excavating blocks).

The command "*history unbal*" in UDEC was used for recording the maximum unbalanced force in the double shear tests. The unbalance force history data of the test under the stiff loading system are plotted in Figure 3.16. The peak value at the beginning of the test is initial non-equilibrium in the model due to the applied initial boundary conditions. When the model achieves equilibrium, the maximum unbalanced force becomes very small. The little variations in the maximum unbalanced force are observed at approximate 1.6 seconds because the discontinuities fail at that instant. The little variations in the records imply the shear failures are in the stable manner.

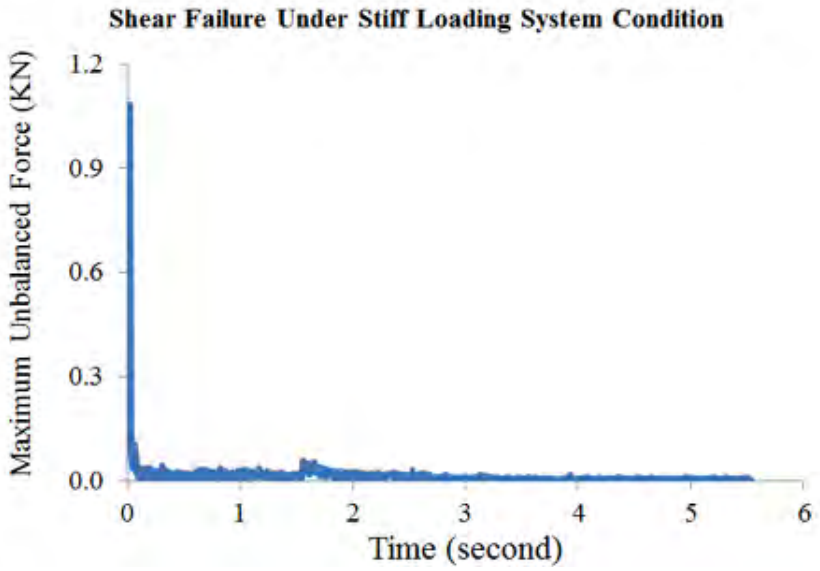

Figure 3.16: Maximum unbalanced force–time plot of the double shear test under the stiff loading system.

The maximum unbalanced forces in the double shear test under the soft loading system are plotted in Figure 3.17. Two large changes are observed at 2.66 and 3.9 seconds, which correspond to the shear failures on the discontinuities under the soft loading condition. The highest value in the maximum unbalanced force records under the soft loading system is larger by 3 orders of magnitudes than that under the stiff loading system, which suggests

unstable shear failures in the soft loading system condition.

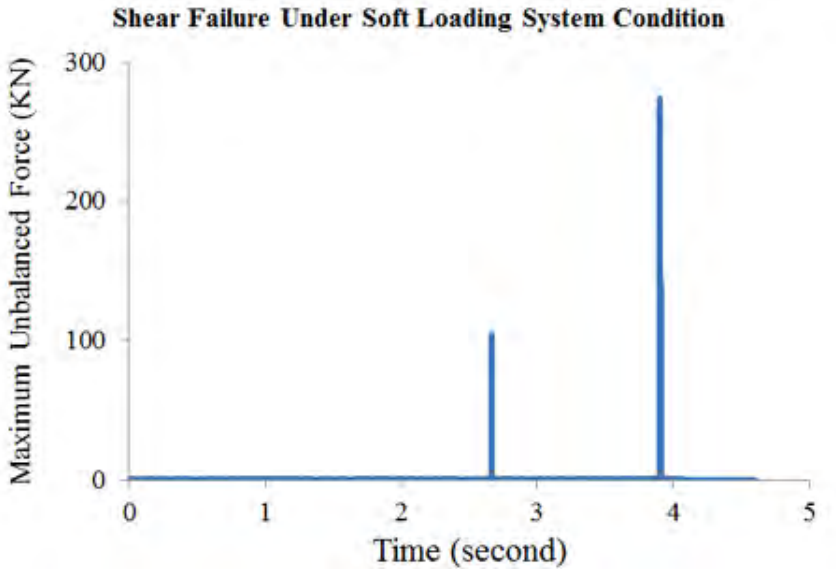

Figure 3.17: Maximum unbalanced force–time plot of the double shear test under the soft loading system.

3.2.5.3 Damped Energy

Another effective means to assess the state and stability of a model is to inspect the energy damped by the mechanical damping in the model. Mechanical damping is used in UDEC to help the model achieve equilibrium as quickly as possible under the applied initial and boundary conditions. The mechanical damping used in this study is referred to as local damping, in which the damping force on a point is proportional to the magnitude of the unbalanced force, and the direction of the damping force is such that energy is always dissipated. In UDEC, the damped energy is the summation of all energy absorbed by local damping.

If damped energy keeps at a relatively small value and changes gradually, it implies that the model is in an equilibrium state and there is no large amount of energy needs to be absorbed in the model. If damped energy exhibits rapid increases and achieves relatively large values, it indicates that sudden instability exists in the model and results in a large

amount of energy that needs to be damped to make the model to reach equilibrium.

The damped energy is monitored in the double shear tests and is presented in the form of accumulated damped energy, i.e., the summation of the damped energy in the model in all steps. The accumulated damped energy–time plot for the test under the stiff loading system is shown in Figure 3.18. They are two regions of relatively quick increases in the accumulated damped energy: the first one at the beginning of the test is because of the existence of the initially applied loading; the second one at approximate 1.6 second is caused by the shear failures of the discontinuities. However, the shear failures seem to be stable depends on the amount and rate of the change in the accumulated damped energy.

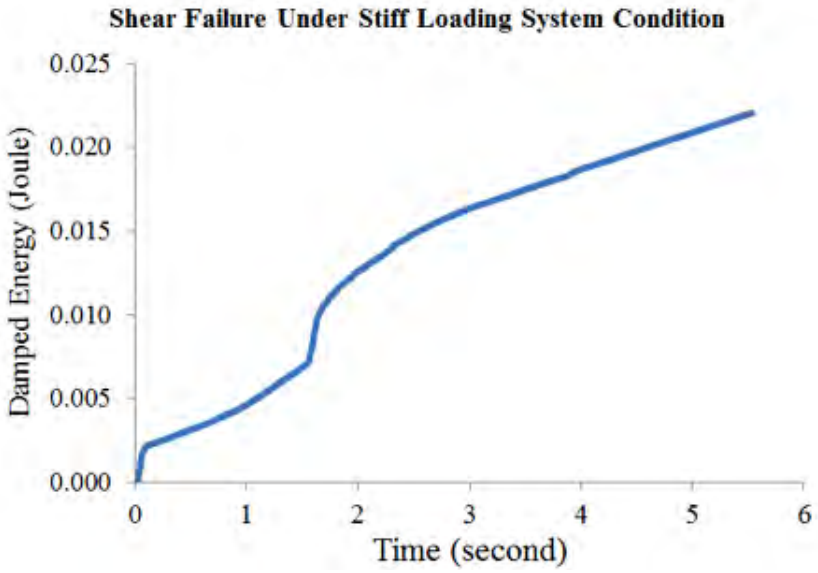

Figure 3.18: Accumulated damped energy–time plot of the double shear test under the stiff loading system.

Figure 3.19 shows the accumulated damped energy–time plot for the test under the soft loading system, in which two rapid and immense changes in the accumulated damped energy are observed. They correspond to the shear failures of the discontinuities at 2.66 and 3.9 seconds, respectively. The maximum amount of the changes in the accumulated damped energy under the soft loading system condition is larger by four to five orders of magnitudes than that under the stiff loading system. These shear failures are considered unstable shear

failures. The intensity of the failures at 3.9 seconds is larger than that at 2.66 seconds, which is also observed in Figure 3.14, Figure 3.15 and Figure 3.17. The reasons for the increases in the intensities of the unstable failures are discussed in Section 3.4.

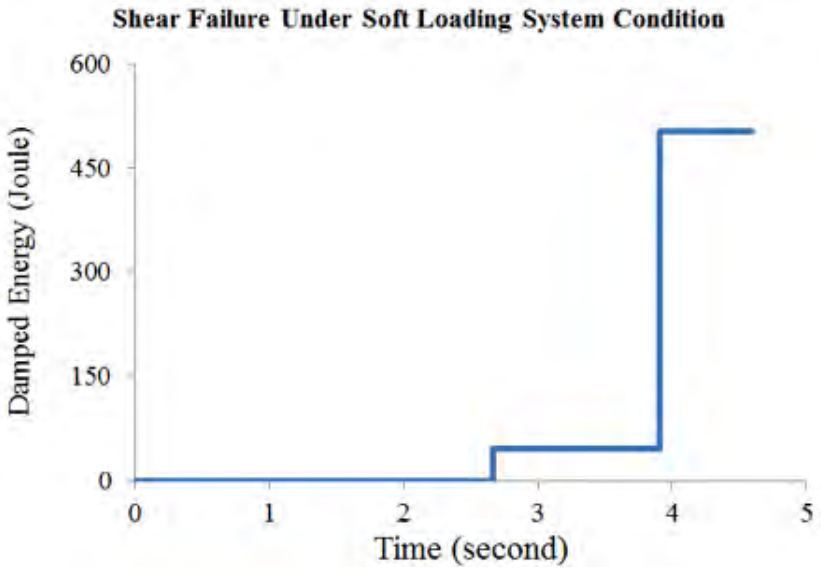

Figure 3.19: Accumulated damped energy–time plot of the double shear test under the soft loading system.

3.3 Double Shear Tests using MC Plasticity Model

Based on the results present in Section 3.2, the CY joint model was shown to successfully simulate stable and unstable shear failures of rock discontinuities. As a comparison, double shear tests were also performed using the MC plasticity joint model on the discontinuities. The UDEC codes for these tests are presented in Section D.3 in Appendix D. The model configuration and the test procedure are the same as the ones used in Section 3.2 except that a different joint model was used. The MC joint model used in the tests has the same shear and normal stiffness as the ones used in the CY joint model (see Table 3.2) and it has a friction angle 38° and zero cohesion. Three tests were done using the MC joint model.

Again, the results of point B are taken as examples. The characteristic behavior of point B simulated by the MC joint model was obtained from the first test with an elastic modulus

of 200 GPa applied to the rock specimen. The shear failure of the discontinuity under the stiff and soft loading systems were modeled in the second and third tests with elastic moduli of 50 GPa and 1 GPa in the rock specimen, respectively.

The results of the tests are shown in Figure 3.20. The red dashed line represents the stiffness of the soft loading system (i.e. elastic modulus of 1 GPa in the rock specimen), and the blue dashed line is the stiffness of the stiff loading system (i.e. elastic modulus of 50 GPa in the rock specimen). The shear stress–displacement curves of three tests are almost the same and they are partly overlapped in Figure 3.20. They all exhibit elastic behaviors before the shear stresses reach the peak strengths, and plastic behaviors after the shear stresses achieve the peak strengths. The results indicate that unstable shear failure of the discontinuity cannot be simulated using the MC joint model since the model is not able to consider the post-peak softening behavior of rock discontinuities.

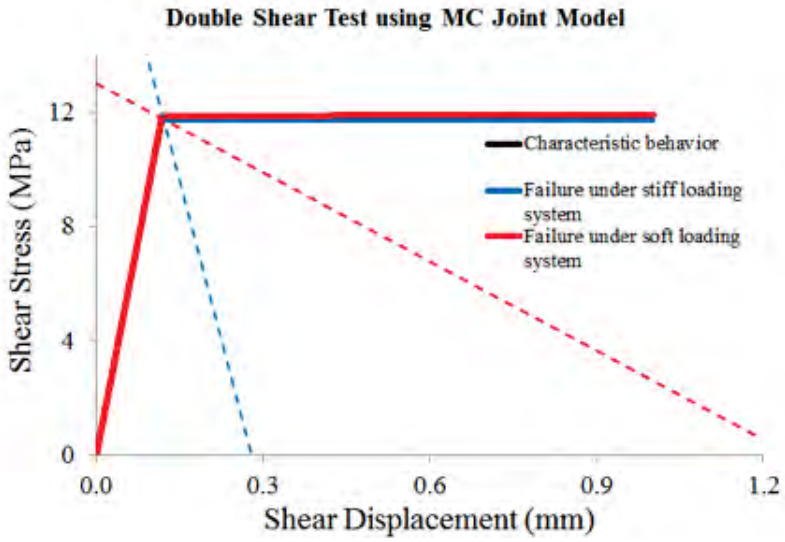

Figure 3.20: Shear stress–displacement curves of point B under different loading systems simulated in the double shear tests with MC joint model.

3.4 Double Shear Tests under Different Normal Constant Stresses

To study unstable shear failure in more complicated loading conditions (e.g. the stability of a geological discontinuity at depth) it is important to investigate the characteristic behav-

iors of the discontinuity that modeled using the CY model under different normal loading conditions. For this purpose, the double shear test with the very stiff rock specimen (i.e. elastic modulus 200 GPa) was repeated under constant normal stresses of 4, 8, 12, 16, 20, 24 and 28 MPa to obtain the characteristic behaviors of the discontinuity under different loading conditions. The properties of the discontinuities in the model are the same as those listed in Table 3.2. The UDEC codes for these tests are shown in Section D.4 in Appendix D.

The shear stress–displacement results are shown in Figure 3.21. The different colored solid lines represent the characteristic behavior of the discontinuity under different constant loading conditions. The dashed lines are the stiffness of the soft loading system (i.e. the rock specimen with an elastic modulus of 1 GPa) and are mainly used to facilitate the comparison of the shear stress drop and the post-peak behavior among different curves. These shear stress–displacement curves indicate that the brittleness (post-peak stiffness) of the simulated discontinuity increases as the applied normal stress increases. The implication of such a behavior is that under the same loading system stiffness condition, the modeled discontinuity poses higher possibility of unstable failure as the depth increases. The amounts of the shear stress drops in the post-peak regions of the curves under different normal loadings are presented in Table 3.5, which shows the shear stress drop increases with increasing normal stress.

Table 3.5: Shear stress drops of the discontinuity under different normal stresses.

Normal Constant Stress (MPa)	4	8	12	16	20	24	28
Shear Stress Drop (MPa)	2.2	3.7	4.8	5.7	6.4	6.8	7.4

Under the soft loading system, the amount of excess energy in the system (i.e. the area between the post-peak curve of the discontinuity and the soft loading system stiffness) increases due to the increase in brittleness and shear stress drop as the normal stress increases (see Figure 3.21). Based on the stiffness criterion, increase in the excess energy results in

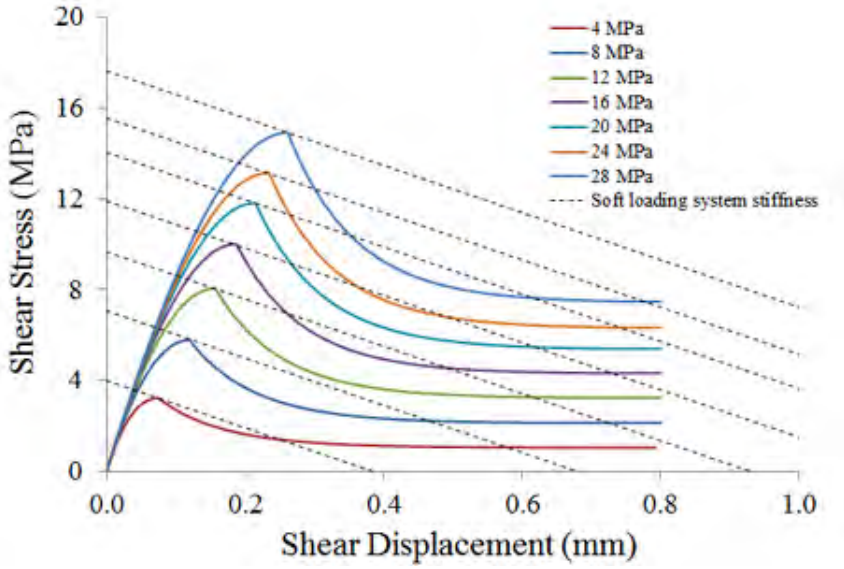

Figure 3.21: Shear stress–displacement curves of the discontinuity under different normal loading stresses (dashed lines: the loading system stiffness of the soft loading system).

larger intensity of unstable failures. This is confirmed by the results of a series of double shear tests under the soft loading system condition (i.e. the rock specimen with 1 GPa elastic modulus) with different normal loadings. The maximum unbalanced force and damped energy of point B are monitored in the tests and used to assess the intensities of the unstable shear failures at that point (see Table 3.6).

Table 3.6: Maximum unbalanced force and damped energy at point B in the double shear tests under the soft loading system condition with different normal stresses.

Normal Constant Stress (MPa)	4	8	12	16	20	24	28
Maximum Unbalanced Force (N)	4.6×10^4	9.4×10^4	1.1×10^5	3.5×10^5	6.8×10^5	2.0×10^6	2.5×10^6
Damped Energy (J)	6.6×10^0	2.0×10^1	2.5×10^1	1.5×10^2	4.4×10^2	4.4×10^3	1.3×10^4

Table 3.6 shows the maximum unbalanced force and damped energy increase as the normal stress increases, which indicates that the intensities of the unstable shear failures at point B increases respectively. The higher intensity of the unstable failures at points C and F (see Figure 3.14, Figure 3.15, Figure 3.17 and Figure 3.19) are also a result of applying a higher normal stress to the tests. Higher normal stresses developed at these points result in higher shear stress drops and brittlenesses, and leads to increased intensities of the unstable failures.

These results compare well with the findings from other researchers (Schneider 1976; Barton et al. 1985; Leichnitz 1985; Flamand et al. 1994) that both stress drop and excess energy increase with increasing normal stress. Also, the increases in shear stress drop are often considered as the main causes of greater rockburst magnitudes as mining goes deeper where discontinuity failures occur under high normal stress conditions. These findings indicate that the CY joint model appropriately simulates the variations in discontinuity behavior under different normal loading conditions.

3.5 Conclusions

This chapter presented a new methodology for numerical simulations of unstable shear failures/slip-type rockbursts using the distinct element program UDEC with the application of the CY joint model in the quasi-static analysis mode. A series of simulations were performed in the model with a double shear test configuration under varying loading system stiffnesses. The rock discontinuities in the simulations exhibit post-peak softening behavior in their shear stress–displacement relations.

The occurrence of stable and unstable shear failures in the double shear model was observed to be in accordance with the stiffness criterion. When a discontinuity failed in shear under a soft loading system, an unstable failure took place. When a stiff loading system existed, a stable shear failure occurred on the discontinuity.

The shear stress–time, shear displacement–time, and shear stress–displacement records of the rock discontinuities in the double shear model showed distinct features which can

be used to assess whether the shear failure was stable or unstable. The shear stress–time and shear displacement–time curves of a stable failure exhibited gradual and continuous changes in the failure process, while that of an unstable failure started to display rapid and discontinuous changes when the failure initiated. The post-peak behavior of a stable failure in its shear stress–displacement relation was the same as the post-peak behavior of the characteristic shear stress–displacement behavior of the discontinuities. The post-peak behavior of an unstable failure followed the stiffness of the loading system.

The records of the maximum unbalanced force and damped energy by mechanical damping in the double shear model were also shown to be the signatures of failure stability. Comparing to the unbalanced force and damped energy records in stable failures, tremendous magnitude and rapid variations in these records were observed in unstable failures.

Three double shear tests were conducted under stiff and soft loading system conditions with the MC joint model assigned to the discontinuities. The results of these tests showed that unstable shear failure could not be simulated in the MC joint model and implied the importance of using the CY joint model for the studies when it is critical to assess whether the shear failure occurs in a stable or unstable manner.

The results of a series of double shear tests with the CY joint model under varying normal stresses showed that the shear strength, post-peak stiffness, and shear stress drop of the discontinuity simulated by the CY joint model increased with increasing normal stress on the discontinuity. These characteristics of the CY joint model are important for analyzing unstable failures of rock discontinuities because the discontinuity post-peak stiffness and shear stress drop directly affect the proneness and intensity of the unstable failures.

CHAPTER 4
APPLICATION I: STABILITY OF A GEOLOGICAL ROCK DISCONTINUITY IN UNDERGROUND COAL MINING CONDITIONS

Failure stability (i.e. stable or unstable failure) in underground mines has not been studied extensively and is still less understood than the concepts implied by the commonly used terms "strength" and "failure". Understanding failure stability should be a priority in locations where rockbursts are likely, such as under high stress and in the presence of brittle discontinuity surfaces. With the validation of the numerical program's capability to simulate stable and unstable shear failures of rock discontinuities as presented in Chapter Three, a model consisting of an existing geological discontinuity in the vicinity of an advancing underground excavation was built in UDEC.

The model is used to study the influence of the excavation on the failure stability of the geological discontinuity. The dimensions of the model are determined in a series of boundary determination tests. The final model has a width of 140 m and a height of 160 m. The excavation area is located in the middle of the model, and the existing geological discontinuity is located 2 m above the excavation. The failure stability of the discontinuity is determined by analyzing shear stress–time, shear displacement–time and shear stress–shear displacement records of the discontinuity in the process of excavating. The loading stiffness of the discontinuity is considered and analyzed in detail, including the influence of the factors such as the excavation extent, the location of the discontinuity and the elastic modulus of the rock material on the loading stiffness and the stability of the discontinuity.

4.1 Determination of Model Boundary

The boundaries of the stability analyses model are determined in a series of numerical tests. Section 4.1 describes the boundary determination tests and the test results.

4.1.1 Model Description

The model for the stability analyses of a geological discontinuity is shown in Figure 4.1. The model includes an underground excavation and an existing rock discontinuity. The width and height of the excavation are 20 m and 2 m, respectively. The discontinuity is located 2 m above the excavation and runs through the model in the horizontal direction. The left and right boundaries of the model are fixed in the horizontal direction, and the top and bottom boundaries are fixed in the vertical and horizontal directions. As illustrated in Figure 4.1, the vertical distance between the center and the top/bottom of the model is represented by d_v, and the horizontal distance between the sides of the excavation area and the corresponding sides of the model is represented by d_h.

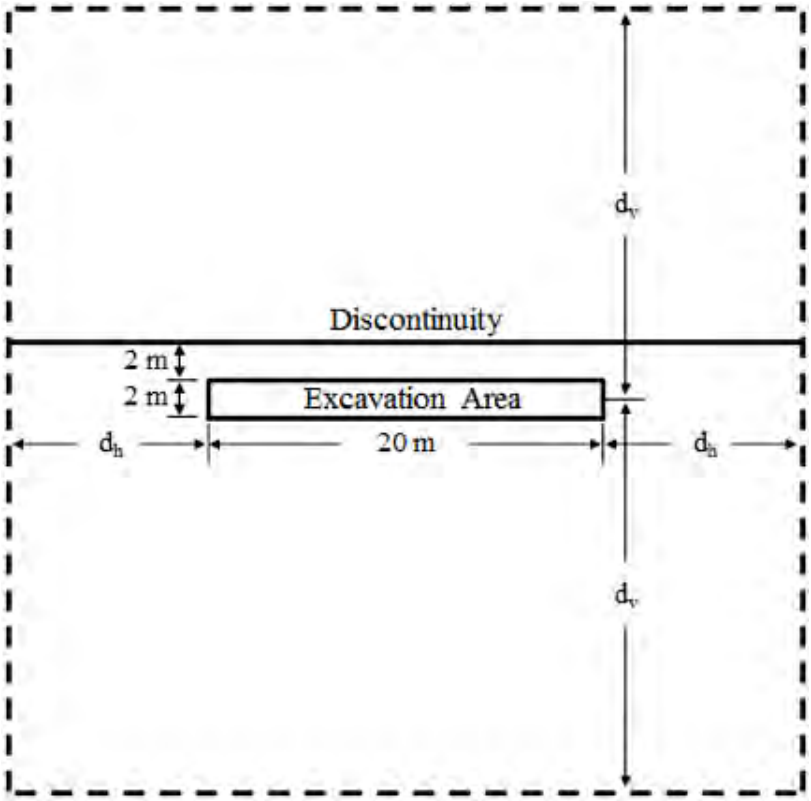

Figure 4.1: Illustration of the model for discontinuity stability test.

Determining the loading stiffness on the discontinuity is very important since it governs the failure stability of the rock discontinuity in the model. The loading stiffness can be af-

fected by the model boundaries if the boundaries are located too close to the excavation area. Hence, the boundary effect on the loading stiffness needs to be eliminated. To determine the model boundaries, a series of numerical tests were designed and performed. The UDEC codes for these tests are shown in Section D.5 in Appendix D. To determine the limits of the boundary, the following procedure was taken:

1. d_v was initially set to a large value of 100 m to eliminate the boundary effect of the top and bottom boundaries on the loading stiffness.

2. Six tests were performed by using six different d_h values of 20, 30, 40, 50, 60 and 70 m in the model.

3. A properd_h value was adopted as the final horizontal boundaries based on the results of these six tests.

4. With the determined horizontal boundaries, eight tests were conducted by varying d_v from 30 m to 100 m with a 10 m increment.

5. A proper d_v was chosen as the vertical boundaries of the model based on the results from the tests with varying d_v.

The model configuration for the first boundary determination test is shown in Figure 4.2. The model has a height of 200 m (i.e. d_v is 100 m) and a width of 60 m (i.e. d_h is 20 m). A rock layer, in which the excavation area is located, is set 2 m below the existing geological discontinuity and assigned the same material properties as the rest of the rocks in the model. In Figure 4.2, the solid black lines represent the numerical discontinuities. For the objective of the study in this chapter, the program was designed so that the rock discontinuity that is above the excavation is the only discontinuity that can fail in shear. The rest of the numerical discontinuities were taken as fictitious discontinuities that used to create the excavation area and mining cuts. The model was further discretized into a mesh of finite-difference triangular zones delineated by the red lines in Figure 4.2.

The discontinuity above the excavation was modeled as the CY joint model. The input parameters of the CY model are the same as that listed in Table 3.2 in Chapter Three. The MC model was assigned to the fictitious discontinuities. An elastic modulus of 70 GPa and a Poison's ratio of 0.2 were used in the elastic model for the rock layer and rocks. Considering the conditions of relatively deep underground mines, the model was assumed an in-situ stress field of 17.5 MPa in the vertical direction and 5.25 MPa in the horizontal direction to simulate an excavation at 700 m depth with the coefficient of lateral stress (k) of 0.3 in the rocks. The bottom-right inset in Figure 4.2 is an enlarged view of an area including the excavation and a part of the discontinuity. Point P, as represented by the black dot in the inset, is the measurement point used in the boundary determination tests. The graph at top-right is an enlarged view of an area around point P showing the details of the finite-difference zones connected to point P.

4.1.2 Loading Stiffness Determination

To determine the model boundaries for the discontinuity stability tests, the largest opening area in the tests (i.e. completed excavation area) was adopted in the boundary determination tests. This is because as the opening area in the model increases, the model boundaries need to be extended to eliminate the boundary effect on loading stiffness. A shear movement was invoked at point P and the corresponding shear stresses in each of the eight adjacent zones were recorded (see Figure 4.2). The sense of the shear movement is indicated by the blue arrows in the inset. The loading stiffness (LS) of point P is then calculated using the equation,

$$LS = \frac{\frac{1}{3}(\sigma_{xy_1} + \sigma_{xy_2} + \sigma_{xy_3} + \sigma_{xy_4} + \sigma_{xy_5} + \sigma_{xy_6} + \sigma_{xy_7} + \sigma_{xy_8})}{d_P} \tag{4.1}$$

where σ_{xy_i} ($i = 1, 2, \ldots, 8$) is the shear stress in zone i, and d_P is the horizontal displacement of point P.

In UDEC, the shear behavior shown in Figure 4.2 (i.e. a shear movement towards right at the upper section of the discontinuity and the same amount of shear movement towards

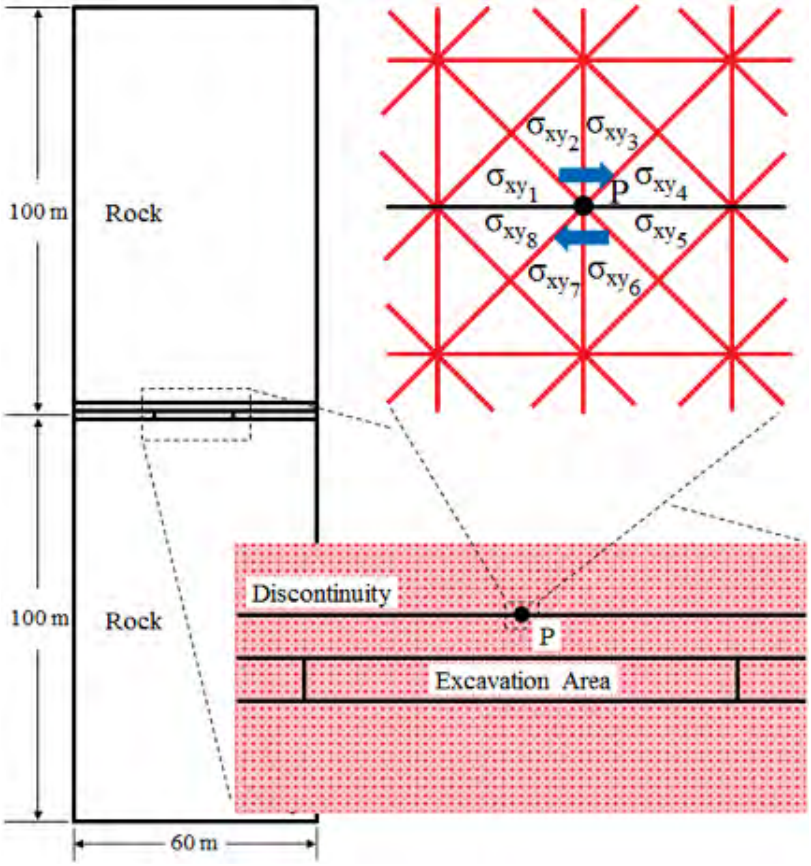

Figure 4.2: Model configuration of the first boundary determination test (the lower inset is an enlarged view of an area around the excavation and the discontinuity; the top-right is an enlarged view of an area around the measurement point P).

left at the lower section of the discontinuity) cannot be achieved in one simulation. However, running two separate simulations in UDEC can achieve the correct behavior along the discontinuity (as shown in Figure 4.2). The rock surrounding the discontinuity is modeled as an elastic material and it behaves similar to a spring. Thus, each side (top and bottom) of the discontinuity can be viewed as a spring, similar to what is shown in Figure 4.3a. By running simulations in both directions separately (e.g. Figure 4.3b and c), the correct behavior of the rock along the discontinuity is achieved. Since the properties of the rock are known, equivalent springs stiffness coefficients k_1 and k_2 can be obtained from the model. The stiffness is a function of the elastic modulus and geometry of a material. If the model is symmetrical in the horizontal direction, k_1 is equal to $k_1^{'}$, and k_2 is the same as $k_2^{'}$.

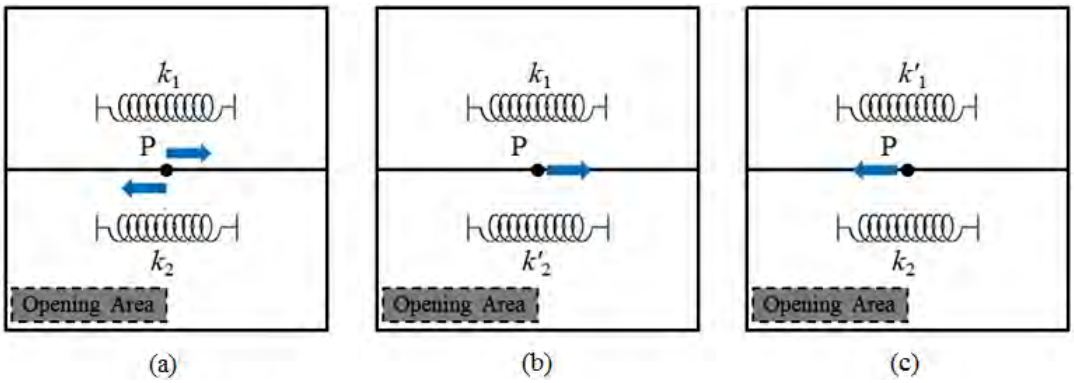

Figure 4.3: Illustrations illustrations of simulations for loading stiffness tests.

Thus, two tests were performed for each variation of d_v and d_h. In first test, a certain displacement toward right was applied at Point P (see Figure 4.4a). In the second test, the same displacement was applied towards left (see Figure 4.4b). By pulling the point in two opposite directions, the shear stresses in the adjacent zones were developed.

Using this method, the calculation of the loading stiffness at point P consists of the loading stiffnesses of the sections above and below the discontinuity. The loading stiffness of the upper section of the model (LS_{upper}) at point P is calculated as,

$$LS_{upper} = \frac{\frac{1}{3}(\sigma_{xy_1} + \sigma_{xy_2} + \sigma_{xy_3} + \sigma_{xy_4})}{d_P} \tag{4.2}$$

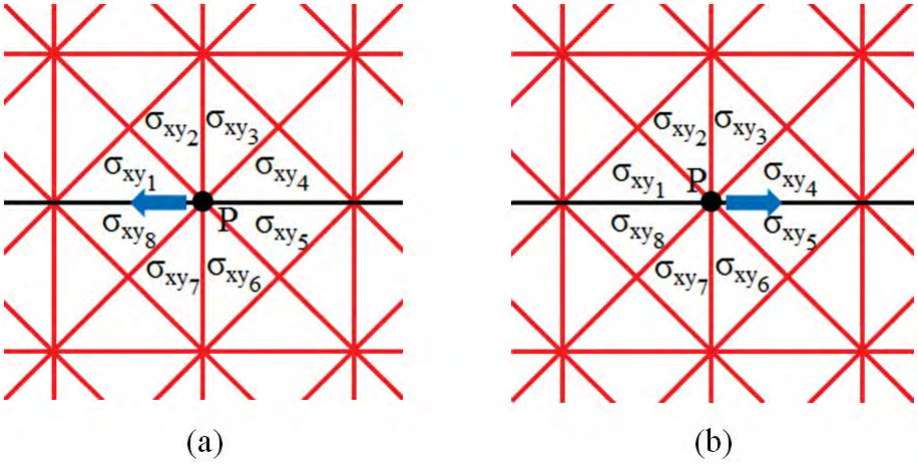

Figure 4.4: Sense of right and left pulls applied to the point P for boundary determination tests.

Similarly, the loading stiffness of the lower part of the model at point P can be computed using equation,

$$LS_{lower} = \frac{\frac{1}{3}(\sigma_{xy_5} + \sigma_{xy_6} + \sigma_{xy_7} + \sigma_{xy_8})}{d_P} \tag{4.3}$$

where σ_{xy_i} ($i = 1, 2, \ldots, 8$) is the shear stress in zone i, and d_P is the horizontal displacement of point P. Due to the symmetry condition of the boundary determination tests in the horizontal direction, the loading stiffness at point P can be taken as the sum of LS_{upper} from the right-pull test and LS_{lower} from the left-pull test, and vice versa.

4.1.3 Boundary Effect on Loading Stiffness

For a fixed value of d_v (i.e. 100 m), six simulations were performed using different d_h values of 20 m, 30 m, 40 m, 50 m, 60 m and 70 m. As discussed in Section 4.1.2, for each d_h, two simulations were performed. The results are shown in Figure 4.5. In Figure 4.5, the vertical axis is loading stiffness and the horizontal axis is the horizontal dimension, d_h. The loading stiffness reduces significantly as d_h increases from 20 to 50 m, and then it stabilizes at larger d_h values. Clearly, d_h less than 50 m leads to unfavorable boundary effects on the loading stiffness at point P. To ensure that boundary effects would not affect the results, 60 m was used for d_h.

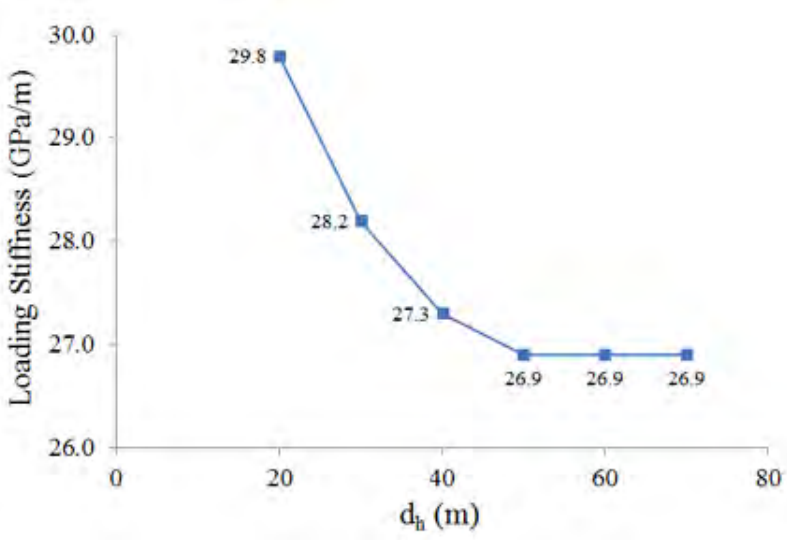

Figure 4.5: Variation of the loading stiffness at point P as d_h changes.

With the determination of the horizontal boundaries, eight tests were performed to determine the vertical boundaries by varying d_v. The results are shown in Figure 4.6, which indicate similar trends to the previous case in that, the boundary effects on the loading stiffness at point P exist when d_v has small values (i.e. 20 m to 60 m), and the loading stiffness is unaffected by the vertical boundaries as d_v becomes greater than 70 m. Based on the results, d_v was set 79 m so that the model height was an even 160 m.

The stress fields (i.e. vertical stress, horizontal stress and shear stress) in the model with the determined boundaries are checked, and it is shown that the determined boundaries have no effect on the stress fields. The contour plots of the stress fields are shown in Appendix B.

4.2 Discontinuity Stability Test

The model description, test procedure and test results are presented in Sections 4.2.1, 4.2.2 and 4.2.3, respectively. The UDEC codes for discontinuity stability test are shown in Section D.6 in Appendix D.

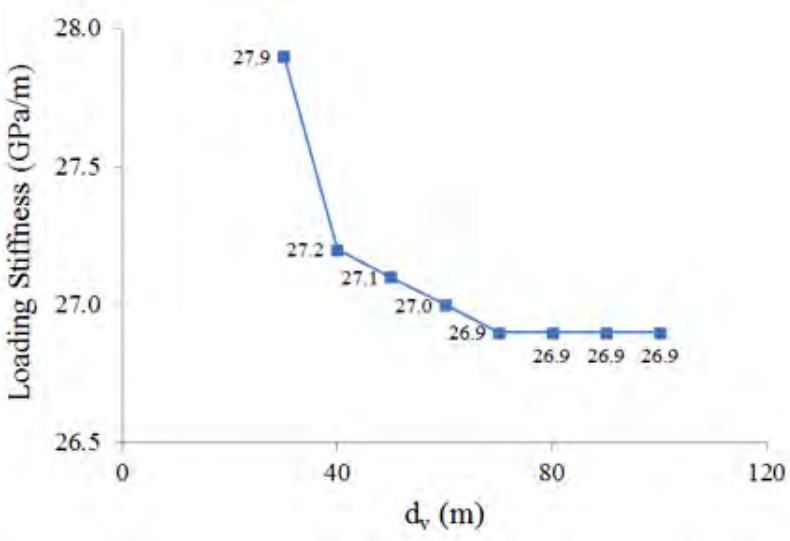

Figure 4.6: Variation of the loading stiffness at point P as d_v changes.

4.2.1 Model Description

The UDEC model, which is shown in Figure 4.7, has the similar configuration as that shown in Figure 4.1 except it has the determined width of 140 m and height of 160 m as obtained from the boundary determination tests. The shaded region in Figure 4.7 represents the excavation area in which mining cuts will be applied. The inset in Figure 4.7 is an enlarged view of the excavation area. The excavation area was divided into 80 slender blocks to simulate a staged excavation. The model was further discretized into a mesh of triangular finite-difference zones.

4.2.2 Test Procedure

Fifteen measurement points along the discontinuity, as shown in the inset in Figure 4.7, were chosen to record shear displacement, shear stress, and normal stress in the stability analysis test. The model was brought to equilibrium before any mining cut was introduced. The excavation area consists of 80 successive mining steps. These steps were initiated sequentially in the direction indicated by the blue arrow in the inset to simulate an advancing mining face. One mining step was simulated by removing one slender block at a time and

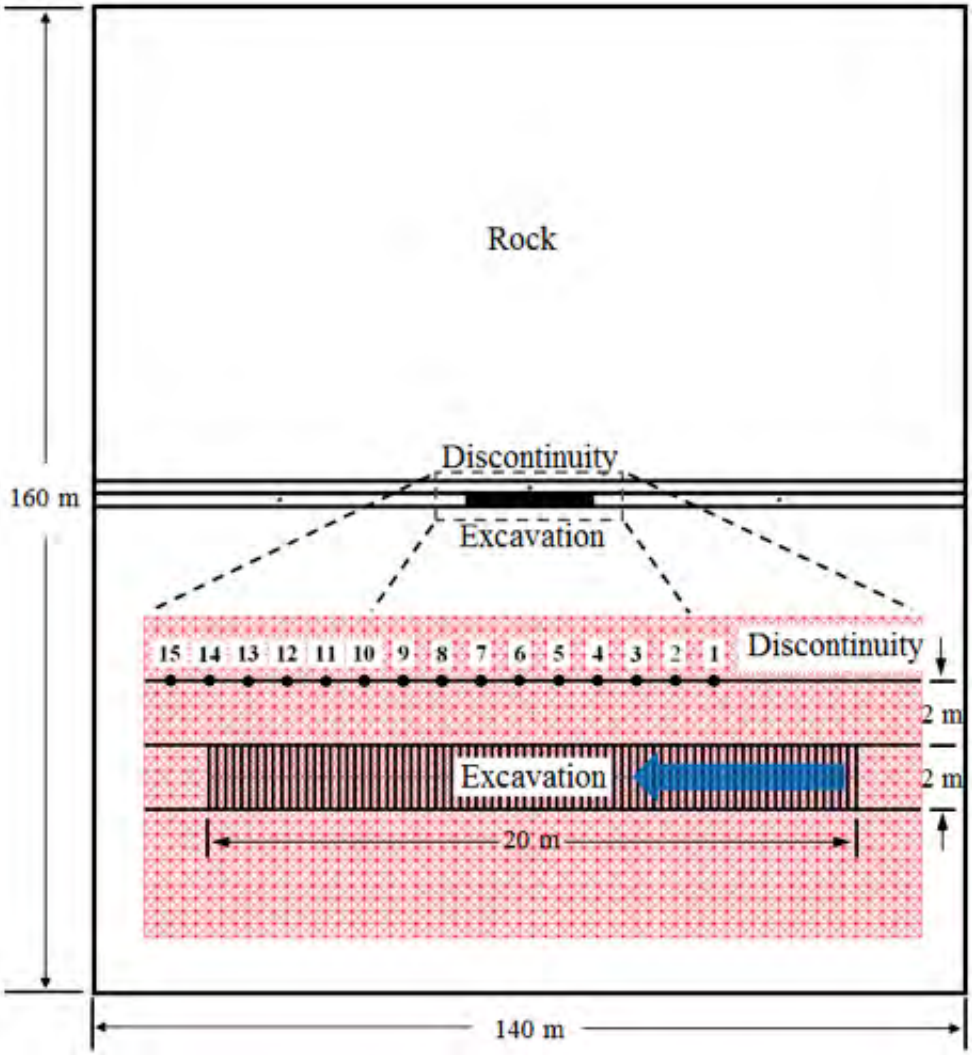

Figure 4.7: Configuration of the model for discontinuity stability analysis.

running the model to equilibrium. This procedure was repeated until all the mining steps in the excavation area were completed.

4.2.3 Test Results

The test results are presented in both graphic and tabulated forms for all the measurement points. The most representative results of stable, semi-stable and unstable failures are also discussed.

4.2.3.1 Plotted Stress and Displacement Results

The normal stress–time curves for all measurement points are plotted in Figure 4.8, The time is the numerical time utilized in the program. Positive normal stress indicates compressive loading. Different colors in Figure 4.8 represent different measurement points. The squares in the curves indicate the recorded data. The small, step-like curved features in the curves show normal stress formation at the measurement points while the model is equilibrating after one mining cut. Once the equilibrium is achieved, the model initiates the next mining step. The vertical sections in the curves with less data points represent the normal stress evolution in the process of conducting mining steps. As the excavation face approaches the location of the measurement points, the normal stresses at the points increase. The normal stresses developed at the measurement points reach their maximum values before the excavation face reaches the locations of the measurement points. As the excavation moves away from the points, the normal stresses decrease.

The shear displacement records of all measurement points are shown in Figure 4.9 as shear displacement–time curves. The positive direction of shear displacement is indicated in the bottom-left inset. Points 1 to 5 experience initially increase-decrease processes in their shear displacements in the positive shear direction. They then increase in the shear displacements in the negative shear direction as the excavation face advances. Points 6 to 9 undergo increase-decrease processes of the shear displacements only in the positive shear direction. Points 10 to 15 experience only increases in the shear displacements in the positive

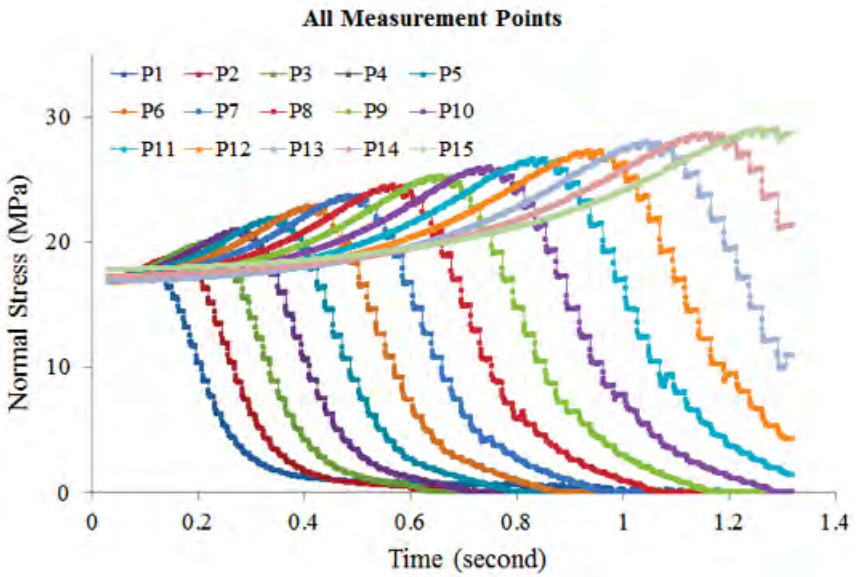

Figure 4.8: Normal stress–time plots of all measurement points in the discontinuity stability test.

shear direction. The shear directions for points 6 to 15 are not reversed in the process of excavating. The changes in the shear displacements of points 1 to 7 are gradual and smooth. Based on the analyses presented in Chapter Three, these measurement points undergo stable shear failures. Rapid changes in the shear displacements are observed at points 8 to13, which implies the occurrence of unstable shear failures at these points.

Shear stress records of all measurement points are plotted in Figure 4.10. The positive shear stress indicates that the shear direction of the points is the same as that in the inset in Figure 4.9. The advancing excavation face results in the changes in the shear stresses on the discontinuity. The shear stresses increase as the excavation face approaches the measurement points, and the maximum shear stresses are reached when the excavation face is close to the points. As the excavation moves away from the points, the shear stresses start to decrease. Points 1 to 6 succeed in sustaining the maximum shear stress mobilized on them without failing. When the excavation face passes these points, their shear stresses start to reduce. No failures occur in this area until about 0.6 seconds. The changes in the shear stresses are gradual for points 1 to 6 in their failure processes, which suggest that stable shear failures

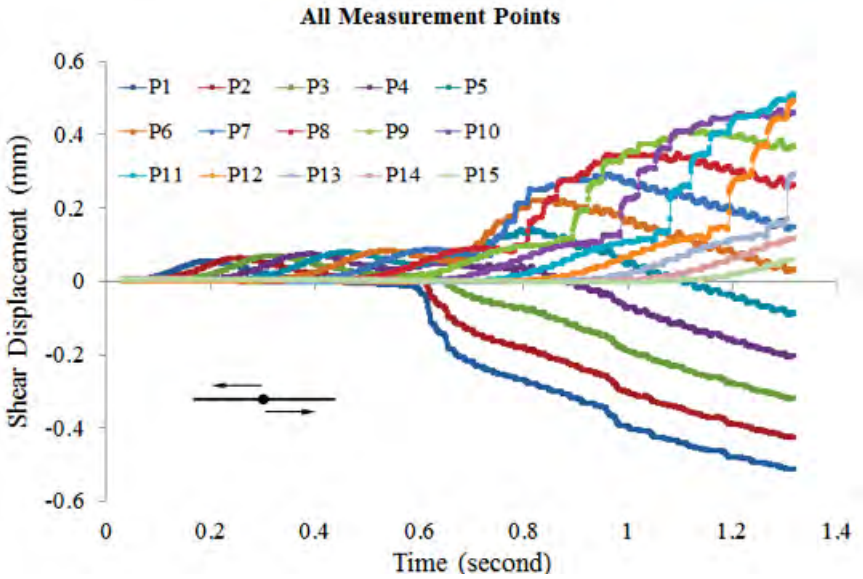

Figure 4.9: Shear displacement–time plots of all measurement points in the discontinuity stability test.

take place. The shear stresses at points 8 to 13 increase suddenly before they reach their maximum values. This is because the shear stresses that previously carried by the contact points that located right in front of points 8 to 13 (not the chosen measurement points) cannot sustain the shear stresses developed on them and experience sudden decreases in the shear stresses. The shear stresses at these contact points are redistributed and transferred to the non-failed points (i.e. points 8 to 13). The additional shear stress exceeds the shear strength at points 8 to 13 and results in shear failures at these points. Rapid decreases in the shear stresses at points 8 to 13 in their failure regions imply unstable shear failures. Point 7 starts to fail at about 0.7 seconds and experiences a small rapid change in the shear stress, which can be considered as a transitional failure state between stable and unstable shear failures (i.e. a semi-stable failure). Points 14 and 15 are in their elastic regimes in the entire excavation process.

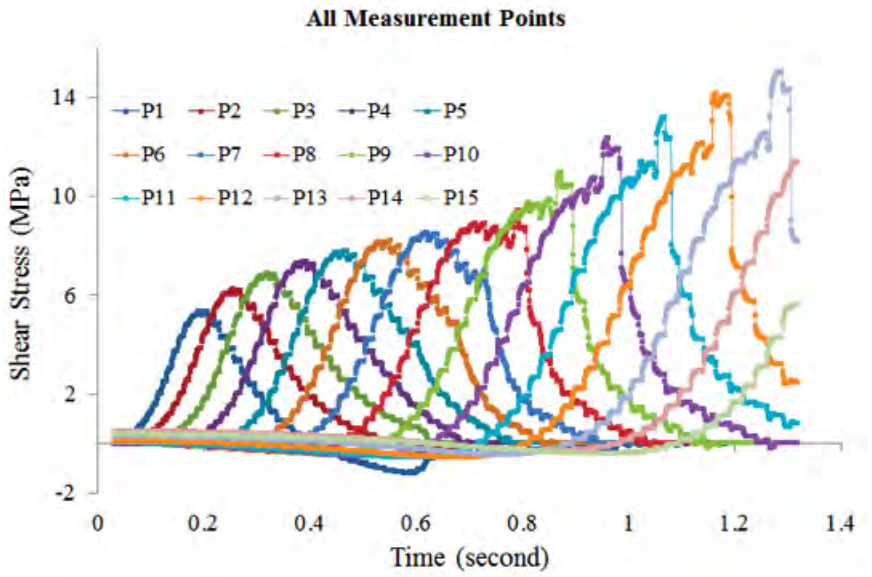

Figure 4.10: Shear stress–time plots of all measurement points in the discontinuity stability test.

4.2.3.2 Tabulated Stress and Displacement Results

More detailed information about shear failures at the measurement points is provided in Table 4.1. Table 4.1 lists the time at which shear failures initiated, the x-coordinate of the measurement points, the location of the excavation face when shear failure occurred, the horizontal distance between each point and the excavation face when the point started to fail, and the failure stability (stable, semi-stable, unstable). The origin (x=0, y=0) of the Cartesian coordinate system is located at the center of the model. The x-axis is in the horizontal direction and oriented to point to right. The y-axis is in the vertical direction and oriented to point upwards. In this coordinate system, the right side and the left side of the excavation area are located at 10 m and -10 m, respectively, on the x-axis.

The results shown in Table 4.1 indicate that, generally, shear failures occur in sequence at the measurement points: failures initiate from the points at the right-hand side and propagate to the left-hand side (from points 1 to 15). Table 4.1 also shows that shear failures of the points take place after the excavation face passes the locations of the measurement points. The horizontal distance between the measurement points and the excavation face at the

instant of shear failure reduces as the failures propagate to the left of the model. Normal stresses as measured by the measurement points increase from 0.76 MPa for point 1 to 12.2 MPa for point 13 as failure occurs. Higher normal stresses lead to higher shear strengths at the points. However, when the strengths are exceeded, they result in higher shear stress drops at points 8 to 13 (see Figure 4.10), which indicates increased intensity of unstable shear failures. At the beginning of the excavation process, stable shear failures occur at measurement points 1 to 6. As the excavation face advances, unstable shear failures start to take place at points 8 to 13 with increased intensity—as signified by the amount of rapid shear stress drop. The changes in failure stability of the points are caused by variations in stress distribution and loading stiffness that occur in the surrounding rock during the mining process.

4.2.3.3 Characteristics of Stable, Semi-stable and Unstable Failure Mechanisms

This section discusses the shear displacements and shear stresses measured at points 5, 7 and 13. These points exhibit the most characteristics behavior of the stable, semi-stable (i.e. the transition state between stable and unstable shear failures) and unstable shear failures, respectively. Their shear displacement–time, shear stress–time and shear stress–displacement curves are plotted and discussed in detail. By analyzing these different types of plots, the failure stability of the measurement points can be determined.

The shear displacement–time plot of point 5 is shown in Figure 4.11. Point 5 starts to fail at 0.6 seconds (Table 4.1), which is marked by the red dashed line in Figure 4.11. Prior to the failure, shear displacement magnitude first increases and then decreases under the influence of the excavation face approaching and moving away from the point. The interval to the left of the red dashed line is the pre-failure regime, and the interval to the right is the post-failure regime. In the pre-failure regime, all elastic shear displacements are in the positive shear direction, although the displacement magnitudes start decreasing as the mining face passes by. In the post-peak regime, the shear displacement first decreases to zero and then becomes negative and starts increasing in magnitude.

Table 4.1: Detailed information about the shear failures at the measurement points in the discontinuity stability analysis.

Points	Time of failure initiation (in seconds)	X-coordinate of measure-ment points (in meters)	X-coordinate of excavation face when failure occurs (in meters)	Horizontal distance between points and face (in meters)	Normal stress at points when failure occurs (in MPa)	Failure stability of points
1	0.584	+5.60	-1.50	7.10	0.76	stable
2	0.604	+4.40	-1.75	6.15	0.29	stable
3	0.502	+3.20	+0.25	2.95	1.30	stable
4	0.518	+2.00	-0.50	2.50	2.68	stable
5	0.604	+0.80	-1.75	2.55	3.31	stable
6	0.659	-0.40	-2.50	2.10	3.93	stable
7	0.732	-1.60	-3.50	1.90	4.70	semi-stable
8	0.814	-2.80	-4.50	1.70	6.03	unstable
9	0.917	-4.00	-5.50	1.50	7.05	unstable
10	0.983	-5.20	-6.50	1.30	8.16	unstable
11	1.070	-6.40	-7.75	1.25	9.40	unstable
12	1.190	-7.60	-8.75	1.15	10.80	unstable
13	1.293	-8.80	-9.75	0.95	12.20	unstable
14	-	-10.00	-	-	-	-
15	-	-11.20	-	-	-	-

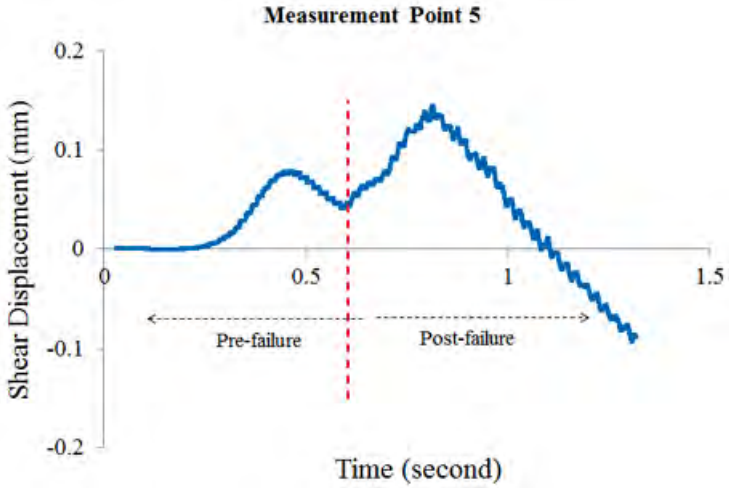

Figure 4.11: Shear displacement–time plot of measurement point 5.

The shear stress–time plot of point 5 is shown in Figure 4.12. As the excavation face advances, the shear stress at point 5 first increases and then decreases with the excavation face moving away from the point until it reaches a constant value of zero. The maximum shear stress is achieved when the excavation face is located close to point 5. No shear failure occurs at point 5 until about 0.6 seconds from the start of the test. After failure, the gradual, continued decrease in shear stress indicates the occurrence of a stable shear failure.

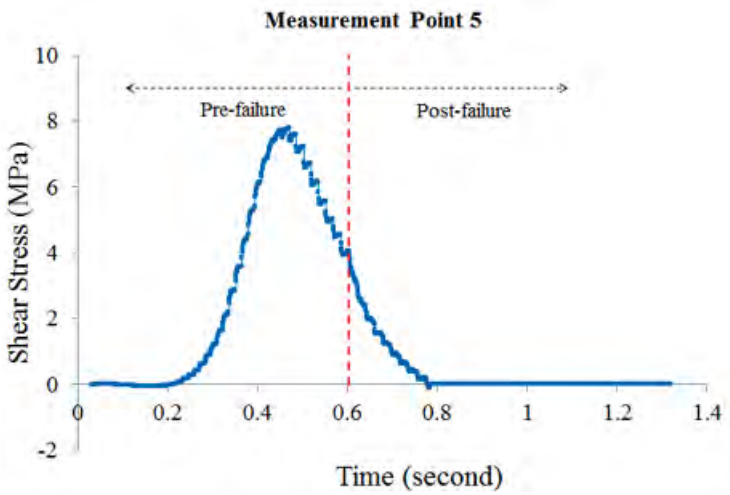

Figure 4.12: Shear stress–time plot of measurement point 5.

Further details of the shear behavior of point 5 are depicted as five distinct stages in Figure 4.13. In the first stage, the shear stress and shear displacement increase as the mining face moves toward the left. The shear stress and shear displacement reach their peak values when the mining face just passes the measurement point (see Figure 4.13a). In the second stage, the shear stress and shear displacement start decreasing as the mining face moves away from the point, which signifies an elastic unloading process (see Figure 4.13b). With the initiation of shear failure at the point in the third stage, the shear stress keeps reducing until it reaches zero, and the shear displacement begins to rise again until it reaches the second peak value of the displacement (see Figure 4.13c). In the fourth stage, the shear stress remains at zero, and the shear displacement decreases to zero in the positive direction (see Figure 4.13d). The reason for this behavior shown in this stage is because the lower section

of the failed discontinuity at point 5 is free to move and pulled left by the redistributed stress as the mining face advances. In the fifth stage, the shear displacement becomes negative and increases in magnitude, which indicates that the shear behavior shown in Figure 4.13e has occurred.

Figure 4.14 shows the shear displacement–time plot of the measurement point 7. Point 7, behaves similarly to Point 5, and exhibits two peaks in its shear displacement plot. The failure occurs at about 0.73 seconds. The pre-failure regime is similar to that of point 5. In the post-failure regime, however, small amounts of rapid and discontinuous increases in the shear displacement indicated by the sparse data points imply that the initiation of the failure at the point has been less stable.

As shown in the shear stress–time curve of point 7 in Figure 4.15, the small rapid decreases in shear stress with relatively sparse data points in its post-failure regime also imply the tendency of having an unstable shear failure. Hence, the shear failure at point 7 is considered as the transition state between stable and unstable shear failures (i.e. a semi-stable failure).

The shear displacement–time and shear stress–time plots of point 13 are shown in Figure 4.16 and Figure 4.17, respectively. The failure occurs at about 1.3 seconds. There is a small rapid increase in shear displacement as well as in shear stress in the pre-failure regime. This is caused by the unstable failures at the contact points located at the right side of point 13 on the discontinuity. In the post-failure regime, a large rapid increase in shear displacement and decrease in shear stress along with sparse data points signify the shear failure at point 13 is in the unstable manner. Point 13 regains its equilibrium after the unstable failure occurs The equilibrium is indicated by the gradual changes in shear displacement and shear stress with dense data points in the post-failure region.

The failure stability of the measurement points can also be identified through analyzing their shear stress–displacement plots. The shear stress–displacement plots of the same measurement points as presented above (points 5, 7 and 13) are shown in Figure 4.18, Figure 4.19 and Figure 4.20.

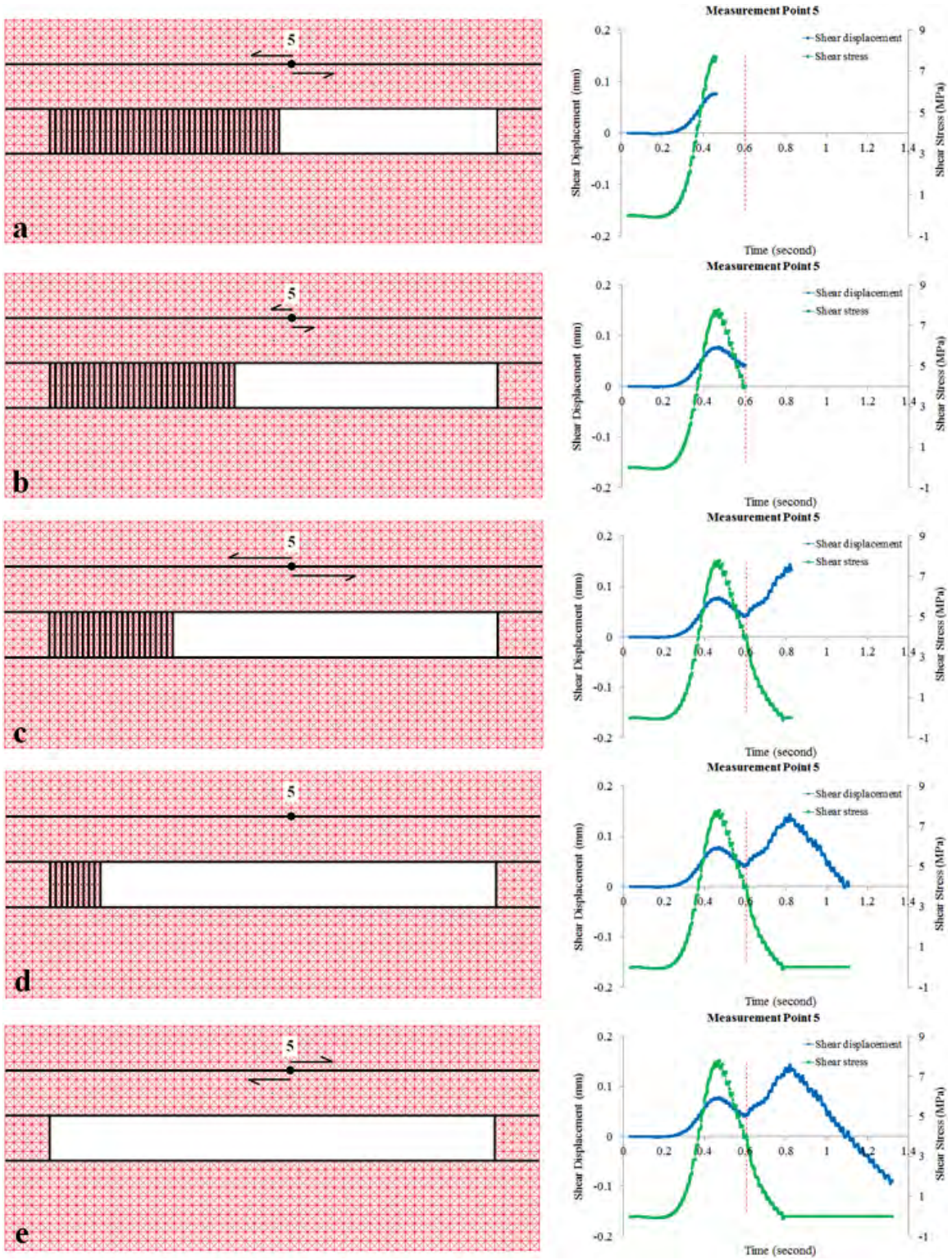

Figure 4.13: Shear displacement–time plot of point 5 in different stages and its corresponding state in the model.

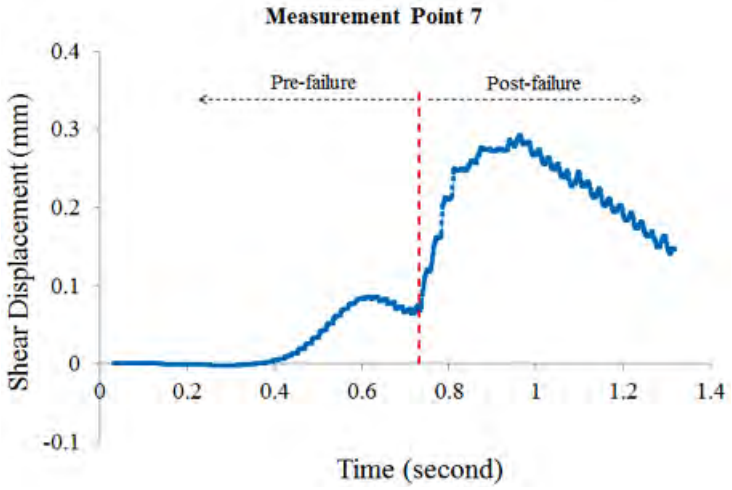

Figure 4.14: Shear displacement–time plot of measurement point 7.

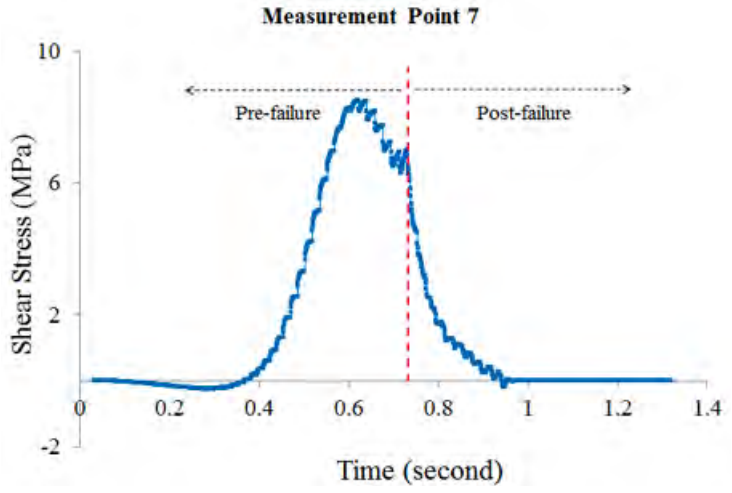

Figure 4.15: Shear stress–time plot of measurement point 7.

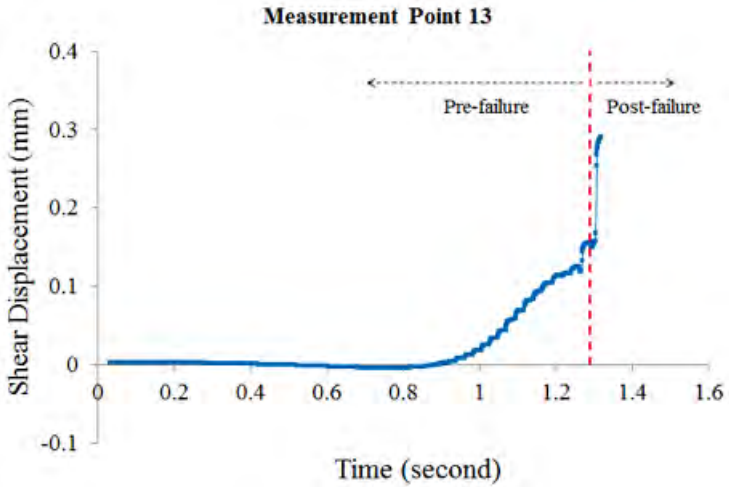

Figure 4.16: Shear displacement–time plot of measurement point 7.

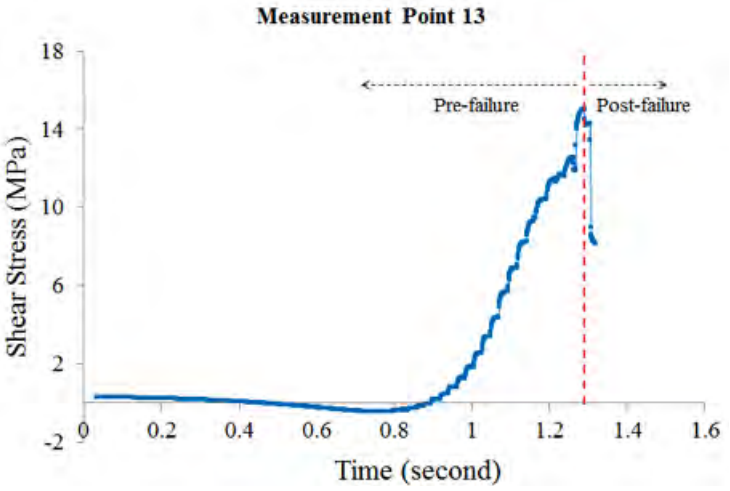

Figure 4.17: Shear stress–time plot of measurement point 7.

In these figures, the shear stress–displacement behaviors that deviate from elastic behaviors indicate failures. The dense data points in the post-failure regime in Figure 4.18 indicate that point 5 experiences a stable failure. The relatively sparse data points in Figure 4.19 imply a semi-stable shear failure occurs at point 7. The sparse data points in Figure 4.20 show an unstable shear failure at point 13.

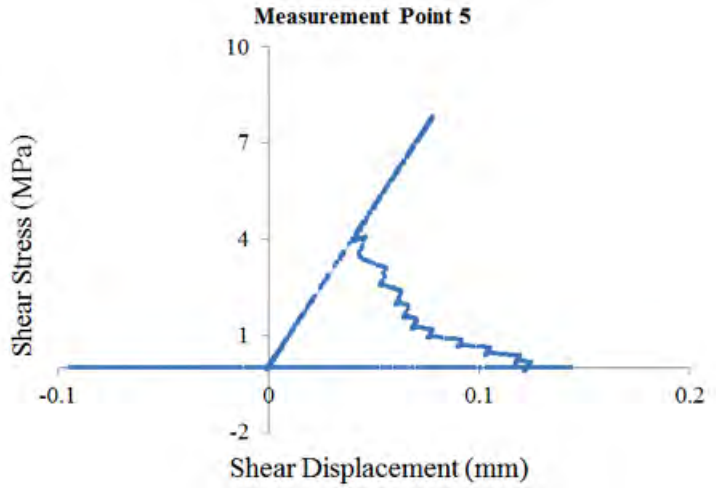

Figure 4.18: Shear stress–displacement plot of measurement point 5.

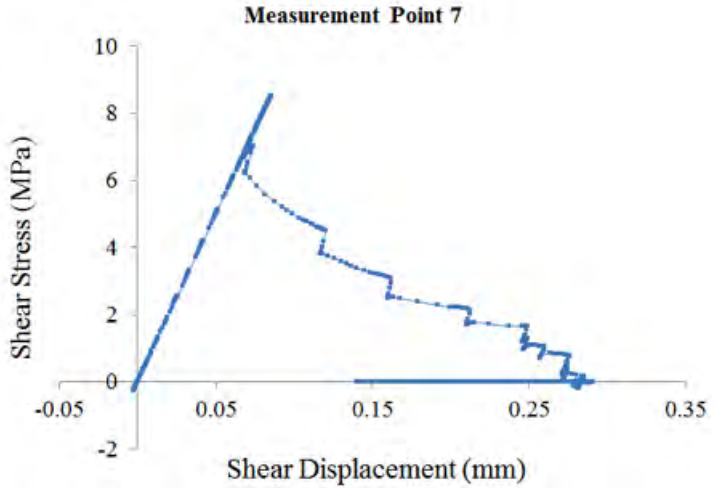

Figure 4.19: Shear stress–displacement plot of measurement point 7.

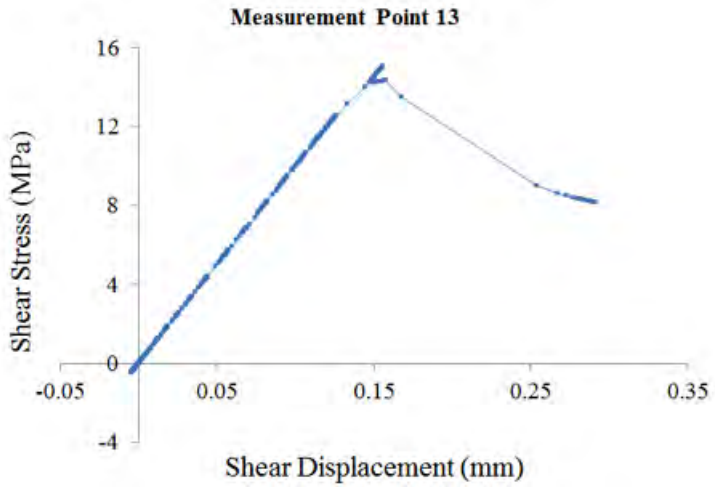

Figure 4.20: Shear stress–displacement plot of measurement point 13.

4.3 Analyses of Loading Stiffness

Loading stiffness plays a significant role in governing the stability of shear failures of rock discontinuities. The larger loading stiffness is, the smaller the tendency of unstable failures occurring for a given discontinuity. Loading stiffness is affected by the excavation extent, the location of the discontinuities relative to the excavation, and the elastic modulus of surrounding rock. The following sections discuss the results from a series of simulations performed to study the influence of these factors on loading stiffness.

4.3.1 Description of Simulations

The model configuration used for the tests for analyzing the effects of geometry and elastic modulus on loading stiffness is shown in Figure 4.21. Three factors are studied individually using the methodology given below:

1. The length of the excavated area is represented by d in Figure 4.21. To investigate the effect of the excavation extent, six different values of d (i.e. 0, 4, 8, 12, 16 and 20 m) were used in six loading stiffness tests. The measurement point for these tests is P_d.

2. For the influence of the distance between the excavation roof and discontinuity, the excavation area was fully excavated and the discontinuity location was changed. The

distance between the excavation roof and discontinuity is represented by h in Figure 4.21. Eight different values of h from 1 to 8 m with 1 m increment were used. The measurement point for the tests is P_h which is located at the center of the discontinuity.

3. To demonstrate the effect of rock elastic modulus on loading stiffness, an elastic modulus of 50 GPa was assigned to the rock.

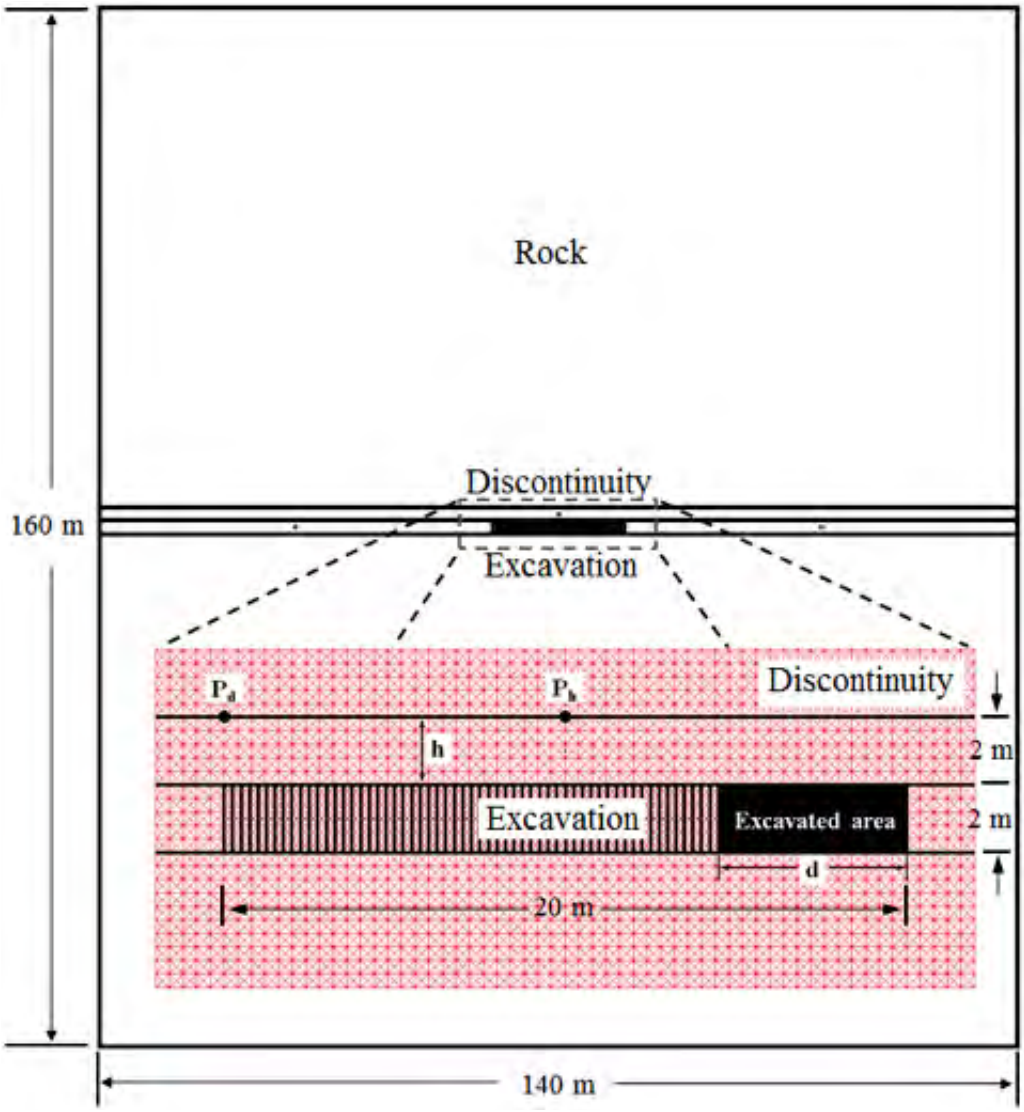

Figure 4.21: Configuration of the tests for effect of the factors.

4.3.2 Test Results

The test results of the effects of the excavation extent, the discontinuity plane location and rock elastic modulus on loading system stiffness are shown in Sections 4.3.2.1, 4.3.2.2 and 4.3.2.3, respectively. The UDEC codes for these tests are shown in Section D.7 in Appendix D.

4.3.2.1 Effect of Excavation Extent

The effect of the excavated length d on the loading stiffness of point P_d is shown in Figure 4.22. The loading stiffness at the point decreases as the excavation length increases. Based on the results shown in Figure 4.22, a length of up to 4 m has no effect on the loading stiffness at the point. As the length increases beyond 4 m, it starts affecting the loading stiffness. The effect of an extensive excavated area becomes significantly larger when the excavation face is close to the measurement point. The change in the loading stiffness from the first test (d = 0 m) to the last test (d = 20 m) is 6.3 GPa/m. The study implies that the extent of mining affects loading stiffness and can potentially change the failure stability of rock discontinuities.

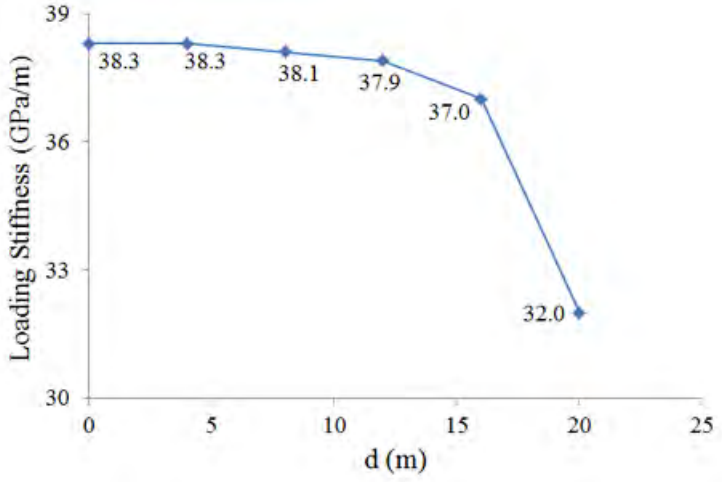

Figure 4.22: Effect of the length of the excavated area on the loading stiffness of point P_d.

4.3.2.2 Effect of Discontinuity Plane Location

The effect of discontinuity plane distance to mining level, h, on the loading stiffness at point P_h is shown in Figure 4.23. The loading stiffness at P_h increases as h becomes larger. In the model with the completed excavation of the model, the loading stiffness at P_h increases to a constant value when the distance between the excavation roof and discontinuity reaches 7 m. Beyond this 7 m distance, the fully excavated area has no influence on the loading stiffness of the point. The loading stiffness at P_h increases 14.3 GPa/m as h increases from 1 m to 8 m. Although only one point P_h is used, the trend of loading stiffness change with increasing distance is expected to be similar along the discontinuity.

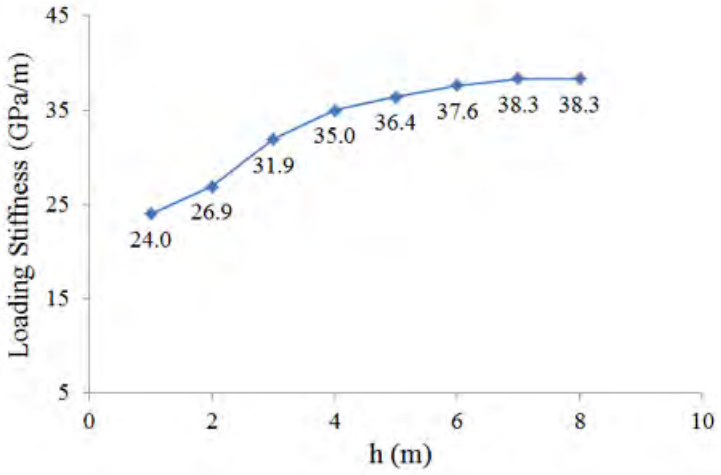

Figure 4.23: Effect of the distance between the excavation roof and discontinuity on the loading stiffness of point P_h.

Based on the results shown in Figure 4.23, it can be deduced that a larger distance h results in a smaller possibility of unstable shear failures for the discontinuity. To demonstrate this effect, the discontinuity stability analysis test was re-conducted with h of 3.5 m applied in the model. Besides the change in the location of the discontinuity (i.e. move up for 1.5 m), the model has the same configuration and properties as the one described in Section 4.2 (see Figure B.1. Fifteen measurement points with the same x-coordinates as the corresponding ones in Section 4.2 were used in the new model.

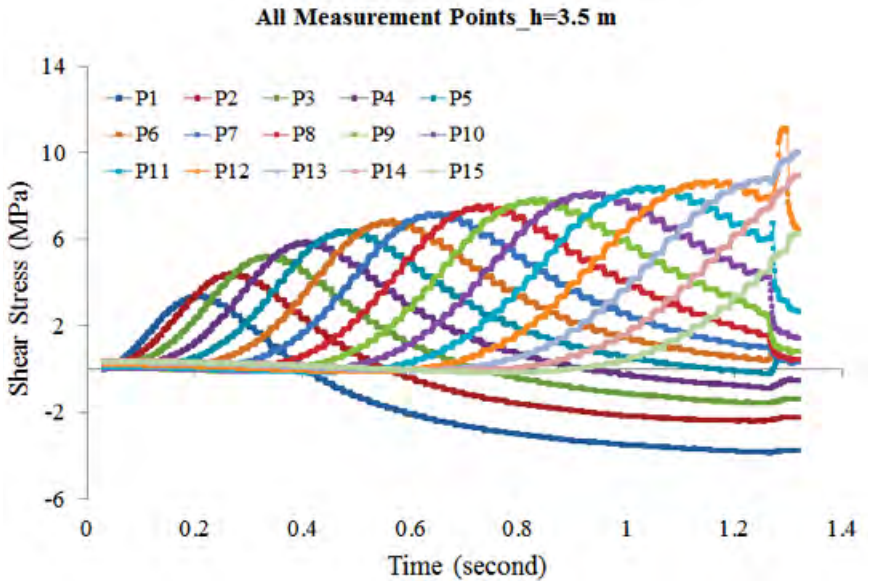

Figure 4.24: Shear stress–time plots of all measurement points in discontinuity stability test with h=3.5 m.

The results of the test are shown in Figure 4.24 in the form of the shear stress–time plots. With h increases to 3.5 m the occurrence of stable shear failures, unstable shear failures, and the intensity of the unstable failures at the measurement points all decrease. Detailed data of the test are listed in Table 4.2. Measurement points 1 to 4 undergo no shear failure. However, the stable failures initiate at these points in the test with h of 2 m (see Table 4.1). The normal stresses at the points of unstable failures are smaller than that in the test with h of 2 m. The results suggest the location of the pre-existing rock discontinuity is important for the failure stability of the discontinuity because it varies the stress distribution and loading stiffness in the model.

4.3.2.3 Effect of Rock Elastic Modulus

To demonstrate the effect of rock elastic modulus on the stability of rock discontinuities, the discontinuity stability test was performed with an elastic modulus of 50 GPa assigned to the rock. The shear stress–time plots of all measurement points are shown in Figure 4.25. Comparing to Figure 4.10 (i.e. shear stress–time plots of the test with an elastic modulus of

Table 4.2: Detailed information about the shear failures at the measurement points in the discontinuity stability analysis with h=3.5 m utilized in the model.

Points	Time of failure initiation (in seconds)	X-coordinate of measure-ment points (in meters)	X-coordinate of excavation face when failure occurs (in meters)	Horizontal distance between points and face (in meters)	Normal stress at points when failure occurs (in MPa)	Failure stability of points
1	-	+5.60	-	-	-	-
2	-	+4.40	-	-	-	-
3	-	+3.20	-	-	-	-
4	-	+2.00	-	-	-	-
5	1.240	+0.80	-9.25	10.05	0.62	stable
6	1.240	-0.40	-9.25	8.85	0.59	stable
7	0.959	-1.60	-6.25	4.65	2.27	stable
8	1.050	-2.80	-7.25	4.45	2.54	stable
9	1.140	-4.00	-8.25	4.25	2.82	stable
10	1.240	-5.20	-9.25	4.05	3.19	semi-stable
11	1.240	-6.40	-9.25	2.85	5.81	unstable
12	1.280	-7.60	-9.50	1.90	9.32	unstable
13	-	-8.80	-	-	-	-
14	-	-10.00	-	-	-	-
15	-	-11.20	-	-	-	-

70 GPa in the rock), more unstable failures are observed at the points, and the intensity of unstable failures are larger.

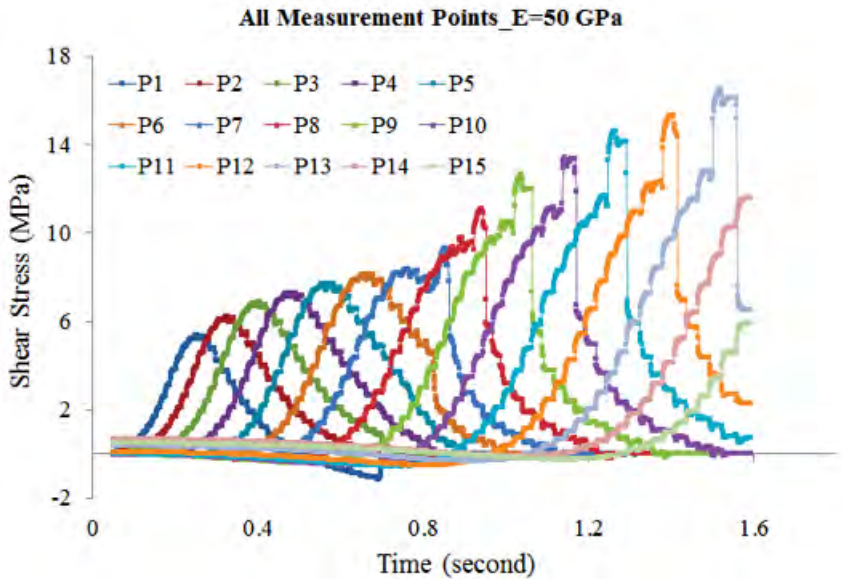

Figure 4.25: Shear stress–time plots of all measurement points in the test with the elastic modulus of 50 GPa applied in the rock.

More detailed information regarding the test is provided in Table 4.3. Measurement points 1 to 5 undergo stable shear failures in the process of excavating. The shear failure of point 6 is considered a semi-stable failure; while the shear failure at point 6 is in the stable manner when use 70 GPa as the rock elastic modulus. Unstable shear failures occur at points 7 to 13, and points 14 and 15 experience no shear failure in the test. The normal stresses developed at the measurement points at the time of unstable failure initiation are larger than that at the corresponding points in Table 3.1. Comparing Figure 4.25 and Figure 4.10, it can be seen that larger shear stresses are mobilized at the points that fail unstably. The results indicate that the smaller elastic modulus can result in more unstable shear failures with higher intensity at the discontinuity, which in a way signifies the importance of the rock properties in underground mines that expected to experience shear failures on existing discontinuities.

Table 4.3: Detailed information about the shear failures at the measurement points in the discontinuity stability analysis with an elastic modulus of 50 GPa assigned to the rock.

Points	Time of failure initiation (in seconds)	X-coordinate of measure-ment points (in meters)	X-coordinate of excavation face when failure occurs (in meters)	Horizontal distance between points and face (in meters)	Normal stress at points when failure occurs (in MPa)	Failure stability of points
1	0.677	+5.60	-1.00	6.60	0.74	stable
2	0.702	+4.40	-1.25	5.65	0.30	stable
3	0.560	+3.20	+0.50	2.70	2.14	stable
4	0.638	+2.00	-0.50	2.50	2.50	stable
5	0.719	+0.80	-1.50	2.30	3.10	stable
6	0.806	-0.40	-2.50	2.10	3.67	semi-stable
7	0.872	-1.60	-3.25	1.65	6.29	unstable
8	0.966	-2.80	-4.25	1.45	7.52	unstable
9	1.060	-4.00	-5.25	1.25	8.57	unstable
10	1.170	-5.20	-6.25	0.95	9.77	unstable
11	1.270	-6.40	-7.25	0.85	10.85	unstable
12	1.380	-7.60	-8.25	0.65	11.85	unstable
13	1.490	-8.80	-9.25	0.45	13.14	unstable
14	-	-10.00	-	-	-	-
15	-	-11.20	-	-	-	-

4.4 Conclusions

The discontinuity stability tests showed that the CY joint model is capable of simulating shear behaviors of discontinuities loaded by a mining process. As the excavation face approaches the location of the measurement points, the normal and shear stresses at the points increased. As the excavation face moves away from the points, the normal and shear stresses started to decrease. The decreases in the shear stresses are gradual and smooth for stable shear failures and rapid and discontinuous for unstable shear failures.

In the mining process, some regions (measurement points 1 to 8) on the discontinuity undergo elastically loading-unloading process before failures occur. Some regions (measurement points 1 to 9) of the discontinuity experience changes in their shear movement directions towards the end of the mining process. Underground mining changes loading stiffness as well as stress distribution in the surrounding rock mass resulting in both stable and unstable shear failures along discontinuities. The occurrence and intensity of unstable failures can be identified by analyzing shear stress and shear displacement records as discussed in this chapter. The intensity of unstable shear failures become larger with increased normal and shear stress magnitudes, and reduced mine stiffness.

Loading stiffness at a given location on the discontinuity is influenced by factors such as the extent of the excavated area, the location of the discontinuity relative to the discontinuity, and the elastic modulus of the surrounding rock in the underground opening. Loading stiffness become smaller with an increase in the excavation extent, a decrease in the distance between the discontinuity and excavation, or a decrease in the rock elastic modulus, which potentially provides a higher proneness and intensity of unstable shear failures.

CHAPTER 5

APPLICATION II: STABILITY OF MINING FACES AND SIDEWALLS IN UNDERGROUND COAL MINING CONDITIONS

In addition to shear failures that occur along existing rock discontinuities as discussed so far, unstable compressive failures also may occur around underground excavations. Unstable compressive failures sometimes lead to strain-type rockbursts and have been studied for many years.

In longwall coal mines, such failures occur mostly at the tail-gate corners and along the sidewalls of head-gates and development entries. In room-and-pillar mining, unstable compressive failures usually occur in pillars and entry sidewalls. The widely accepted criterion for unstable compressive failure is the stiffness criterion, originally proposed by Cook (1965b). According to this criterion, an unstable compressive failure of rocks occurs if the energy imparted by loading system exceeds the amount of the energy that the failing rocks can absorb during the failure. This instability condition exists during the failure of rock if the rock's post-peak slope of its stress–strain curve is steeper than the unloading slope of the loading system (i.e. the surrounding rocks). Otherwise, stable failures take place. This stiffness criterion can be used to successfully explain both stable and unstable compressive failures of rock samples observed in laboratory tests (Kias et al. 2011) and to effectively study unstable compressive failures in pillars. A similar stiffness criterion was proposed by Salomon (1974) and Rice (1983) for unstable shear failures along rock discontinuities (sometimes can cause slip-type rockbursts) and earthquakes as described in Chapter Three and Chapter Four. Despite the development and success in understanding the mechanisms of unstable failures in underground mining conditions, the mechanisms of unstable compressive failures in mining faces, sidewalls and pillars with large width-to-height ratios still require further studies.

This chapter first proposes two possible de-confinement mechanisms of unstable compressive failures in different mining configurations (i.e. mining faces and sidewalls), which take into account the mechanical properties of roof-coal and coal-floor interfaces. These two mechanisms are: 1) *unstable shear failures along the interfaces*, and 2) *existence of weak contact regions*. The chapter then describes a series of numerical simulations for validating the capability of UDEC to simulate stable and unstable compressive failures of rocks. Finally, this chapter presents the numerical simulations for investigating the proposed mechanisms. Ten numerical simulations were performed using UDEC and the CY and Mohr-Coulomb strain softening (MCSS) models. Among these simulations, two simulations were designed for studying the de-confinement caused by unstable shear failures along the interfaces, and the rest eight simulations were used to study the de-confinement resulted from the existence of weak contact regions. Summaries of the numerical simulations are shown in Table 5.1, Table 5.2 and Table 5.3. The results presented in this chapter, clearly indicate the importance of the mechanical properties of the interfaces for the failure stability of sidewalls and mining faces in underground mining conditions.

5.1 Description of Conceptualized Mine Layout Geometries used in Numerical Modeling Studies

The resistance, provided by the roof-coal and coal-floor interfaces, is one of the important factors that maintains the strength and stability of mining faces and sidewalls. However, these interfaces are seldom considered in the available literature as part of analyses of failure stability of mining faces or sidewalls in underground mining conditions. Two mechanisms involving sudden de-confinement at roof-coal and coal-floor interfaces are discussed in this study: 1) de-confinement due to unstable shear failure at the interfaces and 2) de-confinement due to the existence of weak contact regions (i.e. contact regions with no shear strength) on the interfaces.

Table 5.1: Summary of the simulations for the analyses of the de-confinement mechanism involving unstable shear failures along the interfaces.

	Characteristics of the simulations	
Simulations of unstable shear failures along the interfaces	CY joint model along the interfaces (USF-CY)	MC joint model along the interfaces (USF-MC)
Stability of mining faces or sidewalls	Sidewalls	Sidewalls
Unstable compressive failures of coal materials	Yes	No
Corresponding section	5.2.5.2	5.2.5.3
Corresponding figures	Figure 5.30, Figure 5.31, Figure 5.32, Figure 5.33, Figure 5.34	Figure 5.36, Figure 5.37, Figure 5.38, Figure 5.39, Figure 5.40
Comments	Unstable shear failures along the interfaces caused sudden de-confinement of the excavation sidewalls and unstable compressive failures	No sudden de-confinement occurred because the interfaces failed stably, hence stable compressive failures took place

Table 5.2: Summary of the simulations for the analyses of the de-confinement mechanism involving weak contact regions with varying widths of the weak regions.

	Characteristics of the simulations				
Different widths of the weak regions (w_{wr}), a constant width of the barriers of 0.5 m	w_{wr}=0.0 m	w_{wr}=0.5 m	w_{wr}=1.0 m	w_{wr}=1.5 m	w_{wr}=2.0 m
Stability of mining faces or sidewalls	Both	Both	Both	Both	Both
Unstable compressive failures (UCF) at mining faces	No	Yes	Yes	Yes	Yes
Unstable compressive failures at sidewalls	Yes	Yes	Yes	No	No
Corresponding section	5.2.5.4	5.2.5.4	5.2.5.4	5.2.5.4	5.2.5.4
Corresponding figures	Figure C.1 Figure C.2 Figure C.3 Figure C.4 Figure C.5	Figure C.6 Figure C.7 Figure C.8 Figure C.9 Figure C.10	Figure C.11 Figure C.12 Figure C.13 Figure C.14 Figure C.15	Figure C.16 Figure C.17 Figure C.18 Figure C.19 Figure C.20	Figure C.21 Figure C.22 Figure C.23 Figure C.24 Figure C.25
Comments	Same as USF-CY in Table 5.1	Increased UCF at mining faces, decreased UCF at sidewalls	Increased UCF at mining faces, decreased UCF at sidewalls	Increased UCF at mining faces	Increased UCF at mining faces

Table 5.3: Summary of the simulations for the analyses of the de-confinement mechanism involving weak contact regions with varying widths of the barrier.

	Characteristics of the simulations				
Different widths of the barriers (w_b), a constant width of the weak regions of 2.0 m	w_b=0.0 m	w_b=0.5 m	w_b=1.0 m	w_b=1.5 m	w_b=2.0 m
Stability of mining faces or sidewalls	Both	Both	Both	Both	Both
Unstable compressive failures (UCF) at mining faces	Yes	Yes	Yes	No	No
Unstable compressive failures at sidewalls	Yes	No	Yes	Yes	Yes
Corresponding section	5.2.5.5	5.2.5.5	5.2.5.5	5.2.5.5	5.2.5.5
Corresponding figures	Figure C.26 Figure C.27 Figure C.28 Figure C.29 Figure C.30	Figure C.31 Figure C.32 Figure C.33 Figure C.34 Figure C.35	Figure C.36 Figure C.37 Figure C.38 Figure C.39 Figure C.40	Figure C.41 Figure C.42 Figure C.43 Figure C.44 Figure C.45	Figure C.46 Figure C.47 Figure C.48 Figure C.49 Figure C.50
Comments	Many UCFs at mining faces, some UCFs at sidewalls	Increased UCF at mining faces (same as w_{wr}=2.0 m in Table 5.2)	Decreased UCF at mining faces, Increased UCF at sidewalls-	Increased UCF at sidewalls	Decreased UCF at sidewalls

5.1.1 Interface Unstable Shear Failure

Most studies about the stability of sidewalls in underground mines ignore the importance of the roof-coal and coal-floor interfaces, or at best tend to take the interfaces as the materials that exhibit elastic-plastic behaviors, which inherently rules out the possibility of unstable shear failures of the interfaces. According to the findings of Chapters Three and Four, it is highly likely that unstable shear failures that occur along the coal-rock interfaces also impact the stability of sidewalls and mining faces and cause unstable compressive failures. A conceptualized underground mining configuration developed for the studies present in this chapter is shown in Figure 5.1a. In Figure 5.1a, the coal seam is located between roof and floor rock layers. The coal seam is mined into the paper direction, which is signified by the circled cross in Figure 5.1a. Due to the different rock properties between the coal and roof/floor rocks, two interfaces are formed at the roof-coal and coal-floor contacts. In Figure 5.1a, shear stresses are mobilized at the interfaces, and the tendency of shear movements is indicated by the white arrows in the left-bottom graph in Figure 5.1a. Certain conditions, such as the excavation advances into the paper or mining in the adjacent areas, can result in the increases in the shear stresses at the interfaces. When the shear stresses exceed the peak shear strengths of the interfaces, shear failures occur. Commonly, the behaviors of the interfaces are assumed a non-softening elastic-plastic behavior as shown in the bottom-right plot in Figure 5.1a. The blue dash line represents the loading system stiffness of the interfaces in shear direction. Based on the stiffness criterion, only stable shear failures occur at the interfaces, which are modeled as a perfectly plastic material. Due to the stable shear failures along the interfaces, the confinements provided by the interfaces gradually reduce and coal materials in the sidewalls extend horizontally into the opening area (Figure 5.1b). This extension process of the sidewalls is in a slow and stable manner, which results in smooth and continuous decreases in the confinement of the inner section of the sidewalls. The stable de-confinement induces tension in the sidewalls and leads to tensile failures that are manifested as spalling in underground mines. Under this condition,

unstable compressive failures of sidewalls are very difficult, if not impossible.

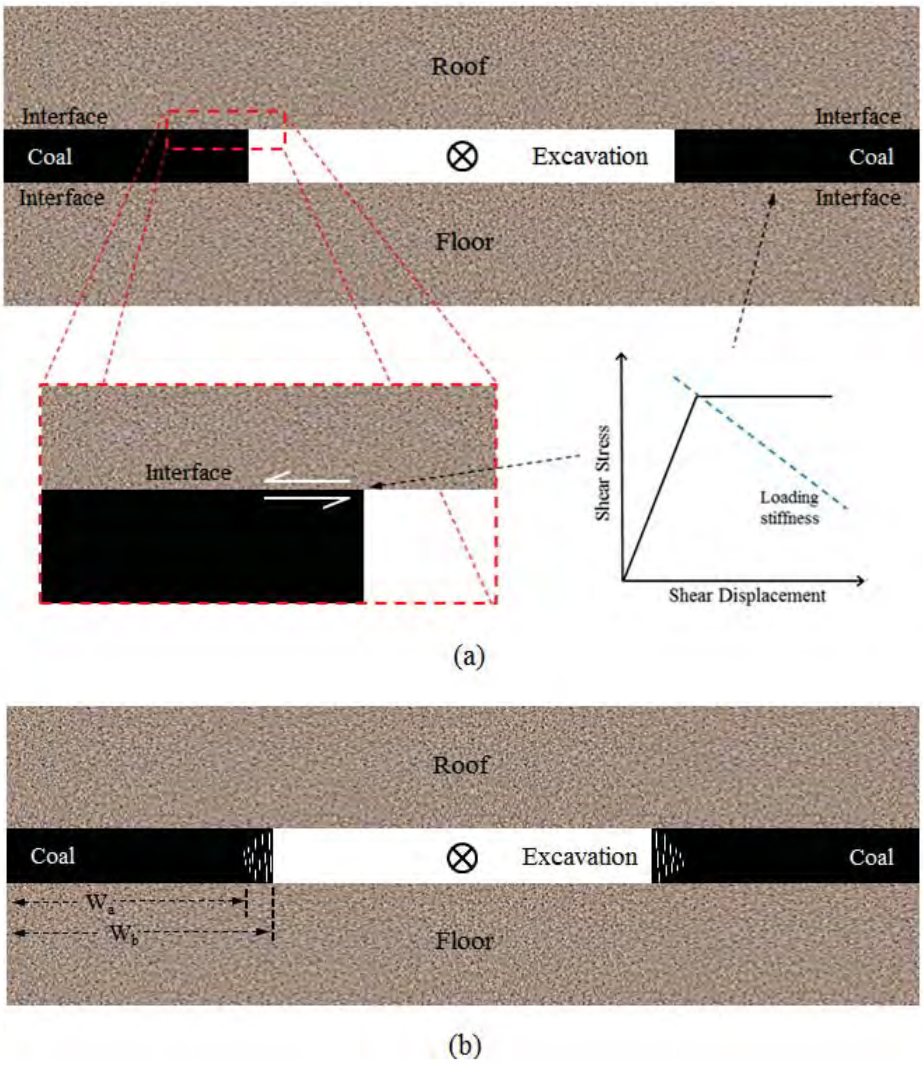

Figure 5.1: Illustrations of sidewall failures caused by stable shear failures along the roof-coal and coal-floor interfaces with mining into the paper: (a) model configuration; and (b) stable shear failures at the interfaces lead to stable compressive failures in the sidewalls.

If the interfaces are considered as exhibiting elastic-softening behavior as shown in the bottom-right plot in Figure 5.2a, stable and unstable shear failures can occur depending on the interface post-peak stiffness and the loading stiffness. Even though the elastic-softening behaviors are actual behaviors of most rock discontinuities, there is no widely accepted way to accurately and efficiently determine the characteristic behaviors of rock joints, bedding planes or faults in underground mining conditions. The lack of means for investigating rock

discontinuity properties limits the advances of many rock mechanics problems. In this study, the mechanisms of unstable compressive sidewall failures are modeled in general ways so that the specific shear behaviors at interfaces are not required.

As discussed in Chapters Three and Four, an unstable shear failure takes place if the post-peak stiffness of rock discontinuity is larger than the loading system stiffness. The area between the post-peak slope of the interfaces and the loading system stiffness line represents the available excess energy that becomes available during shear failures. The confinement provided by the interface to the sidewalls can suddenly reduce when the shear stress exceeds the peak shear strength at the interface under sufficiently soft loading stiffness condition. This rapid reduction of confinement can cause a sudden violent extension of the coal material into the opening area which may manifest as unstable failures of the sidewalls. Such unstable failures can result in flying rock fragments occurring into the openings leading to damage of equipment, delay in production and injury to workers. The horizontal depth of such unstable sidewall failures would be dependent on the interface shear strength and shear stress magnitudes along the interface as well as the excavation height. (Figure 5.2b).

5.1.2 Weak Region at Interface

Considering the significant degree of variability of rock properties, it is plausible to assume that the discontinuity shear strength may vary along coal-rock interfaces. For instance, the shear strength is significantly reduced when discontinuity surfaces have less roughness or are covered by weak infill materials instead of in an intimate contact. The infill materials may consist of completely loose, cohesionless materials resulted from the decomposition and weathering of the rock discontinuities. In this study, the regions at contact interfaces with very low or no shear strength are referred to as *weak regions*. The contact surfaces at interfaces with high shear strength are referred to as *barriers*. In underground mining conditions, the existence of weak regions at the roof-coal and coal-floor interfaces may provide an explanation to unstable compressive failures in mining faces and sidewalls. Figure 5.3a shows a simplified configuration of a mining face. The blue arrow in Figure 5.3 indicates

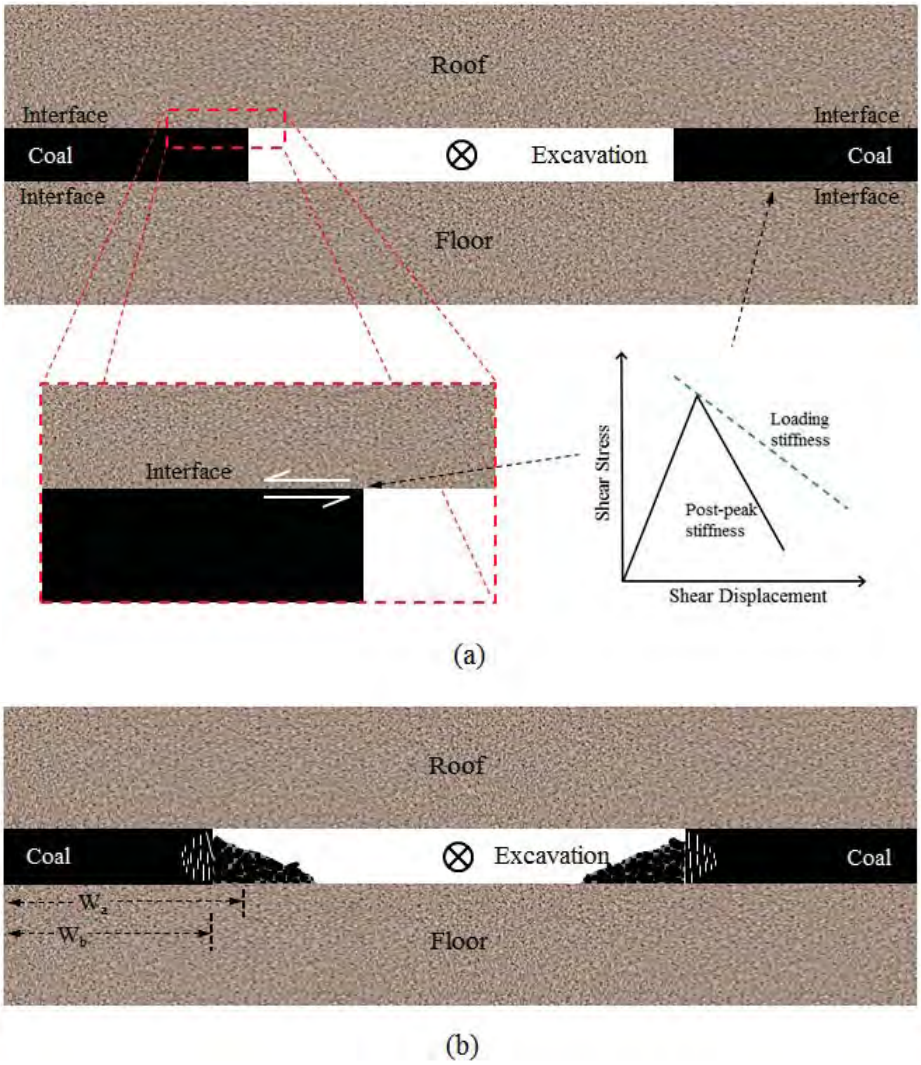

Figure 5.2: Illustrations of sidewall failures caused by unstable shear failures of the roof-coal and coal-floor interfaces with mining into the page: (a) configuration; and (b) unstable shear failures at the interfaces result in unstable compressive failures in the sidewalls.

the direction of the mining. The side of the coal layer under mining can be considered a mining face in longwall mining. There are several assumed existing weak regions located at the interfaces ahead of the mining face (Figure 5.3a). As the mining face advances, the weak regions are exposed as illustrated in Figure 5.3b. Encountering the weak regions in the mining process leads to a sudden de-confinement of the coal materials ahead the mining face, which results in a rapid decrease in the strength of the mining face and unstable compressive failures (Figure 5.3c).

The sides of the coal layer can also be considered as sidewalls with mining advancing into the paper as shown by the circled cross in Figure 5.4. As mining advances, increased shear stresses at the roof-coal and coal-floor interfaces are mobilized and can result in shear failures of the barriers as indicated by the red lines in Figure 5.4b. Interaction between the slipped regions and the pre-existing weak regions lead to rapid de-confinements of the coal material at the sidewall, which results in unstable compressive failures of the sidewall. Presence of large weak regions and small intact regions at the interfaces provide favorable conditions for unstable compressive failures to propagate into the inner section of the coal seam from the sidewall (Figure 5.4c).

5.2 Numerical Study of De-confinement Mechanisms

The de-confinement mechanisms are studied by performing a series of numerical simulations in UDEC.

5.2.1 Modeling Phases

Two mining phases are modeled. In Phase I, the mining of the coal seam advances to left as shown in Figure 5.5 and Figure 5.6. The face loading conditions in this case, for example, would correspond to that of an advancing longwall panel. In Phase II, mining advances into the paper (Figure 5.7), which can be the taken as the loading of sidewall, for example in entries.

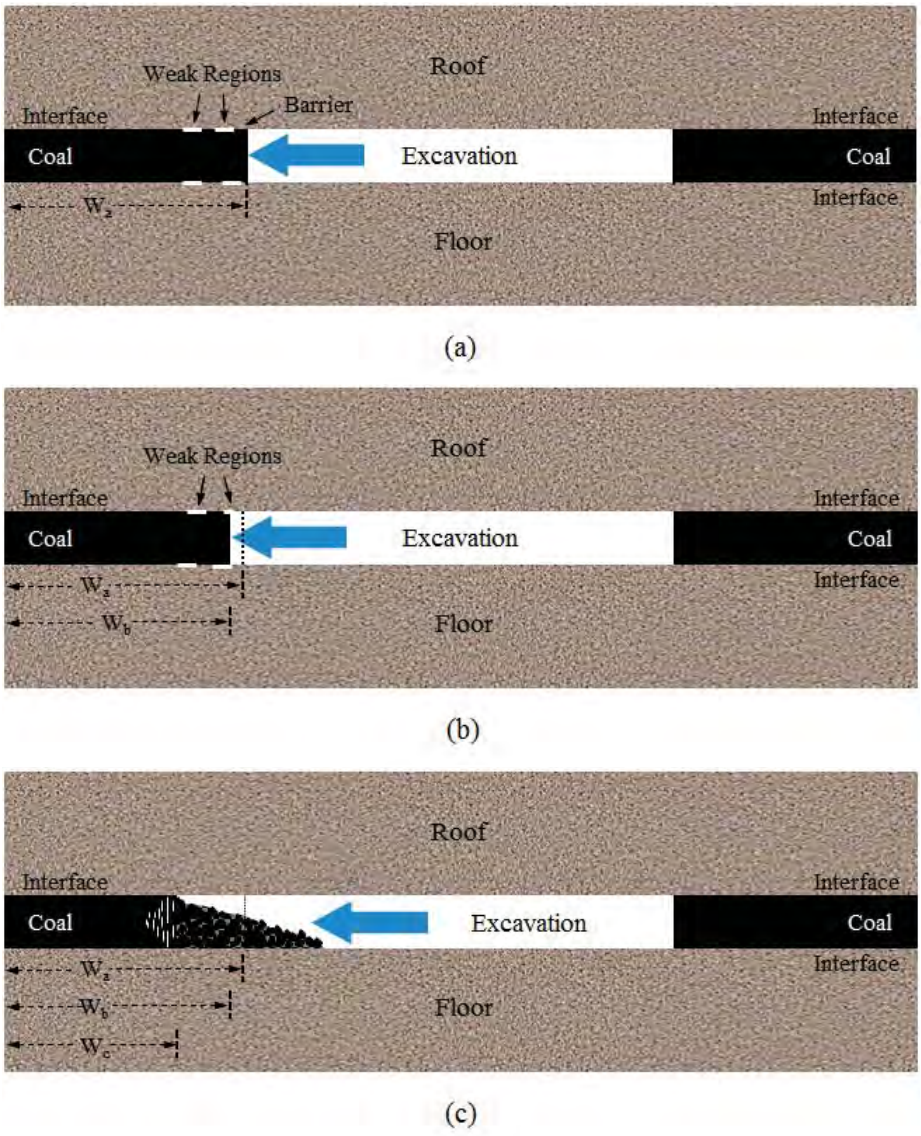

Figure 5.3: Illustrations of failures of a mining face caused by the existence of weak regions along the roof-coal and coal-floor interfaces with mining towards left: (a) original configuration; (b) configuration after one mining cut; and (c) unstable compressive failures of the mining face caused by the presence of weak regions.

Figure 5.4: Illustrations of sidewall failures caused by weak regions along the roof-coal and coal-floor interfaces with mining advancing into the paper: (a) original configuration; (b) unstable shear failures occur at the interfaces; and (c) unstable compressive failures of coal pillar caused by the presence of unstable shear failures and pre-existing weak regions.

The de-confinement mechanisms of unstable compressive failures presented in the previous sections are investigated using the numerical program UDEC. The model configuration is shown in Figure 5.5. The model has a width of 70 m and a height of 160 m. A coal layer is located horizontally in the middle height of the model. The remaining areas are simulated as rock. The top and bottom boundaries of the model are fixed in both horizontal and vertical directions. The left and right boundaries are only fixed in horizontal directions. An in-situ stress field with a vertical stress of 10 MPa and a horizontal stress of 3 MPa is used in the model. The enlarged view of the excavation area is shown in the graph at right in Figure 5.5. The coal layer is divided into hundreds of slender blocks with the numerical discontinuities spaced 0.25 m as represented by the vertical black lines in the graph. The entire model is discretized into a mesh of triangular finite-different zones (red zones) with an average edge length of 0.2 m for the coal layer and an average edge length of 0.4 m for the rocks. An area that is highlighted in blue in the graph will be excavated. The excavation area has a width of 10 m and a height of 2 m and advances in the direction shown by the white arrow.

The plan view of the modeled mining situation in Phase I is schematically shown in Figure 5.6. The model in Figure 5.5 can be considered as the cross-section view of the area indicated by the red line A-A' in Figure 5.6. The blue dash line in the middle of Figure 5.6 is the symmetry line that corresponds to the right boundary in the model in Figure 5.5, and the blue rectangle in Figure 5.6 indicates the excavation area.

The model configuration in Phase II is shown in Figure 5.7. Note the circled cross as the indicator of mining direction into the paper. This phase starts when the Phase I mining reaches the mining extent shown in Figure 5.7. To study the stability of sidewalls as mining advances into the paper, a constant vertical velocity is applied at the top and bottom of the model, as indicated by the vertical arrows in Figure 5.7, to simulate increases in the normal stresses due to the mining. According to Peng and Chiang (1984), normal stresses at the sidewalls can be increased up to 3.5 times of the in-situ normal stress due to mining face advancing. In Phase II, the model is run for 40,000 steps with the constant vertical velocity

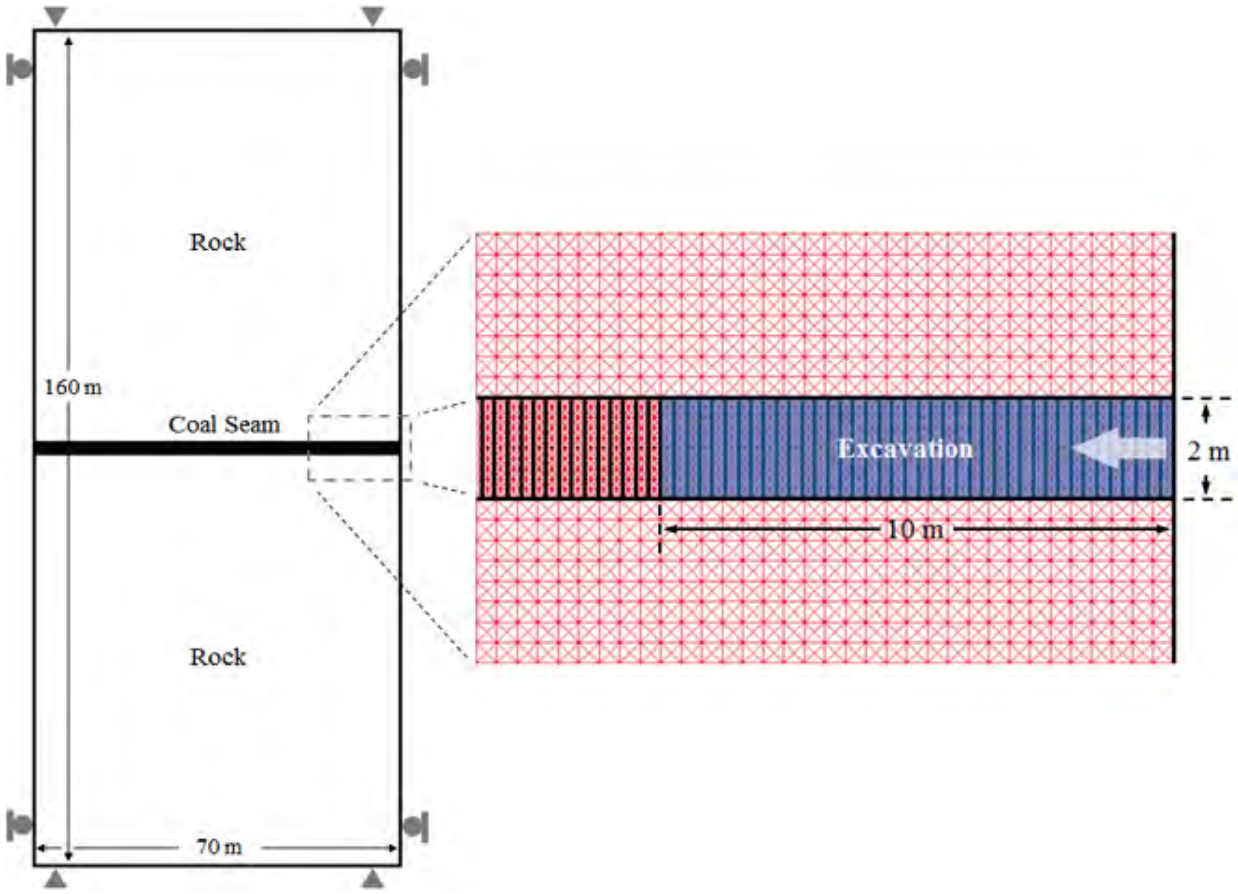

Figure 5.5: Configuration of the model for studies of de-confinement mechanisms in Phase I.

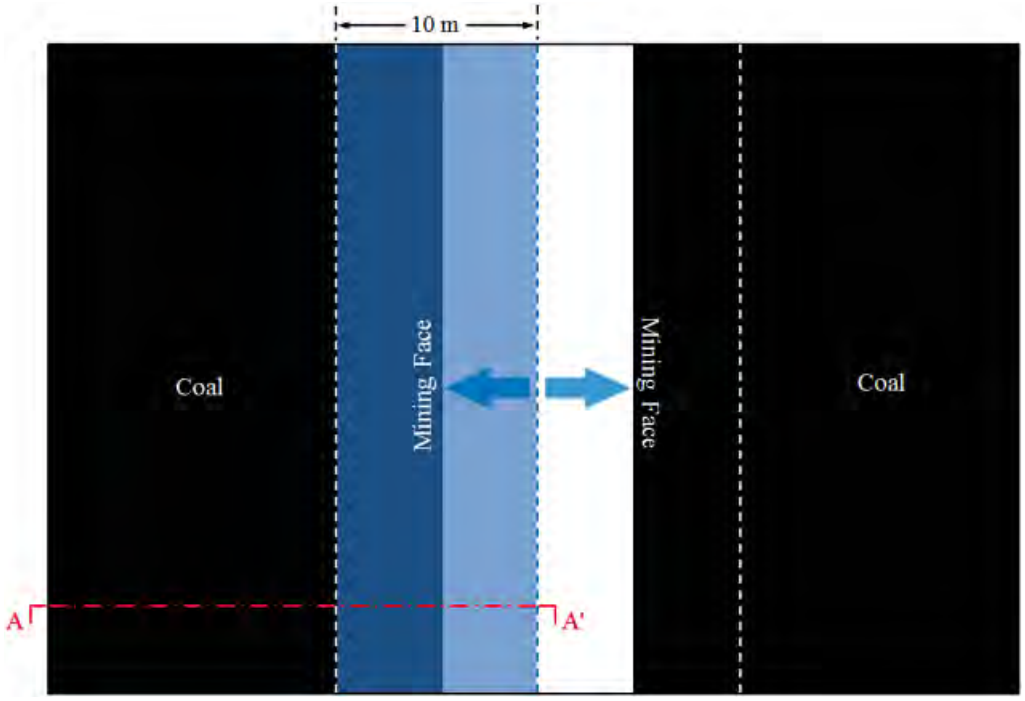

Figure 5.6: Schematic plan view of the mining condition modeled in Phase I for studies of the de-confinement mechanisms of mining faces.

at the top and bottom of the model to result in normal stresses in the sidewalls that are approximately 2 times of the in-situ normal stress.

The plan view of the condition modeled in Phase II is shown in Figure 5.8. The cross-section view of the area indicated by the red line B-B' is represented by the model in Figure 5.7. In Figure 5.8, the blue arrow shows the mining direction, and the blue dashed line represents the symmetry line that corresponds to the right boundary in the model in Figure 5.7. The vacant area at the left of the symmetry line represents the completely excavated area in Figure 5.7.

5.2.2 Organization of Simulations in Different Phases

As mentioned in section 5.2.1, two de-confinement mechanisms need to be simulated in the model. For each mechanism, a number of simulations are conducted with different configurations of the roof-coal and coal-floor interfaces. The organization of the simulations is shown in Figure 5.9.

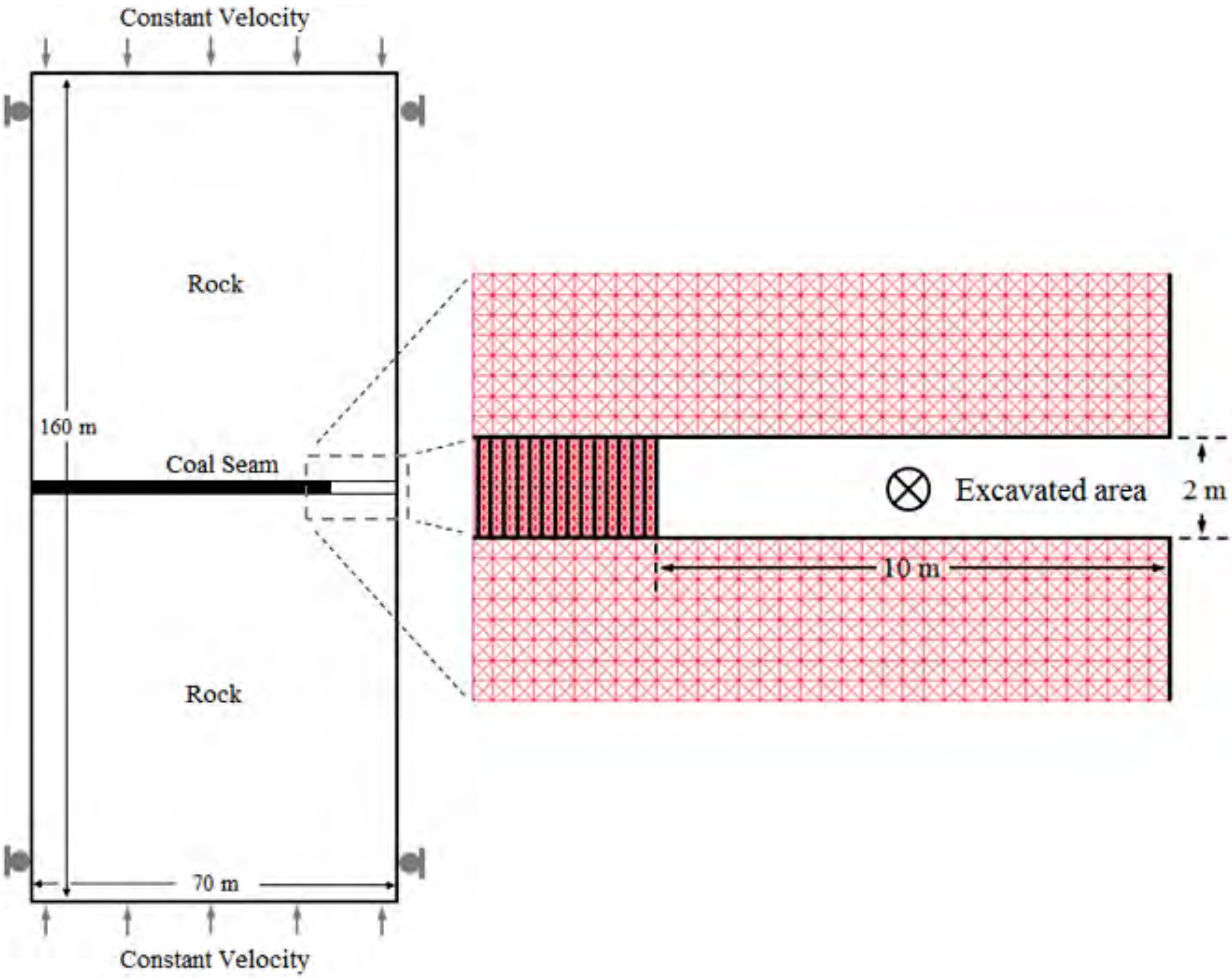

Figure 5.7: Configuration of the model in Phase II for studies of de-confinement mechanisms.

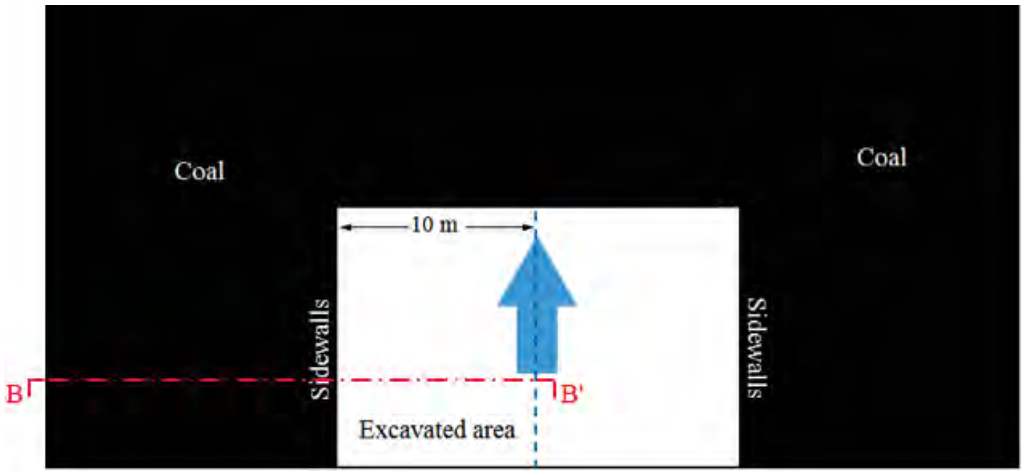

Figure 5.8: Schematic plan view of the mining condition modeled in Phase II.

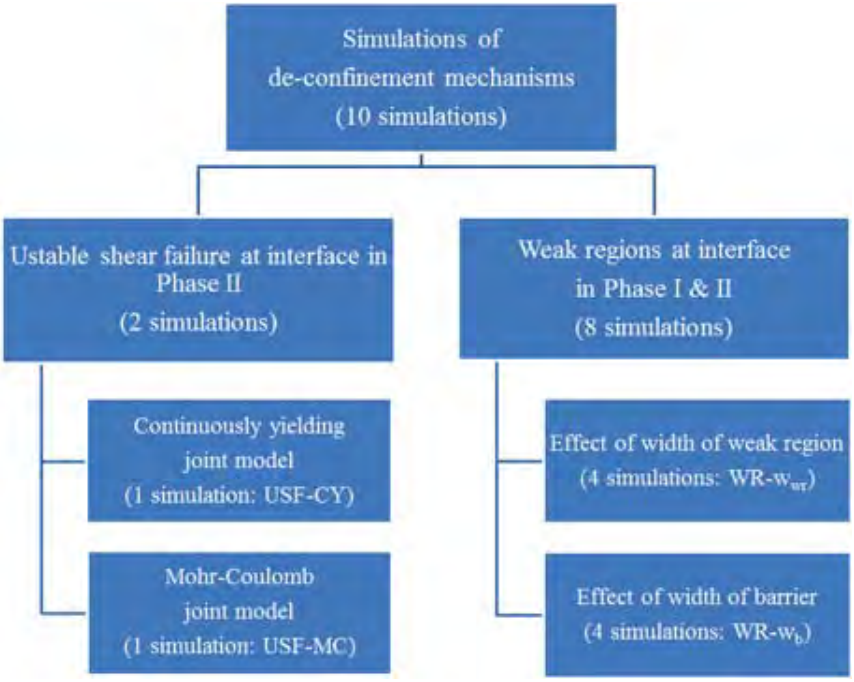

Figure 5.9: Organization of numerical simulations for de-confinement mechanisms.

Unstable compressive failures (UCF) of sidewalls resulted from unstable shear failures (USF) of the interfaces are studied by conducting two simulations in Phase II. In one simulation the CY joint model is assigned to the interfaces, while in another simulation the plastic MC joint model is used at the interfaces. These two simulations are denoted by USF-CY and USF-MC, respectively.

Unstable compressive failures of mining faces and sidewalls involving the existence of weak regions at the interfaces are simulated with varying widths of the weak regions and barriers. Four simulations are performed to study the influence of the width of weak regions w_{wr}, in which the width of the barrier w_b is kept a constant value of 0.5 m while w_{wr} has different values of 0.5, 1.0, 1.5 and 2.0 m. These simulations are denoted by $WR - w_{wr}$. Along with USF-CY (can be considered as w_{wr} of 0.0 m), the results of five simulations with w_b of 0.5 m and w_{wr} varying from 0.0 to 2.0 m in a 0.5 m increment are available for analyzing the effect of w_{wr} on stability of mining faces and sidewalls. Similarly, five simulations are used to investigate the effect of w_b on the stability of mining faces and sidewalls. These

simulations have a constant w_{wr} of 2.0 m with w_b of 0.0, 0.5, 1.0, 1.5 and 2.0 m and are denoted by $WR - w_b$. Among these five $WR - w_b$ simulations, the one with w_{wr} of 2.0 m and w_b of 0.5 m exists in $WR - w_b$ simulations. Therefore, only four simulations (i.e. w_b of 0.0 m, 1.0 m, 1.5 m and 2.0 m) need to be performed in $WR - w_{wr}$.

$WR - w_b$ and $WR - w_{wr}$ simulations in Phase I as shown in Figure 5.10 and Phase II as shown in Figure 5.11, are used to study unstable failures of mining faces (i.e. the mechanism in Figure 5.3) and sidewalls (i.e. the mechanism in Figure 5.4), respectively. In Figure 5.10 and Figure 5.11, the roof-coal and coal-floor interfaces are modeled as the CY joint model. The green lines at the interfaces represent the weak regions.

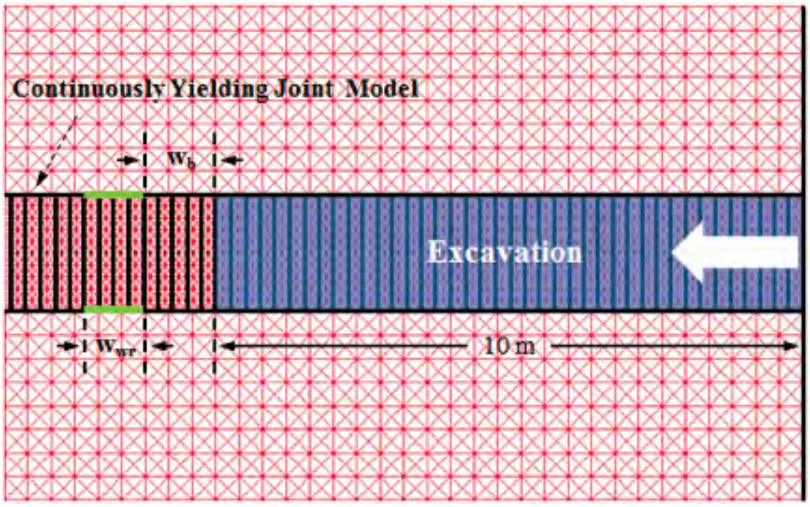

Figure 5.10: Configuration of $WR - w_b$ and $WR - w_{wr}$ simulations in Phase I for analyzing mining face stability.

5.2.3 Constitutive Models

In all simulations the elastic constitutive model is assigned to the rock layers above and below the coal layer, and the MCSS model is used for the coal layer (see Figure 5.12). The MC joint model is used at the interfaces for USF-MC simulation, while the CY joint model is assigned to the interfaces for USF-CY, $WR - w_b$ and $WR - w_{wr}$ simulations.

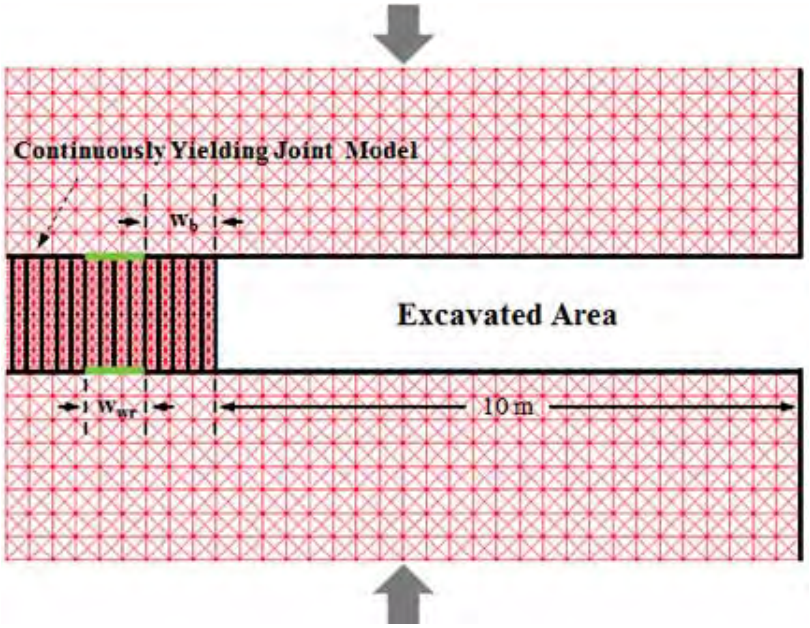

Figure 5.11: Configuration of WR − w_b and WR − w_{wr} simulations in Phase II for analyzing sidewall stability.

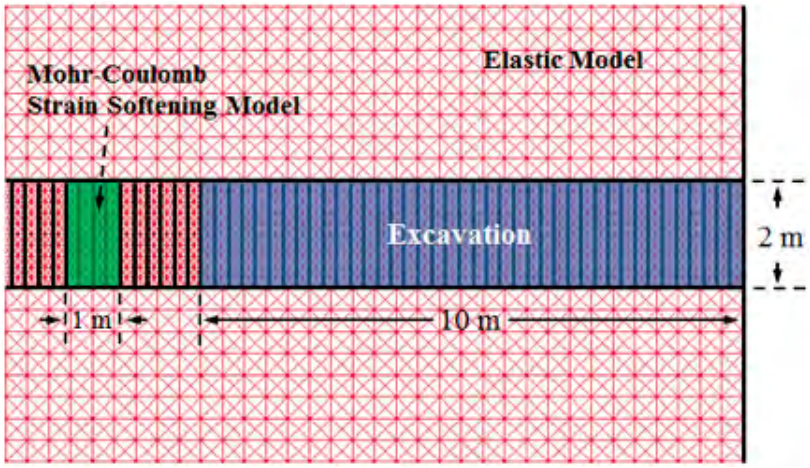

Figure 5.12: Constitutive models in simulations and the geometry of the model for validation of UDEC.

5.2.4 Validation of UDEC for Modeling Unstable Compressive Failure

To investigate the proposed de-confinement mechanisms of unstable compressive failures at the mining faces and sidewalls, the ability of the numerical program UDEC to simulate stable and unstable failures of rocks in compression needs to be validated. The signatures that identify unstable compressive failures also need to be established.

An effective means to analyze stable and unstable compressive failures of rocks is implementing laboratory uniaxial compressive strength (UCS) test. According to the stiffness criterion, an unstable failure occurs when the post-peak stiffness of the rock is larger than the loading system stiffness. In the process of an unstable failure, strain energy stored in the loading system suddenly releases and contributes to the unstable failure. The rock specimen modeled in this section has an elastic-softening behavior. The rock specimen that calibrated to exhibit a given vertical stress–strain behavior is placed between two platens that represent the testing machine. The configuration that includes the specimen and the platens is used for two tests to simulate stable and unstable compressive failures. The shape, size, and properties of the specimen are kept the same for all tests. However, the loading system stiffness is varied by changing the elastic modulus of the loading platens.

5.2.4.1 Modeled UCS Test

The rock specimen has a characteristic vertical stress–strain behavior with a post-peak softening region, as schematically shown in Figure 5.13a. The rock specimen will be calibrated to have the material properties that are close to given target values through a series of calibration tests. The target properties of the specimen are listed in Table 5.4. The UDEC codes for UCS tests are shown in Section D.8 in Appendix D.

As shown in Figure 5.13b, the specimen is rectangular in shape with a width of 1 m and a height of 2 m placed between a pair of loading platens with a width of 1 m and a height of 1 m. The specimen is loaded by applying a constant axial displacement at the ends of the loading platens as indicated by the vertical arrows in Figure 5.13b. Figure 5.14 shows

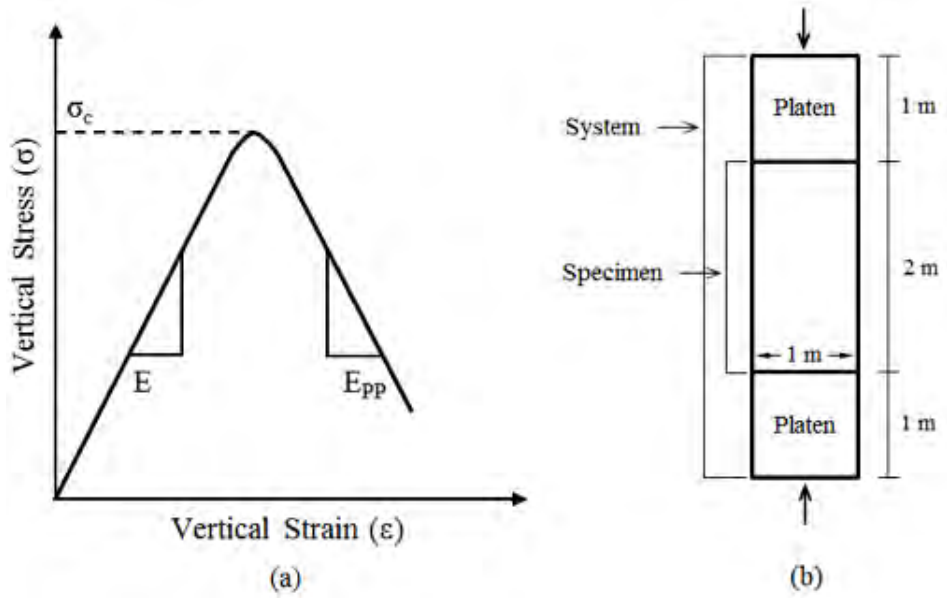

Figure 5.13: Illustrations of the behavior of the simulated specimen and model configuration.

Table 5.4: Target material properties of the rock specimen and properties of the calibrated specimen.

	Elastic Modulus (E)	Poisson's Ratio (ν)	Uniaxial Compressive Strength (σ_c)	Post-Peak Modulus (E_{pp})
Specimen Target Value	4.0 GPa	0.2	7.6 MPa	-4.0 GPa
Calibrated Specimen	4.0 GPa	0.2	7.6 MPa	-4.0 GPa

the configuration of the actual model in UDEC. The vertical discontinuities in the specimen are fictitious discontinuities. The spacing for the vertical fictitious discontinuities is 0.25 m. Two horizontal discontinuities are interfaces between the loading platens and the specimen. The blocks in the model are further discretized into triangular finite-difference zones with an average edge length of 0.2 m for the rock specimen and an average edge length of 0.4 m for the platens. The geometry and configuration (i.e. spacing of the fictitious discontinuities and size of zones) of the specimen is the same as the highlighted area in green in Figure 5.12, which ensures the direct relation between the study in this section and the model for the de-confinement mechanism analyses.

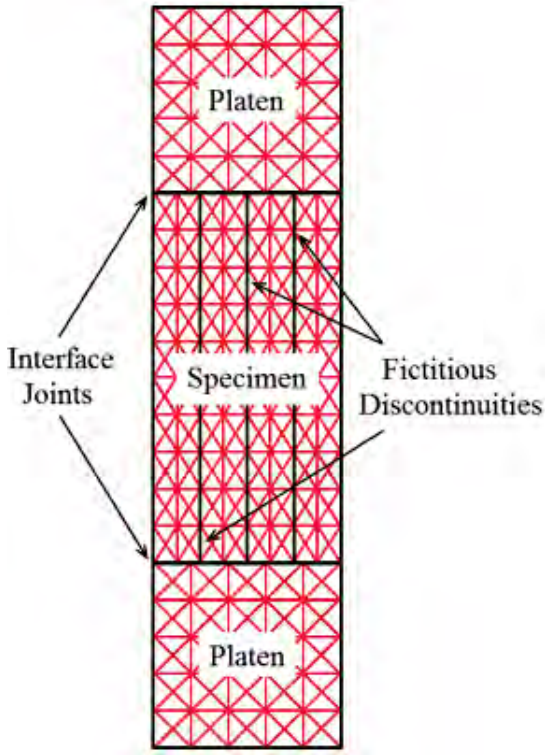

Figure 5.14: Model configuration of UCS test in UDEC.

The results of the UCS tests are presented in the form of vertical stress–strain plots similar to that shown in Figure 5.15 and Figure 5.16. The vertical stresses in the specimen are measured at ten record points that are evenly distributed at the middle height of the specimen. The vertical stresses are plotted versus two distinct measurements of vertical

strain: one by considering only the vertical strain of the specimen (strain measured at the top and bottom of the specimen) and the other by considering the vertical strain of the entire system (strain measured at the top and bottom of the entire system). These two types of strain measurements are referred to as *specimen strain* and *system strain* respectively, as shown in Figure Figure 5.13b. Figure 5.15 shows expected curves of the stable and unstable failure of the specimen in terms of the specimen strain measurement. During stable failure the vertical stress–strain curve follows the material characteristic curve as indicated by the solid line in Figure 5.15. The dashed line (Figure 5.15) shows unstable failure, where the totally destroyed specimen does not have a post-peak curve and the strain measured is that of the platens during their elastic rebound.

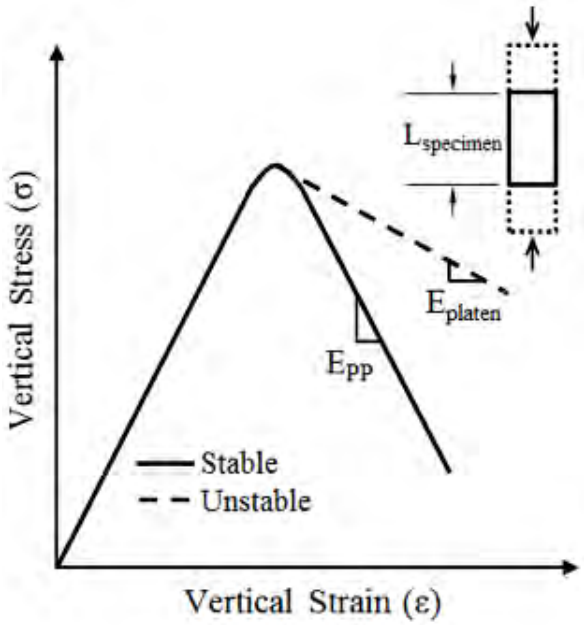

Figure 5.15: Vertical stress–strain behavior if measured at the specimen ends (specimen strain measurement).

Figure 5.16 illustrates the expected plots of the stable and unstable failure using the system strain measurement. The solid line represents stable failure in terms of the system strain where the steady failure of the material in a stiff loading system condition results in a post-peak slope given by the composite stiffness of the specimen and the platens. The dashed

line represents unstable failure of the specimen under soft loading system conditions (i.e. soft elastic platens). The system strain measurement records unstable failure as a rapid loss of load. The difference in the pre-peak slope of two vertical stress–strain plots is due to the difference in the platen elastic moduli (i.e. 50 GPa and 1 GPa) of different loading systems. The space between the peaks of the stable and unstable curves denotes the additional strain in the soft platens that rebounds elastically at failure.

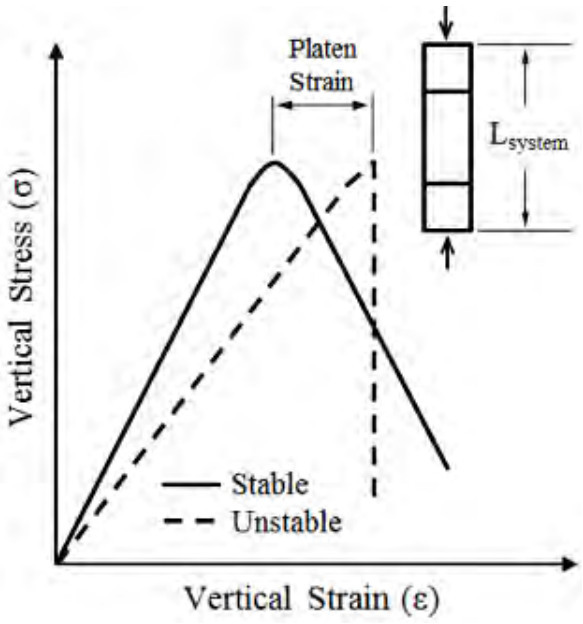

Figure 5.16: Vertical stress–strain behavior if measured at the platen ends (system strain measurement).

5.2.4.2 Model Calibration

In the UCS tests elastic constitutive model is assigned to the loading platens, and MCSS model is applied to the specimen. The MC joint model is utilized in the vertical fictitious joints and the CY joint model is implemented at the interfaces at the platen-specimen contacts. Different loading system stiffness is achieved by adjusting the elastic modulus of the loading platens. The specimen is calibrated to have the target properties by adjusting the input parameters of the MCSS model.

To calibrate the specimen, a large elastic modulus of 400 GPa and a Poisson's ratio of 0.2 are assigned to the platens to simulate a very stiff loading system that analogous to a very stiff loading machine in laboratory UCS tests. The vertical stress–strain (specimen strain) plot, shown in Figure 5.17, of the calibrated specimen is obtained through a series of calibration simulations with the UCS test configuration. Elastic modulus and Poisson's ratio are both calculated using the values at the origin and the point on the pre-peak portion of the curve at 50% of the peak stress. The residual strength of the specimen is due to the residual strength assigned in the MCSS model. This strength approximately considers the residual strength resulted from block interlocking after failure.

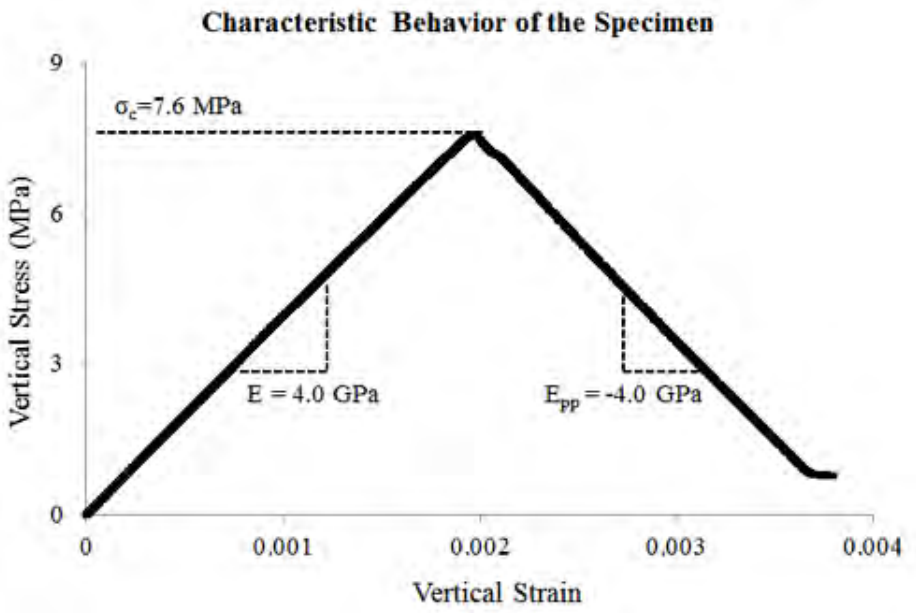

Figure 5.17: Characteristic vertical stress–strain curve of the calibrated specimen measured in terms of the specimen strain.

The material properties of the calibrated specimen are shown in Table 5.4. The target values are also included in Table 5.4 for comparison. It is shown in the table that the model is well calibrated and has the same values as the target properties. The input parameters of the MC joint model, the CY joint model and the MCSS model for the calibrated specimen are listed in Table 5.5, Table 5.6 and Table 5.7, respectively.

Table 5.5: Input parameters of the MC joint model for the fictitious joints in the calibrated specimen.

Parameter Symbols	Description	Value
jk_n	Joint normal stiffness	50 GPa/m
jk_s	Joint shear stiffness	50 GPa/m
jcoh	Joint cohesion	1.0×10^{20} Pa
jfric	Joint friction angle	90°
jdil	Joint dilation	90°
jten	Joint tensile strength	1.0×10^{20} Pa

Table 5.6: Input parameters of the CY model for the interfaces in the calibrated model.

Parameter Symbols	Description	Value
jk_n	Joint normal stiffness	50 GPa/m
jk_s	Joint shear stiffness	50 GPa/m
je_n	Joint normal stiffness exponent	0
je_s	Joint shear stiffness exponent	0
jfric	Joint intrinsic friction angle	20°
jif	Joint initial friction angle	50°
jr	Joint roughness parameter	0.1 mm

Table 5.7: Input parameters of MCSS model for the calibrated rock specimen.

Cohesion (plastic strain, cohesion/MPa)	0.00000, 2.2
	0.00005, 2.2
	0.03600, 0.2
Friction Angle (plastic strain, friction angle/deg.)	0.00000, 23.0
	0.00002, 30.0
	0.00780, 30.0
Dilation Angle (plastic strain, dilation/deg.)	0.0000, 15.0
	0.0005, 15.0
	0.0010, 5.0
	0.0015, 5.0

Within the MCSS model, the parameters of cohesion, friction angle and dilation angle for the specimen are adjusted as the specimen plastic strain achieves pre-defined values. For example, in Table 5.7, the third row in the dilation angle section means that when the specimen plastic strain within a zone reaches 0.0010, the dilation angle will be changed to 5.0° in the zone.

5.2.4.3 Test Procedure

For the tests of specimen failure mode, the calibrated specimen is loaded in two tests by the platens with different elastic modulus values of 50 GPa and 1 GPa. As shown in Figure 5.18, the platens with elastic modulus of 50 GPa represent the stiff loading system (the blue dash line), and the platens with elastic modulus of 1 GPa represent the soft loading system (the red dash line). Note that in these two tests, the only change in the model is the elastic modulus of the platens (i.e. loading system stiffness).

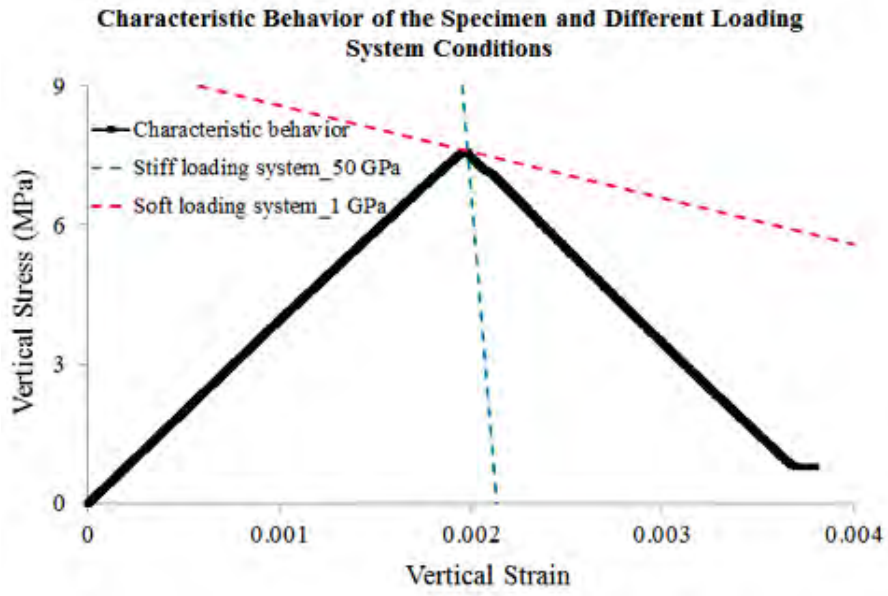

Figure 5.18: Characteristic behavior of the calibrated specimen and loading system stiffnesses of different UCS tests.

5.2.4.4 Test Results using Specimen Strain Measurement

The vertical stress–strain plots measured in terms of the specimen strain in different loading stiffness conditions are shown in Figure 5.19. The plots are shown in the form of lines with markers. Each marker represents a record in the model. The lines show the connection between adjacent records. Figure 5.19 shows the pre-peak behaviors of the specimen under different loading system conditions are the same. Only the pre-peak curve under the soft loading condition (the red line) is visible in Figure 5.19 as the other curves (the black and blue lines) are covered by the red line. The post-peak behaviors of the specimen are completely different. Under the stiff loading system (50 GPa) the specimen's post-peak behavior is identical to the post-peak behavior of the material characteristic curve and has a dense distribution of records. This indicates that the failure of the specimen takes place in a stable manner. In the soft loading system condition the post-peak modulus of the specimen approximates that of the platen modulus of 1 GPa and exhibits a sparse distribution of the records in the failure regime. This implies the occurrence of rapid platen rebound during an unstable failure of the specimen.

The post-peak moduli of the specimens' vertical stress–strain curves with the specimen strain measurement are shown in Table 5.8. The values in Table 5.8 are in accord with the previously described stable/unstable failure conditions. The values shown in Table 5.8 have been colored in accordance to how it failed. The values in red are expected and measured specimen post-peak moduli for the unstable failure, and the values in blue are expected and measured specimen post-peak moduli for the stable failure. For the unstable failure, the measured specimen post-peak modulus matches the platen elastic modulus. For the stable failure the measured specimen post-peak modulus matches the characteristic material post-peak modulus.

Similar to the analyses presented in Section 3.2.4 in Chapter Three, vertical stress–time and vertical displacement–time plots can also be used to distinguish the failure mode of the specimen. As such, the vertical stress–time plots of the specimen under the stiff and soft

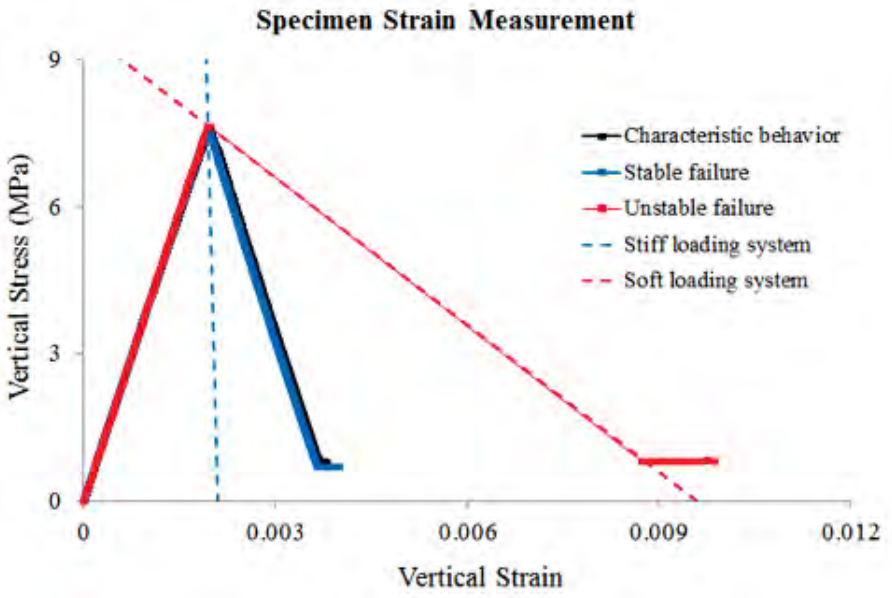

Figure 5.19: Specimen vertical stress–strain plots measured as the specimen strain in different loading systems.

Table 5.8: Comparison of post-peak moduli among tests.

	Platen E (GPa)	Measured Specimen E_{pp} (GPa)	Material Characteristic E_{pp} (GPa)
Soft	1.0	-1.0	-4.0
Stiff	50.0	-4.0	-4.0

loading system conditions are shown in Figure 5.20. The time record in Figure 5.20 is the numerical time utilized in the model. The pre-peak slopes of the curves are not comparable because the time record in the model is affected by the timestep that is a function of the stiffness of the finite-difference zones in the model.

The dense data records in their pre-peak regimes indicate a gradual build-up of the vertical stresses in the specimen. The dense data records and declined slope in the post-peak regime of the specimen under the stiff loading system condition (the blue curve) implies a smooth and continuous decrease in the vertical stress over a relatively long period of time. This behavior suggests that the specimen experiences a stable failure. The existence of no data records and the almost vertical slope in the specimen post-peak regime in the soft loading system condition (the red line) indicates that a rapid and discontinuous decrease in the vertical stress over a relatively short time period, which evidences an unstable failure takes place. Once the specimen finds an equilibrium state again after the unstable failure, dense data records are observed.

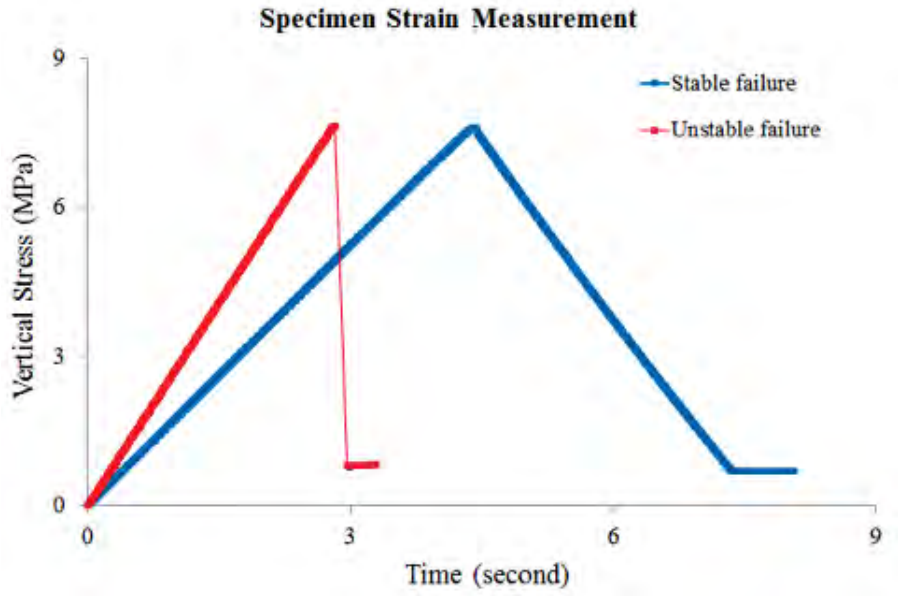

Figure 5.20: Specimen vertical stress–time plots in different loading system conditions.

The vertical strain–time plots of the specimen under the stiff and soft loading system conditions are shown in Figure 5.21. A gradual increase in the vertical strain of the specimen with densely distributed data records in the stiff loading condition implies that the failure of the specimen is in a stable manner. A rapid and discontinuous increase in the vertical strain along with less data records in the specimen failure regime indicate the failure of the specimen is in an unstable manner under the soft loading system condition.

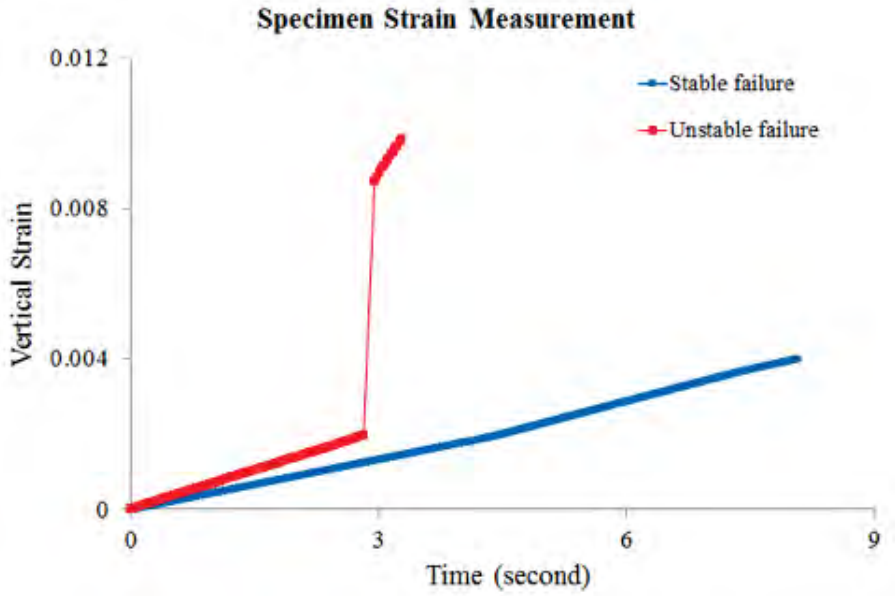

Figure 5.21: Specimen vertical strain–time plots under different loading system conditions.

5.2.4.5 Test Results using System Strain Measurement

The vertical stress–strain plots measured in terms of the system strain under different loading stiffness conditions are shown in Figure 5.22. The behavior of the specimen under the stiff loading system condition (the blue curve) approximates the specimen characteristic behavior (the black curve), which implies that the specimen experiences a stable failure. The rapid and discontinuous decrease in the vertical stress for the specimen under the soft loading system condition (the red curve) indicates the failure is in an unstable manner.

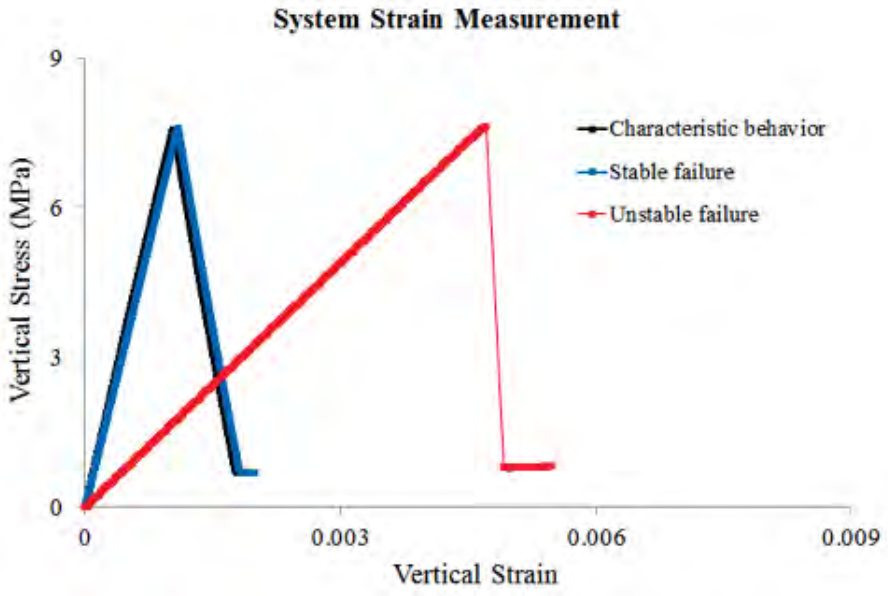

Figure 5.22: System vertical stress–strain plots under different loading conditions.

5.2.4.6 Other Signatures of Unstable Failure

As shown in previous sections, the post-peak behavior of the specimen can be used as a signature to determine the failure stability (stable failure or unstable failure) of the specimen. As discussed in Chapter Three, there are other parameters in these tests can be considered as signatures as well, such as the maximum unbalanced force and mass damping work. The concepts of the maximum unbalanced force and damped energy in the program are introduced in Sections 3.2.5.2 and 3.2.5.3 in Chapter Three. The records of the maximum unbalanced force for the test with the stiff loading system are shown in Figure 5.23. The maximum unbalanced force varies in a range of very small values (0.0 to 0.4 KN). The maximum unbalanced forces at the initiation of the failure and in the post-failure regime are larger than that in the pre-failure regime.

The maximum unbalanced force records of the test under the soft loading system condition are presented in Figure 5.24. The peak value observed at the initiation of the unstable failure in the records exceeds 80 KN. Based on the records it can be seen that the larger values of the maximum unbalanced force appear in a very short period of time, which indicates

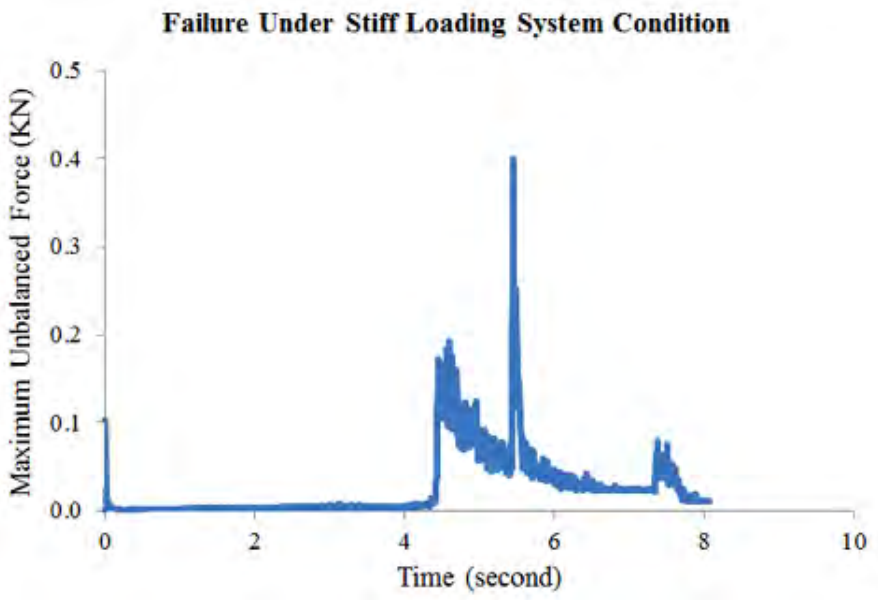

Figure 5.23: Maximum unbalanced force in the test for stable failure.

that the unstable failure occurs very quickly. Large unbalanced forces in the unstable failure imply that the failure is in unstable manner. Once the specimen finds an equilibrium state after the unstable failure, the maximum unbalanced force reduces to very small values.

The damped energy records in the tests under the stiff and soft loading system conditions are shown in Figure 5.25 and Figure 5.26 respectively. Under the stiff loading system, the damped energy starts to gradually increase when the failure occurs in the specimen. The maximum value of the damped energy in the stiff loading system case is about 16 Joules. In the soft loading system condition, however, the damped energy increases rapidly to a large amount at the moment of failure. The maximum value achieves almost 18,000 Joules. Comparing the damped energy records in two tests, the failure stability of the specimen can be easily identified. The specimen failure in the soft loading system results in damped energy that is three orders in magnitude larger than that in the test under the stiff loading system condition. The large amounts of damped energy along with a very short failure time signify the existence of unstable failure in the specimen loading under the soft loading system.

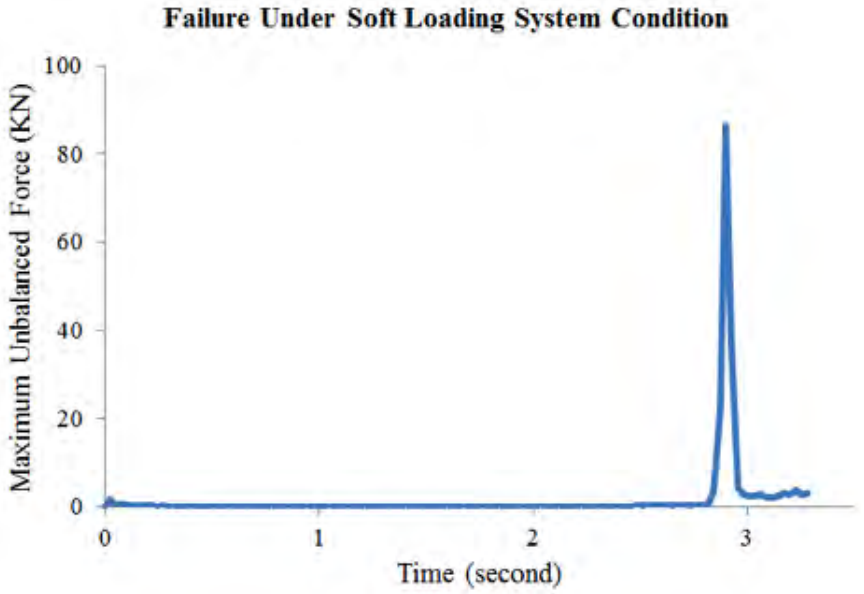

Figure 5.24: Maximum unbalanced force in the test for unstable failure.

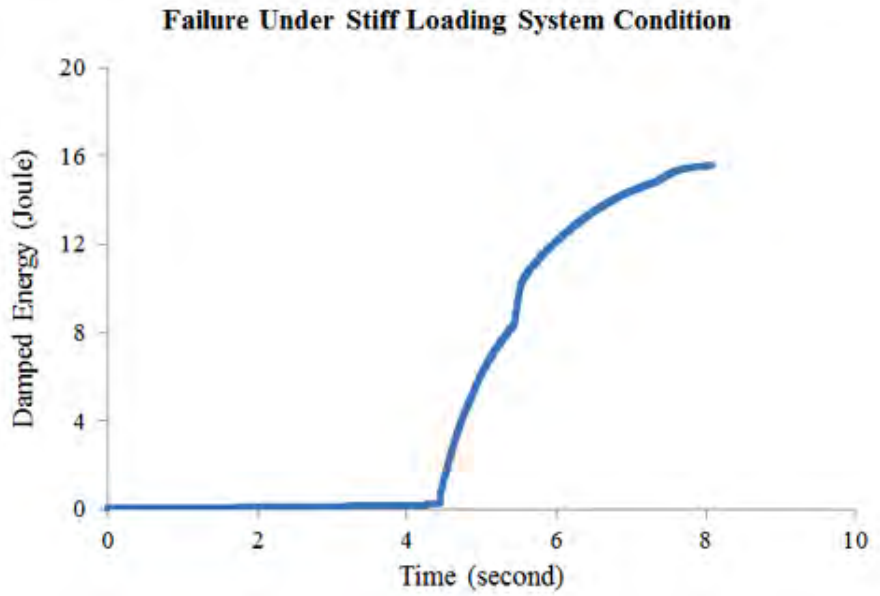

Figure 5.25: Accumulated damped energy in the test for stable failure.

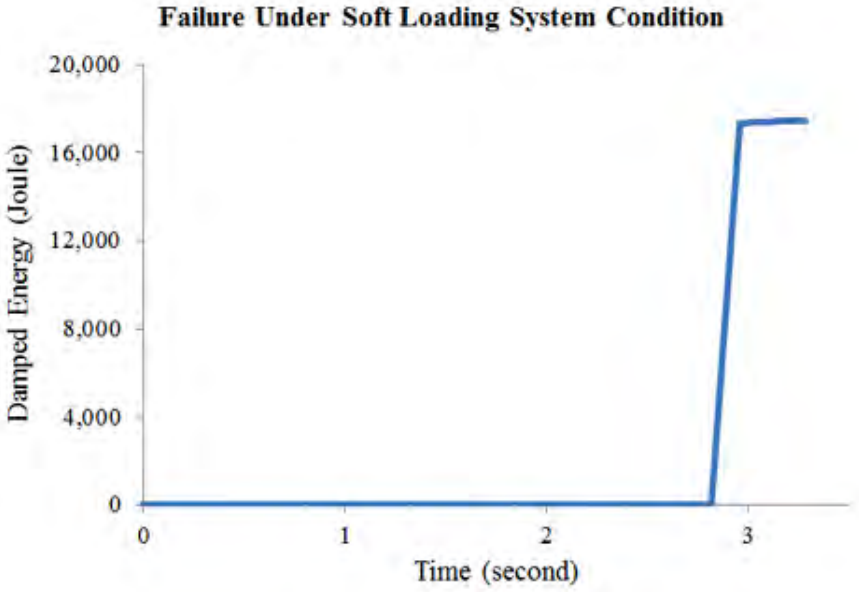

Figure 5.26: Accumulated damped energy in the test for unstable failure.

5.2.5 De-confinement Simulation Studies

Based on the results presented in the previous section, the program UDEC has been shown to be able to simulate stable and unstable compressive failures of rock materials. Based on this validation of UDEC, the numerical studies of the de-confinement mechanisms of unstable compressive failures at mining faces and sidewalls are performed.

5.2.5.1 Measurements in Model

In the models many measurements are utilized to record the mechanical behaviors of the interfaces and coal materials in the simulation processes. These measurements are categorized into two types: one is the measurements at the interfaces that are referred to as *measurement points*, and the other one is the measurements within the coal layer that are referred to as *measurement regions*. As indicated by the black dots in Figure 5.27, ten measurement points P1 to P10 at the roof-coal interface are chosen to record shear stress, shear displacement, and normal stress in the simulations in both Phase I and II.

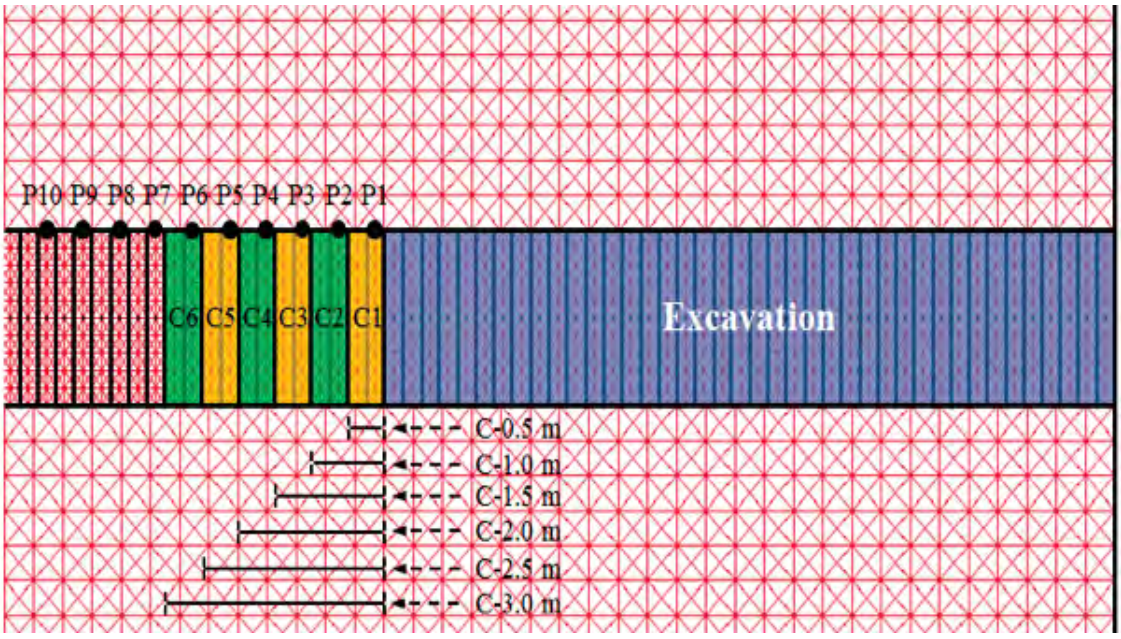

Figure 5.27: Measurement points and regions for de-confinement mechanism analyses in USF-CY, USF-MC and WR $-$ w_{wr} simulations.

Six measurement regions indicated by the yellow and green rectangles in Figure 5.27 are adopted in USF-CY, USF-MC and WR $-$ w_{wr} simulations in both Phase I and II. They have the same width of 0.5 m and height of 2 m and represented by C1 to C6.

Five measurement regions with different widths are also utilized in the simulations. As shown in Figure 5.27, these measurement regions are with widths of 1.0, 1.5, 2.0, 2.5 and 3.0 m and are represented by C-1.0 m, C-1.5 m, C-2.0 m, C-2.5 m and C-3.0 m, respectively. When analyzing regions with different widths, C1 is the same as C-0.5 m. Normal stresses are recorded in these 11 measurement regions (six measurement regions with the same width and five measurement regions with increased width) by taking the averaged vertical stress along the middle height of the regions.

In WR $-$ w_b simulations, more measurement regions are required because the weak region reaches 4.0 m into the coal layer from the excavated area in the simulation with w_{wr} of 2.0 m and w_{wb} of 2.0 m. Therefore 17 measurement regions are used in WR $-$ w_b the simulations as shown in Figure 5.28.

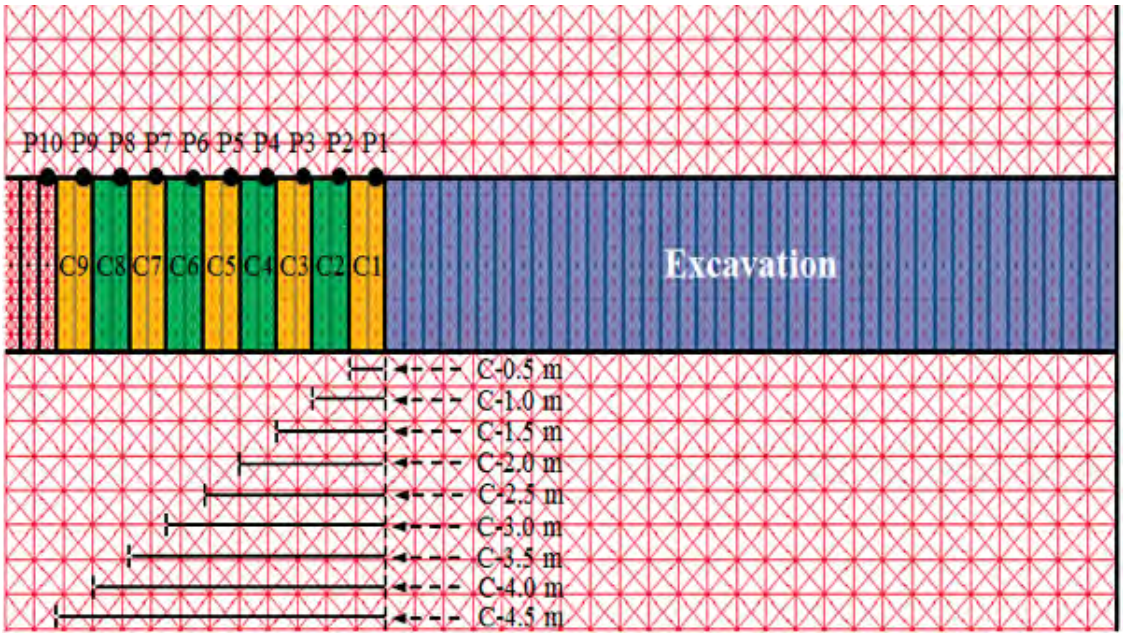

Figure 5.28: Measurement points and regions for de-confinement mechanism analyses in WR – w_b simulations.

5.2.5.2 Unstable Failure of Sidewall due to Unstable Shear Failure at Interface – CY Model

The results of USF-CY simulation, as highlighted in orange in Figure 5.29, are presented in this section. The records of shear stress, shear displacement, normal stress of all measurement points, and normal stress in the measurement regions are plotted against numerical time. The UDEC codes for USF-CY simulation are shown in Section D.9 in Appendix D.

The normal stress–time plots of all measurement points for USF-CY simulation are shown in Figure 5.30. In the simulation, the CY joint model with properties shown in Table 5.6 was assigned to the roof-coal and coal-floor interfaces. To conduct the simulation in Phase II, the model in Phase I needs to be performed first (i.e. the excavation area needs to be completed). Therefore, the measurement records in Phase I are also plotted in Figure 5.30 although they are not used to analyze sidewall unstable failures caused by unstable shear failures at the interfaces. The dashed line in Figure 5.30 represents the instant that the model changes from Phase I to Phase II. The records in Phase I are also shaded in blue.

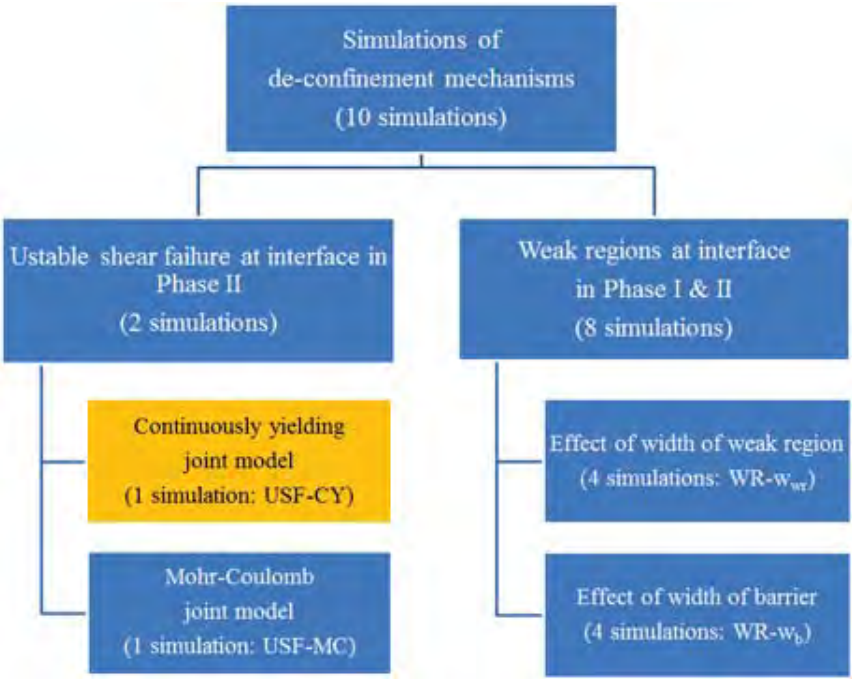

Figure 5.29: Representative component of USF-CY simulation in the organization chart.

Generally, normal stresses at the measurement points increase as the mining face moves into the paper. Points 1 to 3 did not experience increases in normal stress because the coal material under these measurement points had failed in Phase I and could not support any additional stresses. The rapid decreases in normal stress at the measurement points at 2.1 seconds are signatures of unstable compressive failures at the sidewall, which will be discussed in the normal stress–time plots of the measurement regions in Figure 5.33 and Figure 5.34. The normal stresses at points 7 to 10 keep building up since the coal materials beneath these points are still in their elastic regimes.

The shear stress records in Phase II are very important for analyzing shear failures at the roof-coal interface. In Figure 5.31, generally the shear stresses at the interface increase in step with each excavation step. Measurement points 1 to 3 experience rapid decreases in their shear stresses, which imply unstable shear failures at these points. The shear stresses at measurement points 4 to 7 increase as shear failures occur at points 1 to 3. This is because points 1 to 3 experience failures and unable to carry the shear loads they used to carry, and

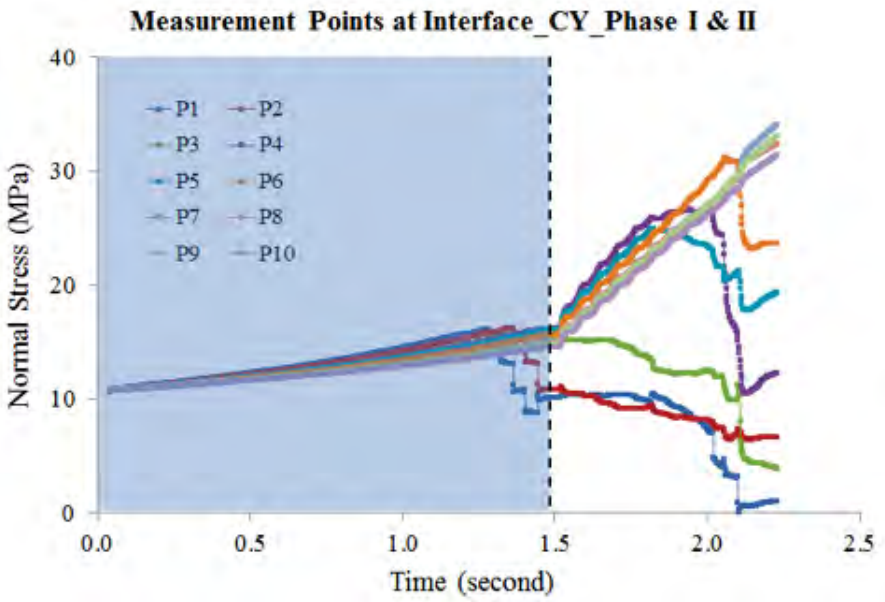

Figure 5.30: Normal stress–time curves of the measurement points in USF-CY simulation.

the shear stresses are transferred into the non-failed regions of the interface, which are points 4 to 7.

The shear displacements at the interface are plotted against numerical time in Figure 5.32. The shear displacements are very small until unstable shear failures occur at points 1 to 3, which are signified as rapid increases in the shear displacements at about 2.0 and 2.1 seconds. This also confirms the occurrence of unstable shear failure at these points that were observed in Figure 5.32.

To analyze the stability of the sidewall, normal stresses in the coal layer are presented. The normal stress–time plots obtained in the measurement regions with a constant width of 0.5 m and with increased width are shown in Figure 5.33 and Figure 5.34, respectively. Figure 5.33 indicates the coal materials in regions C1 and C2 had failed under the loading in Phase I and therefore could not sustain any additional stress in Phase II. The coal in regions C3 to C6, however, do not fail in Phase I and start to carry more load as Phase II initiated. Based on the study presented in Section 5.2.4, rapid decreases in normal stress and sparse data points at about 2.1 seconds for C2 to C5 indicate unstable compressive failures at the

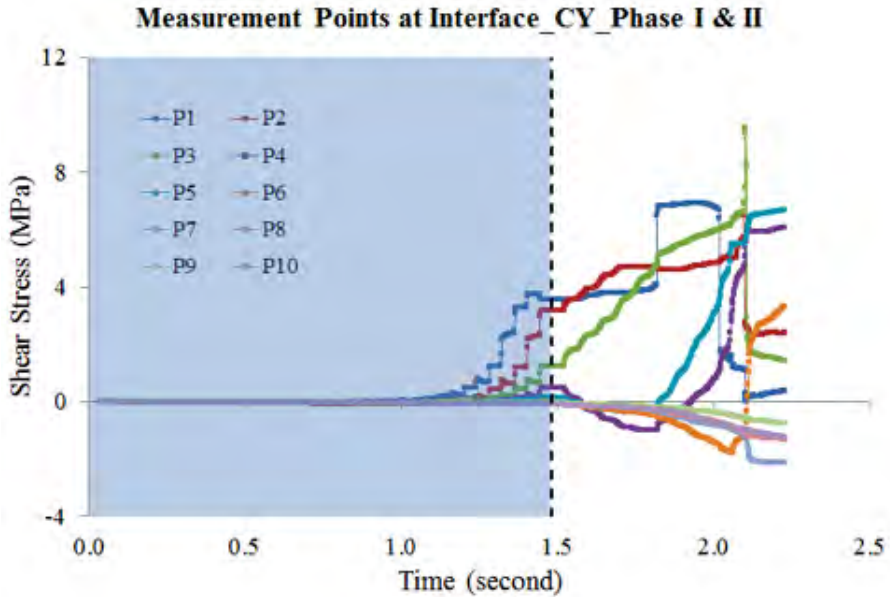

Figure 5.31: Shear stress–time curves of the measurement points in USF-CY simulation.

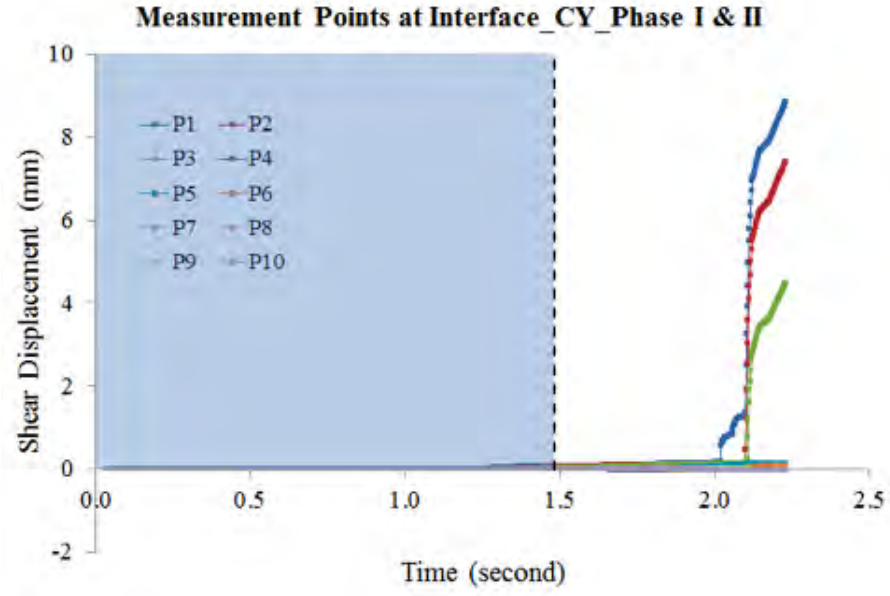

Figure 5.32: Shear displacement–time curves of the measurement points in the USF-CY simulation.

sidewall. These unstable compressive failures are caused by sudden de-confinement (due to unstable shear failures) at the coal/roof and coal/floor interfaces at the interfaces. If there is no interface unstable shear failure, no unstable compressive failure at the sidewall can occur (see Section 5.2.5.3). The unstable failure in C4 has the highest intensity (i.e. largest rapid drop in normal stress) among the measurement regions. C6 does not experience failure in the simulation. The failure region extends approximately 2.5 m into the coal layer from the sidewall.

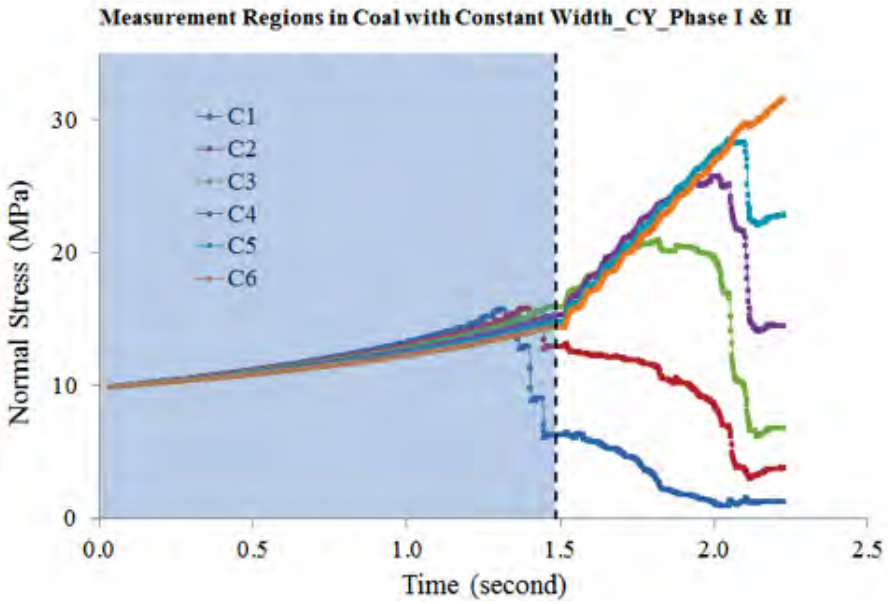

Figure 5.33: Normal stress–time curves of the measurement regions with a constant width of 0.5 m in USF-CY simulation.

The plots in Figure 5.34 act as supplementary information for analyzing the stability of the sidewall. The results plotted in Figure 5.34, show the averaged behaviors of larger regions of coal materials and may reveal additional information in certain conditions. In this case, Figure 5.34 suggests that the measurement regions with increased widths cannot reveal the distance of the failures into the coal layer because the normal stresses are averaged over the regions.

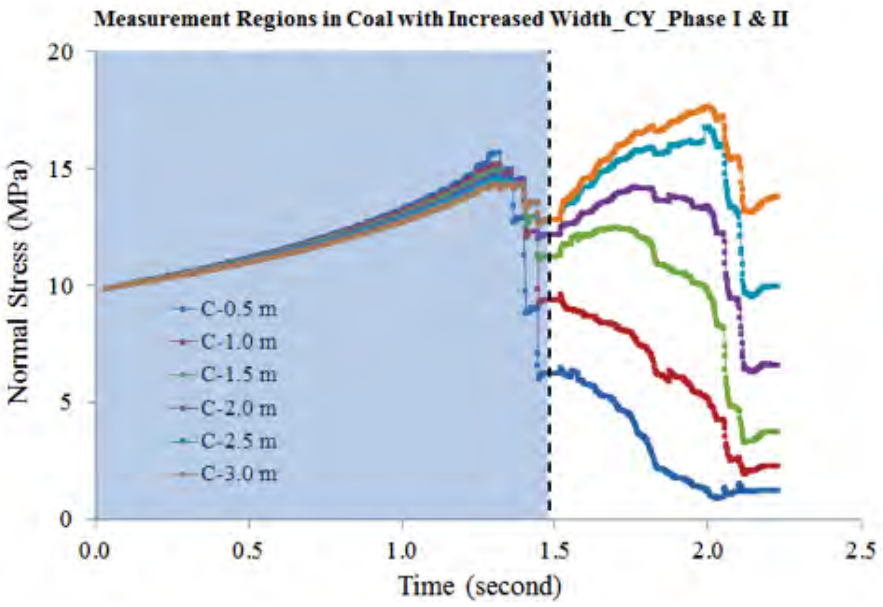

Figure 5.34: Normal stress–time curves of the measurement regions with increased widths in USF-CY simulation.

5.2.5.3 Unstable Failure of Sidewall due to Unstable Shear Failure at Interface – MC Model

The results of USF-MC simulation, as indicated by the orange area in Figure 5.35, are presented below. The UDEC codes for USF-MC simulation are shown in Section D.10 in Appendix D. Normal stress–time plots in Figure 5.36 show that the normal stresses at P1 and P2 decrease in Phase II due to the inability of the coal beneath points P1 and P2 to carry any additional normal stress (see Figure 5.39). The normal stresses at points P3 to P10 increase as the loading in Phase II starts. After a certain loading, P3 and P4 experience decreases in normal stress while P5 to P10 keep carrying more normal stresses.

The shear stress–time records in Figure 5.37 show that the shear stresses at the measurement points increase with the initiation of Phase II. P1 and P2 undergo stable shear failures indicated by gradual and smooth decreases in their shear stresses. No shear failures were observed at other points. Similarly, the shear displacements in Figure 5.38 show gradual changes as the mining of the coal progresses, which confirms that the measurement points experience either no failure or stable failures.

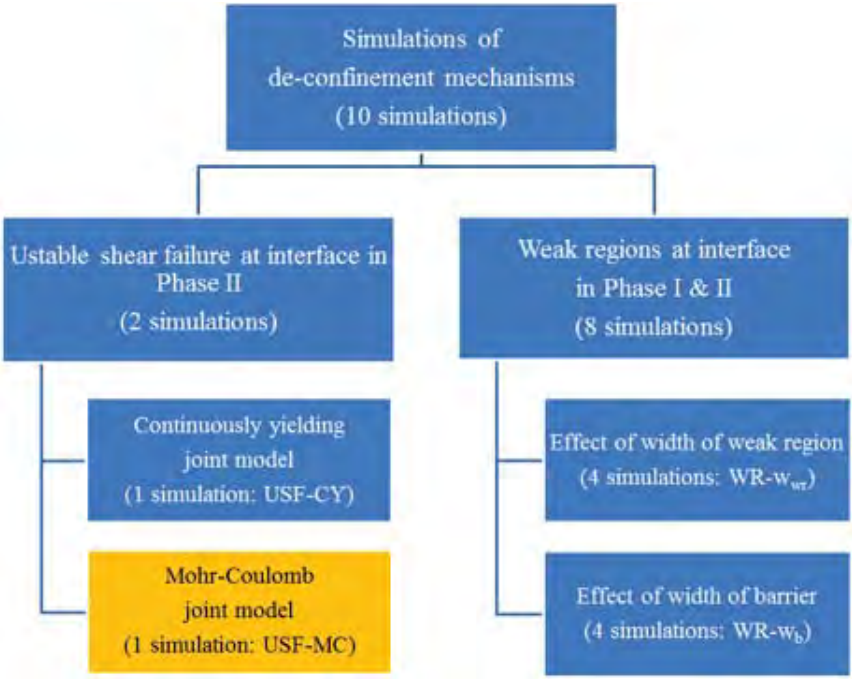

Figure 5.35: Representative component of USF-MC simulation in the organization chart.

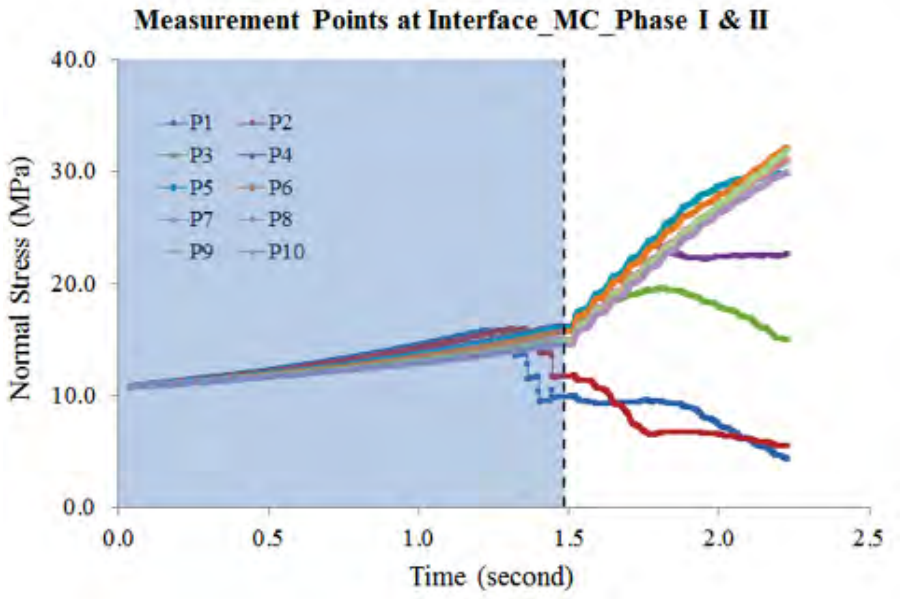

Figure 5.36: Normal stress–time curves of the measurement points in USF-MC simulation.

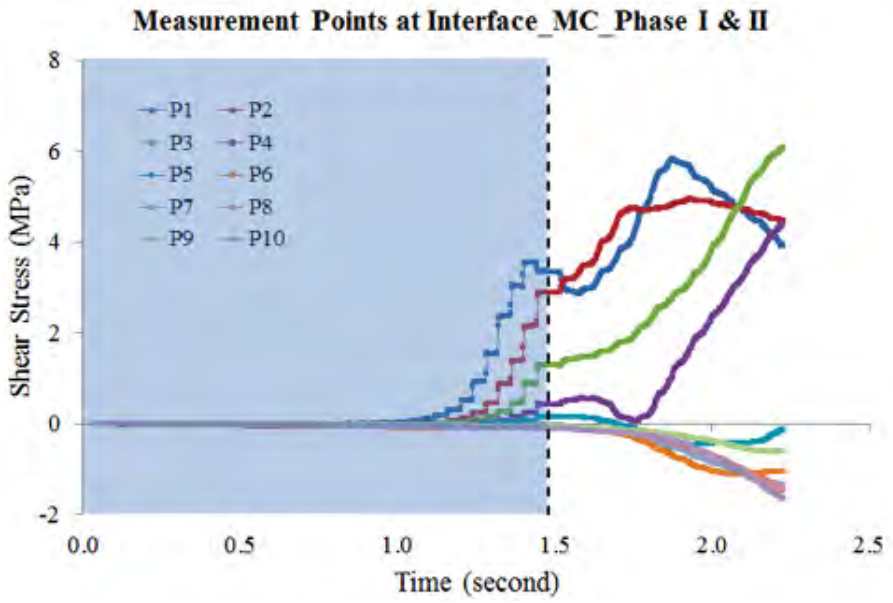

Figure 5.37: Shear stress–time curves of the measurement points in USF-MC simulation.

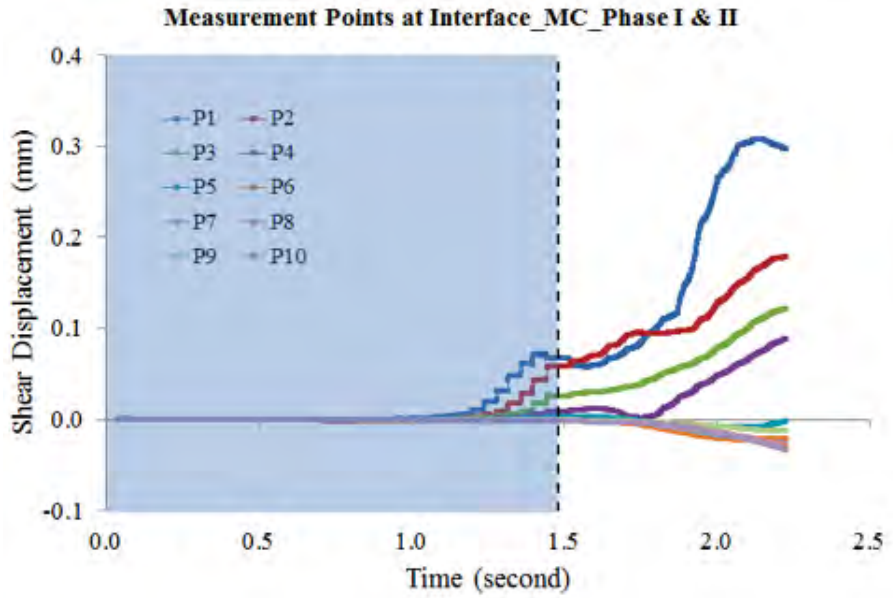

Figure 5.38: Shear displacement–time curves of the measurement points in USF-MC simulation.

Normal stresses measured in the coal layer are shown in Figure 5.39 and Figure 5.40. Measurement regions with a constant width (Figure 5.39) indicate that compressive failures occur in C1, C2 and C3 (failures extend 1.5 m into the coal layer). Absence of rapid drops in normal stress within these regions implies that the failures behave in a stable manner. Measurement points with increased width (Figure 5.40) show that failures occurred in a coal region with a width of 2.0 m although there is no failure exists in C4 (see Figure 5.39). This is because the averaged normal stress over 2.0 m width takes into account the failures of C1, C2 and C3.

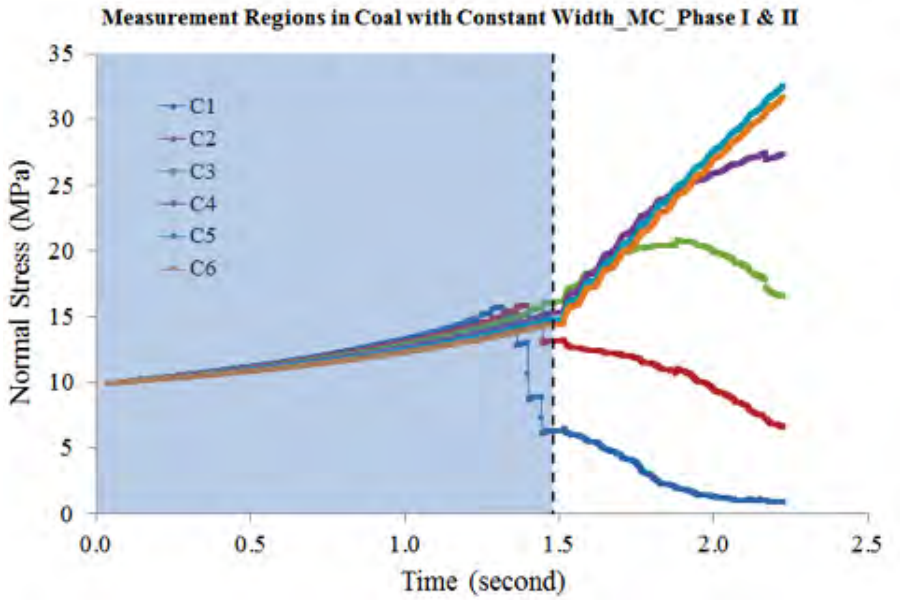

Figure 5.39: Normal stress–time curves of the measurement regions with a constant width of 0.5 m in USF-MC simulation.

5.2.5.4 Unstable Compressive Failure of Mining Face and Sidewall due to Weak Region at Interface – Varying w_{wr}

Four simulations with a constant w_b of 0.5 m and varying w_{wr} of 0.5, 1.0, 1.5 and 2.0 m, as indicated by the orange area in Figure 5.41, were performed. The UDEC codes for WR – w_{wr} simulations are shown in Section D.11 in Appendix D. Along with the previous simulation with w_{wr} of 0 m (the green area in Figure 5.41), the results of five simulations in

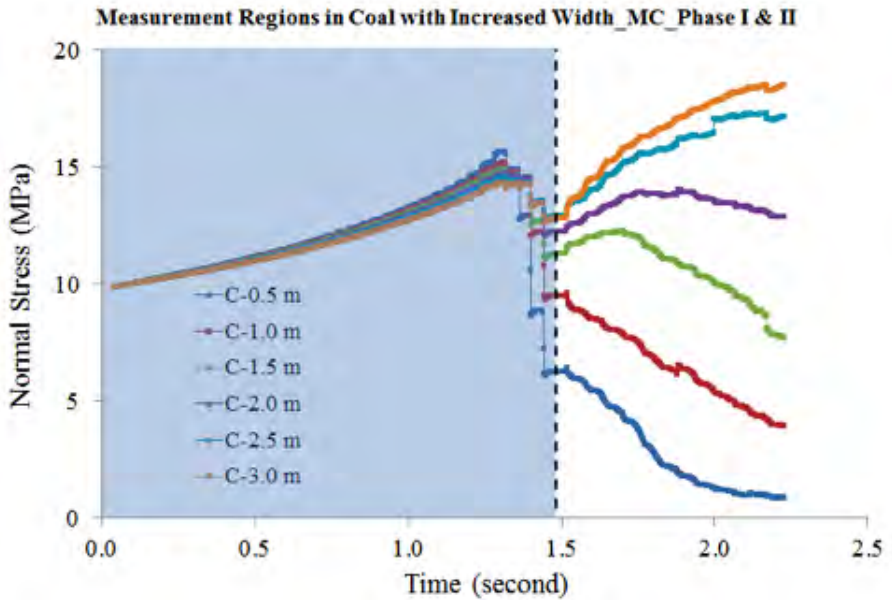

Figure 5.40: Normal stress–time curves of the measurement regions with increased widths in USF-MC simulation.

Phase I and Phase II can be used to analyze the effects of w_{wr} on the stability of the mining face and sidewall, respectively. The results of three most representative simulations with w_{wr} of 0.5, 1.5, and 2.0 m are presented in this section. Complete results of all five simulations can be found in Section C.1 in Appendix C.

Based on the results of the WR $-$ w_{wr} simulations, various instability issues occurred due to the existence of the weak regions at the roof-coal and floor-coal interfaces in underground mining conditions. If weak regions at interfaces exist ahead of the mining face, more unstable failures occur at the mining face as it advances toward the weak regions. If larger weak regions at roof-coal and coal-floor interfaces exist at the interfaces close to the sidewalls of an excavation, larger shear displacements at the interfaces (larger horizontal extensions of the coal material at the sidewalls toward the excavation) and larger regions of failures at the sidewalls are observed. The trends of the results obtained through in measurements with increasing w_{wr} are described as follows,

(1) In Phase I, more unstable compressive failures occur at the mining face (see the dotted rectangles in Figure 5.42, Figure 5.43 and Figure 5.44).

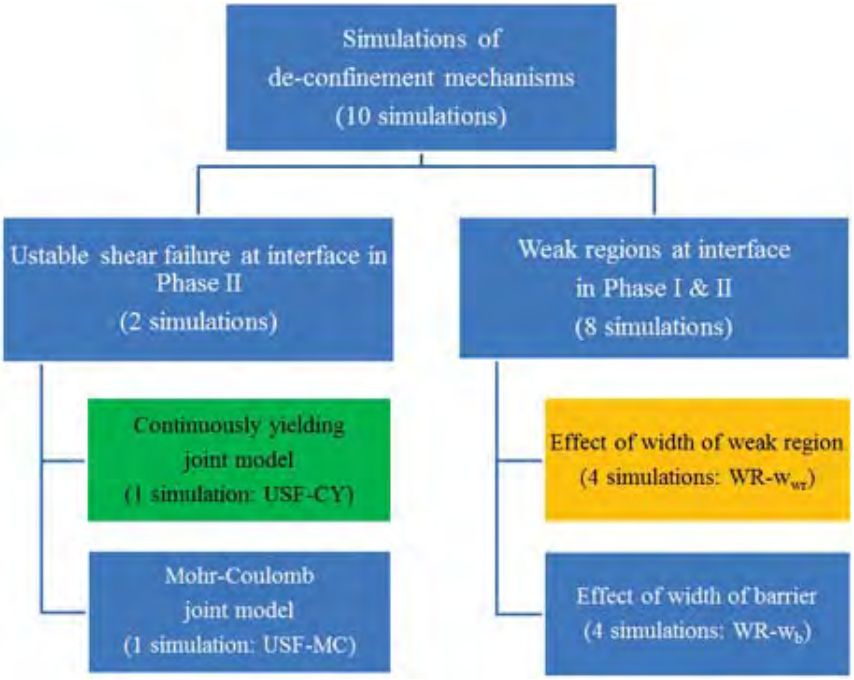

Figure 5.41: Representative components of USF-CY and WR $-$ w_{wr} simulations in the organization chart.

(2) In Phase I, magnitudes of the unstable compressive failures at the mining face increase (see the dotted rectangles in Figure 5.42, Figure 5.43 and Figure 5.44).

(3) In Phase I, increased unstable shear failures take place at the interface (see the dotted rectangles in Figure 5.45, Figure 5.46 and Figure 5.47).

(4) In Phase I, the intensities of unstable shear failures increase (see the dotted rectangles in Figure 5.45, Figure 5.46 and Figure 5.47).

(5) In Phase I, larger regions at the interface experience shear failures (see the dotted rectangles in Figure 5.48, Figure 5.49 and Figure 5.50).

(6) In Phase I, larger shear displacements are observed (see the dotted rectangles in Figure 5.48, Figure 5.49 and Figure 5.50).

(7) In Phase II, the failure regions at the sidewall increase (see the dashed rectangles in Figures Figure 5.42, Figure 5.43 and Figure 5.44).

(8) In Phase II, less unstable compressive failures are observed at the sidewall (see the dashed rectangles in Figure 5.42, Figure 5.43 and Figure 5.44).

(9) In Phase II, increased unstable shear failures at the interfaces are observed in Phase II (see the dashed rectangles in Figure 5.45, Figure 5.46 and Figure 5.47).

(10) In Phase II, the intensities of the unstable shear failures increase (see the dashed rectangles in Figure 5.45, Figure 5.46 and Figure 5.47).

(11) In Phase II, larger areas at the interface undergo shear failures (see the dashed rectangles in Figure 5.48, Figure 5.49 and Figure 5.50).

(12) In Phase II, the maximum shear displacement increase (see the dashed rectangles in Figure 5.48, Figure 5.49 and Figure 5.50).

The normal stress–time curves of the measurement regions in the simulations with w_{wr} of 0.5, 1.5 and 2.0 m are shown in Figure 5.42, Figure 5.43 and Figure 5.44, respectively. The drops of normal stress at about 1.5 seconds (i.e. the dotted rectangles) are caused by the removal of mining cuts in Phase I. When interpret the simulation results, the simulation with no weak region, which is the simulation represented by the box shaded in green in Figure 5.41, is taken as the basic case. The amount of normal stress drops in the basic case represents slight failures at the mining face caused completely by removing coal materials in each mining cut. Increased amount of failed regions and larger rapid stress drops in Figure 5.42, Figure 5.43 and Figure 5.44 imply that increased unstable compressive failures with higher intensities take place at the mining face as w_{wr} increasing. Figure 5.42, Figure 5.43 and Figure 5.44 also indicate the strength of the coal materials at the mining face significantly decrease in both Phase I and II with increases in w_{wr}. The severely failed regions (i.e. low residual strength shown in the dashed rectangles in the figures) in the coal layer extend more than 3.0 m into the mining face with w_{wr} of 2.0 m. In Phase II, less unstable compressive failures were observed in the measurement regions with increasing w_{wr}.

Figure 5.45, Figure 5.46 and Figure 5.47show the shear stress–time plots of the measurement points for the simulations with w_{wr} of 0.5, 1.5 and 2.0 m, respectively. In Figure 5.45,

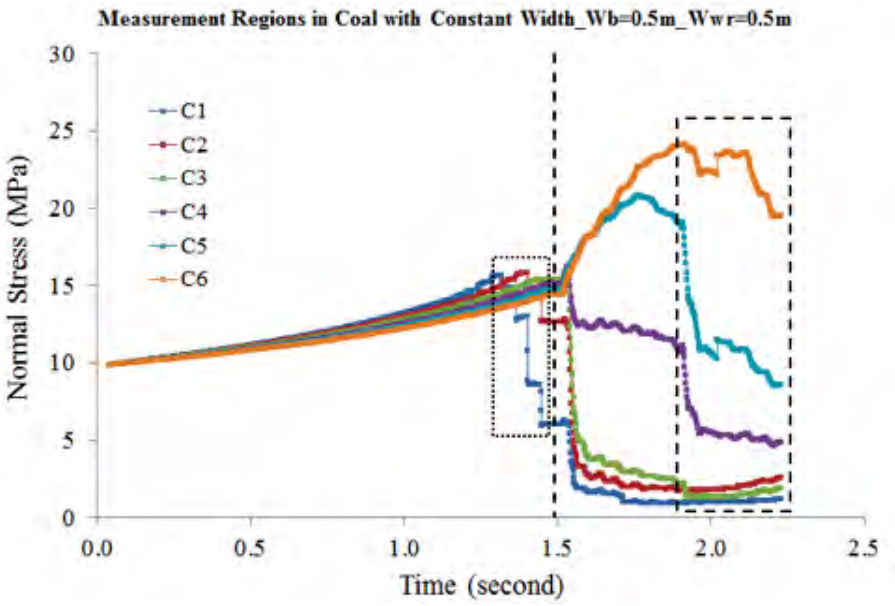

Figure 5.42: Normal stress–time curves of the measurement regions with a constant width in WR – w_{wr} simulation with w_b = 0.5 m and w_{wr} = 0.5 m.

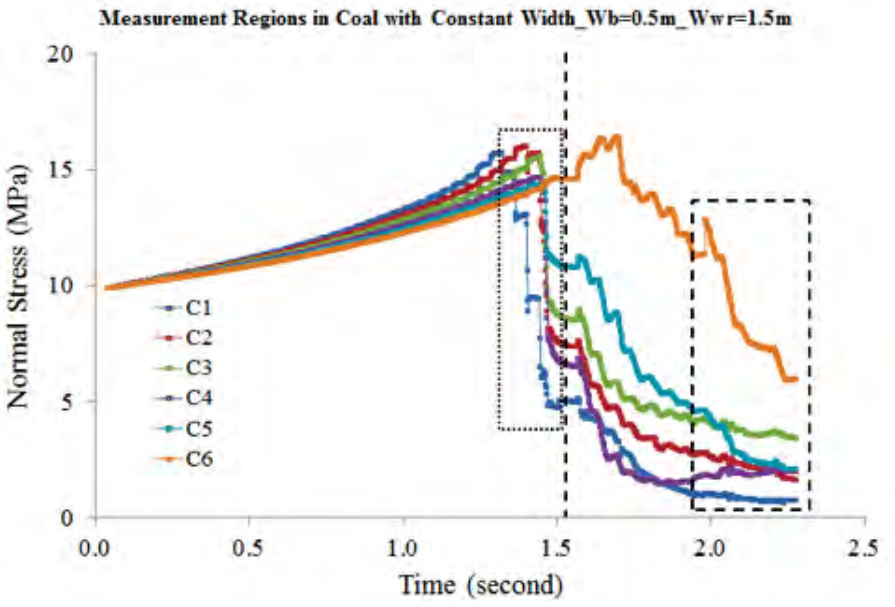

Figure 5.43: Normal stress–time curves of the measurement regions with a constant width in WR – w_{wr} simulation with w_b = 0.5 m and w_{wr} = 1.5 m.

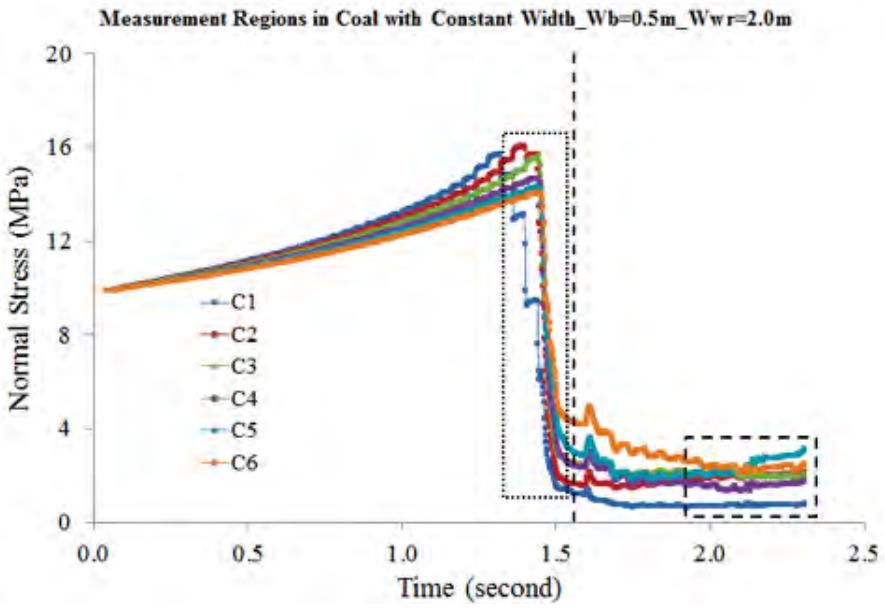

Figure 5.44: Normal stress–time curves of the measurement regions with a constant width in WR − w_{wr} simulation with w_b = 0.5 m and w_{wr} = 2.0 m.

no unstable shear failure occurs at the measurement points in Phase I. However, unstable shear failures indicated by rapid decreases in shear stress are observed at P1 in Phase I in Figure 5.46 and Figure 5.47. During unstable shear failures the shear stresses at P1 and maybe other points near P1 that failed but are not taken as measurement points are instantly transferred to the closest intact contact at the interface. In Figure 5.46, the transferred stress is carried by P5 and P6, as shown by the rapid increases in shear stress in the figure, due to the inability of the weak region between P1 and P5 to sustain shear stress. For the same reason, P6 and P7 in Figure 5.47 carry the shear stresses transferred from the failed points, such as P1 and probably other failed points close to P1. The amount of the shear stress drops at P1 and shear stress increases at the intact contacts shown in Figure 5.45, Figure 5.46 and Figure 5.47 suggest that the intensities of unstable shear failures in Phase I increase as w_{wr} increases.

The shear displacement–time curves of the simulations with w_{wr} of 0.5, 1.5 and 2.0 m are plotted in Figure 5.48, Figure 5.49 and Figure 5.50, respectively. The measurement points that experience shear failures in Phase I, which are highlighted by the dotted rectangles in

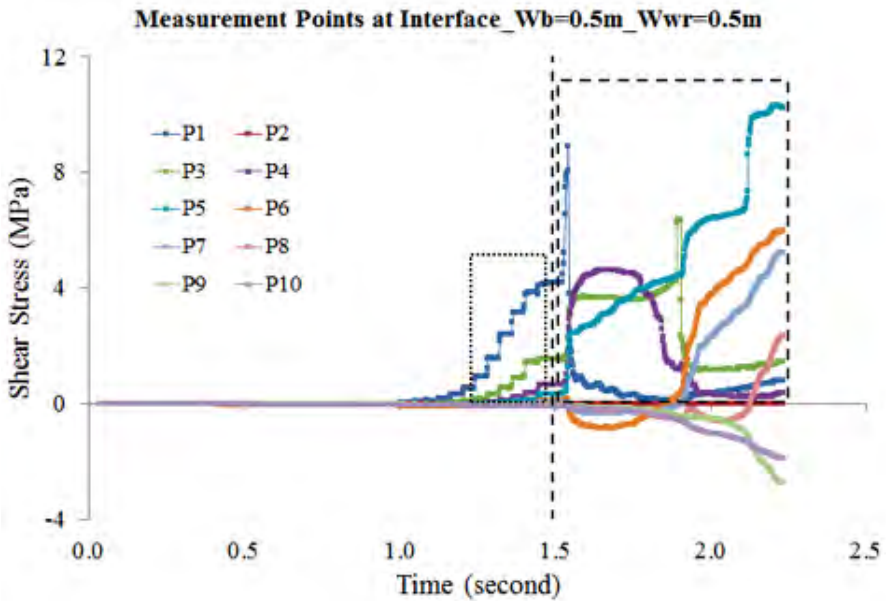

Figure 5.45: Shear stress–time curves of the measurement points in WR – w_{wr} simulation with $w_b = 0.5$ m and $w_{wr} = 0.5$ m.

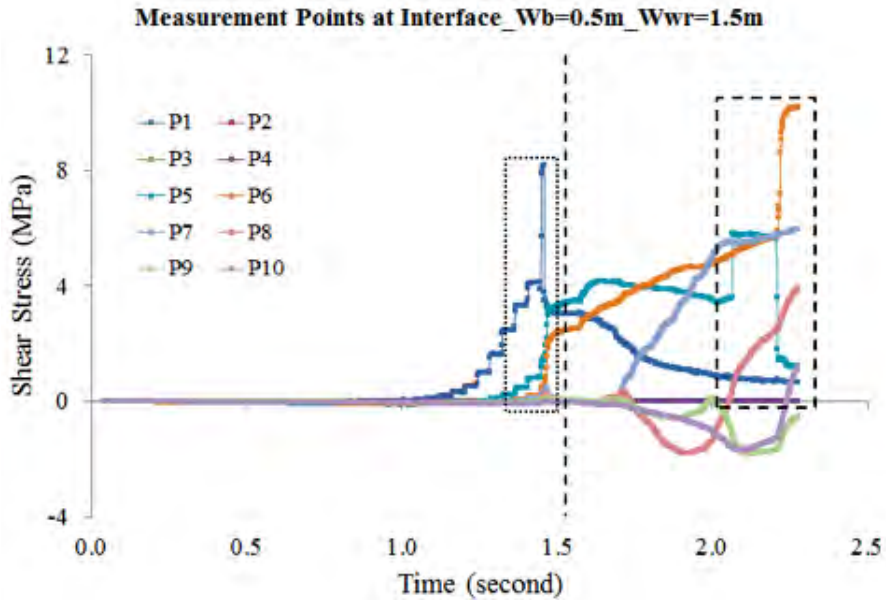

Figure 5.46: Shear stress–time curves of the measurement points in WR – w_{wr} simulation with $w_b = 0.5$ m and $w_{wr} = 1.5$ m.

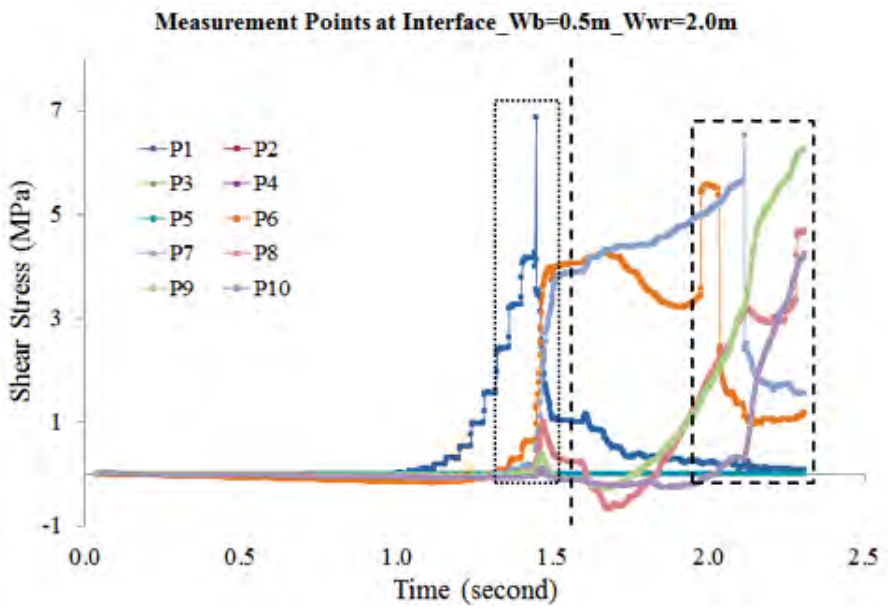

Figure 5.47: Shear stress–time curves of the measurement points in WR – w_{wr} simulation with w_b = 0.5 m and w_{wr} = 2.0 m.

the figures, increase as w_{wr} increases. In Figure 5.48, there are two measurement points undergo relatively large shear displacements in Phase I. In Figure 5.49, there are four measurement points experience relatively large shear displacements in Phase I. In Figure 5.50, five measurement points undergo relatively large shear displacements in Phase I. The shear displacements of the measurement points under shear failures become larger with increases in w_{wr}. The larger area and displacement of the shear failures are mainly caused by the slips at the weak regions at the interface.

Similarly, more measurement points and larger shear displacements are seen in Phase II in Figure 5.48, Figure 5.49 and Figure 5.50 (the dashed rectangles) as w_{wr} increases. Four measurement points with a maximum displacement of 0.03 m, five points with a maximum displacement of 0.046 m, and seven points with a maximum displacement of 0.071 m are observed in Phase II in Figure 5.48, Figure 5.49 and Figure 5.50, respectively.

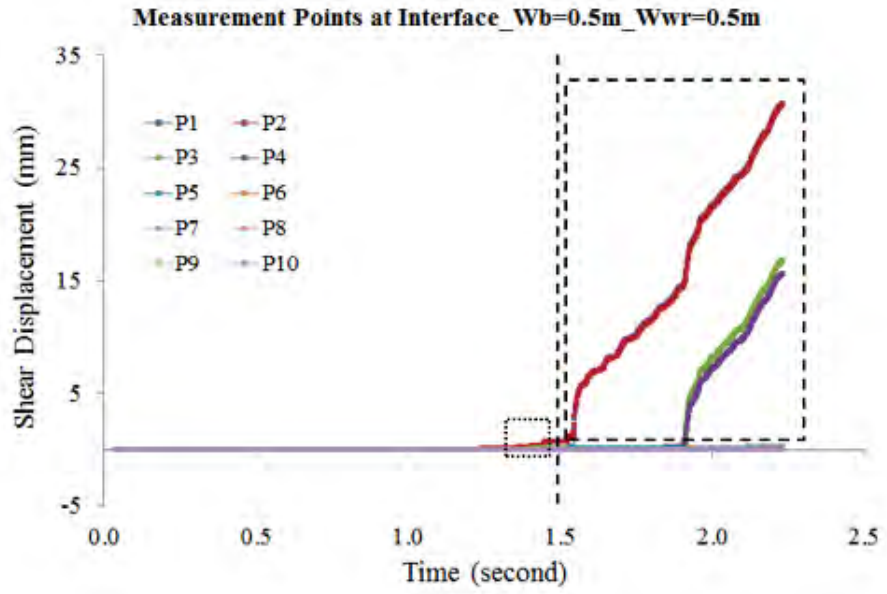

Figure 5.48: Shear displacement–time curves of the measurement points in WR – w_{wr} simulation with $w_b = 0.5$ m and $w_{wr} = 0.5$ m.

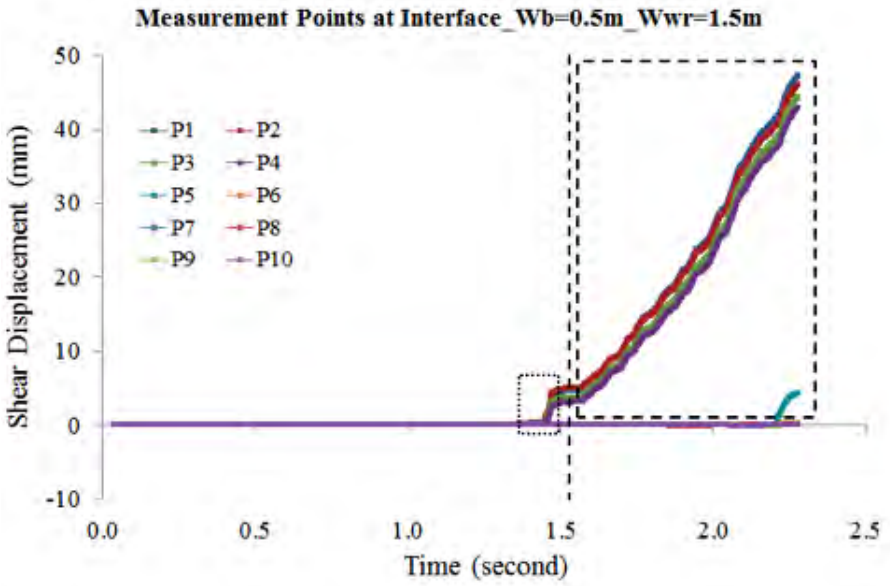

Figure 5.49: Shear displacement–time curves of the measurement points in WR – w_{wr} simulation with $w_b = 0.5$ m and $w_{wr} = 1.5$ m.

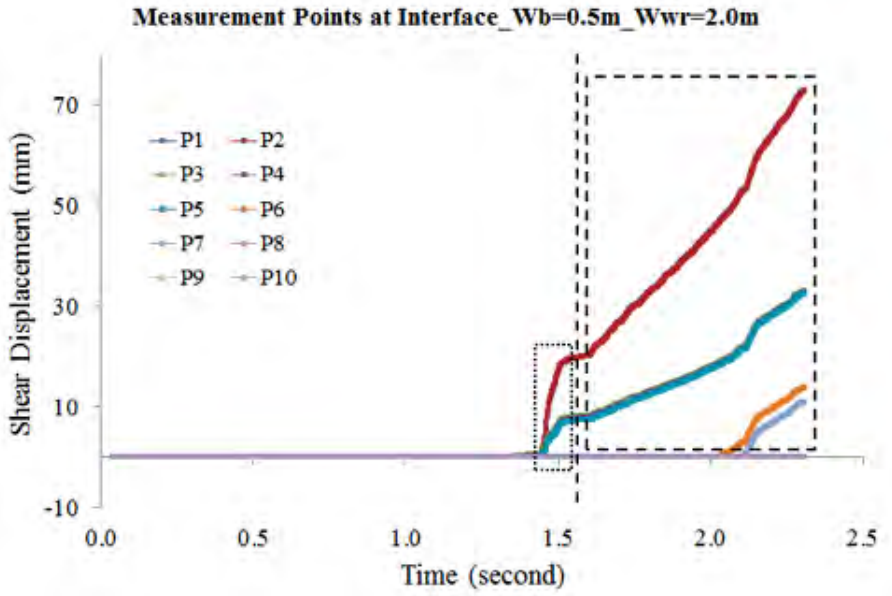

Figure 5.50: Shear displacement–time curves of the measurement points in WR – w_{wr} simulation with w_b = 0.5 m and w_{wr} = 2.0 m.

5.2.5.5 Unstable Compressive Failure of Mining face and Sidewall due to Weak Region at Interface – Varying w_b

The results of WR – w_b simulations are shown in this section. Five simulations with a constant w_{wr} of 2.0 m and varying w_b of 0.0, 0.5, 1.0, 1.5 and 2.0 m were performed. The UDEC codes for WR – w_b simulations are shown in Section D.12 in Appendix D. These simulations contribute to the component of the de-confinement mechanism investigation represented by the orange block in Figure 5.51 for the effects of w_b on the stability of mining faces and sidewalls. The results of four most representative simulations with w_b of 0.0, 0.5, 1.5 and 2.0 m are presented in this section. Complete results of five simulations can be found in Section C.2 in Appendix C.

The results suggest that in underground mining operations the w_b at the roof-coal and floor-coal interfaces, similar to the w_{wr}, can affect the stability of mining faces and sidewalls. The observations from the simulations with increasing w_b are summarized below,

(1) In Phase I, regions of instabilities at the mining face first increase and then decrease (see the dotted rectangles in Figure 5.52, Figure 5.53, Figure 5.54 and Figure 5.55).

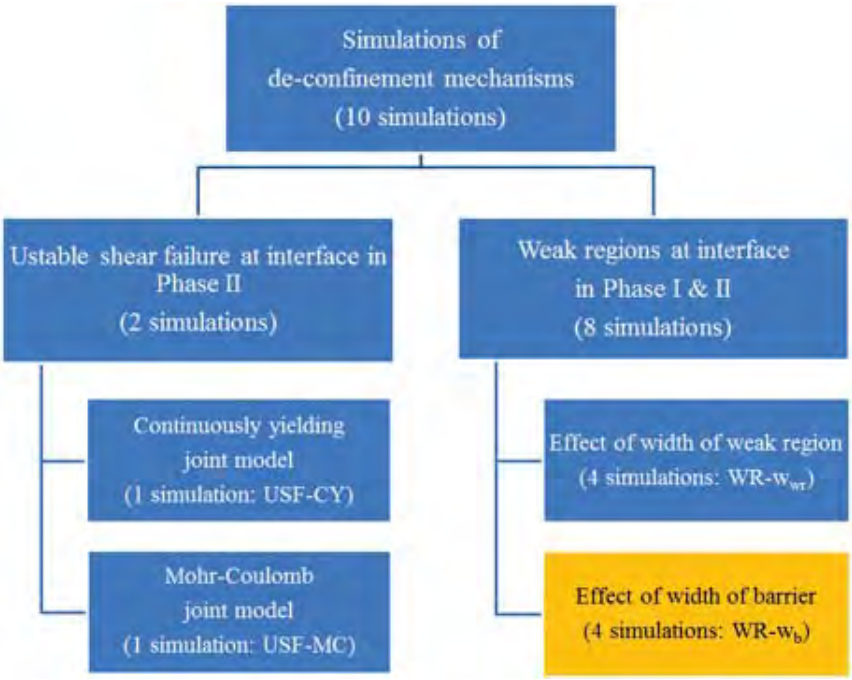

Figure 5.51: Representative component of WR $-$ w_b simulations in the organization chart.

(2) In Phase I, magnitudes of the unstable compressive failures at the mining face first increase and then decrease (see the dotted rectangles in Figure 5.52, Figure 5.53, Figure 5.54 and Figure 5.55).

(3) In Phase I, regions of unstable shear failures reduce (see the dotted rectangles in Figure 5.56, Figure 5.57, Figure 5.58 and Figure 5.59).

(4) In Phase I, intensities of unstable shear failures first increase and then reduce (see the dotted rectangles in Figure 5.56, Figure 5.57, Figure 5.58 and Figure 5.59).

(5) In Phase I, regions experienced slips at the interfaces first increase and then decrease (see the dotted rectangles in Figure 5.60, Figure 5.61, Figure 5.62 and Figure 5.63).

(6) In Phase I, smaller magnitudes of slips at the interface are shown (see the dotted rectangles in Figure 5.60, Figure 5.61, Figure 5.62 and Figure 5.63).

(7) In Phase II, the regions of unstable compressive failures in the sidewall first decrease, then increase, and decrease again (see the dashed rectangles in Figure 5.52, Figure 5.53, Figure 5.54 and Figure 5.55).

(8) In Phase II, the intensities of unstable compressive failures at the sidewall first increase and then decrease (see the dashed rectangles in Figure 5.52, Figure 5.53, Figure 5.54 and Figure 5.55).

(9) In Phase II, the residual compressive strengths in the sidewall increase (see the dashed rectangles in Figure 5.52, Figure 5.53, Figure 5.54 and Figure 5.55).

(10) In Phase II, the areas at the interfaces experienced unstable shear failures first increase and then decrease (see the dashed rectangle in Figure 5.56, Figure 5.57, Figure 5.58 and Figure 5.59).

(11) In Phase II, the intensities of unstable shear failures first increase and then decrease (see the dashed rectangle in Figure 5.56, Figure 5.57, Figure 5.58, Figure 5.59, Figure 5.60, Figure 5.61, Figure 5.62 and Figure 5.63).

(12) In Phase II, the maximum shear displacement first increases and then decreases (see the dashed rectangle in Figure 5.60, Figure 5.61, Figure 5.62 and Figure 5.63).

The normal stress–time curves of the measurement regions are shown in Figure 5.52, Figure 5.53, Figure 5.54 and Figure 5.55 for the simulations with w_b of 0.0, 0.5, 1.5 and 2.0 m, respectively. The results show that the numbers and intensities of unstable compressive failures at the mining face increase as w_b increased from 0.0 to 0.5 m. Unstable compressive failures in Figure 5.53 (dotted rectangle) occurred in a short term with relatively large intensities when the mining face close to its final location. Small unstable compressive failures are observed in C1 and C2 when w_b increased to 1.5 and 2.0 m (dotted rectangles in Figure 5.54 and Figure 5.55). The unstable failures in these two simulations are resulted from the mining cuts and not affected by the weak regions since these failures are similar to the failures in the USF-CY simulation (Figure 5.33). The residual strength in the coal material after Phase I generally increase with w_b increasing from 0.0 to 2.0 m, except for the simulation with w_b of 0.5 m. Areas and intensities of unstable compressive failures at the sidewall reduce as w_b changes from 0.0 to 0.5 m. The areas that experience unstable failures increase significantly with increased intensities when w_b increases from 0.5 to 1.5 m,

and that start to decrease as w_b changes from 1.5 to 2.0 m.

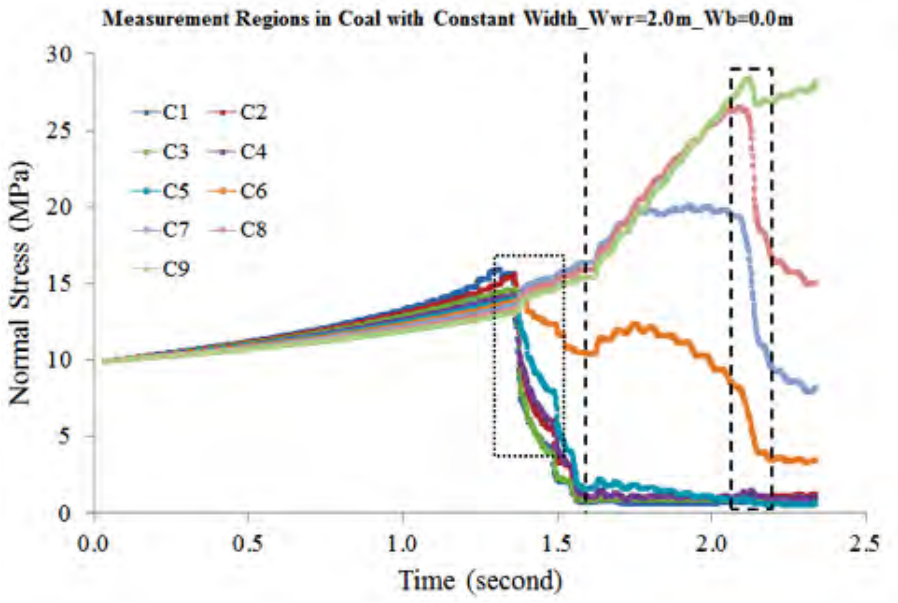

Figure 5.52: Normal stress–time curves of the measurement regions with a constant width in WR − w_b simulation with w_{wr} = 2.0 m and w_b = 0.0 m.

The shear stress–time curves are shown in Figure 5.56, Figure 5.57, Figure 5.58 and Figure 5.59 for w_b of 0.0, 0.5, 1.5 and 2.0 m, respectively. The rapid increase in shear stress at P5 in Figure 5.56 is resulted from the unstable shear failures at the points close to P5. The amount of the measurement points that undergo unstable shear failures decrease as w_b increases. No unstable shear failure is observed for w_b of 1.5 and 2.0 m. The simulation with w_b of 0.5 m has the highest intensity of unstable shear failures in Phase I among these simulations. In Phase II, the measurement points undergo unstable shear failures increase with w_b changes from 0.0 to 1.5 m, and that decrease as w_b increases from 1.5 to 2.0 m. The largest intensity of unstable shear failure in Phase II is observed in the simulation with w_b of 2.0 m.

The shear displacement–time curves for w_b of 0.0, 0.5, 1.5 and 2.0 m are shown in Figure 5.60, Figure 5.61, Figure 5.62 and Figure 5.63, respectively. The simulation with w_b of 0.5 m results in the largest areas of slip in Phase I. No slip occurs at the interface in Phase I when w_b increases to 1.0 m. The shear displacement of the slipped points with w_b of 0.0 is

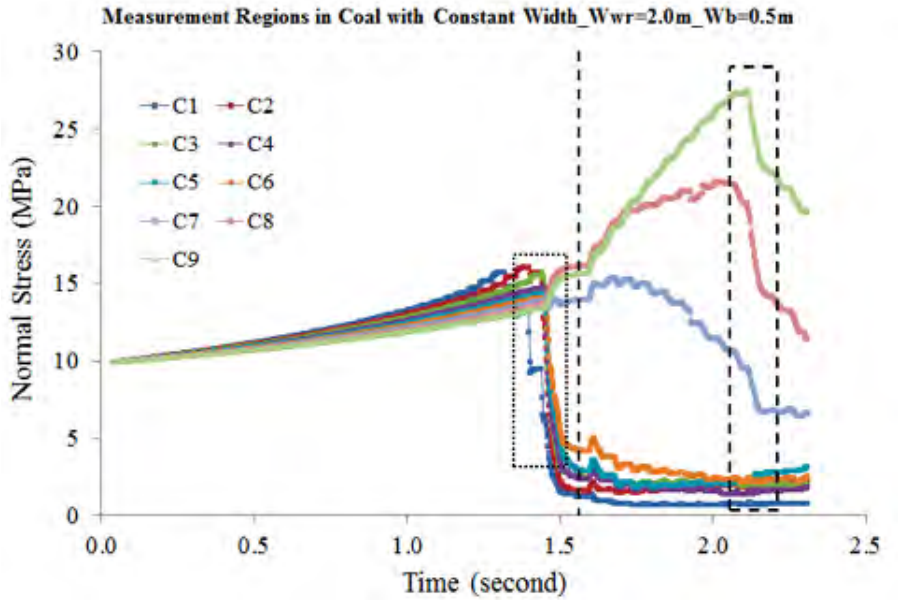

Figure 5.53: Normal stress–time curves of the measurement regions with a constant width in WR − w_b simulation with w_{wr} = 2.0 m and w_b = 0.5 m.

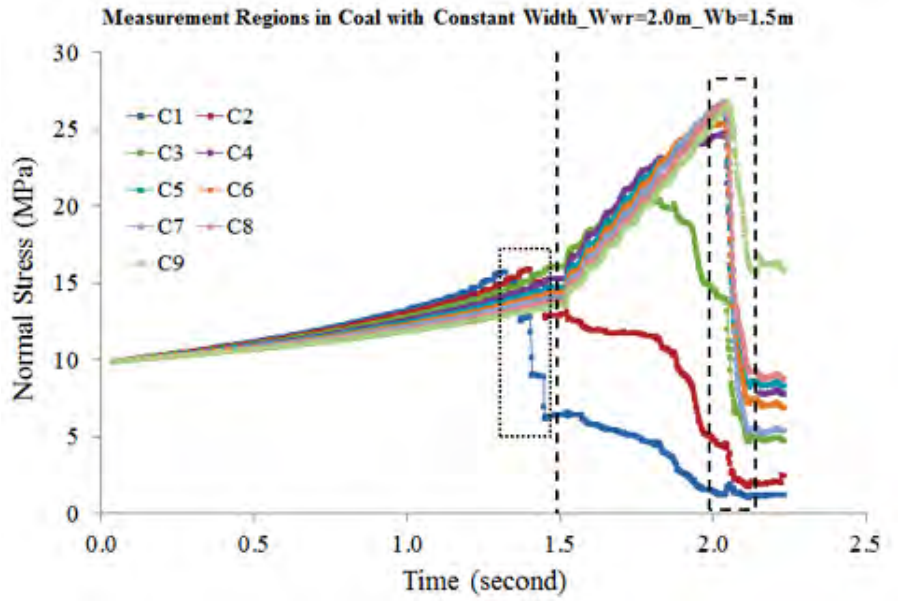

Figure 5.54: Normal stress–time curves of the measurement regions with a constant width in WR − w_b simulation with w_{wr} = 2.0 m and w_b = 1.5 m.

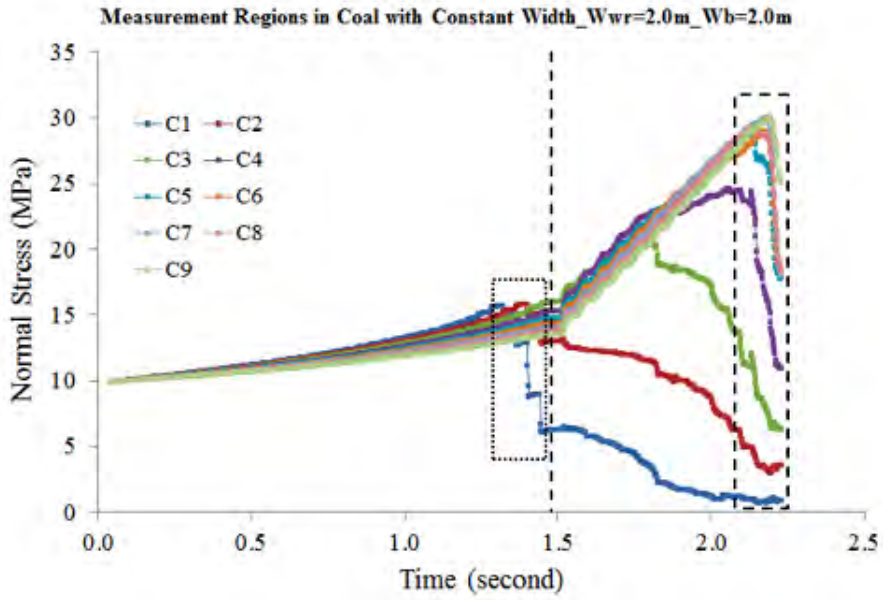

Figure 5.55: Normal stress–time curves of the measurement regions with a constant width in WR – w_b simulation with w_{wr} = 2.0 m and w_b = 2.0 m.

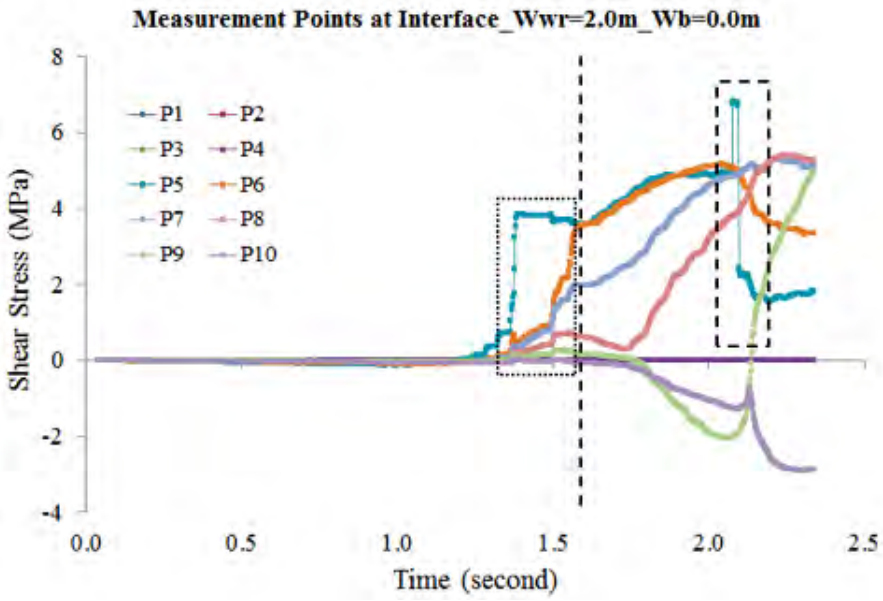

Figure 5.56: Shear stress–time curves of the measurement points in WR – w_b simulation with w_{wr} = 2.0 m and w_b = 0.0 m.

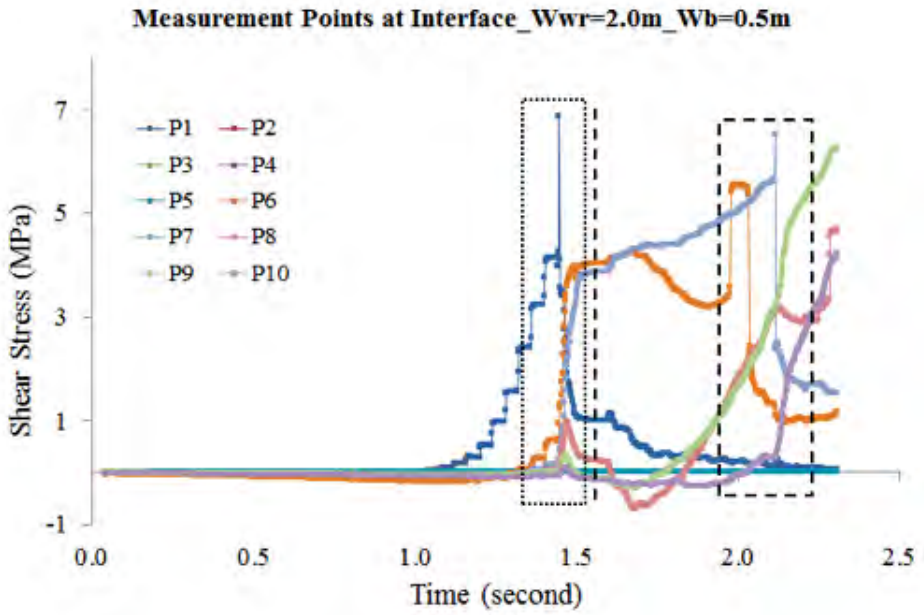

Figure 5.57: Shear stress–time curves of the measurement points in WR – w_b simulation with w_{wr} = 2.0 m and w_b = 0.5 m.

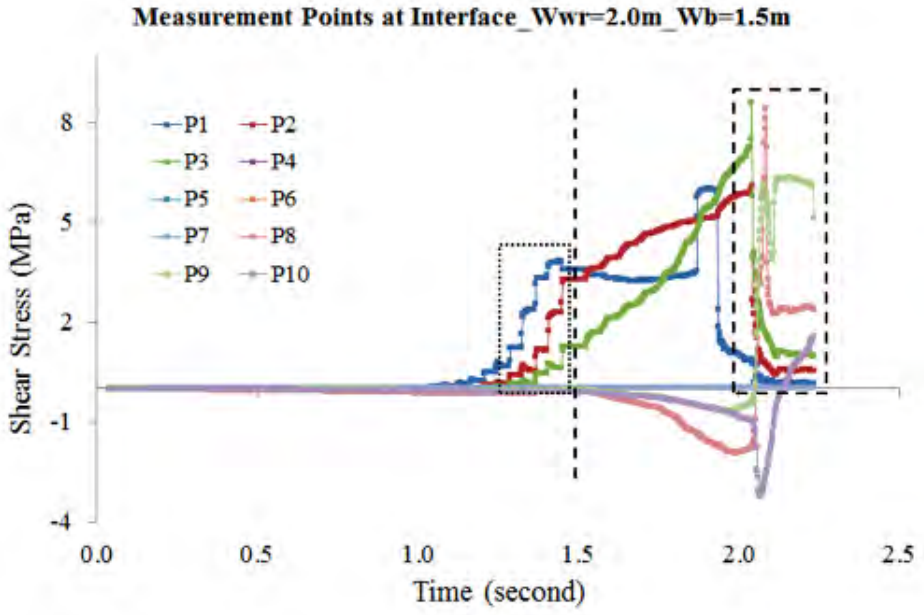

Figure 5.58: Shear stress–time curves of the measurement points in WR – w_b simulation with w_{wr} = 2.0 m and w_b = 1.5 m.

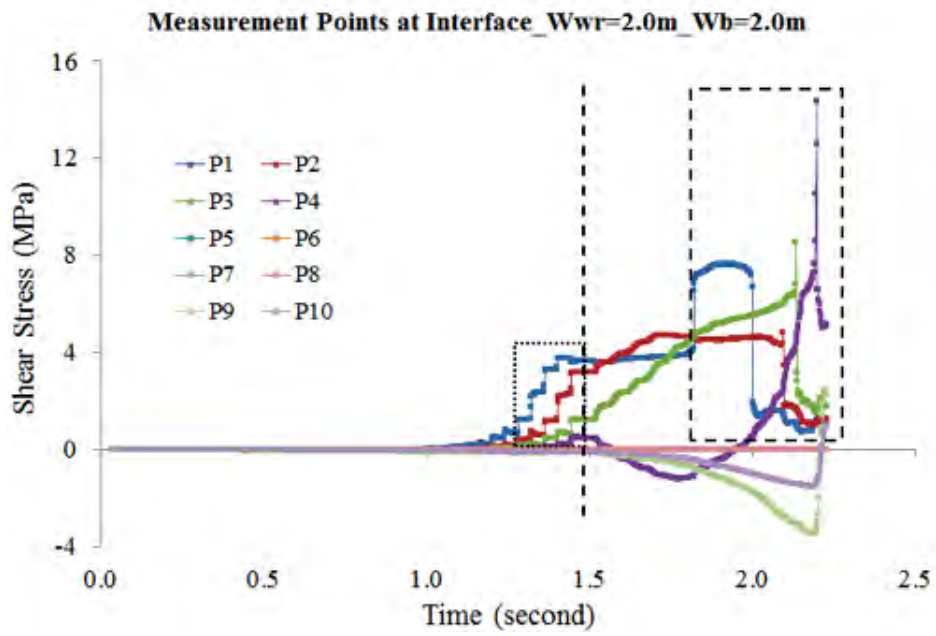

Figure 5.59: Shear stress–time curves of the measurement points in WR – w_b simulation with w_{wr} = 2.0 m and w_b = 2.0 m.

larger than that with w_b of 0.5 m. The maximum shear displacement in Phase II is observed in the simulation with w_b of 0.5 m. As w_b increases from 0.5 to 2.0 m, more measurement points experience shear while the maximum shear displacements of these points decrease.

5.3 Discussions

The clear distinctions between the results of USF-MC (Figure 5.36 to Figure 5.40) and USF-CY (Figure 5.30 to Figure 5.34) simulations indicate that the post-peak softening behaviors of the roof-coal and coal-floor interfaces are very important for analyzing stability of sidewalls, and the commonly used elastic-plastic behaviors can be insufficient. The interfaces with post-peak softening behavior provide a possible mechanism for unstable compressive failures at sidewalls in underground mining conditions. The results suggest that unstable compressive failure at sidewalls can be resulted from sudden de-confinements at the roof-coal and coal-floor interfaces due to unstable shear failures at the interfaces. The more intense the unstable shear failure, the more intense the unstable compressive failures at sidewalls.

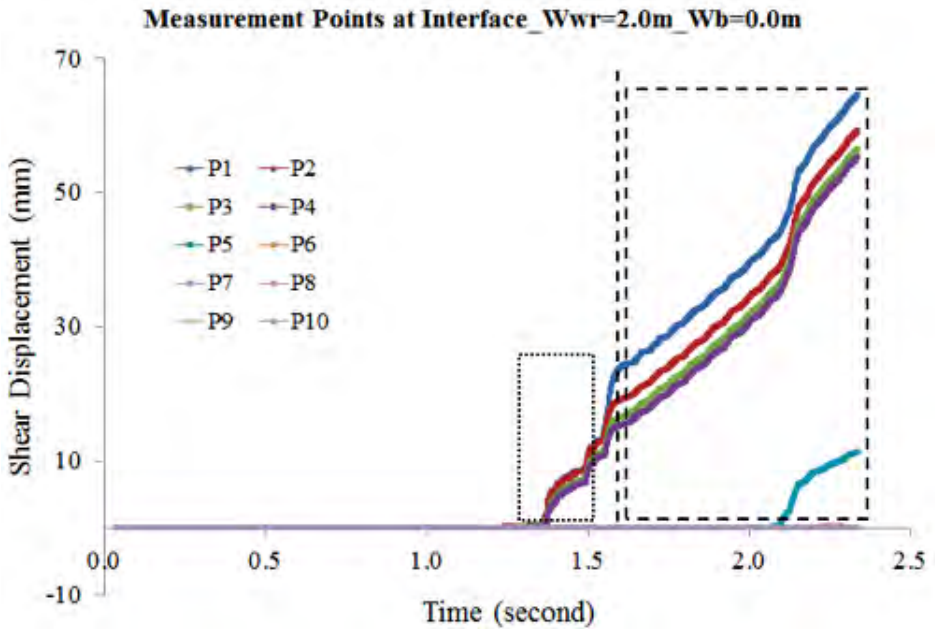

Figure 5.60: Shear displacement–time curves of the measurement points in WR − w_b simulation with w_{wr} = 2.0 m and w_b = 0.0 m.

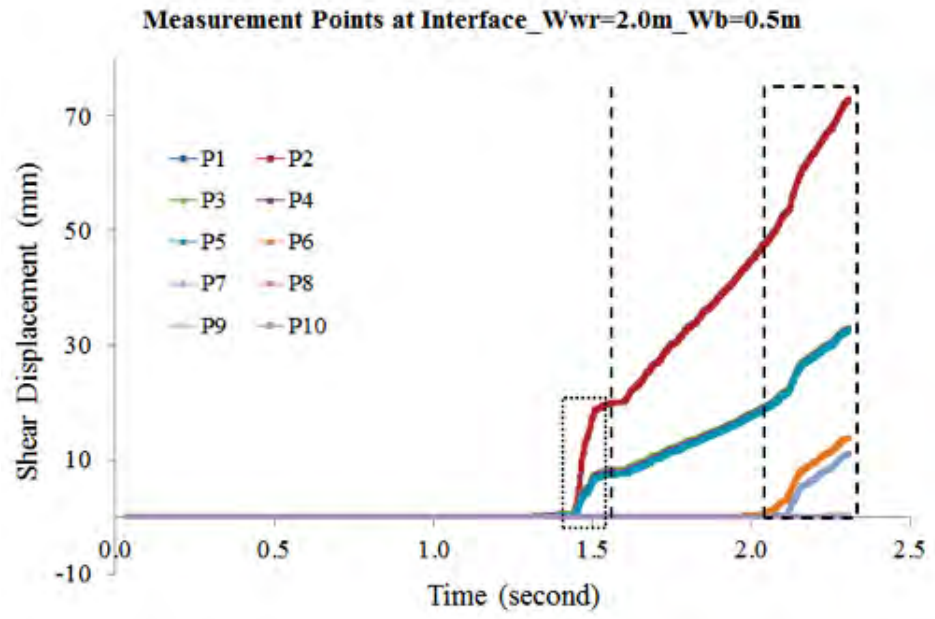

Figure 5.61: Shear displacement–time curves of the measurement points in WR − w_b simulation with w_{wr} = 2.0 m and w_b = 0.5 m.

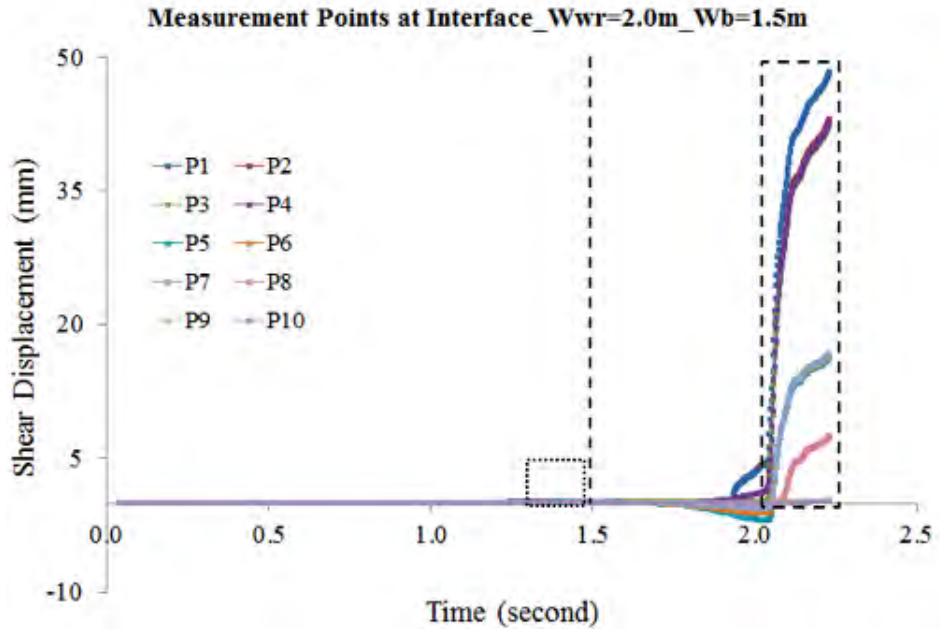

Figure 5.62: Shear displacement–time curves of the measurement points in WR − w_b simulation with w_{wr} = 2.0 m and w_b = 1.5 m.

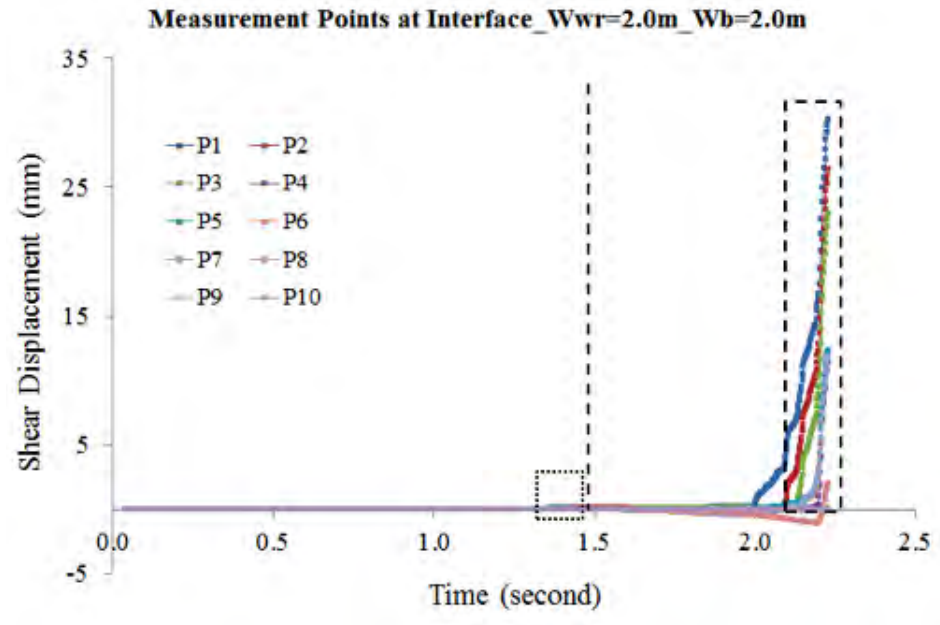

Figure 5.63: Shear displacement–time curves of the measurement points in WR − w_b simulation with w_{wr} = 2.0 m and w_b = 2.0 m.

The intensity of unstable shear failure of the interfaces is governed by the normal stress applied on them, the stiffness of the surrounding rock and the mechanical properties (characteristic behaviors) of the interfaces. Increased mining depth results in increased normal stress levels, which can lead to increased unstable shear failures at roof-coal and coal-floor interfaces, and hence potentially more unstable compressive failures at sidewalls.

The loading stiffness at the coal-host rock interfaces largely depends on the elastic modulus of the rock and the layout (geometry) of mining operations. Larger openings or the rocks with small elastic modulus tend to result in small loading stiffness, which provides higher possibility of unstable shear failures. The mechanical properties of the interfaces are critical because shear stress drop and post-peak stiffness of shear stress–displacement behaviors significantly affect the proneness and intensity of unstable shear failures. The mechanical properties of discontinuities are highly dependent upon the discontinuity compressive strength, the discontinuity roughness and the contact conditions of the discontinuity surfaces (whether the discontinuities are clean and closed or open and filled with infill material). High compressive strength and roughness along the discontinuity result in high shear strength, which increase the potential of large shear stress drops if failure occurs. The existence of infill at discontinuity contacts can significantly affect the mechanical properties of the discontinuity. Various tests have been performed by several researchers to investigate the effect of infill thickness on the shear behavior of discontinuities (Goodman 1970; Ladanyi and Archambault 1977; Lama 1978; Papaliangas et al. 1993). They found that the discontinuity shear strength and the shear stress drop generally decrease as the thickness of the infill material increases. Based on the numerical simulations in this study and the previously known mechanical behaviors of rock discontinuities, in underground mining conditions there are some factors that can be problematic and result in stability issues, such as unstable failures. These factors are the roof-coal and coal-floor interfaces with hard contacts (high compressive strength of the interfaces), high surface roughness and clean surface (no infill material) under soft loading stiffness conditions caused by the surrounding rocks of low

elastic modulus or large openings can be problematic.

The infill material commonly reduces the strength and shear stress drop of rock discontinuities, which decreases the proneness and intensity of unstable shear failures of the rock discontinuities. However, low cohesive strength and friction of infill material can also lead to instabilities. As indicated by the results of $WR - w_{wr}$ and $WR - w_b$ simulations, the weak regions at the roof-coal and coal-floor interfaces caused unstable compressive failures at the mining face and sidewall. In $WR - w_{wr}$ simulations, as the width of the weak regions increases more unstable compressive failures with higher intensities occurred at the mining face. This is because with the increased width of the weak regions, larger shear stresses are developed at the barriers (w_b of 0.5 m) between the weak regions and the mining face and lead to unstable shear failures of the barriers. With the sudden failure of the barriers the weak regions start to fail rapidly due to the inability of carrying shear stress, which forms sudden failures of large areas at the interfaces and results in large scale of sudden de-confinements. Under the effects of the de-confinement at the interfaces, unstable compressive failures at the mining face are initiated. As the weak region width increased, less unstable compressive failures occurred at the sidewall due to lower normal stress at the interfaces and lower strength of the coal materials after the Phase I simulations.

As the barrier width increases, less unstable compressive failures occur at the mining face because the barrier with a certain width can sustain the shear stresses developed on it and does not fail during the mining process. The intact interfaces result in confined mining face and slight unstable compressive failures (completely resulted from the mining cuts). However, larger barrier width does not necessarily lead to less unstable failures at sidewalls. In the $WR - w_b$ simulations, the barrier width of 1.0 m and 1.5 m with weak regions of 2.0 m caused many unstable shear failures at the interfaces and hence serious unstable compressive failures at the sidewall. This is because the larger normal stresses are developed at the barrier with widths of 1.0 and 1.5 m, which makes the barrier capable of carrying larger shear stresses before they fail. Once unstable shear failures occur at the

barriers, large areas at the barrier fail at the same time. When the barrier width reaches 2.0 m, less unstable failure occur at the interfaces and the sidewall because the areas at the interfaces that experience unstable shear failures at the same time becomes smaller and the effect of the weak regions reduces. It can be imagined that the weak regions located at a large distance, for example 20 m, from sidewalls (i.e. w_b of 20 m) will not influence the stability of the sidewalls.

The de-confinement mechanisms proposed in this study may also be used to analyze unstable failures in pillars with large width-to-height ratios. It is known that width-to-height ratio of pillars has significant effect on the axial stress–strain behavior of the pillars. This was illustrated by Das (1986) in laboratory tests on Indian coal specimens. As shown in Figure 5.64, the peak strength, post-peak stiffness, and residual strength of the specimens increase as the specimens' width-to-height ratio increases. The behavior of the coal specimens approaches an elastic-plastic behavior in their axial stress–strain relations when the width-to-height ratio reaches about 8.

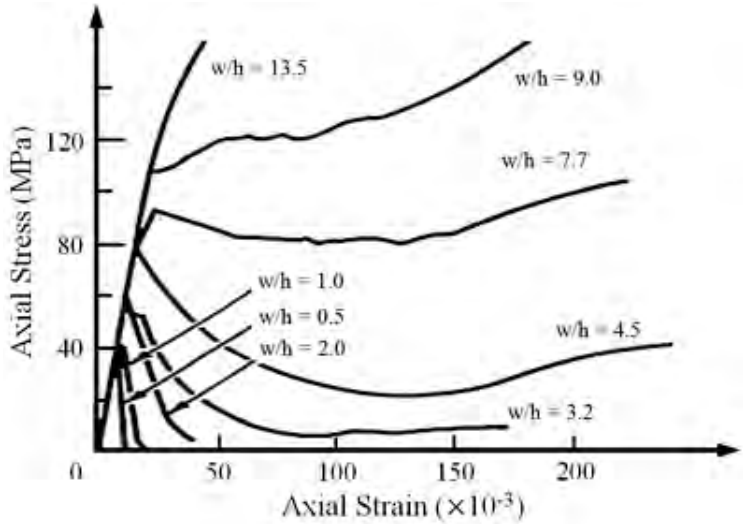

Figure 5.64: Effect of the width-to-height ratio on the behavior of Indian coal specimens (Das 1986).

The effect of width-to-height ratio on behaviors of rock materials is also shown by Madden (1987) by conducting UCS tests on sandstone samples (see Figure 5.65). Figure 5.65 shows

that the axial stress–strain curves of the two materials (i.e. Indian coal and sandstone) are similar at equivalent width-to-height ratios. Although these results are obtained in laboratory scale tests, they shed light on the changes in peak strength, post-peak stiffness, and residual strength of pillars in underground mines due to changes in their shapes.

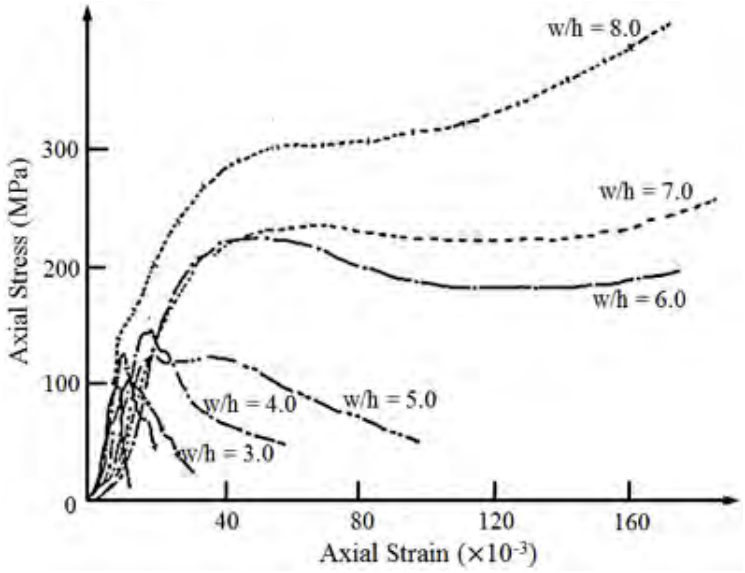

Figure 5.65: Effect of the width-to-height ratio on the behavior of sandstone samples in UCS tests (Madden 1987).

If consider the stiffness criterion and the effect of width-to-height ratio on rock materials, it is logically to conclude that large-scale unstable compressive failures/strain-type rockbursts cannot occur in pillars with large width-to-height ratio (e.g. w/h of 8) because the loading stiffness can never be less than the post-peak stiffness of pillars that exhibit elastic-plastic behaviors. Small-scale unstable compressive failures may occur at the sides of the pillars. However, this is not the situation observed in some underground mines. For instance, a rockburst accident occurred in the south barrier section of the main west in the Crandall Canyon Mine in August 6, 2007 (Gates et al. 2007). The accident involved unstable compressive failures in several pillars with width-to-height ratio of about 7 (i.e. pillars with a width of 60 feet and a height of 8 feet). Many large pillars completely failed. The conflict between the stiffness criterion and real cases of rockbursts in underground mines

infers that there possibly are other mechanisms involved in unstable compressive failures of larger width-to-height ratio pillars. Consider a pillar with large width-to-height ratio as a very small "sidewall", unstable shear failures and weak regions at the roof-pillar and pillar-floor interfaces can result in completely destruction of the pillar in the form of unstable compressive failures.

The de-confinement mechanisms are advanced based on the characteristics of the coal-rock contact properties and mining geometries. These mechanisms provide possible explanations to the occurrences of extensive failures in pillars or sidewalls in some rockburst cases, such as the ones described in (Gates et al. 2007; Whyatt and Loken 2009).

5.4 Conclusions

Taking into consideration the mechanical behaviors of roof-coal and coal-floor interfaces, de-confinement mechanisms were proposed to explain unstable compressive failures at mining faces and sidewalls in underground mining conditions. Several conclusions can be drawn from the numerical simulations:

• Unstable shear failures at interfaces can cause unstable compressive failures/rockbursts at sidewalls.

• Competent wall rocks of interfaces, clean contacts at interfaces, large roughness, deeply located interfaces, soft surrounding rocks, and adjacent large openings are favorable factors for unstable shear failures at interfaces and unstable compressive failures at sidewalls.

• The interaction between weak regions at interfaces and unstable shear failures at barriers can result in unstable compressive failures/rockbursts at mining faces and sidewalls.

• Interfaces with loose, cohesionless infill materials can be problematic for controlling rockburst events.

• In some conditions, the existence of a barrier between weak regions and excavations makes more serious unstable failures.

Based on the information presented above, it is shown that the interfaces between the coal seam and roof/floor rocks can be very important and need to be considered in underground

mines that have potential unstable failure problems.

CHAPTER 6
CONCLUSIONS AND FUTURE WORK

Shear failures along rock discontinuity planes and compressive failures in rocks are known to occur in deep underground mines and tunnels due to stress redistribution caused by advancing excavations or mining operations. Such failures can be in either stable or unstable manner. Unstable failures can result in rockbursts (also known as bumps), which lead to damages of equipment, injuries of workers and delays of production. The objective of this thesis is to develop numerical modeling methodologies that can help with improving the understanding of the mechanisms of unstable failures in underground coal mines.

The main parameters that are considered for discontinuity shear failures are the shear failure characteristic of the discontinuity and the loading characteristic of the mining geometry in terms of its system stiffness. The main parameters considered for compressive failures are sudden de-confinements of mining faces and sidewalls due to unstable shear failures and existence of weak contact regions at the roof-coal and coal-floor interfaces. The numerical model Universal Distinct Element Code (UDEC) was selected for simulations of discontinuity and rock failures. The continuously yielding (CY) joint model was used as the constitutive model for the discontinuity and the roof-coal and coal-floor interfaces. The Mohr-Coulomb strain softening (MCSS) model was used in the coal layer to simulate the elastic-softening behavior of the coal materials.

6.1 Conclusions

The key findings of the studies are summarized below.

- UDEC with the CY joint model can be a useful tool for studying shear failure stability of rock discontinuities in relation to occurrence of rockburst events in underground mines.

- UDEC with the MCSS model is capable of simulating stable and unstable compressive failures of rock materials.

- The signatures of unstable failures include sudden, discontinuous changes in stress and displacement along the discontinuity/in the rock material, as compared to smooth and gradual response in the case of stable failures.

- Mining advances change the loading stiffness of the surrounding rocks, which in turn affects the stability of discontinuity shear failures and can result in both stable and unstable shear failures along existing rock discontinuities.

- Competent wall rocks of interfaces, clean contacts at interfaces, large roughness, deeply located interfaces, soft surrounding rocks and reduced loading system caused by extensive mining are favorable factors for unstable shear failures to occur in underground mines.

- As normal stress on the discontinuity increases, the proneness and intensity of unstable shear failures increase.

- The proneness and intensity of unstable shear failures increase with increasing excavation extent, decreasing distance between the discontinuity and excavation and decreasing elastic modulus of rock.

- Unstable shear failures at coal-rock interfaces can cause unstable compressive failures in coal layers resulting in violent rib failures.

- Patches of weak regions at coal-rock interfaces possibly promote de-confinement causing unstable compressive failures at mining faces and sidewalls. Hence, the interfaces with loose, cohesionless infill materials can be problematic for management and control of rockburst problems in underground mines.

6.2 Future Work

More realistic and complex conditions, for example, multiple, intersecting rock discontinuities under the influence of sequential mining operations, can be studied based on the established methodologies and validated numerical program in this thesis.

Obtaining sufficient geological data, e.g., properties of roof and floor strata in real mining conditions, realistic stress fields and properties and locations of existing rock discontinuities can improve the quality of the unstable failure analyses in underground mining conditions.

The established methodologies can be extended to three-dimensional modeling. With three-dimensional models, back analyses of unstable failures in historical cases can be performed to calibrate the parameters in the models. The calibrated models may able to provide useful information about possible locations and intensities of unstable failures in the future mining operations and prevent serious rockburst events from occurring.

Laboratory scale physical tests should be designed and carried out to validate the proposed de-confinement mechanisms of unstable compressive failures of coal materials.

The built-in energy functions in UDEC can possibly be used as signatures of unstable failures for mine-scale measurement. Further studies are needed to validate and apply these energy functions for unstable failure analyses.

REFERENCES CITED

Agapito, J. F. T. and R. R. Goodrich (2000). Five stress factors conducive to bumps in utah, usa, coal cines. In *Proceedings of the19th International Conference on Ground Control in Mining*, Morgantown, WV.

Agapito, J. F. T., R. R. Goodrich, and M. Moon (1997). Dealing with coal bursts at deer creek. *Min. Eng.*, 31–37.

Amitrano, D. (2006). Rupture by damage accumulation in rocks. *Int. J. Fracture 139*(3-4), 369–381.

ANSYS-news (1985-1988). *ANSYS* (1-4 ed.). Huston: Swanson Analysis Systems.

Babcock, C. O. and D. L. Bickel (1984). Constraint – the missing variable in the coal burst problem. In *The 25th U.S. Symposium on Rock Mechanics (USRMS)*, Evanston, IL, pp. 639–647.

Badr, S., R. Mendoza, S. Kieffer, M. D. G. Salamon, and U. Ozbay (2003). Numerical modeling of longwalls in deep coal mines. In *The 22nd International Conference on Ground Control in Mining*, pp. 37–43.

Bahaaddini, M., G. Sharrock, and B. K. Hebblewhite (2011). A comparison of physical and numerical experiments on artificial jointed rock masses using pfc3d. In Sainsbury, Hart, Detournay, and Nelson (Eds.), *Continuum and Distinct Numerical Modeling in Geomechanics*, Number 06-02.

Bandis, S. C., A. C. Lumsden, and N. R. Barton (1983). Fundamental of rock joint deformation. *Int. J. Rock Mech. Min. Sci. 20*, 249–268.

Bardetpp, J. P. (1989). Finite element analysis of rockburst as surface instability. *Comput. Geotech. 8*, 177–193.

Barron, L. R. (1990). Longwall stability analysis of a deep, bump prone western coal mine – case study. In *The 9th Conference on Ground Control in Mining*, pp. 142–149.

Barton, N., S. Bandis, and K. Bakhtar (1985). Strength, deformation and conductivity coupling of rock joints. *Int. J. Rock Mech. Min. Sci. 2*(3), 121–140.

Barton, N. R. (1972). A study of rock-joint deformation. *Int. J. Rock Mech. Min. Sci. 9*, 579–602.

Barton, N. R. and V. Choubey (1977). The shear strength of rock joints in theory and practice. *Rock Mech. 10*, 1–34.

Bieniawski, Z. T. (1967). Mechanism of brittle fracture of rocks, parts i, ii, and iii. *Int. J. Rock Mech. Min. Sci. 4*, 395–430.

Bigarre, P., K. Ben-Slimane, and J. Tinucci (1993). Three-dimensional modeling of fault-slip rockbursting. In *Proceedings of Rockbursts and Seismicity in Mines*, pp. 315–319.

Board, M. (1989). *Examination of the use of continuum versus discontinuum models for design and performance assessment for the Yucca Mountain site*. Itasca Consulting Group, Inc.

Bolstad, D. D. (1990). Keynote lecture: rockburst control research by the u.s. bureau of mines. In *Proceeding of the Second Symposium on Rockburst and Seismicity in Mines*, Rotterdam, pp. 371–375. A. A. Balkema.

Bukowska, M. (2006). The probability of rockburst occurrence in the upper silesian coal basin area dependent on natural mining conditions. *J. Min. Sci. 42*(6).

Burgert, W. and H. Lippmann (1981). Models of translator rock bursting in coal. *Int. J. Rock Mech. Min. Sci. 18*, 285–294.

Cai, M. (2008). Influence of stress path on tunnel excavation response – numerical tool selection and modeling strategy. *Tunn. Undergr. Sp. Tech. 23*, 618–628.

CAMIRO-Mining-Division (1990). *Mining in burst-prone ground, Rockburst Research Handbook*, Volume 1. CAMIRO Mining Division.

Chen, Z. H., C. A. Tang, and R. Q. Huang (1997). A double rock sample model for rockbursts. *Int. J. Rock Mech. Min. Sci. 34*(6), 991–1000.

Cho, N., C. D. Martin, and D. C. Sego (2007). A clumped particle model for rock. *Int. J. Rock Mech. Min. Sci. 44*, 997–1010.

Coates, D. F. (1965). *Rock Mechanics Principles*. Roger Duhamel, F.R.S.C.

Cook, N. G. W. (1965a). The failure of rock. *Int. J. Rock Mech. Min. Sci. 2*, 389–403.

Cook, N. G. W. (1965b). A note on rockbursts considered as a problem of stability. *J. South Afr. Int. Min. and Metallurgy 65*, 437–446.

Cook, N. G. W. (1978). *An industry guide to the amelioration of hazards of rockbursts and rockfalls*. Chamber of Mines of South Africa.

Cook, N. G. W., E. Hoek, J. P. G. Pretorius, W. D. Ortlepp, and M. D. G. Salamon (1966). Rock mechanics applied to the study of rockbursts. *J. South Afr. Int. Min. and Metallurgy*, 435–528.

Crouch, S. L. and C. Fairhurst (1974). Mechanics of coal mine bumps. *256*, 317–323.

Cubitt, J. M. and B. Shaw (1976). The geological implications of steady-state mechanisms in catastrophe theory. *Mathematical Geology 8*(6), 657–662.

Cundall, P. A. (1971). A computer model for simulating progressive large-scale movements in blocky rock systems. In *Proceedings of the Symposium of the International Society for Rock Mechanics*, Volume 1, Nancy, France.

Cundall, P. A. (1976). Explicit finite difference methods in geomechanics. In *Proceedings of the EF Conference on Numerical Methods in Geomechanics*, Volume 1, Blacksburg, Virginia.

Cundall, P. A. (1988). Formulation of a three-dimensional distinct element model – part i. a scheme to detect and represent contacts in a system composed of many polyhedral blocks. *Int. J. Rock Mech. Min. Sci. 25*(3), 107–116.

Cundall, P. A. (2000). Numerical experiments on rough joints in shear using a bonded particle model. In F. K. Lehner and J. L. Urai (Eds.), *Aspects of Tectonic Faulting (Festschrift in Honour of Georg Mandl)*, Berlin, pp. 1–9.

Cundall, P. A. and R. D. Hart (1984). Analysis of block test no. 1 inelastic rock mass behavior: phase 2 – a characterization of joint behavior (final report). Itasca Consulting Group Report, Rockwell Hanford Operations, Subcontract SA-957.

Cundall, P. A. and J. V. Lemos (1990). Numerical simulation of fault instabilities with a continuously-yielding joint model. In Fairhurst (Ed.), *Rockbursts and Seismicity in Mines*, pp. 147–152.

Cundall, P. A. and O. D. L. Strack (1979). A discrete numerical model for granular assemblies. *Geotech. 29*, 47–65.

Das, M. N. (1986). Influence of width/height ratio on the post-failure behavior of coal. *Intl. J. Min Geol. Eng.* (4), 79–87.

Elmo, D. and D. Stead (2003). An integrated numerical modeling-discrete fracture network approach applied to the characterization of rock mass strength of naturally fractured pillars. *Rock Mech. Rock Eng. 43*, 3–19.

Espinosa, H. D. and P. D. Zavattieri (2003a). A grain level model for the study of failure initiation and evolution in polycrystalline brittle meterials part i: theory and numerical implementation. *Mech. Mater. 35*, 333–364.

Espinosa, H. D. and P. D. Zavattieri (2003b). A grain level model for the study of failure initiation and evolution in polycrystalline brittle meterials part ii: numerical examples. *Mech. Mater. 35*, 365–394.

Feng, X. T., P. Z. Pan, and H. Zhou (2006). Simulation of the rock microfracturing process under uniaxial compression using an elasto-plastic cellular automation. *Int. J. Rock Mech. Min. Sci. 43*, 1091–1108.

Flamand, R., G. Archambault, S. Gentier, J. Riss, and A. Rouleau (1994). An experimental study of the shear behavior of irregular joints based on angularities and progressive degradation of the surfaces. In *Proceedings of the Can. Geotech Conf.*, pp. 253–262.

Gates, R. A., M. Gauna, T. A. Morley, J. R. O'Donnell-Jr., G. E. Smith, T. R. Watkins, C. A. Weaver, and J. C. Zelanko (2007). Underground coal mine, fatal underground coal burst accidents. Report of investigation, Mine Safety and Health Administration, 1100 Wilson Boulevard, Arlington, Virginia, 22209.

Gibowicz, S. J. (1984). The mechanism of large mining tremors in poland. In N. C. Gay and E. H. Wainwright (Eds.), *Rockbursts and Seismicity in Mines, S. African Inst. Min. Metall. Symp.*, Volume 6, pp. 17–28.

Golshani, A., M. Oda, Y. Okui, and T. Takemura (2007). Numerical simulation of the excavation damaged zone around an opening in brittle rock. *Int. J. Rock Mech. Min. Sci. 44*, 835–845.

Goodman, R. E. (1970). The deformability of joints. In *In determination of the insitu modulus of deformation of rocks*, Volume 477, pp. 174–196. Special technical publication (ASTM).

Griffiths, D. V., G. A. Fenton, and C. B. Lemons (2002). Probabilistic analysis of underground pillar stability. *Int. J. Numer. Anal. Met. 26*, 775–791.

Hagan, T. O., A. M. Milev, S. M. Spottiswoode, M. W. Hildyard, M. Grodner, A. J. Rorke, G. J. Finnie, N. Reddy, A. T. Haile, K. B. LeBron, and D. M. Grave (2001). Simulated rockburst experiment-an overview. *J. South Afr. Int. Min. and Metallurgy*, 217–222.

Hagan, T. O., A. M. Milev, S. M. Spottiswoode, B. Vakalisa, and N. Reddy (1998). *Improvement of worker safety through the investigation of the site response to rockbursts* (Draft Final Project Report ed.). Safety in Mines Research Advisory Committee.

Hajiabdolmajid, V., P. K. Kaiser, and C. D. Martin (2002). Modelling brittle failure of rock. *Int. J. Rock Mech. Min. Sci. 39*, 731–741.

Hart, R., M. Board, B. Brady, B. O'Hearn, and G. Allan (1988). Examination of fault-slip induced rockbursting at the strathcona mine. In P. A. C. et al. (Ed.), *Key Questions in Rock Mechanics*, pp. 369–379.

Hart, R., P. A. Cundall, and J. V. Lemos (1988). Formulation of a three-dimensional distinct element model – part ii. mechanical calculations for motion and interaction of a system composed of many polyhedral blocks. *Int. J. Rock Mech. Min. Sci. 25*(3), 117–125.

Hazzard, J. F., D. S. Collins, W. S. Pettitt, and R. P. Young (2002). Simulation of unstable fault slip in granite using a bonded-particle model. *Pageoph. 159*, 221–245.

He, M. C., J. L. Miao, and J. L. Feng (2010). Rock burst process of limestone and its acoustic emission characteristics under true-triaxial unloading conditions. *Int. J. Rock Mech. Min. Sci. 47*, 286–298.

He, M. C., W. Nie, L. Q. Han, and L. J. Ling (2010). Microcrack analysis of sanya granite fragments from rockburst tests. *Min. Sci. Technol. 20*, 238–243.

He, M. C., W. Nie, Z. Y. Zhao, and C. Cheng (2011). Micro- and macro-fractures of coarse granite under true-triaxial unloading conditions. *Min. Sci. Technol. 21*, 389–394.

He, M. C., W. Nie, Z. Y. Zhao, and W. Guo (2012). Experimental investigation of bedding plane orientation on the rockburst behavior of sandstone. *Rock Mech. Rock Eng. 45*(3), 311–326.

Hedley, D. G. F. and J. E. Udd (1989). The canada-ontario-industry rockburst project. *Pageoph. 129*, 661–672.

Henley, S. (1976). Catastrophe theory models in geology. *Mathematical Geology 8*(6).

Holland, C. T. (1958). Cause and occurrence of coal mine bumps. *Min. Eng. 9*, 994–1004B.

Holland, C. T. and E. Thomas (1954). Coal-mine bumps: some aspects of occurrence, cause, and control. *U.S. Bureau of Mines Bulletin*, 535–537.

Hudson, J. A., E. T. Brown, and C. Fairhurst (1971). Optimizing the control of rock failure in servo-controlled laboratory tests. *Rock Mech. 3*, 217–224.

Hudson, J. A., S. L. Crouch, and C. Fairhurst (1972). Soft, stiff and servo-controlled testing machines: a review with reference to rock failure. *Engineering Geology 6*, 155–189.

Iannacchione, A. (1990). Behavior of a coal pillar prone to burst in the southern appalachian basin of the united states. In C. Fairhurst (Ed.), *Rockbursts and Seismicity in Mines*, pp. 295–300. A.A. Balkema.

Iannacchione, A. T. and J. C. Zelanko (1995a). Occurrence and remediation of coal mine bumps: a historical review. In *Special Publication 01-95, NTIS No. PB95-211967*, pp. 27–67. U.S. Department of the Interior, Bureau of Mines.

Iannacchione, A. T. and J. C. Zelanko (1995b). Pillar mechanics of coal mine bursts: a control strategy. In *Proceedings of 16th World Mining Congress*, Sofia, Bulgaria.

Ishida, T., H. Shimizu, S. Murata, and T. Kanagawa (2009). Importance of inhomogeneity in rock fracturing deduced from distinct element simulation and in-situ direct shear test. In *Proceedings of the 7th International Symposium on Rockburst and Seismicity in Mines (Keynote Presentation)*, Dalian, China, pp. 3–16.

Itasca-Consulting-Group (1987). Evaluation of rockburst potential at the hanford site. Technical report.

Itasca-Consulting-Group (2010). *UDEC (Universal Distinct Element Code), Version 4.0*. Minneapolis, MN: Itasca Consulting Group Inc.

Jaiswal, A. and B. K. Shrivastva (2009). Numerical simulation of coal pillar strength. *Int. J. Numer. Anal. Met. 46*, 779–788.

Jenkins, F. M., G. A. Conway, J. G. Dwyer, and S. P. Signer (2006). 50 years of rock mechanics research (1995-2005): the effect on safety in u.s. underground mines. In *The 41st U.S. Symposium on Rock Mechanics (USRMS): 50 Years of Rock Mechanics-Landmarks and Future Challenges*, Golden, Colorado, USA.

Jing, L. (2003). A review of techniques, advances and outstanding issues in numerical modeling for rock mechanics and rock engineering. *Int. J. Rock Mech. Min. Sci. 40*(283-353).

Kaiser, P. K. and C. A. Tang (1998). Numerical simulation of damage accumulation and seismic energy release during brittle rock failure – part ii: rib pillar collapse. *Int. J. Rock Mech. Min. Sci. 35*(2), 123–134.

Karami, A. and D. Stead (2008). Asperity degradation and damage in the direct shear test: a hybrid fem-dem approach. *Rock Mech. Rock Eng. 41*(2), 229–266.

Kias, E. M. C., R. Gu, R. Garvey, and U. Ozbay (2011). Modeling unstable rock failure during a uniaxial compressive strength test. In *The 45th US Rock Mechanics/Geomechanics Symposium*, San Francisco, CA.

Krishnamurthy, R. and S. B. Shringarputale (1990). Rockburst hazards in kolar gold fields. In *Proceedings of the Second Symposium on Rockburst and Seismicity in Mines*, Rotterdam, pp. 411–419. A. A. Balkema.

Ladanyi, H. K. and G. Archambault (1977). Shear strength and deformability of filled indented joints. In *Proc. 1st Int. Symp. Geotech. Structural Complex Formations*, Capri, pp. 317–326.

Lama, R. D. (1978). Influence of clay fillings on shear behavior of joints. In *Proc. 3rd Congr. Int. Assoc. Eng. Geol.*, Volume 2, Madrid, pp. 27–34.

Lan, H., C. Derek-Martin, and B. Hu (2010). Effect of heterogeneity of brittle rock on micromechanical extensile behavior during compression loading. *J. Geophys. Res. 115*(B01202).

Leichnitz, W. (1985). Mechanical properties of rock joints. *Int. J. Rock Mech. Min. Sci. 22*, 313–321.

Lemos, J. V. (1987). *A distinct element model for dynamic analysis of jointed rock with application to dam foundations and fault motion*. Ph. D. thesis, University of Minnesota.

Li, T., M. F. Cai, and M. Cai (2007). A review of mining-induced seismicity in china. *Int. J. Rock Mech. Min. Sci. 44*, 1149–1171.

Li, T., M. F. Cai, S. Zhang, and L. Sun (2004). Highlight on threats from mining-induced earthquakes. In *Proceedings of the 1st International Forum for City Earthquake Prevention and Disaster Mitigation*, pp. 114–123.

Li, Z., L. Dou, C. Lu, Z. Mu, and A. Cao (2008). Study on fault induced rock bursts. *J. China Uni. Min. Tech. 18*, 321–326.

Linkov, A. M. (1996). Rockbursts and the instability of rock masses. *Int. J. Rock Mech. Min. Sci. 33*(7), 727–732.

Lobo-Guerrero, S. and L. E. Vallejo (2005). Discrete element method evaluation of granular crushing under direct shear test conditions. *J. Geotech. Geoenviron. 131*(10), 1295–1300.

Lu, Y. B., Q. M. Li, and G. W. Ma (2010). Numerical investigation of the dynamic compressive strength of rocks based on split hopkinson pressure bar tests. *Int. J. Rock Mech. Min. Sci. 47*, 829–838.

Ma, G. W., X. J. Wang, and F. Ren (2011). Numerical simulation of compressive failure of heterogeneous rock-like materials using sph method. *Int. J. Rock Mech. Min. Sci. 48*(3), 353–363.

Madden, B. J. (1987). Coal pillar design-can increased extraction be achieved safely? In *Mine Safety and Health Congress*, Johannesburg.

Maleki, H. and B. White (1997). Geotechnical factors influencing violent failure in u.s. mines. In E. Broch, A. Myrvang, and G. Stjern (Eds.), *Proceedings of International Symposium on Rock Support: Applied Solution for Underground Structures*, pp. 208–221.

MasIvars, D., M. E. Pierce, C. Darcel, J. Reyes-Montes, D. O. Potyondy, R. P. Young, and P. A. Cundall (2011). The synthetic rock mass approach for jointed rock mass modeling. *Int. J. Rock Mech. Min. Sci. 48*, 219–244.

McGarr, A., S. M. Spottiswoode, and N. C. Gay (1975). Relationship of mine tremors to induced stresses and to rock properties in the focal region. *Bull. Seismol. Soc. Am. 65*, 981–993.

Milev, A. M., S. M. Spottiswoode, A. J. Rorke, and G. J. Finnie (2001). Seismic monitoring of a simulated rockburst on a wall of an underground tunnel. *J. South Afr. Int. Min. and Metallurgy*, 253–260.

Muller, W. (1991). Numerical simulation of rock bursts. *Min. Sci. Technol. 12*(1), 27–42.

Ortlepp, W. D. (2005). Keynote lecture: Rasim comes of age-a review of the contribution to the understanding and control of mine rockbursts. In Y. Potvin and M. Hudyma (Eds.), *Controlling Seismic Risk: Sixth International Symposium on Rockburst and Seismicity in Mines proceedings*, Australia. Australian Centre for Geomechanics.

Ortlepp, W. D. and T. R. Stacey (1994). Rockburst mechanisms in tunnels and shafts. *Tunn. Undergr. Sp. Tech. 9*(1), 59–65.

Pan, Y. and A. Li (2010). Fold catastrophe model of strike-slip fault earthquake. *Applied Mathematics and Mechanics (English Version) 31*(3), 349–362.

Pan, Y., A. Li, and Y. Qi (2009). Fold catastrophe model of dynamic pillar failure in asymmetric mining. *Min. Sci. Technol. 19*, 49–57.

Pan, Y., Y. Zhang, and G. Yu (2006). Mechanism and catastrophe theory analysis of circular tunnel rockburst. *Applied Mathematics and Mechanics (English Version) 27*(6), 841–852.

Pan, Y. S., Z. H. Li, and M. T. Zhang (2003). Distribution, type, mechanism and prevention on rockburst in china. *Chinese Journal of Rock Mechanics and Engineering 22*(11), 1844–1851.

Papaliangas, T., S. R. Hencher, A. C. Lumsden, and S. Manolopoulou (1993). The effect of frictional fill thickness on the shear strength of rock discontinuities. *Int. J. Rock Mech. Min. Sci. 30*(2), 81–91.

Park, E. S., C. D. Martin, and R. Christiansson (2004). Simulation of the mechanical behavior of discontinuous rock masses using a bonded-particle model. In *Gulf Rocks 2004, the 6th North America Rock Mechanics Symposium (NARMS)*, Number 04-480, Houston, Texas.

Park, J. W. and J. J. Song (2009). Numerical simulation of a direct shear test on a rock joint using a bonded-particle model. *Int. J. Rock Mech. Min. Sci. 46*, 1315–1328.

Peng, S. and A. M. Johnson (1972). Crack growth and faulting in cylindrical specimens of chelmsford granite. *Int. J. Rock Mech. Min. Sci. 9*, 37–86.

Peng, S. S. (1973). Time dependent aspects of rock behavior as measured by a servo-controlled hydraulic testing machine. *Int. J. Rock Mech. Min. Sci. 10*, 235–246.

Peng, S. S. and H. S. Chiang (1984). *Longwall Mining*. Department of Mining Engineering, College of Mineral and Energy Resources, West Virginia University.

Pietruszczak, S. and Z. Mroz (1980). Numerical analysis of elastic-plastic compression of pillars accounting for material hardening and softening. *Int. J. Rock Mech. Min. Sci. 17*, 199–207.

Qian, Q. and X. Zhou (2011). Quantitative analysis of rockburst for surrounding rocks and zonal disintegration mechanism in deep tunnels. *J. Rock Mech. Geotech. Eng. 3*(1), 1–9.

Qin, S., J. J. Jiao, C. A. Tang, and Z. Li (2006). Instability leading to coal bumps and non-linear evolutionary mechanisms for a coal-pillar-and-roof system. *Int. J. Solids Struct. 43*, 7407–7423.

Qin, S., J. J. Jiao, S. Wang, and H. Long (2001). A nonlinear catastrophe model of instability of planar-slip slope and chaotic dynamical mechanisms of its evolutionary process. *Int. J. Solids Struct. 38*, 8093–8109.

Rice, J. R. (1983). Constitutive relations for fault slip and earthquake instabilities. *Pageoph. 121*, 443–475.

Ryder, J. A. (1988). Excess shear stress in the assessment of geologically hazardous situations. *J. South Afr. Int. Min. and Metallurgy 88*(1), 27–39.

Sainsbury, B., M. Pierce, and D. MasIvars (2008). Simulation of rock mass strength anisotropy and scale effects using a ubiquitous joint rock mass (ujrm) model. In Hart, Detourmay, and Cundall (Eds.), *Continuum and Distinct Element Numerical Modeling in Geo-Engineering*, Number 06-02.

Salamon, M. D. G. (1974). Rock mechanics of underground excavations. In *Proc. 3rd Cong. Int. Soc. Rock. Mech.*, pp. 951–1099.

Salamon, M. D. G., J. A. Ryder, and N. C. Officer (1964). Elastic analysis of displacements and stresses induced by mining of seam or reef deposits. *The South African Institute of Mining Metallurgy*.

Schneider, H. J. (1976). The friction and deformation behavior of rock joint. *J. Rock Mech. 8*, 169–184.

Scholz, C. H., P. Molnar, and T. Johnson (1972). Detailed studies of frictional sliding in granite and implications for earthquake mechanism. *J. Geophys. Res. 77*, 6392–6406.

Shi, G. H. and R. E. Goodman (1984). Discontinuous deformation analysis. In *Proceedings of the 25th U.S. Symposium on Rock Mechanics*, pp. 269–277.

Shi, Z., Z. Luo, D. Peng, and Z. He (1996). Application of catastrophe theory to the analyses of mechanism of faulting movement. *J. Xi'an Eng. Uni.* (1-8).

Shimizu, H., T. Koyama, T. Ishida, M. Chijimatsu, T. Fujita, and S. Nakama (2010). Distinct element analysis for class ii behavior of rocks under uniaxial compression. *Int. J. Rock Mech. Min. Sci. 47*, 323–333.

Simon, R. (1999). *Analysis of fault-slip mechanisms in hard rock mining*. Ph. D. thesis, Department of Mining and Metallurgical Engineering, McGill University, Montreal, Canada.

Spottiswoode, S. M. (1990). Volume excess shear stress and cumulative seismic moments. In Fairhurst (Ed.), *Rockbursts and Seismicity in Mines*, Balkema, pp. 39–43.

Stiller, H., E. Hurtig, H. Grosser, and P. Knoll (1983). On the nature of mining tremors. *J. Earthq. Pred. Res. 2*(57-67).

Sun, J., Q. Zhu, and W. Lu (2007). Numerical simulation of rock burst in circular tunnels under unloading conditions. *J. China Uni. Min. Tech. 17*(4), 552–556.

Tang, C. A. (1997). Numerical simulation of progressive rock failure and associated seismicity. *Int. J. Rock Mech. Min. Sci. 34*, 249–262.

Tang, C. A. and S. Q. Kou (1998). Crack propagation and coalescence in brittle materials under compression. *Eng. Fract. Mech. 61*, 311–324.

Vacek, J., J. Vacek, and J. Chocholousova (2008). Rock burst mechanics: insight form physical and mathematical modeling. *Acta Polytechnica 48*(6), 38–44.

Wang, S. Y., K. C. Lam, S. K. Au, C. A. Tang, W. C. Zhu, and T. H. Yang (2006). Analytical and numerical study on the pillar rockbursts mechanism. *Rock Mech. Rock Eng. 39*(5), 445–467.

Wang, S. Y., S. W. Sloan, M. L. Huang, and C. A. Tang (2011). Numerical study of failure mechanism of serial and parallel rock pillars. *Rock Mech. Rock Eng. 44*, 179–198.

Wang, Y. and F. Tonon (2009). Modeling triaxial test on intact rock using discrete element method with membrane boundary. *J. Eng. Mech. 135*(9), 1029–1037.

Wang, Z., L. Zhang, and H. Guo (2011). Catastrophe theory analysis on asymmetric mining pillar dynamic failure. *Applied Mathematics and Materials 71-78*, 4662–4667.

Wawersik, W. R. and C. A. Fairhurst (1970). A study of brittle rock fracture in laboratory compression experiments. *Int. J. Rock Mech. Min. Sci. 7*, 561–575.

Whyatt, J. K., W. Blake, T. J. Williams, and B. G. White (2002). Sixty years of rockbursting in the coeur d' alene district of northern idaho, usa: lessons learned and remaining issues. In *Proceedings of the 109th Annual Exhibit and Meeting, Society for Mining, Metallurgy, and Exploration*, Volume 2, Phoenix, AZ, pp. 164–174.

Whyatt, J. K. and M. C. Loken (2009). Coal bumps and odd dynamic phenomena – a numerical investigation. In *The 28th International Conference on Ground Control in Mining*, Morgantown, WV, pp. 175–180.

Yacoub, T. E. and J. H. Curran (1999). Analysis of post-peak pillar behavior using the enhanced displacement discontinuity method. In Amadei, Kranz, Scott, and Smeallie (Eds.), *Rock Mechanics for Industry*, pp. 169–176.

Yan, F., X. Feng, R. Chen, K. Xia, and C. Jin (2012). Dynamic tensile failure of the rock interface between tuff and basalt. *Rock Mech. Rock Eng. 45*(3), 341–348.

Zou, D., H. D. S. Miller, and P. K. Kaiser (1989). Numerical study of violent rock failure by stick-slip on joints. *Min. Sci. Technol. 9*, 241–251.

APPENDIX A - THE IMPORTANT FORMULATIONS AND THE PARAMETERS OF THE CY JOINT MODEL

In the CY joint model, the relationship between incremental normal stress and normal displacement is expressed as

$$\triangle\sigma_n = k_n \triangle\mu_n \tag{A.1}$$

where k_n is the normal stiffness. In this study, the normal stiffness of a discontinuity is defined as the ratio of applied normal stress to normal displacement and it has a unit of Pa/m. The normal stiffness k_n is given by

$$k_n = a_n \sigma_n^{e_n} \tag{A.2}$$

to simulate the observed increase of stiffness with increase in normal stress, where a_n and e_n are input parameters of the joint model.

The response to shear loading exhibits irreversible, nonlinear behavior from the onset of shearing. Figure 3.1 shows a typical shear stress-displacement curve for monotonic loading under a constant normal stress. The shear stress increment is taken as

$$\triangle\tau = F k_s \triangle u_s \tag{A.3}$$

where the shear stiffness k_s can also be expressed as a function of normal stress

$$k_s = a_s \sigma_n^{e_s} \tag{A.4}$$

The tangent modulus is governed in A.3 by the factor F, which depends on the distance from the actual stress curve to the "target" or bounding strength curve τ_m, as shown in Figure 3.1

$$F = \frac{(1 - \frac{\tau}{\tau_m})}{1 - r} \tag{A.5}$$

The factor r, which is initially set to zero, is intended to restore the elastic stiffness immediately after a load reversal by assigning $r = \tau/\tau_m$ (therefore,) whenever $sgn(\triangle u_s)$

is not equal to $sgn(\triangle u_s(old))$ ($sgn(x)$ is the sign function that extracts the sign of a real number). The bounding strength is given by

$$\tau_m = \sigma_n \tan \phi_m sgn(\triangle u_s) \tag{A.6}$$

The parameter ϕ_m can be understood as the friction angle that would apply if the joint were to dilate at the maximum dilation angle. As the damage accumulates, this angle is continuously reduced according to the equation

$$\triangle \phi_m = \frac{1}{R(\phi_m - \phi)\triangle u_s^p} \tag{A.7}$$

where the plastic displacement increment is defined as

$$\triangle u_s^p = (1 - F) \left| \triangle u_s \right| \tag{A.8}$$

and ϕ is the basic or intrinsic friction angle (residual friction angle) of the rock surface. R is a material parameter which expresses the joint roughness with dimension of length.

Nine input parameters are introduced through A.1 to A.8: a_n, e_n, k_n, a_s, e_s, k_s, ϕ_m, ϕ, and R. Conceptualization and experimental determination of the first eight parameters exhibits no difficulty. However, the roughness parameter R needs to be defined in formal detail for its experimental determination. The CY joint model does not explicitly consider the scale effect of discontinuities. Nevertheless, the length scale defined by the roughness parameter R may sufficiently represent the scale effect (Board, 1989).

Table A.1: Parameters of the CY joint model.

Parameter	Description
a_n	Joint normal stiffness (input)
e_n	Joint normal stiffness exponent (input)
a_s	Joint shear stiffness (input)
e_s	Joint shear stiffness exponent (input)
R	Joint roughness parameter (input)
$\phi_m^{(i)}$	Joint initial friction angle
ϕ	Intrinsic friction angle (input)
ϕ_m	Effective friction angle (input)
k_n	Normal stiffness defined as a function of σ_n (input)
k_s	Shear stiffness defined as a function of σ_n (input)
τ	Shear stress on the joint
τ_m	Failure or "bounding" shear stress
$\triangle u_s$	Current shear displacement increment
$\triangle u_s^{(old)}$	Previous shear displacement increment
u_s^p	Accumulated plastic shear displacement
r	The stress ratio at the last reversal ($r = 0$, initially)
i	Effective dilation angle

APPENDIX B - VALIDATION OF STRESS STATE FOR DISCONTINUITY STABILITY MODEL

The vertical stress, horizontal stress and shear stress distributions in the discontinuity stability analysis model with the chosen boundaries (i.e. a width of 140 m and a height of 160 m) and fully excavated area are shown in Figure B.1, Figure B.2 and Figure B.3, respectively. For vertical stress and horizontal stress, positive values indicate tension, and negative values indicate compression. The in-situ stress field in the model was taken as vertical and horizontal stresses being principal stresses with magnitudes of 17.5 and 5.25 MPa, respectively.

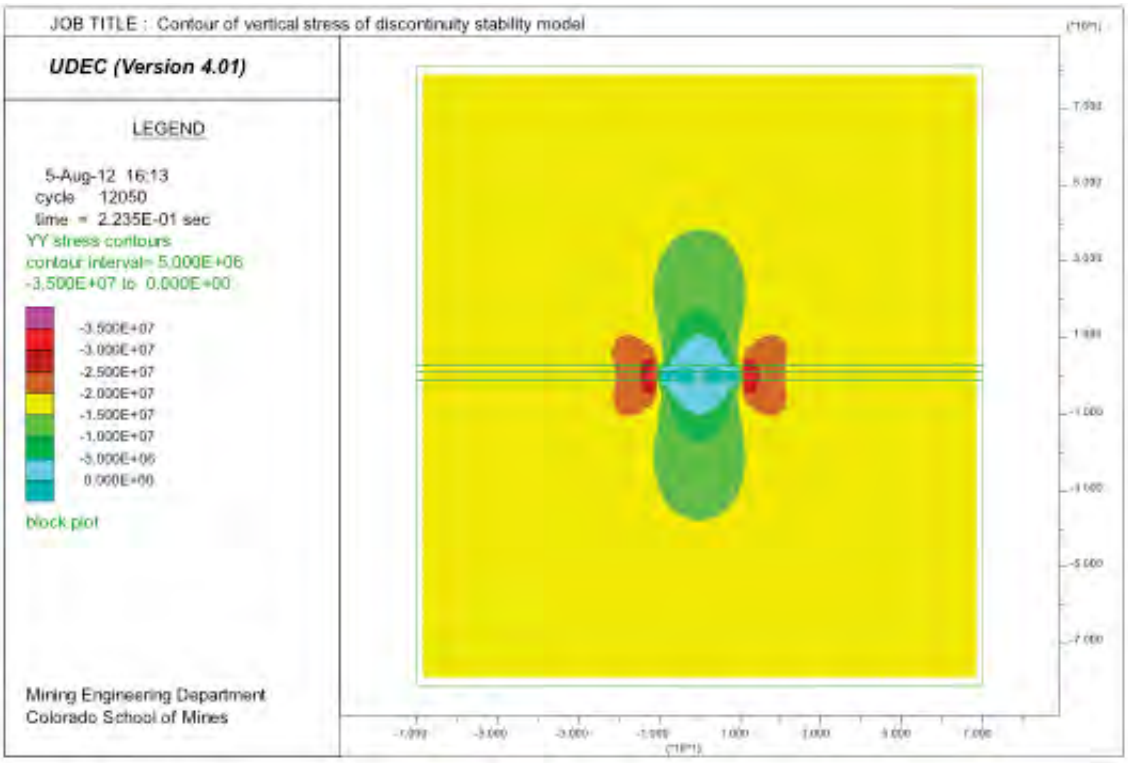

Figure B.1: Contour of vertical stress in the model for stability analysis of the discontinuity.

Figure B.1shows the vertical stress distribution in the fully excavated model. The vertical stresses above and below the excavation area are less than in-situ stress, and that at the sides

of the excavation are larger than in-situ stress. The rest of the areas in the model are in the in-situ stress field.

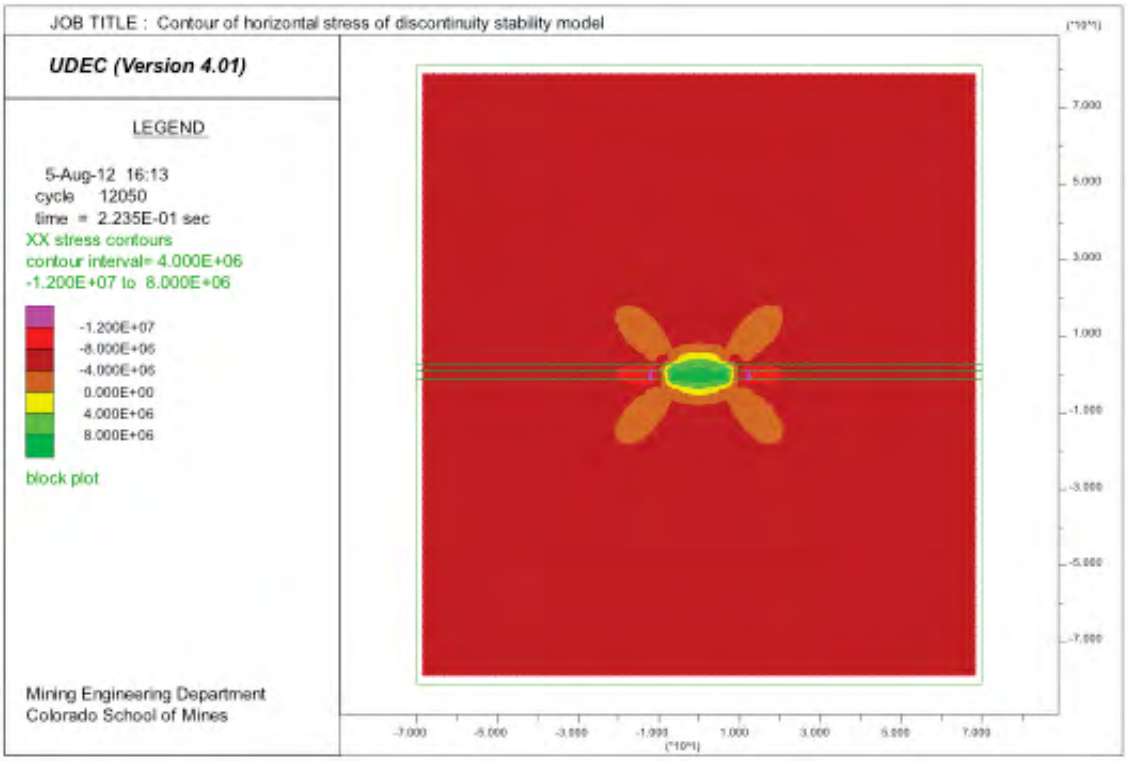

Figure B.2: Contour of horizontal stress in the model for stability analysis of the discontinuity.

Figure B.2shows the the horizontal stress distribution in the model. The horizontal stresses at the sides of the excavation are larger than the in-situ stress due to the excavated area, and that at the corners of the excavation (i.e. lobed regions in the figure) are less than the in-situ stress. Tensional stresses are formed at the top and bottom of the excavation area. The horizontal stress remains as the in-situ stress at the rest of the areas in the model.

The distribution of the shear stress in the model is shown in Figure B.3, and the sign convention of positive shear stress is shown in Figure B.4. Higher shear stresses are developed near the corners of the excavation as indicated by the lobed regions in the figure. Away from these regions, the shear stress is in its in-situ state. As shown in Figure B.1, Figure B.2 and Figure B.3, the boundaries of the model determined in the previous tests present no

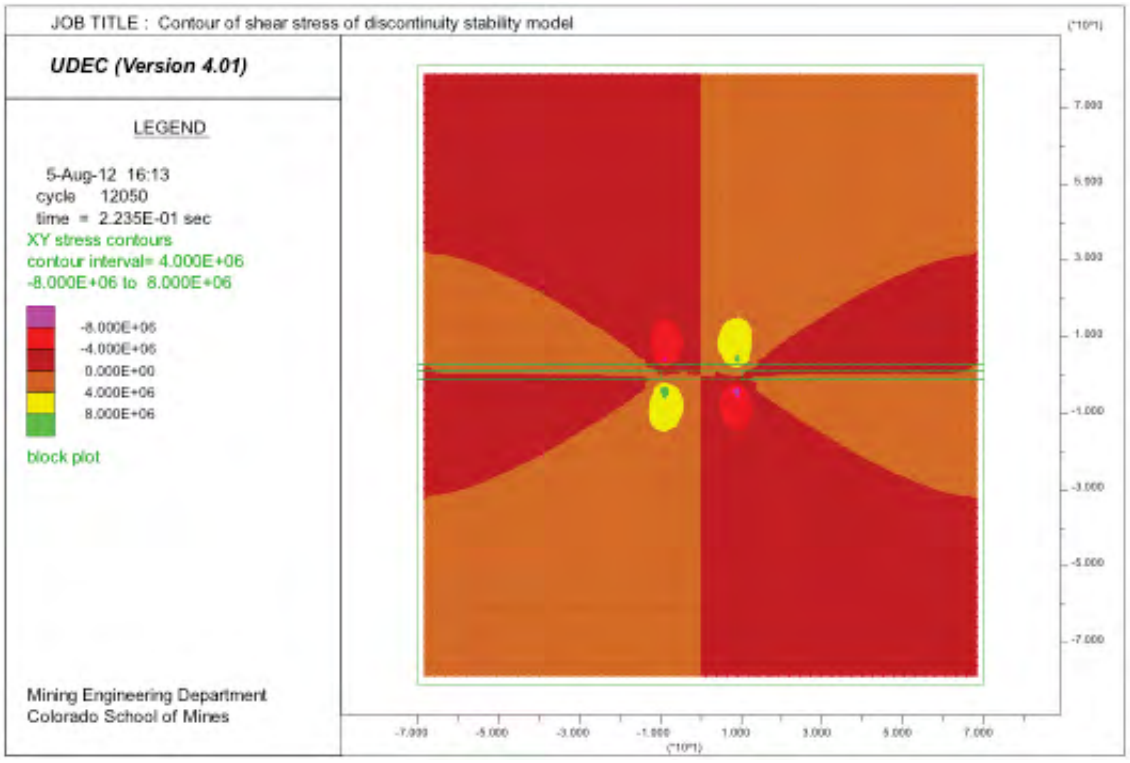

Figure B.3: Contour of shear stress in the model for stability analysis of the discontinuity.

boundary effect on not only loading stiffness but also stress distributions in the model.

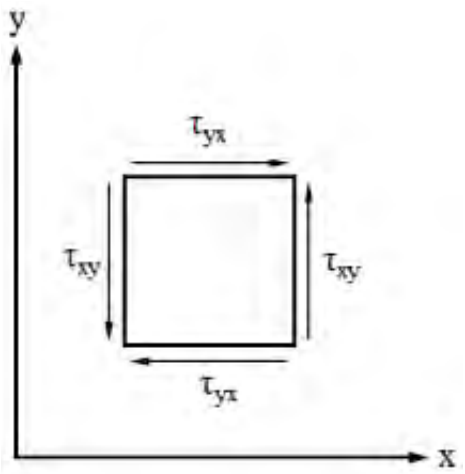

Figure B.4: Sign convention for positive shear stress component.

APPENDIX C - RESULTS OF DE-CONFINEMENT MECHANISM STUDIES

C.1 Results of Simulations with Different Widths of Weak Regions (w_{wr}) and A Constant Barrier Width (w_b) of 0.5 m.

The records of shear stress, shear displacement of the interfaces and normal stress of the coal materials are presented for each simulation.

C.1.1 w_{wr} = 0.0 m.

The normal stress–time curve is shown in Figure C.1.

The shear stress–time curve is shown in Figure C.2.

The shear displacement–time curve is shown in Figure C.3.

The normal stress–time curves of the measurement regions with a constant width is shown in Figure C.4.

The normal stress–time curves of the measurement regions with increased width is shown in Figure C.5.

C.1.2 w_{wr} = 0.5 m.

The normal stress–time curve is shown in Figure C.6.

The shear stress–time curve is shown in Figure C.7.

The shear displacement–time curve is shown in Figure C.8.

The normal stress–time curves of the measurement regions with a constant width is shown in Figure C.9.

The normal stress–time curves of the measurement regions with increased width is shown in Figure C.10.

C.1.3 w_{wr} = 1.0 m.

The normal stress–time curve is shown in Figure C.11.

The shear stress–time curve is shown in Figure C.12.

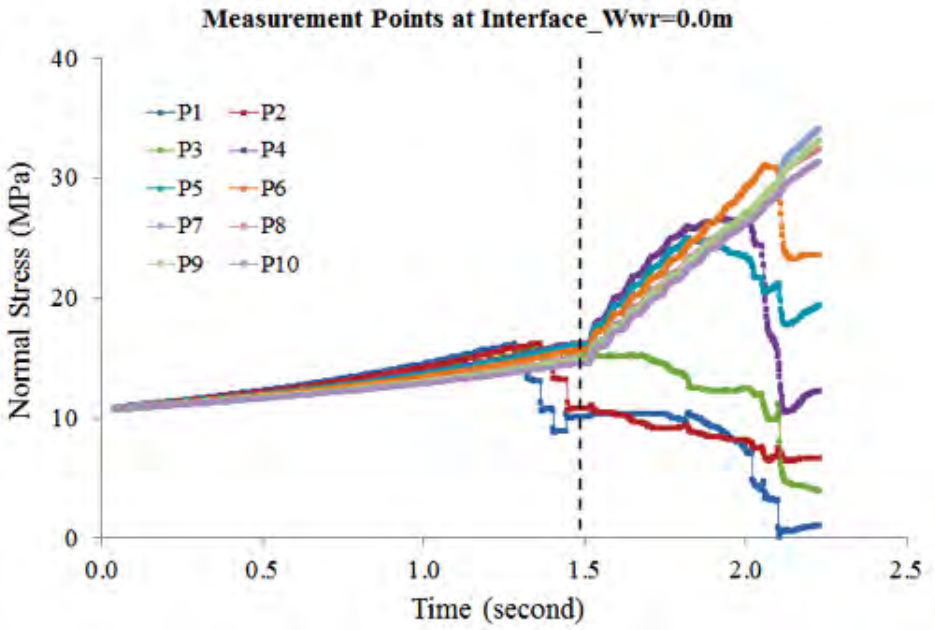

Figure C.1: Normal stress–time curves of the measurement points in WR – w_{wr} simulation with w_{wr} = 0.0 m.

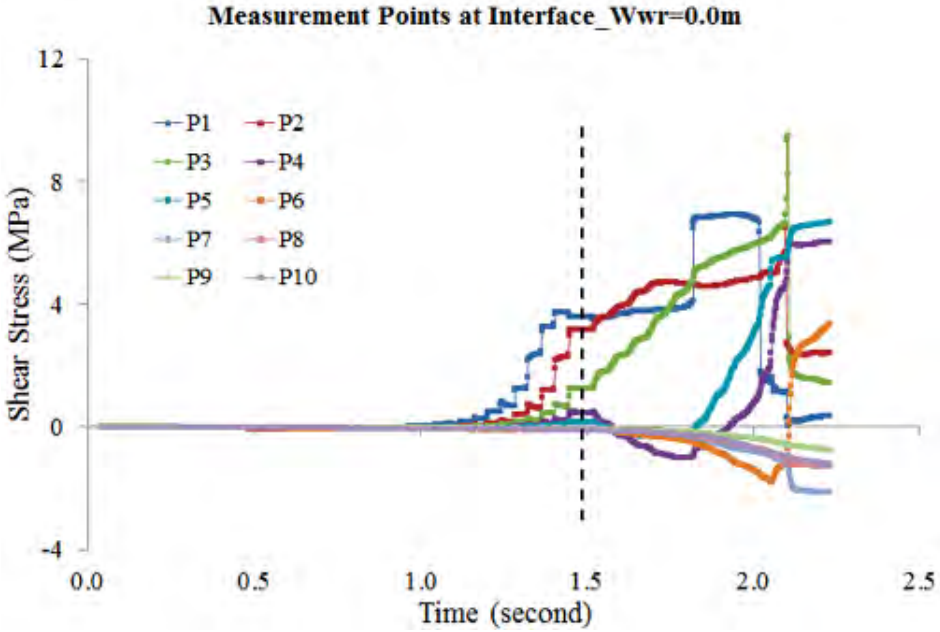

Figure C.2: Shear stress–time curves of the measurement points in WR – w_{wr} simulation with w_{wr} = 0.0 m.

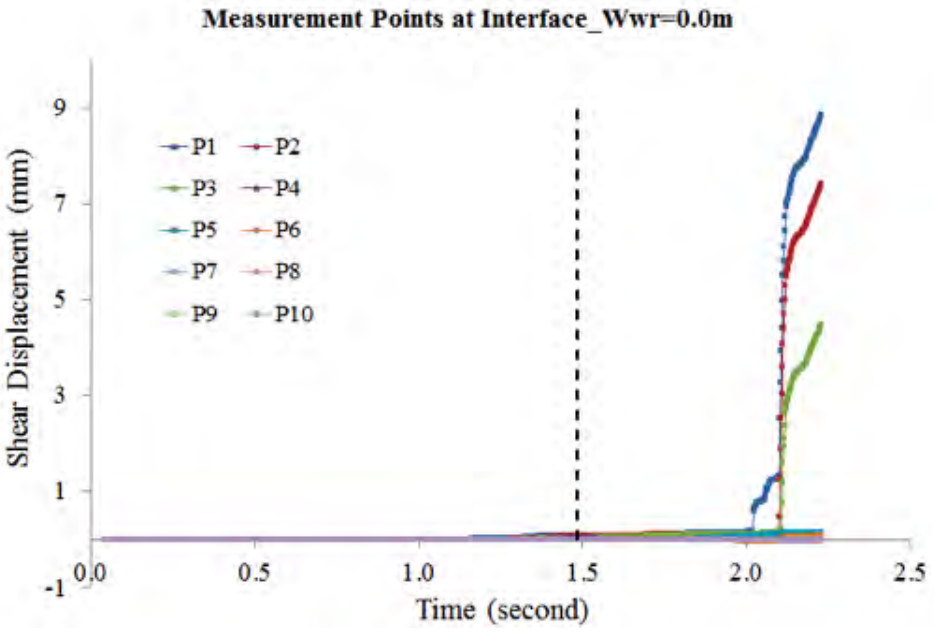

Figure C.3: Shear displacement–time curves of the measurement points in WR – w_{wr} simulation with $w_{wr} = 0.0$ m.

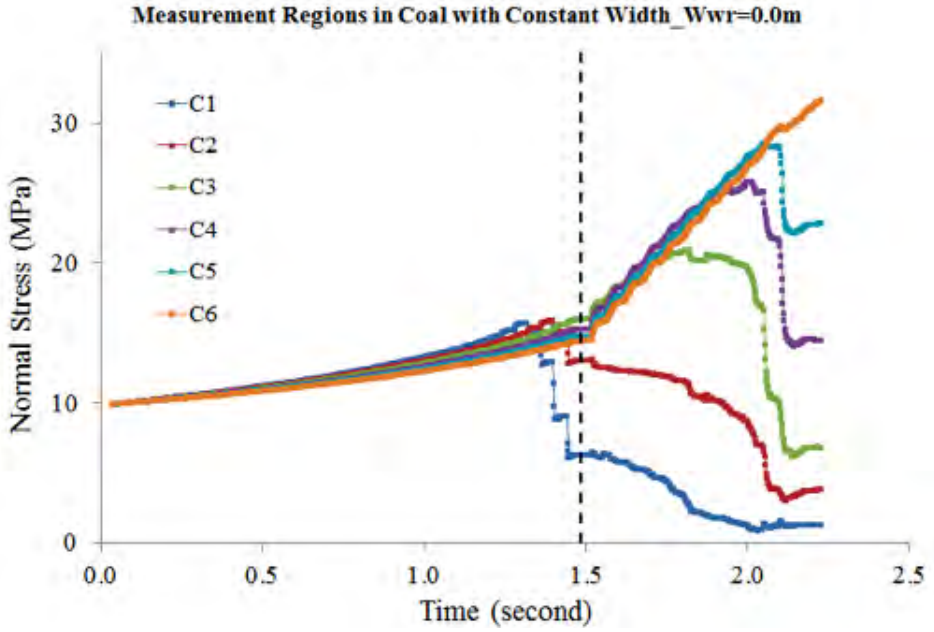

Figure C.4: Normal stress–time curves of the measurement regions with a constant width in WR – w_{wr} simulation with $w_{wr} = 0.0$ m.

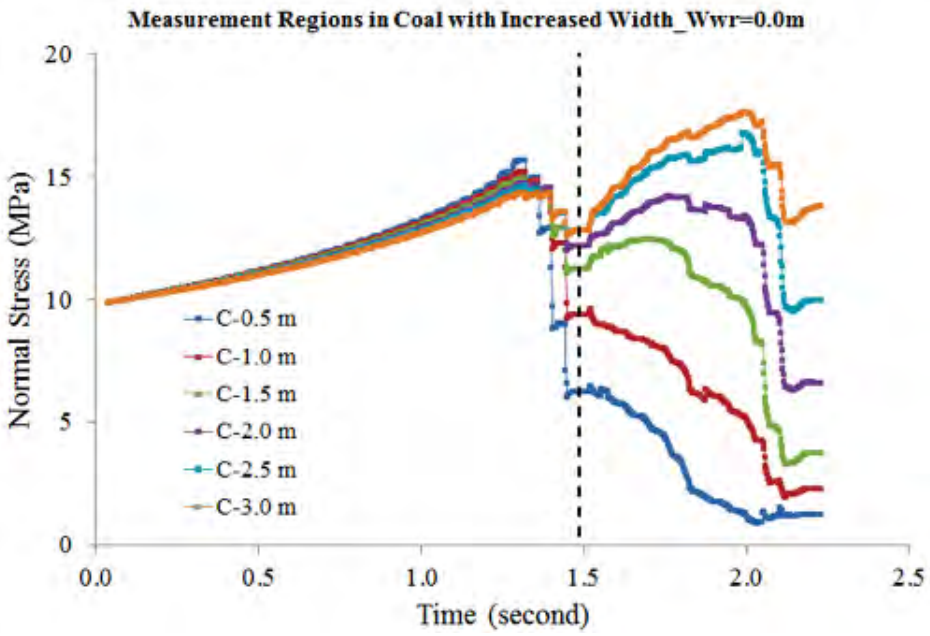

Figure C.5: Normal stress–time curves of the measurement regions with increased widths in WR − w_{wr} simulation with w_{wr} = 0.0 m.

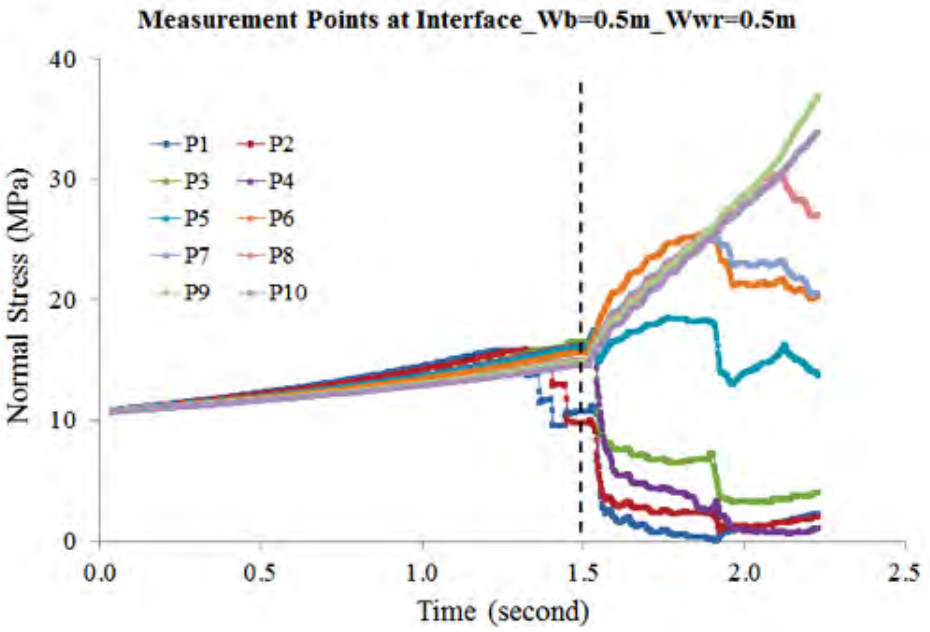

Figure C.6: Normal stress–time curves of the measurement points in WR − w_{wr} simulation with w_{wr} = 0.5 m.

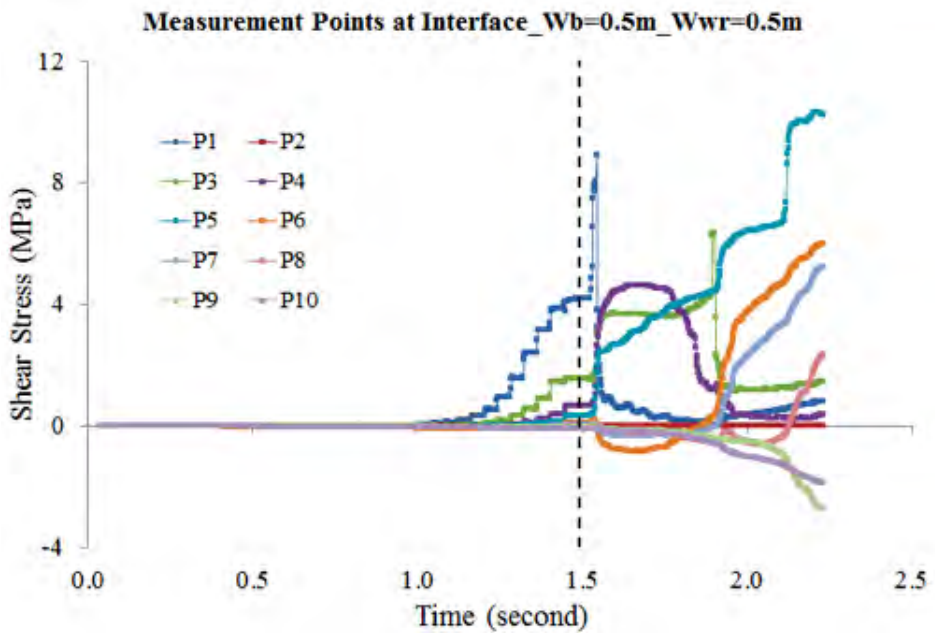

Figure C.7: Shear stress–time curves of the measurement points in WR – w_{wr} simulation with $w_{wr} = 0.5$ m.

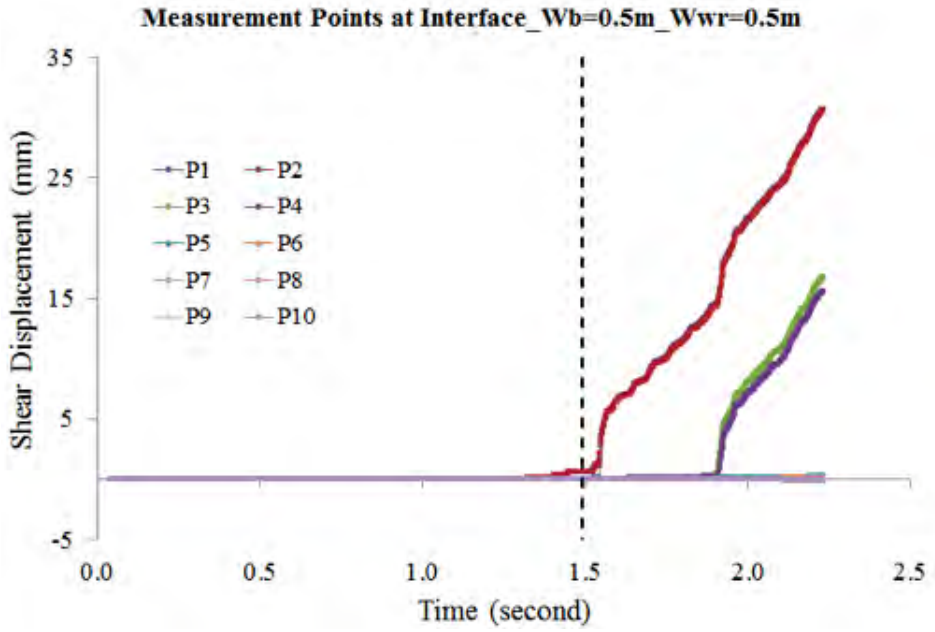

Figure C.8: Shear displacement–time curves of the measurement points in WR – w_{wr} simulation with $w_{wr} = 0.5$ m.

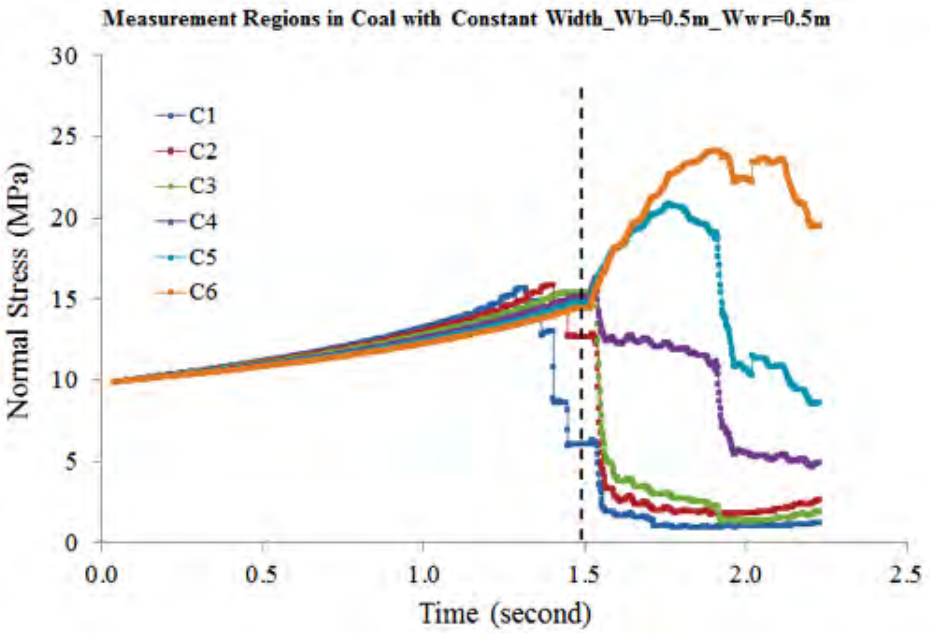

Figure C.9: Normal stress–time curves of the measurement regions with a constant width in WR – w_{wr} simulation with w_{wr} = 0.5 m.

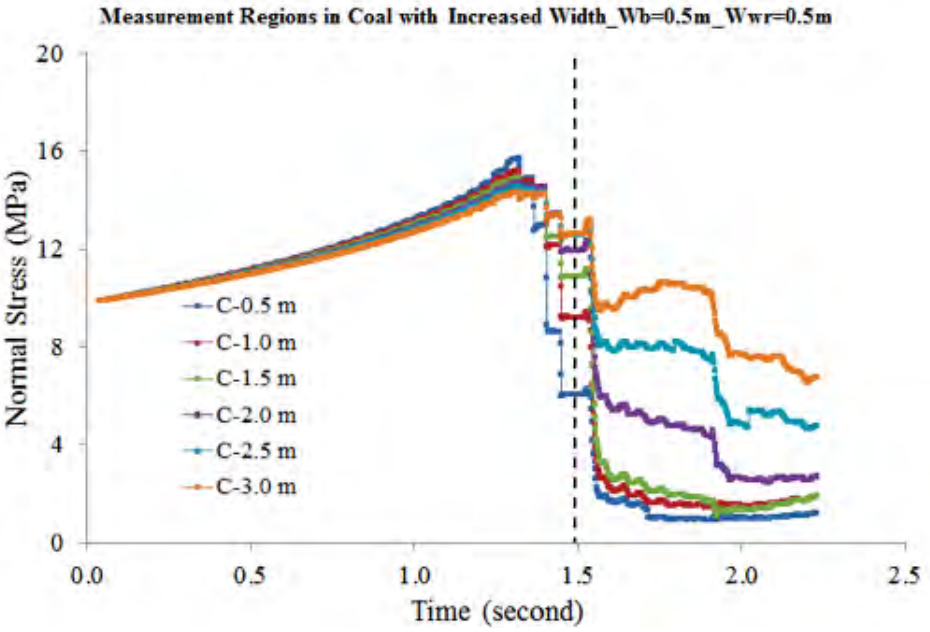

Figure C.10: Normal stress–time curves of the measurement regions with increased widths in WR – w_{wr} simulation with w_{wr} = 0.5 m

The shear displacement–time curve is shown in Figure C.13.

The normal stress–time curves of the measurement regions with a constant width is shown in Figure C.14.

The normal stress–time curves of the measurement regions with increased width is shown in Figure C.15.

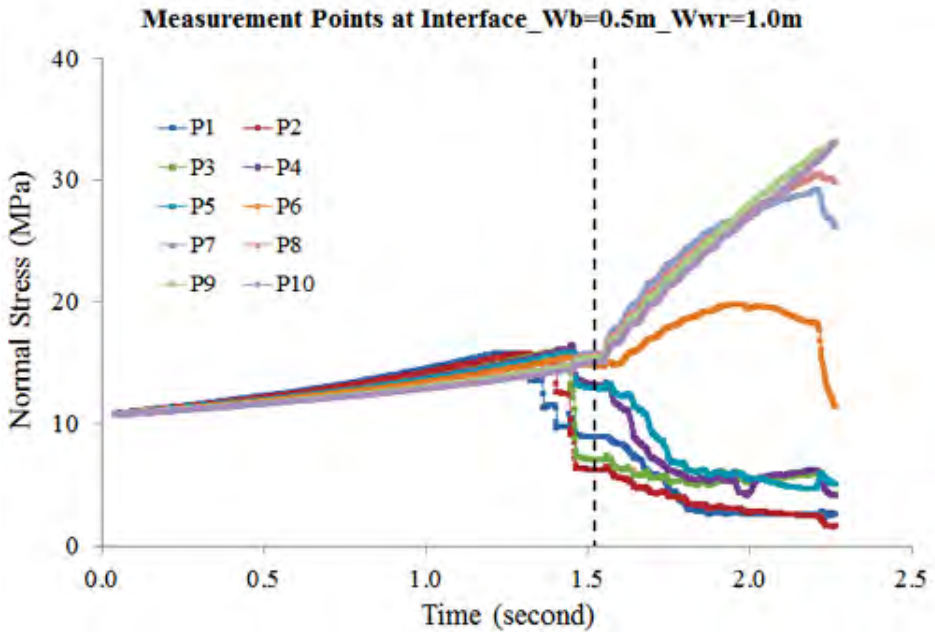

Figure C.11: Normal stress–time curves of the measurement points in WR – w_{wr} simulation with w_{wr} = 1.0 m.

C.1.4 w_{wr} = 1.5 m.

The normal stress–time curve is shown in Figure C.16.

The shear stress–time curve is shown in Figure C.17.

The shear displacement–time curve is shown in Figure C.18.

The normal stress–time curves of the measurement regions with a constant width is shown in Figure C.19.

The normal stress–time curves of the measurement regions with increased width is shown in Figure C.20.

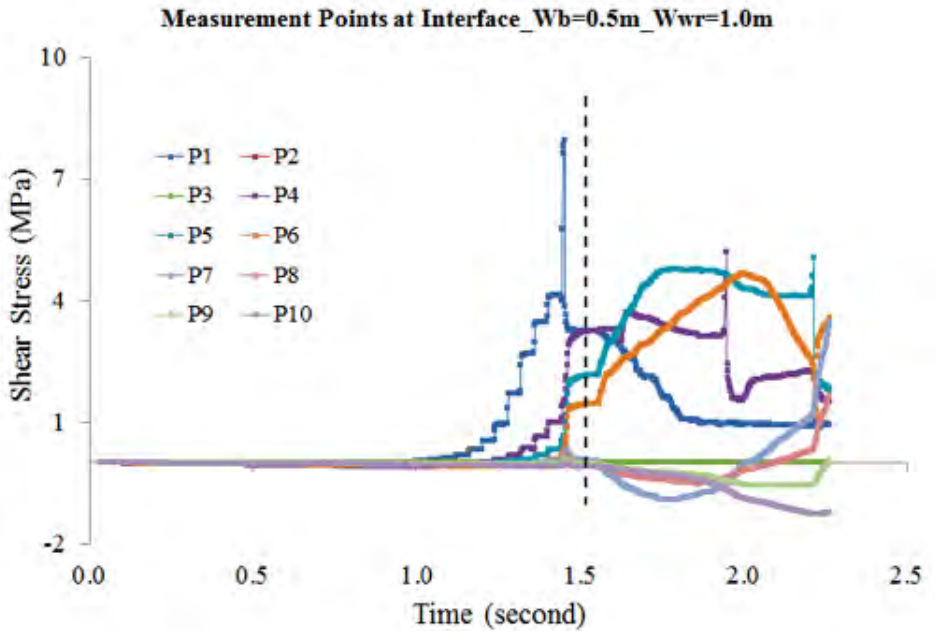

Figure C.12: Shear stress–time curves of the measurement points in WR – w_{wr} simulation with w_{wr} = 1.0 m.

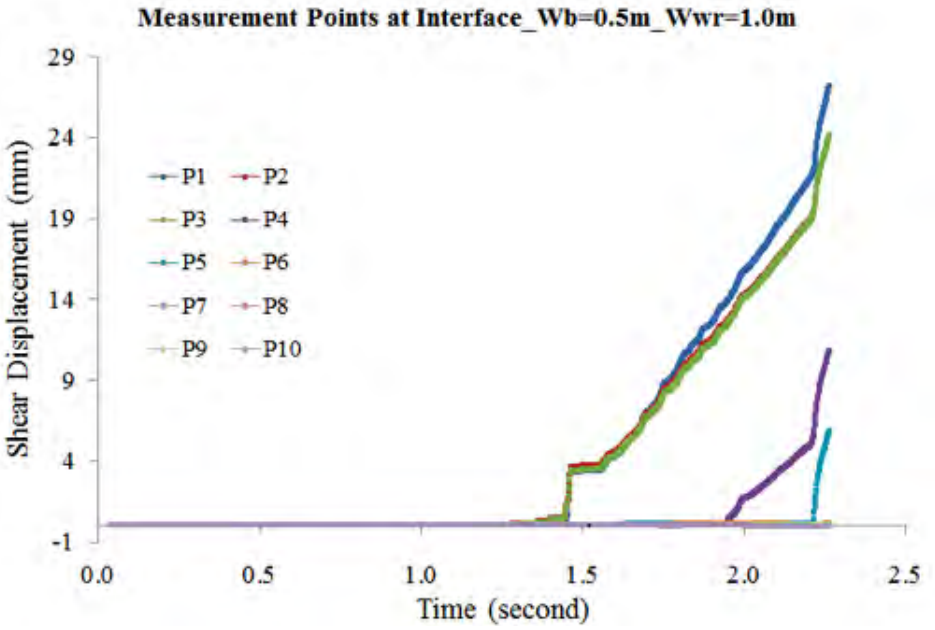

Figure C.13: Shear displacement–time curves of the measurement points in WR – w_{wr} simulation with w_{wr} = 1.0 m.

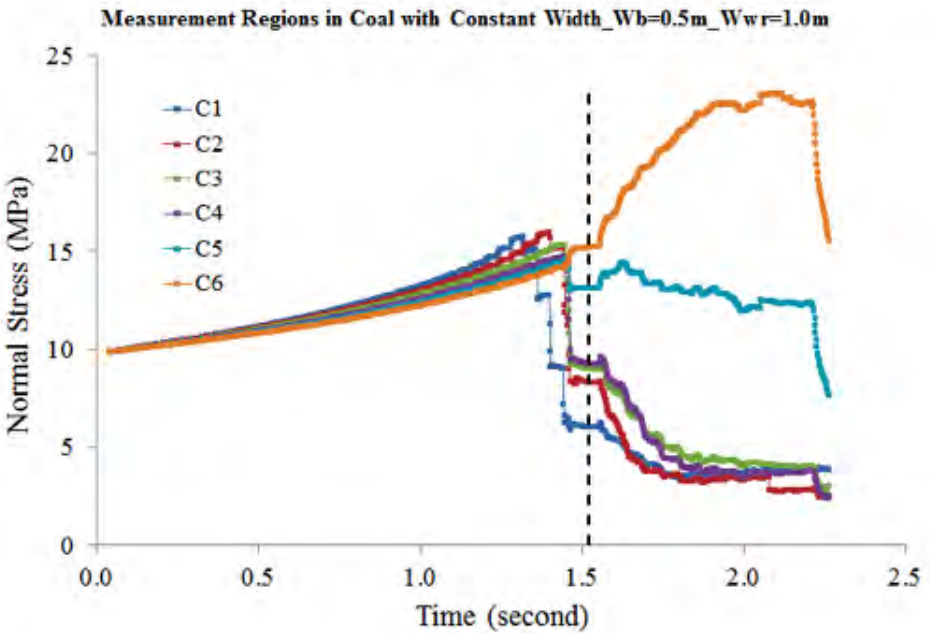

Figure C.14: Normal stress–time curves of the measurement regions with a constant width in WR – w_{wr} simulation with w_{wr} = 1.0 m.

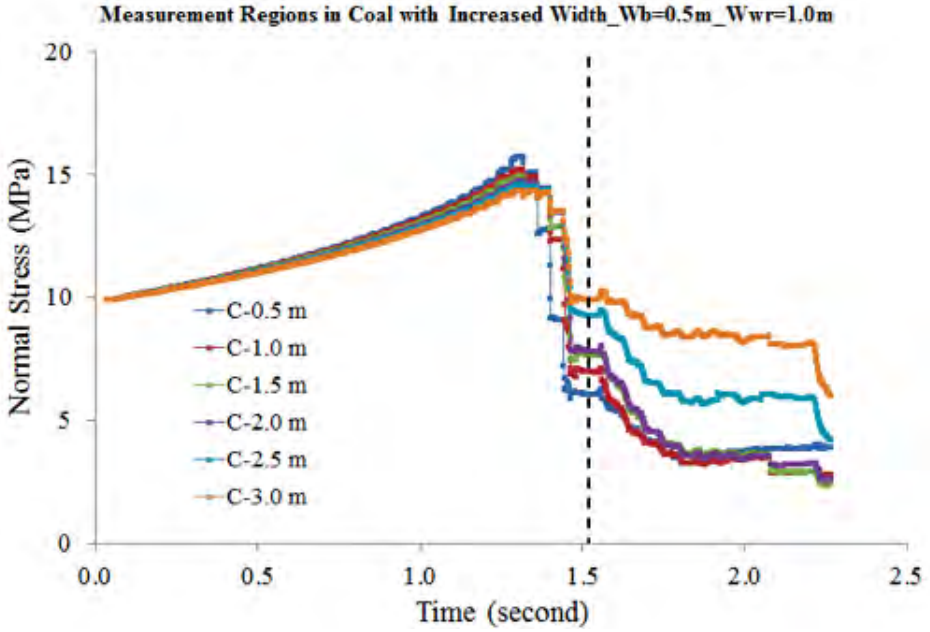

Figure C.15: Normal stress–time curves of the measurement regions with increased widths in WR – w_{wr} simulation with w_{wr} = 1.0 m

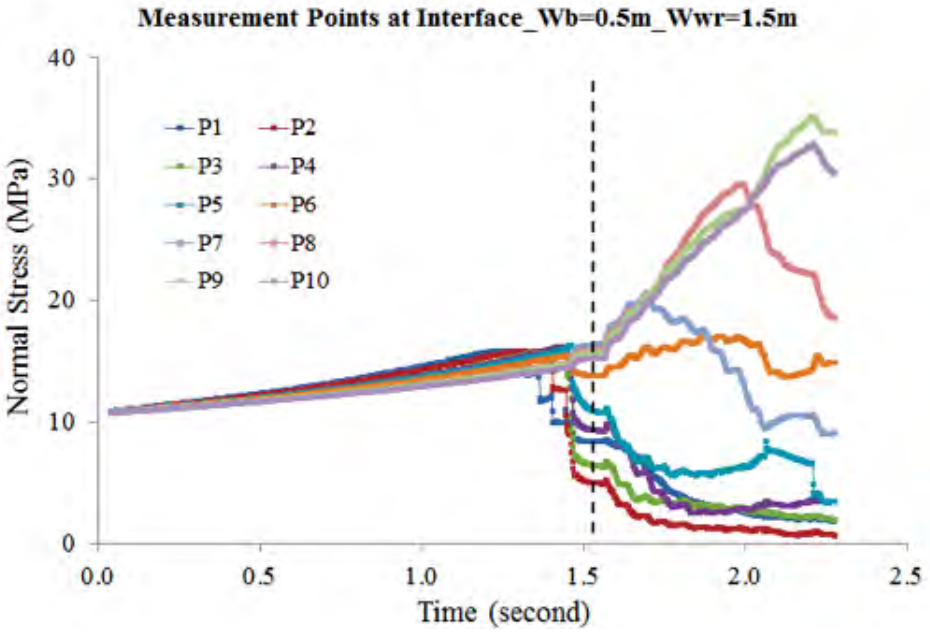

Figure C.16: Normal stress–time curves of the measurement points in WR – w_{wr} simulation with w_{wr} = 1.5 m.

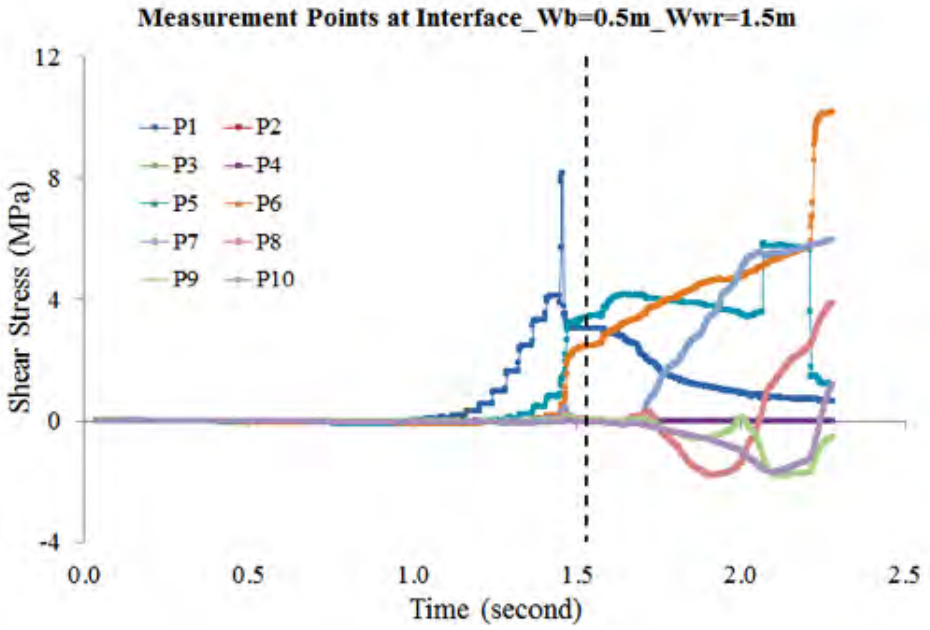

Figure C.17: Shear stress–time curves of the measurement points in WR – w_{wr} simulation with w_{wr} = 1.5 m.

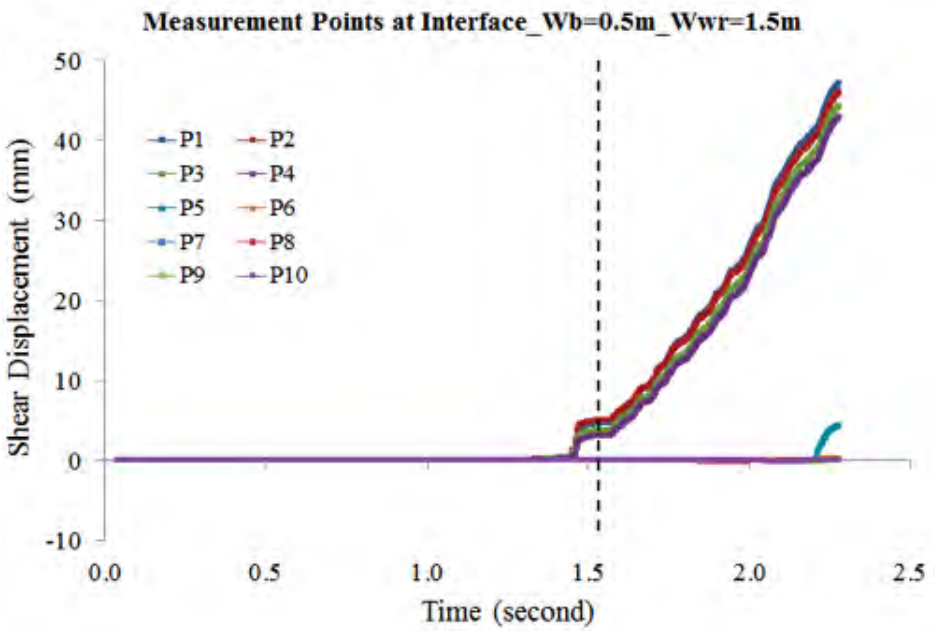

Figure C.18: Shear displacement–time curves of the measurement points in WR – w_{wr} simulation with w_{wr} = 1.5 m.

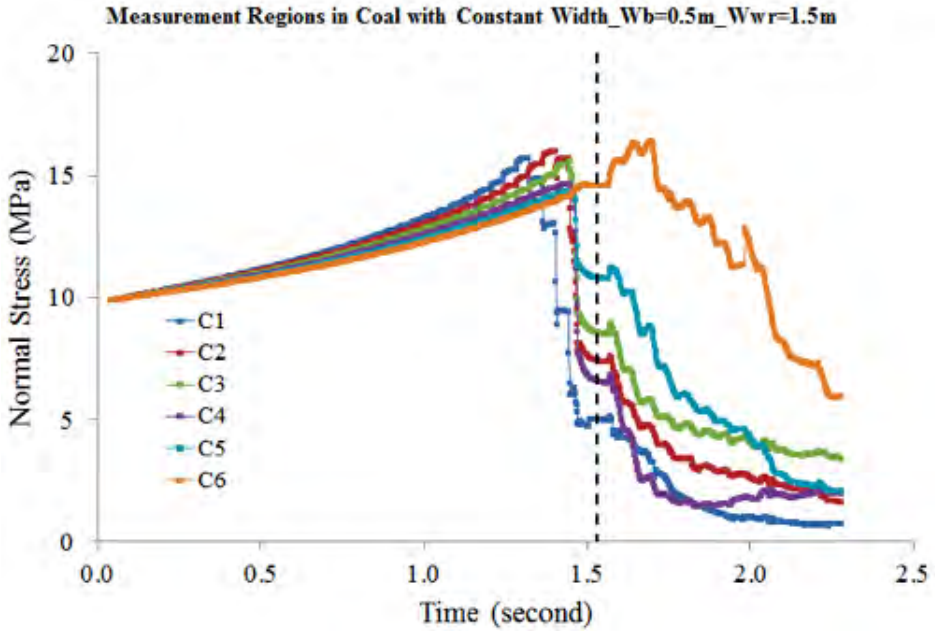

Figure C.19: Normal stress–time curves of the measurement regions with a constant width in WR – w_{wr} simulation with w_{wr} = 1.5 m.

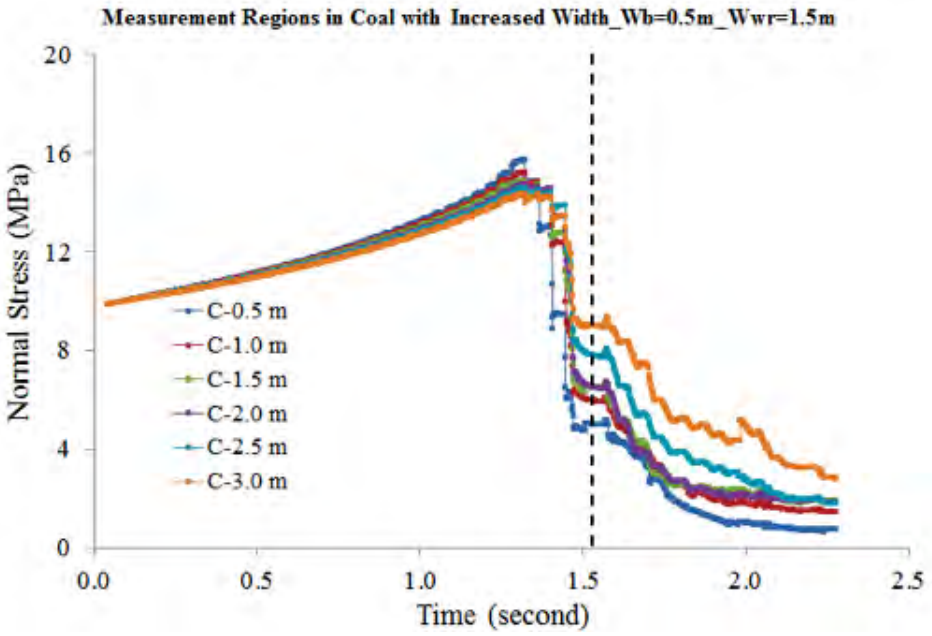

Figure C.20: Normal stress–time curves of the measurement regions with increased widths in WR – w_{wr} simulation with w_{wr} = 1.5 m

C.1.5 w_{wr} = 2.0 m.

The normal stress–time curve is shown in Figure C.21.

The shear stress–time curve is shown in Figure C.22.

The shear displacement–time curve is shown in Figure C.23.

The normal stress–time curves of the measurement regions with a constant width is shown in Figure C.24.

The normal stress–time curves of the measurement regions with increased width is shown in Figure C.25.

C.2 Results of Tests with Different Barrier Widths (w_b) and A Constant Weak Region Width (w_{wr}) of 2.0 m.

The records of shear stress, shear displacement of the interfaces and normal stress of the coal materials are presented for each simulation.

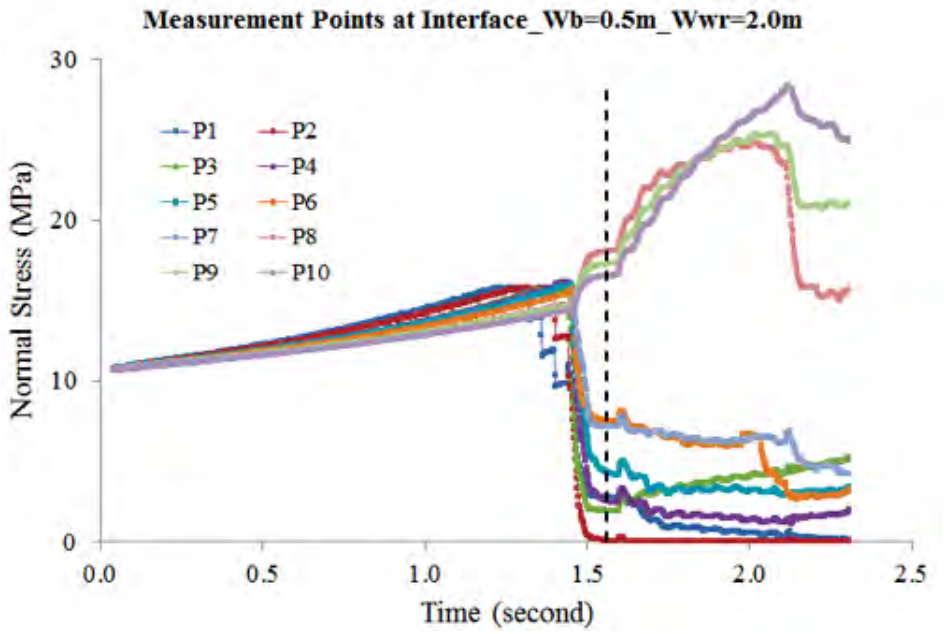

Figure C.21: Normal stress–time curves of the measurement points in WR − w_{wr} simulation with w_{wr} = 2.0 m.

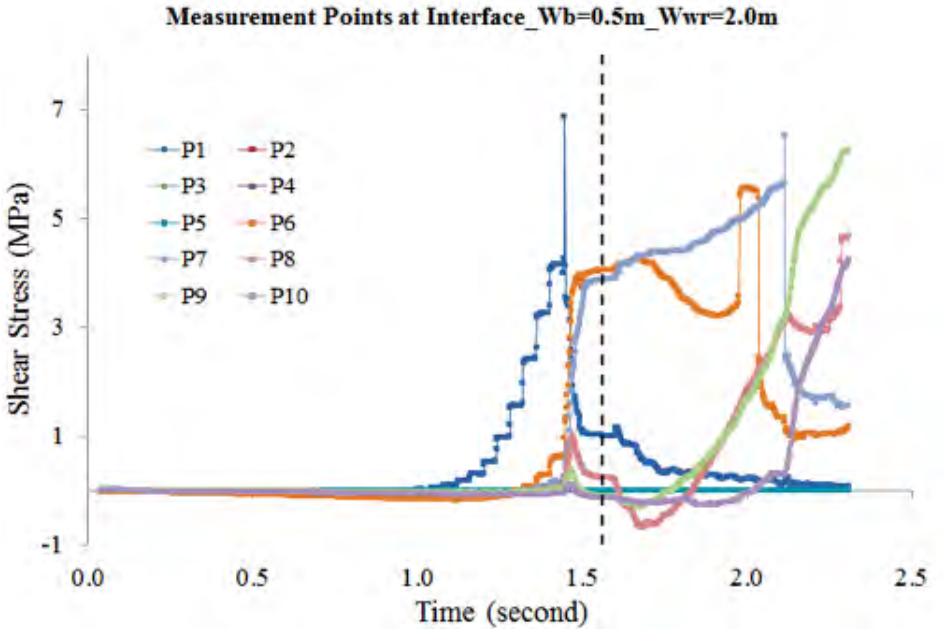

Figure C.22: Shear stress–time curves of the measurement points in WR − w_{wr} simulation with w_{wr} = 2.0 m.

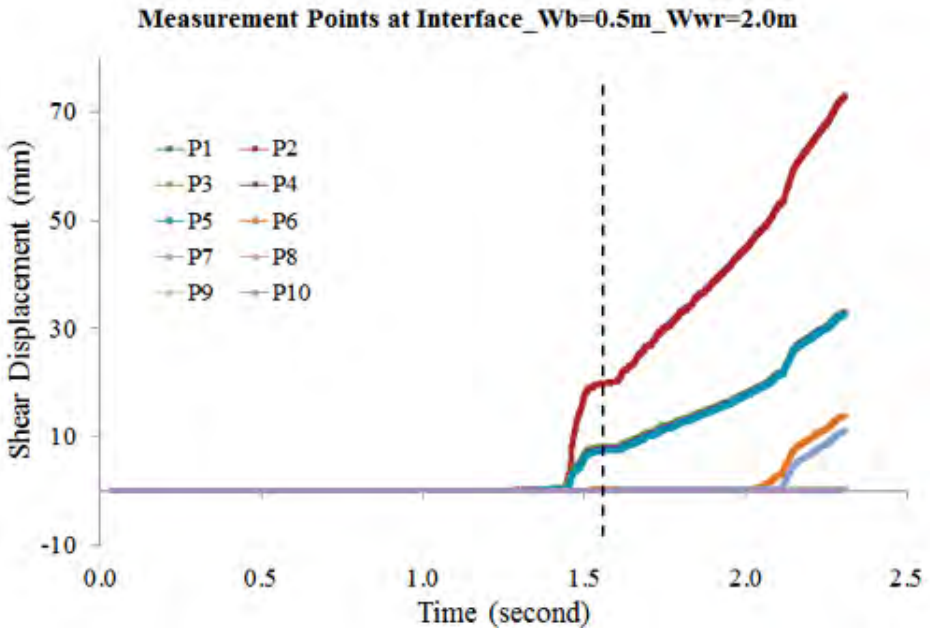

Figure C.23: Shear displacement–time curves of the measurement points in WR – w_{wr} simulation with w_{wr} = 2.0 m.

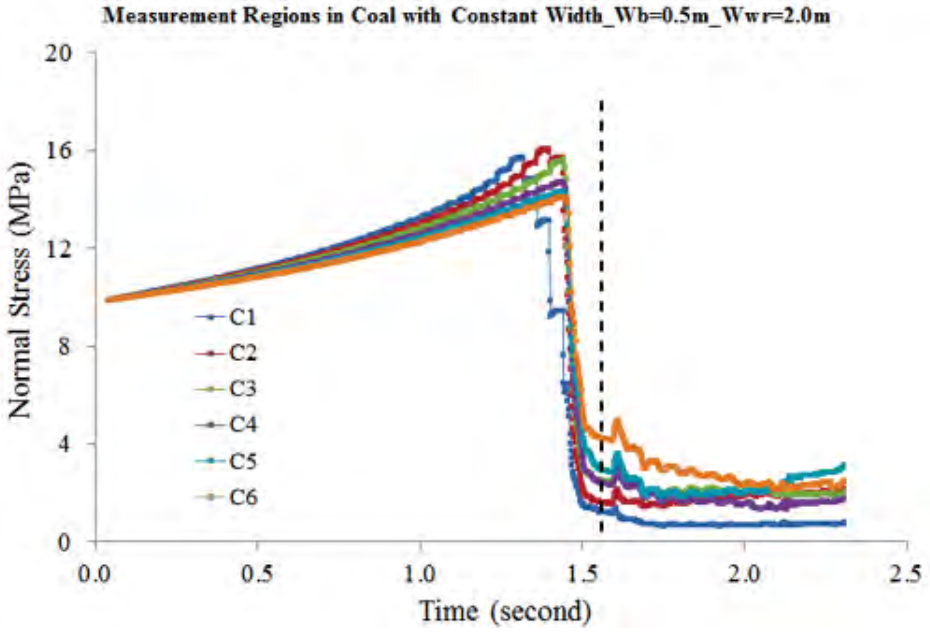

Figure C.24: Normal stress–time curves of the measurement regions with a constant width in WR – w_{wr} simulation with w_{wr} = 2.0 m.

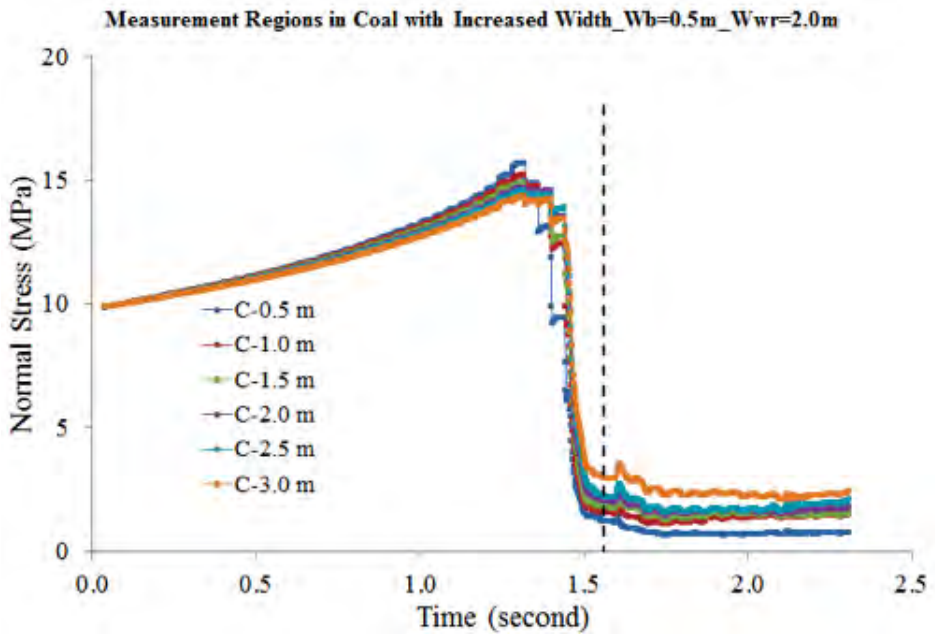

Figure C.25: Normal stress–time curves of the measurement regions with increased widths in WR – w_{wr} simulation with w_{wr} = 2.0 m

C.2.1 w_b = 0.0 m.

The normal stress–time curve is shown in Figure C.26.

The shear stress–time curve is shown in Figure C.27.

The shear displacement–time curve is shown in Figure C.28.

The normal stress–time curves of the measurement regions with a constant width is shown in Figure C.29.

The normal stress–time curves of the measurement regions with increased width is shown in Figure C.30.

C.2.2 w_b = 0.5 m.

The normal stress–time curve is shown in Figure C.31.

The shear stress–time curve is shown in Figure C.32.

The shear displacement–time curve is shown in Figure C.33.

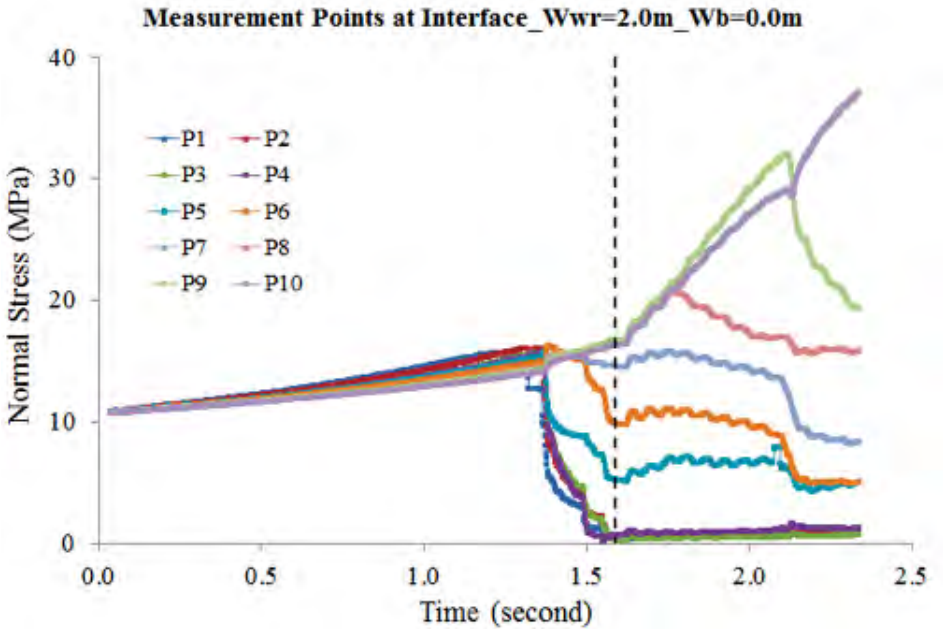

Figure C.26: Normal stress–time curves of the measurement points in WR $-$ w_b simulation with w_{wr} = 2.0 m and w_b = 0.0 m.

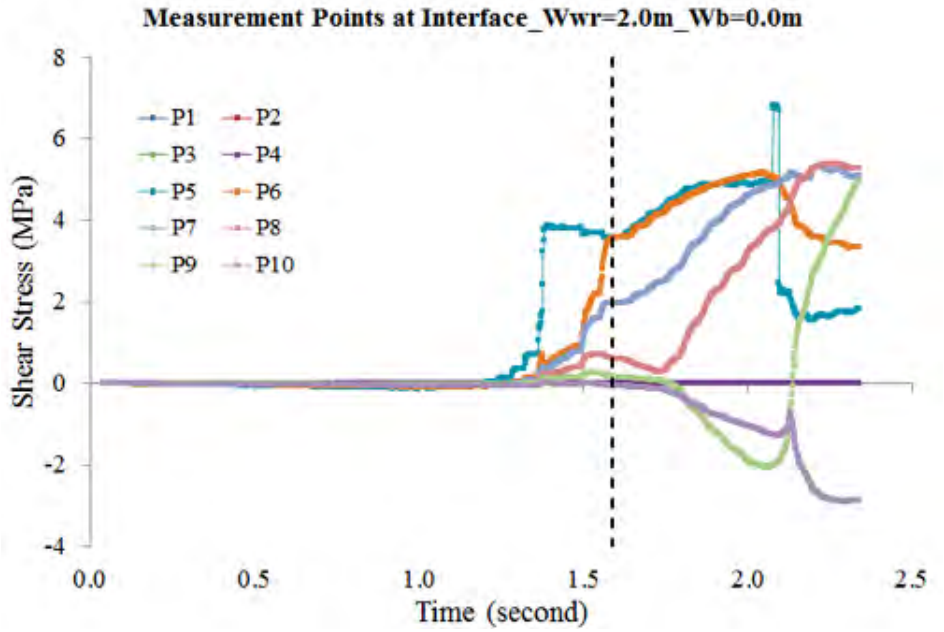

Figure C.27: Shear stress–time curves of the measurement points in WR $-$ w_b simulation with w_{wr} = 2.0 m and w_b = 0.0 m.

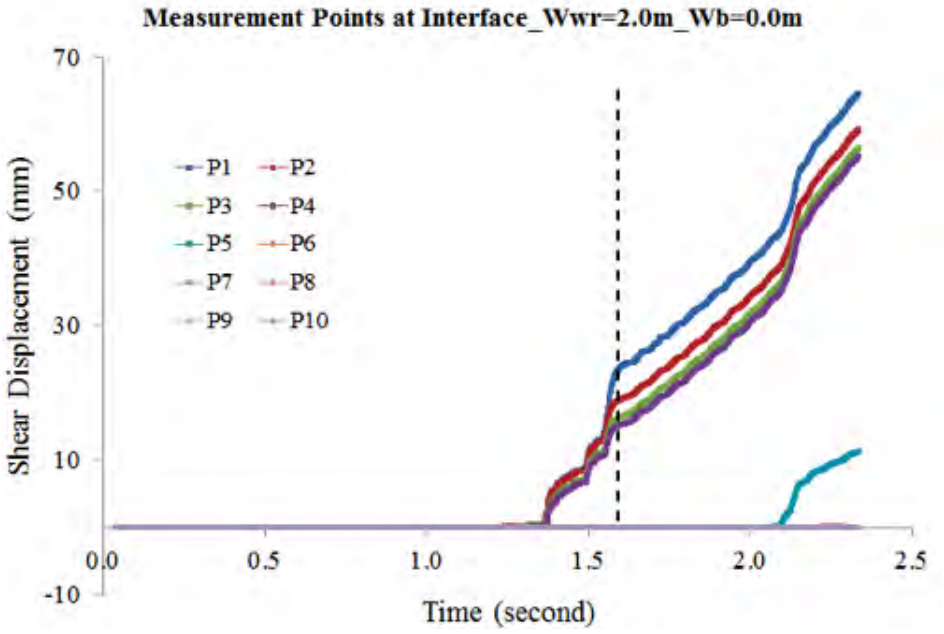

Figure C.28: Shear displacement–time curves of the measurement points in WR – w_b simulation with w_{wr} = 2.0 m and w_b = 0.0 m.

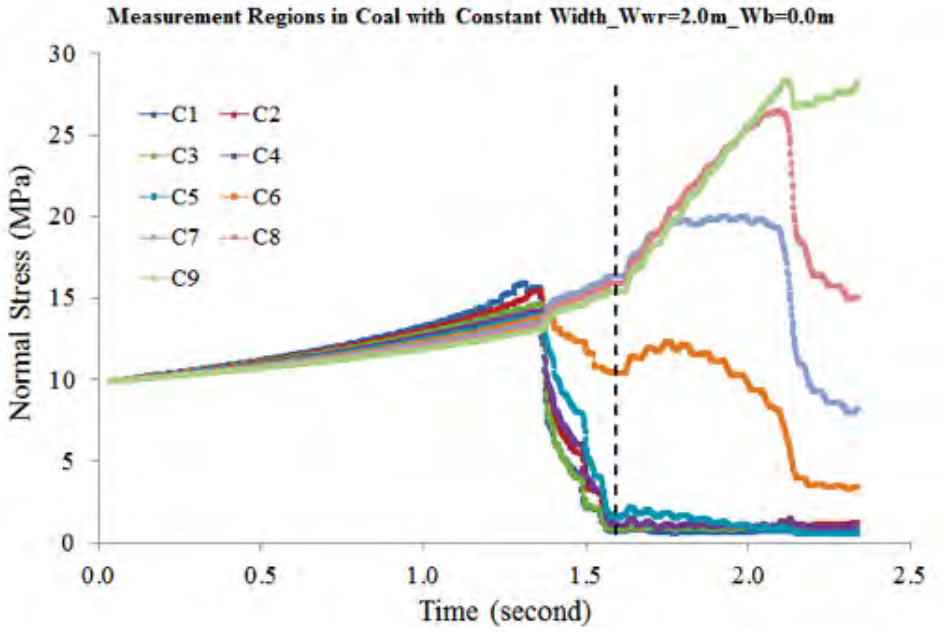

Figure C.29: Normal stress–time curves of the measurement regions with a constant width in WR – w_b simulation with w_{wr} = 2.0 m and w_b = 0.0 m.

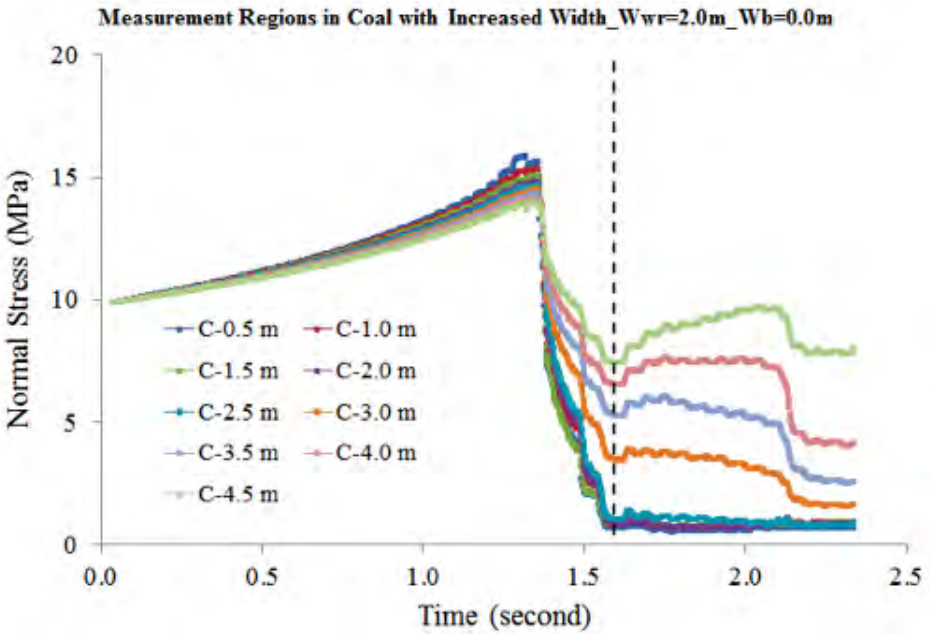

Figure C.30: Normal stress–time curves of the measurement regions with increased widths in WR – w_b simulation with w_{wr} = 2.0 m and w_b = 0.0 m.

The normal stress–time curves of the measurement regions with a constant width is shown in Figure C.34.

The normal stress–time curves of the measurement regions with increased width is shown in Figure C.35.

C.2.3 w_b = 1.0 m.

The normal stress–time curve is shown in Figure C.36.

The shear stress–time curve is shown in Figure C.37.

The shear displacement–time curve is shown in Figure C.38.

The normal stress–time curves of the measurement regions with a constant width is shown in Figure C.39.

The normal stress–time curves of the measurement regions with increased width is shown in Figure C.40.

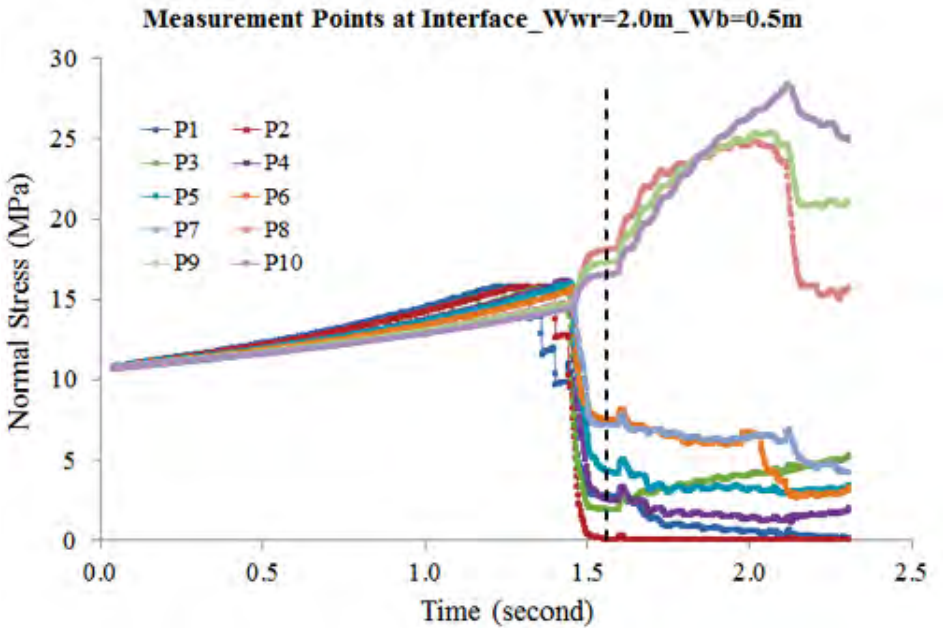

Figure C.31: Normal stress–time curves of the measurement points in WR $-$ w_b simulation with w_{wr} = 2.0 m and w_b = 0.5 m.

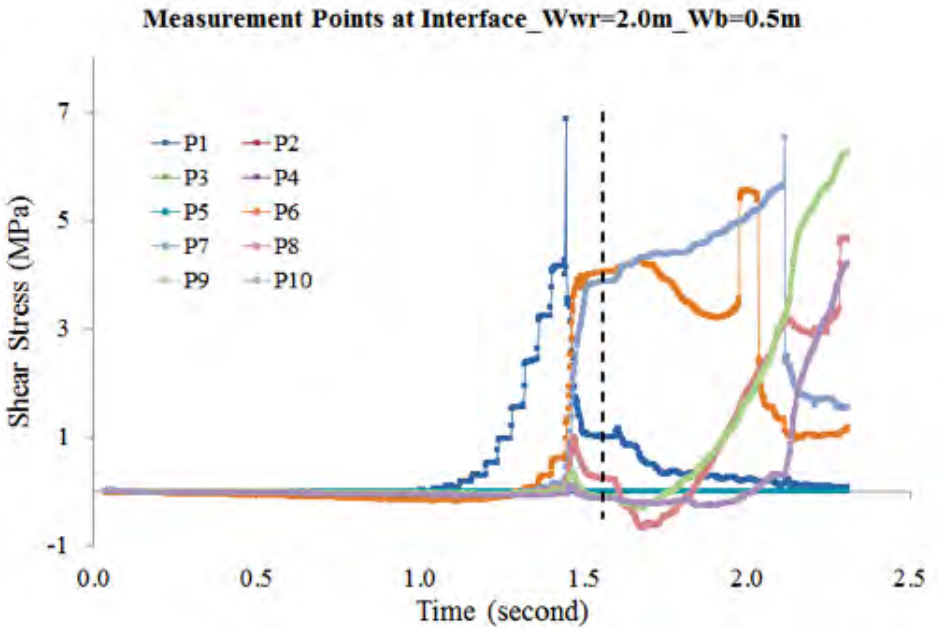

Figure C.32: Shear stress–time curves of the measurement points in WR $-$ w_b simulation with w_{wr} = 2.0 m and w_b = 0.5 m.

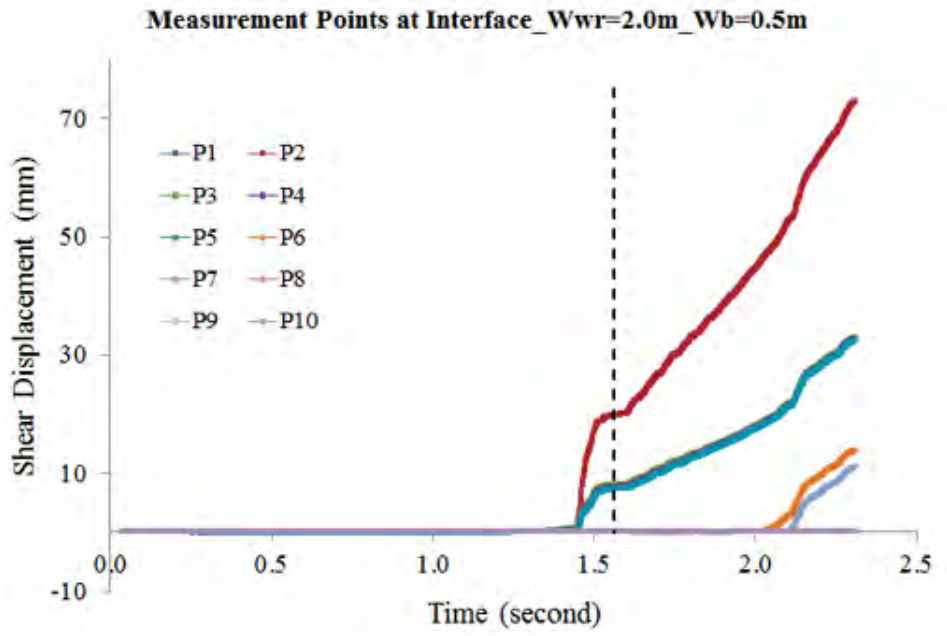

Figure C.33: Shear displacement–time curves of the measurement points in WR − w_b simulation with w_{wr} = 2.0 m and w_b = 0.5 m.

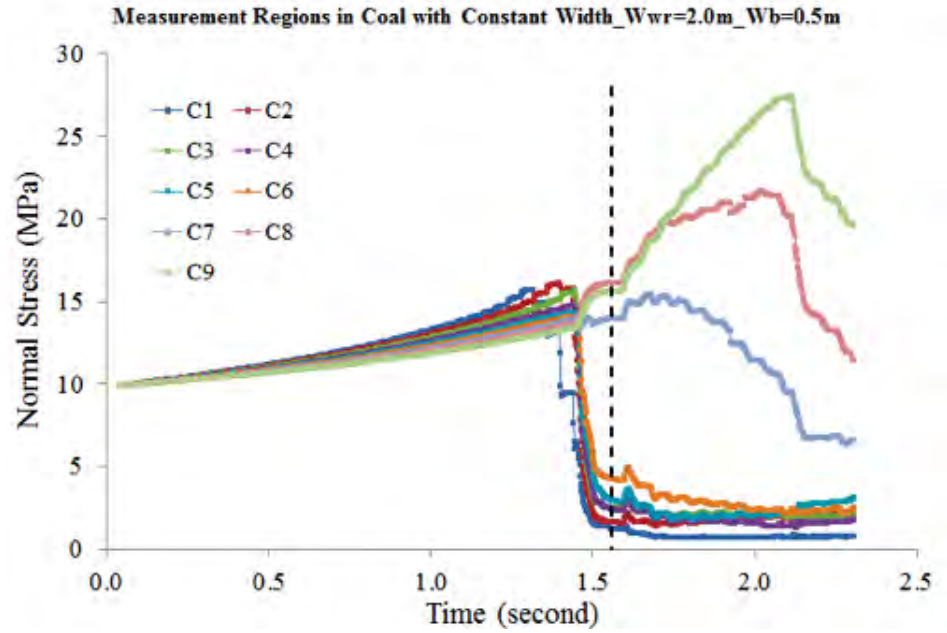

Figure C.34: Normal stress–time curves of the measurement regions with a constant width in WR − w_b simulation with w_{wr} = 2.0 m and w_b = 0.5 m.

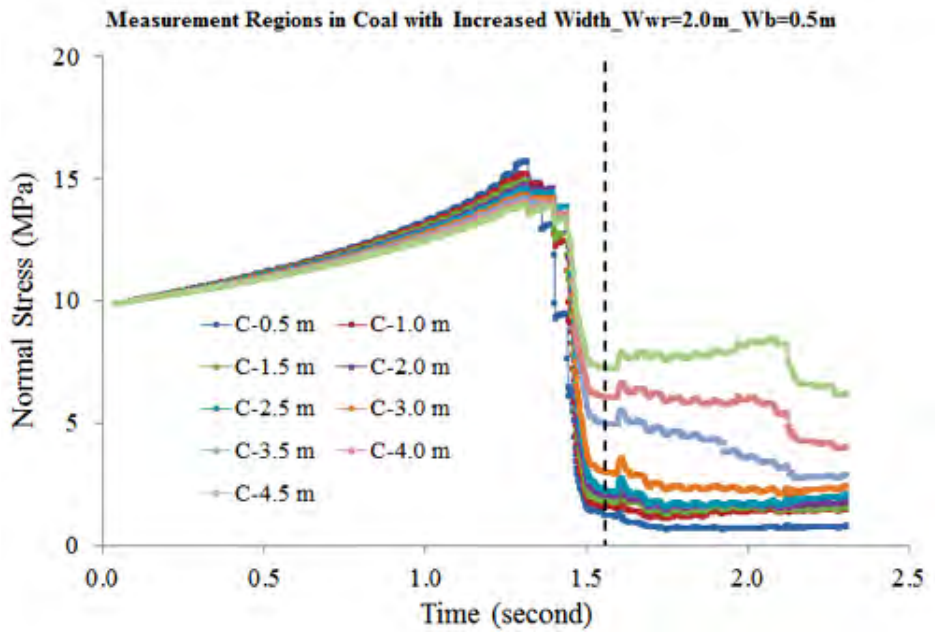

Figure C.35: Normal stress–time curves of the measurement regions with increased widths in WR − w_b simulation with w_{wr} = 2.0 m and w_b = 0.5 m.

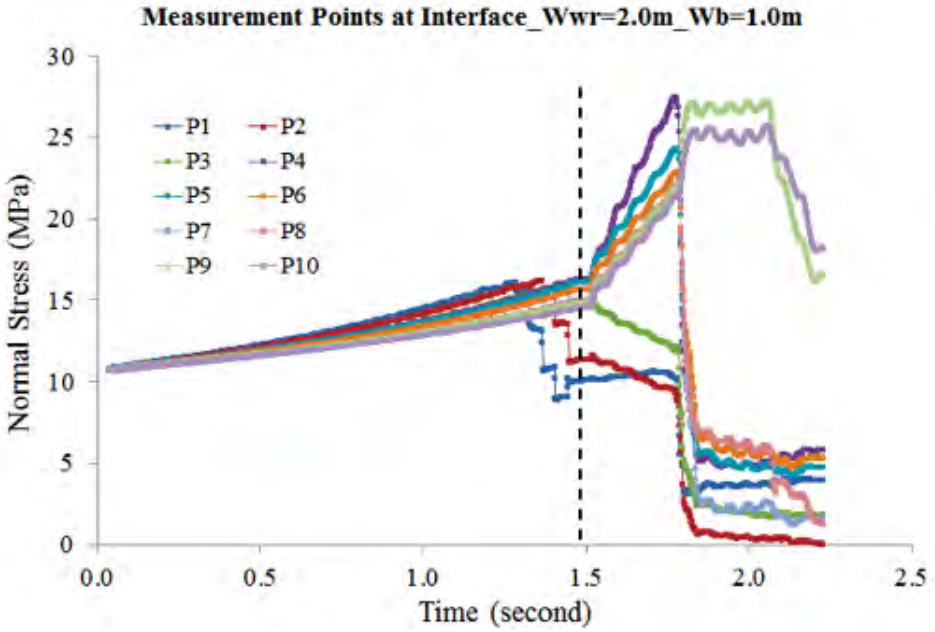

Figure C.36: Normal stress–time curves of the measurement points in WR − w_b simulation with w_{wr} = 2.0 m and w_b = 1.0 m.

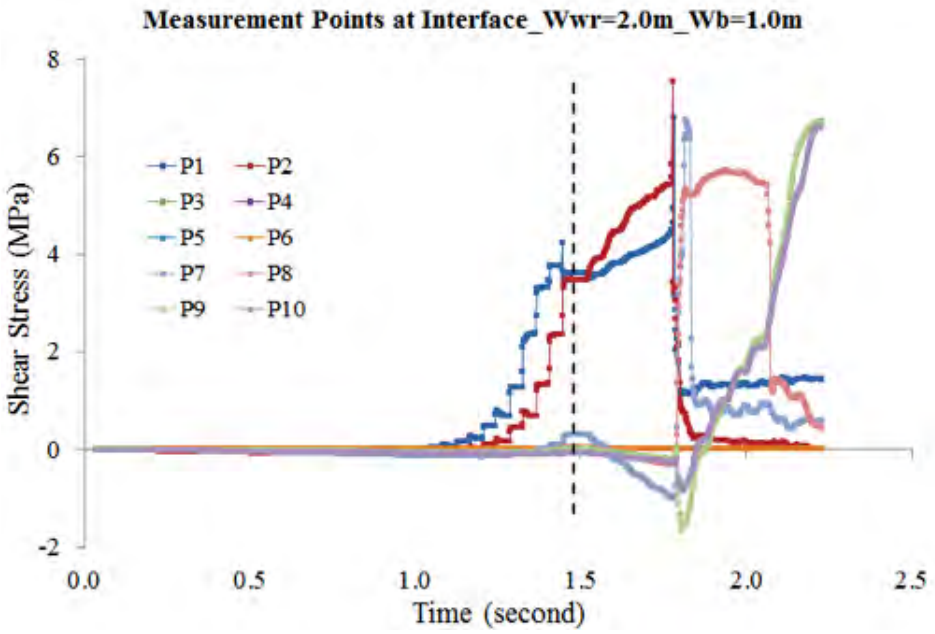

Figure C.37: Shear stress–time curves of the measurement points in WR − w_b simulation with w_{wr} = 2.0 m and w_b = 1.0 m.

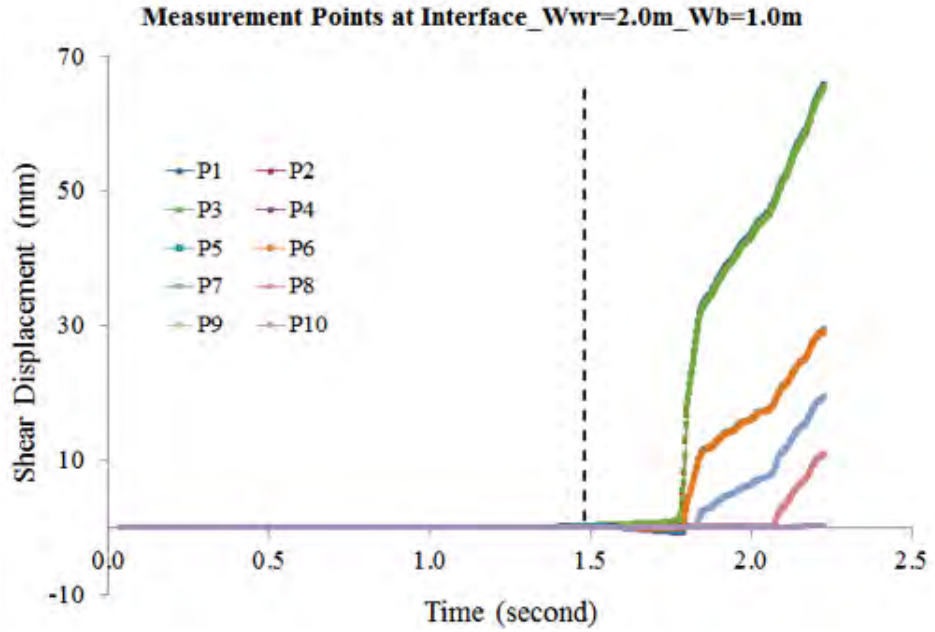

Figure C.38: Shear displacement–time curves of the measurement points in WR − w_b simulation with w_{wr} = 2.0 m and w_b = 1.0 m.

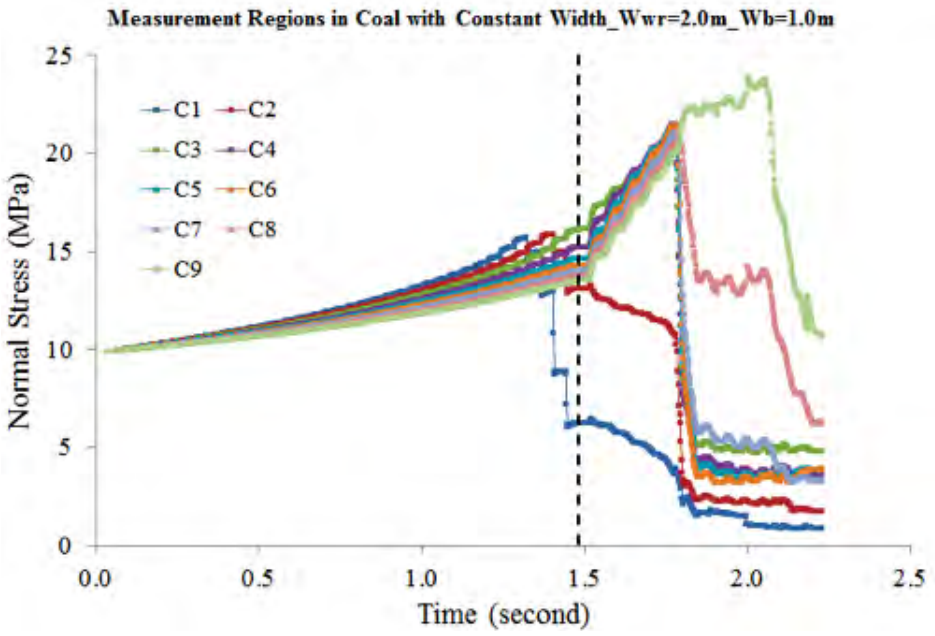

Figure C.39: Normal stress–time curves of the measurement regions with a constant width in WR – w_b simulation with w_{wr} = 2.0 m and w_b = 1.0 m.

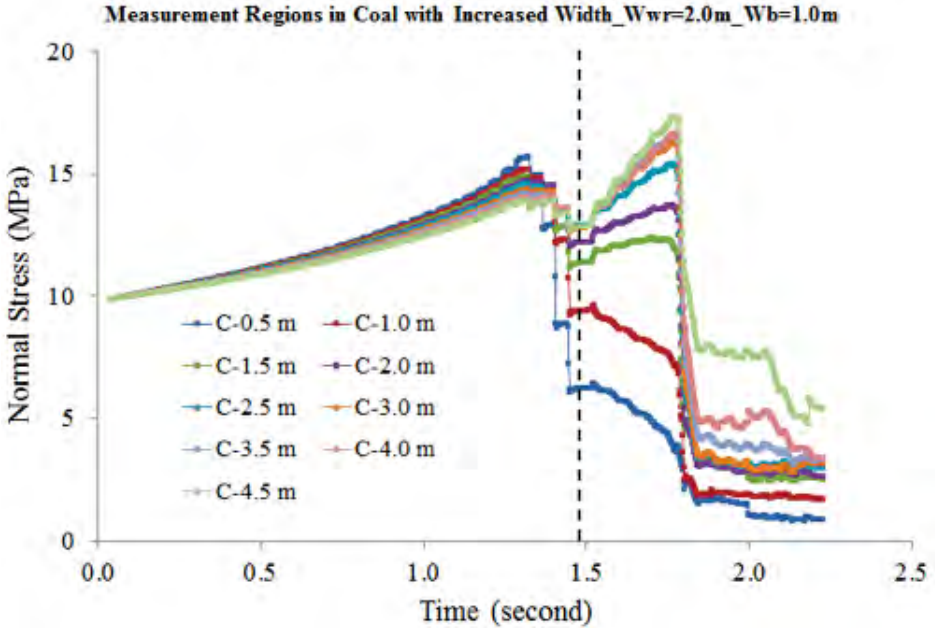

Figure C.40: Normal stress–time curves of the measurement regions with increased widths in WR – w_b simulation with w_{wr} = 2.0 m and w_b = 1.0 m.

C.2.4 $w_b = 1.5$ m.

The normal stress–time curve is shown in Figure C.41.

The shear stress–time curve is shown in Figure C.42.

The shear displacement–time curve is shown in Figure C.43.

The normal stress–time curves of the measurement regions with a constant width is shown in Figure C.44.

The normal stress–time curves of the measurement regions with increased width is shown in Figure C.45.

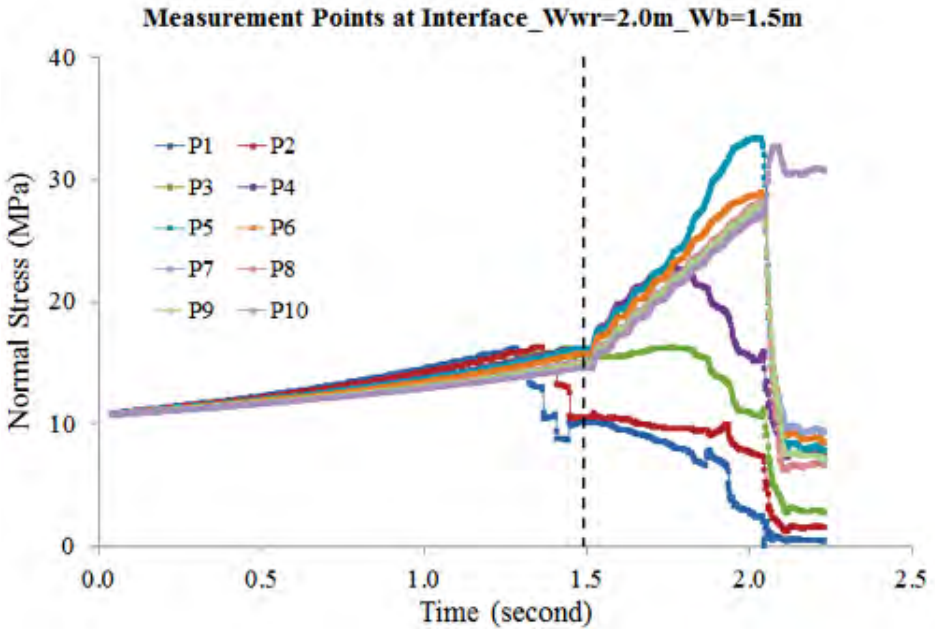

Figure C.41: Normal stress–time curves of the measurement points in WR $-$ w_b simulation with $w_{wr} = 2.0$ m and $w_b = 1.5$ m.

C.2.5 $w_b = 2.0$ m.

The normal stress–time curve is shown in Figure C.46.

The shear stress–time curve is shown in Figure C.47.

The shear displacement–time curve is shown in Figure C.48.

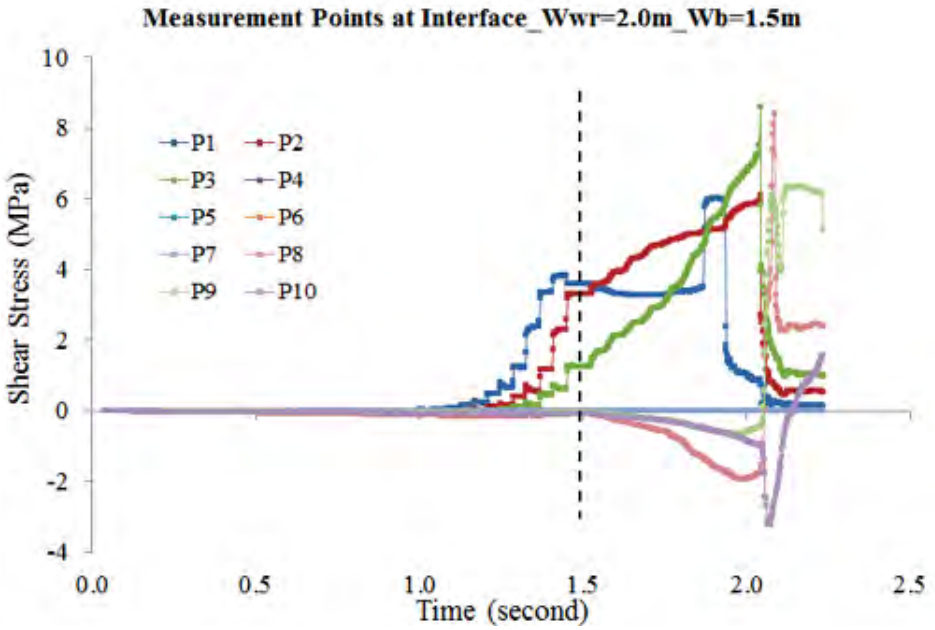

Figure C.42: Shear stress–time curves of the measurement points in WR $-$ w_b simulation with w_{wr} = 2.0 m and w_b = 1.5 m.

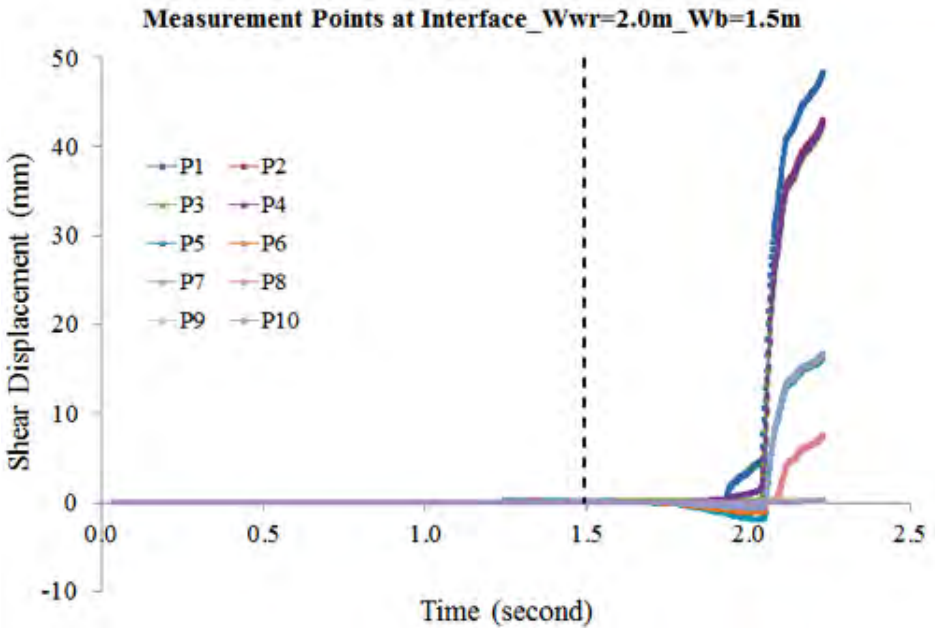

Figure C.43: Shear displacement–time curves of the measurement points in WR $-$ w_b simulation with w_{wr} = 2.0 m and w_b = 1.5 m.

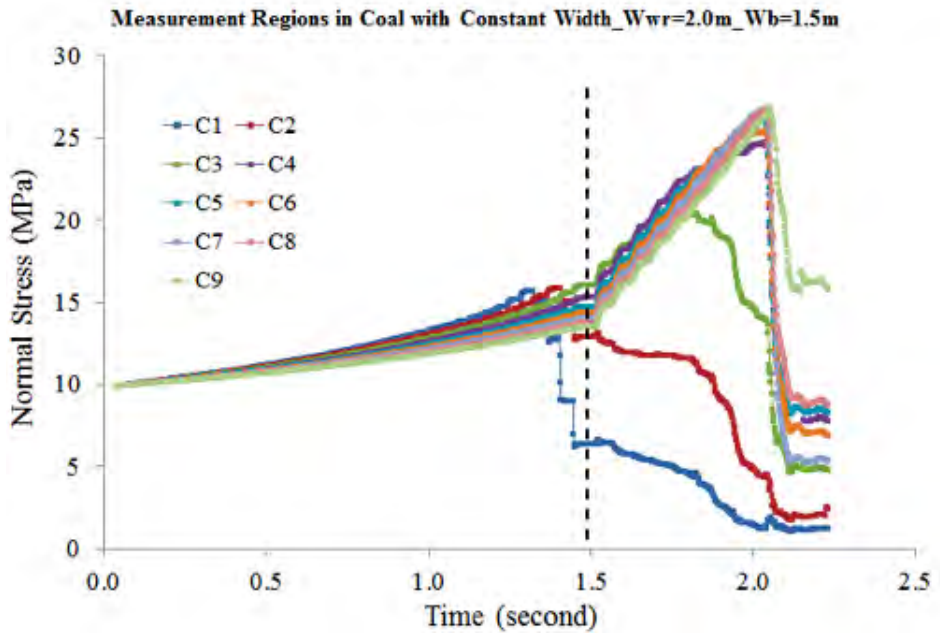

Figure C.44: Normal stress–time curves of the measurement regions with a constant width in WR – w_b simulation with w_{wr} = 2.0 m and w_b = 1.5 m.

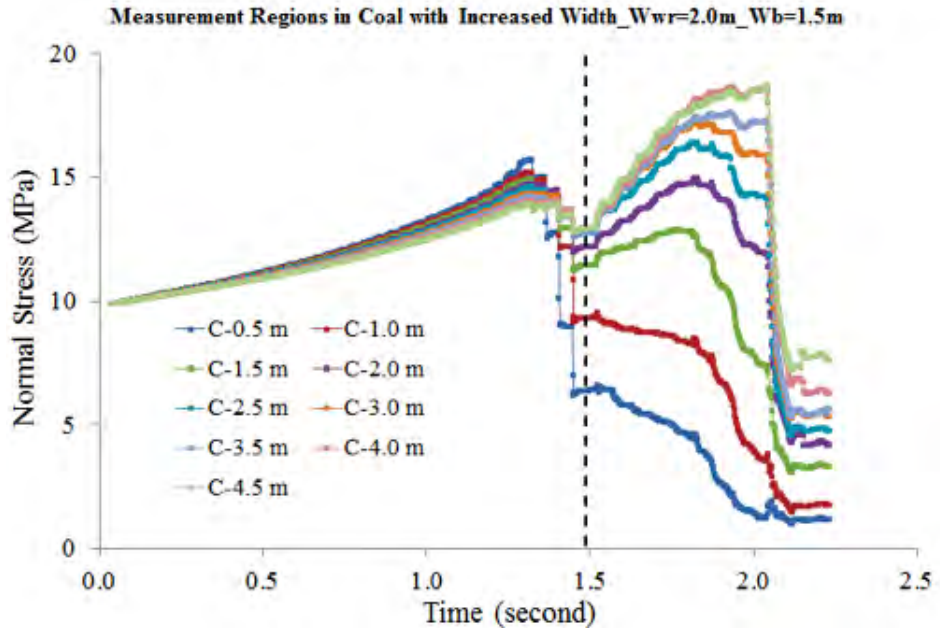

Figure C.45: Normal stress–time curves of the measurement regions with increased widths in WR – w_b simulation with w_{wr} = 2.0 m and w_b = 1.5 m.

The normal stress–time curves of the measurement regions with a constant width is shown in Figure C.49.

The normal stress–time curves of the measurement regions with increased width is shown in Figure C.50.

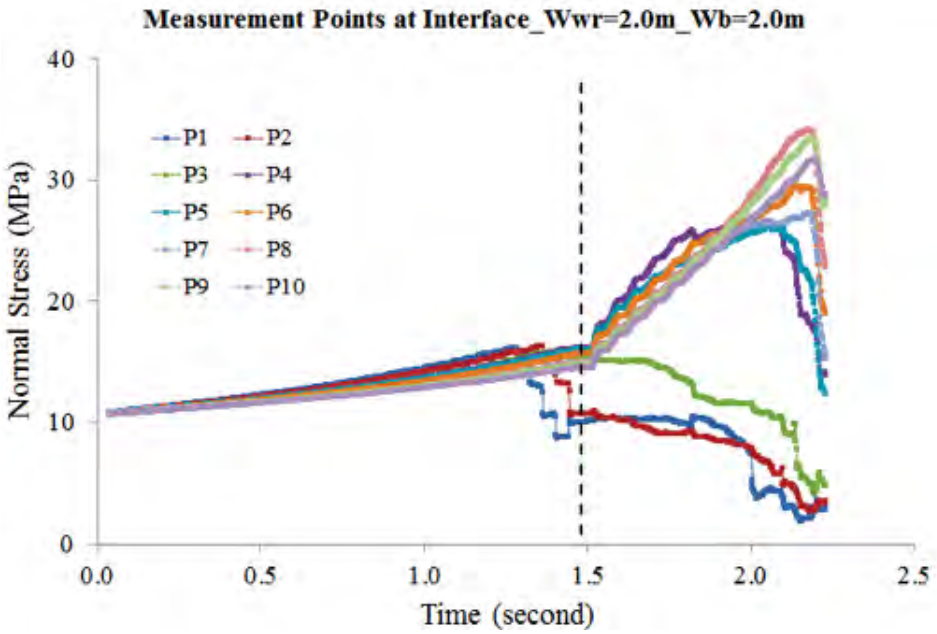

Figure C.46: Normal stress–time curves of the measurement points in WR – w_b simulation with w_{wr} = 2.0 m and w_b = 2.0 m.

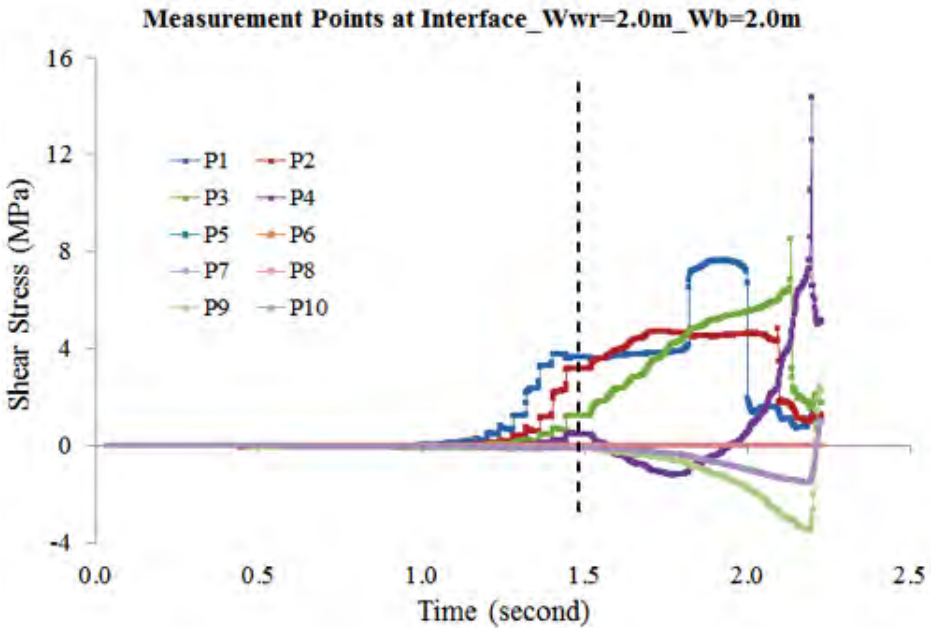

Figure C.47: Shear stress–time curves of the measurement points in WR $-$ w_b simulation with w_{wr} = 2.0 m and w_b = 2.0 m.

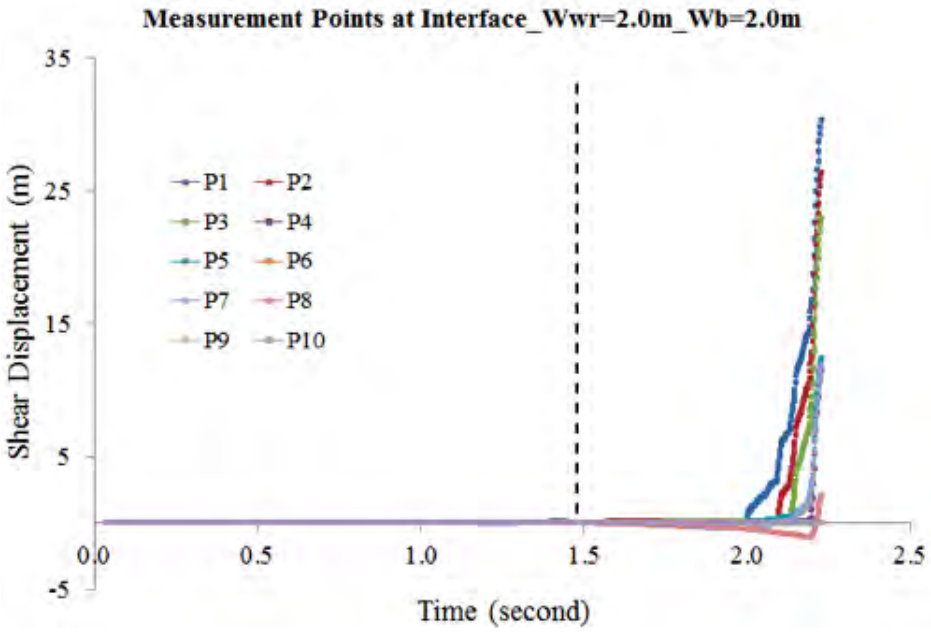

Figure C.48: Shear displacement–time curves of the measurement points in WR $-$ w_b simulation with w_{wr} = 2.0 m and w_b = 2.0 m.

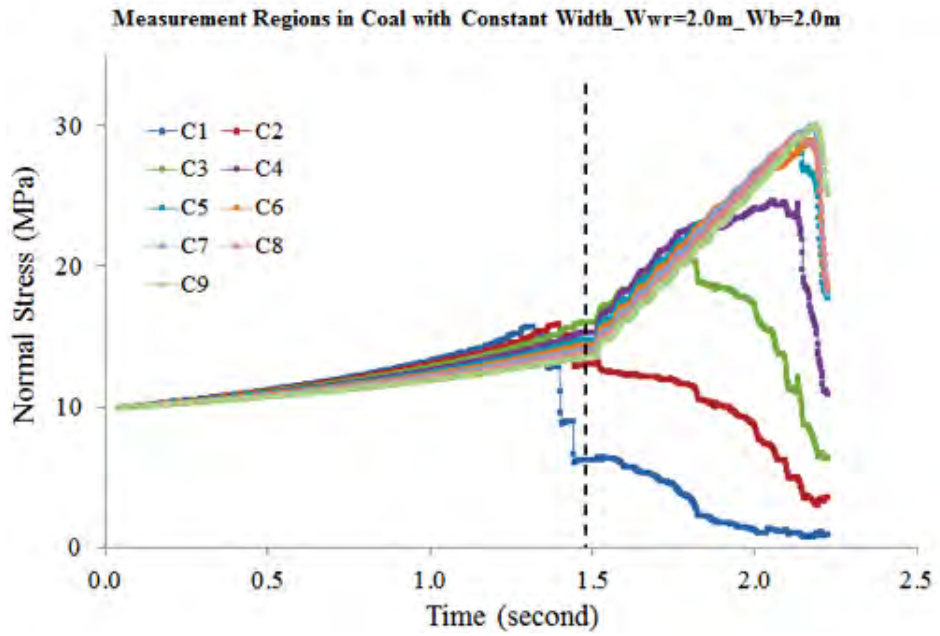

Figure C.49: Normal stress–time curves of the measurement regions with a constant width in WR − w_b simulation with w_{wr} = 2.0 m and w_b = 2.0 m.

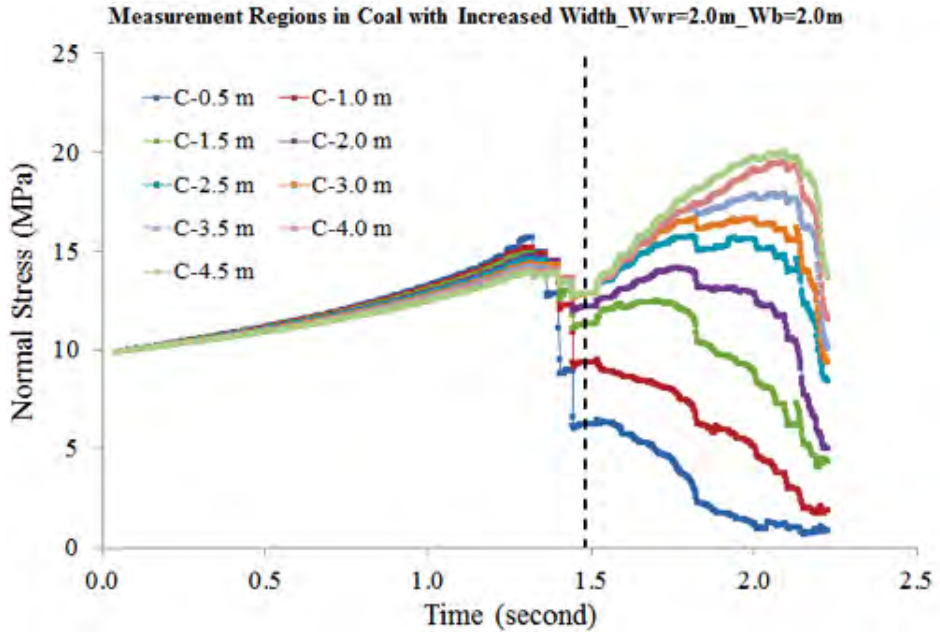

Figure C.50: Normal stress–time curves of the measurement regions with increased width in WR − w_b simulation with w_{wr} = 2.0 m and w_b = 2.0 m.

APPENDIX D - UDEC CODES FOR THE SIMULATIONS

D.1 Double Shear Tests under Constant Normal Loading

200 GPa

```
config
round 3.0E-4
edge 6.0E-4
set ovtol 3.0E-4
; === model geometry===
block 0,0 0,0.3 0.3,0.3 0.3,0
crack 0,0.2 0.3,0.2
crack 0,0.1 0.3,0.1
crack 0.05,0.2 0.05,0.1
crack 0.25,0.2 0.25,0.1
delete 0,0.05 0.1,0.2
delete 0.25,0.3 0.1,0.2
; ===generate finite-difference zones===
gen 0.05,0.25 0.1,0.2 quad 0.1 0.2
gen 0.0,0.3 0.2,0.3 quad 0.4 0.2
gen 0.05,0.3 0.0,0.1 quad 0.4 0.2
; ===assign constitutive models and material properties===
prop mat=1 d=7.65E3 k=1111111.1E6 g=833333.3E6 ;E=2000 GPa, nu=0.2
prop mat=2 d=2.60E3 k=111111.1E6 g=83333.3E6 ;E=200 GPa, nu=0.2
change mat=1 range 0.0,0.3 0.0,0.1
change mat=1 range 0.0,0.3 0.2,0.3
change mat=2 range 0.05,0.25 0.1,0.2
```

```
joint model cy
set jcondf=cy
joint jkn=100.0E9 jks=100.0E9 jen=0.0 jes=0.0 jfric=30.0 jif=59.3 jr=1.0e-4
; ===apply boundary conditions===
bound stress (0,0,-10.0E6) range 0.0,0.3 -0.0001,0.0001 ;bottom
bound stress (0,0,-10.0E6) range 0.0,0.3 0.2999,0.3001 ;top
bound xvel=0 range 0.0,0.3 -0.0001,0.0001 ;bottom
bound xvel=0 range 0.0,0.3 0.2999,0.3001 ;top
bound xvel=0 range -0.0001,0.0001 0.0,0.3 ;left
bound xvel=0 range 0.2999,0.3001 0.0,0.3 ;right
; ===run the model to equilibrium===
solve
; ===record shear stress===
history sstress 0.05,0.20 ;point A
history sstress 0.15,0.20 ;point B
history sstress 0.25,0.20 ;point C
history sstress 0.05,0.10 ;point D
history sstress 0.15,0.10 ;point E
history sstress 0.25,0.10 ;point F
; ===record shear displacement===
history sdis 0.05,0.20 ;point A
history sdis 0.15,0.20 ;point B
history sdis 0.25,0.20 ;point C
history sdis 0.05,0.10 ;point D
history sdis 0.15,0.10 ;point E
history sdis 0.25,0.10 ;point F
; ===record normal stress===
```

history nstress 0.05,0.20 ; point A

history nstress 0.15,0.20 ; point B

history nstress 0.25,0.20 ; point C

history nstress 0.05,0.10 ; point D

history nstress 0.15,0.10 ; point E

history nstress 0.25,0.10 ; point F

; ===record maximum unbalanced force===

hist unbalanced

; ===apply shear load by imposing x-velocity over the left side of the rock specimen===

bou xvel=0.001 range 0.049,0.051 0.09,0.21

; ===record energy components in the model===

set energy on hist energy

; ===run the model===

step 800000

50 GPa

Replace the command in 200 GPa case "prop mat=2 d=2.60E3 k=111111.1E6 g=83333.3E6" with "prop mat=2 d=2.60E3 k=27777.8E6 g=20833.3E6".

Replace the command in 200 GPa case "step 800000" with "step 600000".

1 GPa

Replace the command in 200 GPa case "prop mat=2 d=2.60E3 k=111111.1E6 g=83333.3E6" with "prop mat=2 d=2.60E3 k=555.55E6 g=416.65E6".

Replace the command in 200 GPa case "step 800000" with "step 2500000".

D.2 Loading Stiffness Tests

50 GPa

config

round 3.0E-4

edge 6.0E-4

; === model geometry===

block 0.05,0.15 0.05,0.20 0.25,0.20 0.25,0.15

; ===generate finite-difference zones===

gen 0.05,0.25 0.15,0.2 quad 0.2 0.2

; ===assign constitutive models and material properties===

prop mat=2 d=2.60E3 k=2.778E10 g=2.083E10 ;E=50 GPa, nu=0.2

change mat=2 range 0.05 0.25 0.1 0.2

; ===apply boundary conditions===

bound xvel=0 range 0.0,0.3 0.1499,0.1501 ;bottom

bound yvel=0 range 0.0,0.3 0.1499,0.1501 ;bottom

; ===run the model to equilibrium===

solve

; ===apply a horizontal velocity over the top of the model===

bou xvel=0.001 range 0.0 0.25 0.199 0.201

; ===record horizontal displacement===

history xdisplace 0.15,0.2

; ===record shear stress===

history sxy 0.10016388,0.191684

history sxy 0.13347653,0.1750088

history sxy 0.16680992,0.17499158

history sxy 0.2001642,0.19164954

; ===run the model===

cycle 20000

1 GPa

Replace the command in 50 GPa "prop mat=2 d=2.60E3 k=2.778E10 g=2.083E10" with "prop mat=2 d=2.60E3 k=555.55E6 g=416.65E6".

D.3 Double Shear Tests using MC Plasticity Model

200 GPa

config

round 3.0E-4

edge 6.0E-4

set ovtol 3.0E-4

; === model geometry===

block 0,0 0,0.3 0.3,0.3 0.3,0

crack 0,0.2 0.3,0.2

crack 0,0.1 0.3,0.1

crack 0.05,0.2 0.05,0.1

crack 0.25,0.2 0.25,0.1

delete 0,0.05 0.1,0.2

delete 0.25,0.3 0.1,0.2

; ===generate finite-difference zones===

gen 0.05,0.25 0.1,0.2 quad 0.1 0.2

gen 0.0,0.3 0.2,0.3 quad 0.4 0.2

gen 0.05,0.3 0.0,0.1 quad 0.4 0.2

; ===assign constitutive models and material properties===

prop mat=1 d=7.65E3 k=1111111.1E6 g=833333.3E6 ;E=2000GPa, nu=0.2

prop mat=2 d=2.60E3 k=111111.1E6 g=83333.3E6 ;E=200GPa, nu=0.2

change mat=1 range 0.0,0.3 0.0,0.1

change mat=1 range 0.0,0.3 0.2,0.3

change mat=2 range 0.05,0.25 0.1,0.2

prop jmat=1 jkn=100.0E9 jks=100.0E9 jfric=38.0 jcoh=0.0

change jmat=1

; ===apply boundary conditions===

```
bound stress (0,0,-10.0E6) range 0.0,0.3 -0.0001,0.0001 ;bottom
bound stress (0,0,-10.0E6) range 0.0,0.3 0.2999,0.3001 ;top
bound xvel=0 range 0.0,0.3 -0.0001,0.0001 ;bottom
bound xvel=0 range 0.0,0.3 0.2999,0.3001 ;top
bound xvel=0 range -0.0001,0.0001 0.0,0.3 ;left
bound xvel=0 range 0.2999,0.3001 0.0,0.3 ;right
; ===run the model to equilibrium===
solve
; ===record shear stress===
history sstress 0.05,0.20 ;point A
history sstress 0.15,0.20 ;point B
history sstress 0.25,0.20 ;point C
history sstress 0.05,0.10 ;point D
history sstress 0.15,0.10 ;point E
history sstress 0.25,0.10 ;point F
; ===record shear displacement===
history sdis 0.05,0.20 ;point A
history sdis 0.15,0.20 ;point B
history sdis 0.25,0.20 ;point C
history sdis 0.05,0.10 ;point D
history sdis 0.15,0.10 ;point E
history sdis 0.25,0.10 ;point F
; ===record normal stress===
history nstress 0.05,0.20 ; point A
history nstress 0.15,0.20 ; point B
history nstress 0.25,0.20 ; point C
history nstress 0.05,0.10 ; point D
```

history nstress 0.15,0.10 ; point E

history nstress 0.25,0.10 ; point F

; ===record maximum unbalanced force===

hist unbalanced

; ===apply shear load by imposing x-velocity over the left side of the rock specimen===

bou xvel=0.001 range 0.049,0.051 0.09,0.21

; ===record energy components in the model===

set energy on hist energy

; ===run the model===

step 800000

50 GPa

Replace the command in 200 GPa case "prop mat=2 d=2.60E3 k=111111.1E6 g=83333.3E6" with "prop mat=2 d=2.60E3 k=27777.8E6 g=20833.3E6".

Replace the command in 200 GPa case "step 800000" with "step 600000".

1 GPa

Replace the command in 200 GPa case "prop mat=2 d=2.60E3 k=111111.1E6 g=83333.3E6" with "prop mat=2 d=2.60E3 k=555.55E6 g=416.65E6".

Replace the command in 200 GPa case "step 800000" with "step 2500000".

D.4 Double Shear Tests under Different Normal Constant Stresses

Normal stress = 4 MPa

config

round 3.0E-4

edge 6.0E-4

set ovtol 6.0E-4

; === model geometry===

block 0,0 0,0.3 0.3,0.3 0.3,0

crack 0,0.2 0.3,0.2

```
crack 0,0.1 0.3,0.1
crack 0.05,0.2 0.05,0.1
crack 0.25,0.2 0.25,0.1
delete 0,0.05 0.1,0.2
delete 0.25,0.3 0.1,0.2
; ===generate finite-difference zones===
gen 0.05,0.25 0.1,0.2 quad 0.1 0.2
gen 0.0,0.3 0.2,0.3 quad 0.4 0.2
gen 0.05,0.3 0.0,0.1 quad 0.4 0.2
; ===assign constitutive models and material properties===
prop mat=1 d=7.65E3 k=1111111.1E6 g=833333.3E6 ;E=2000 GPa, nu=0.2
prop mat=2 d=2.60E3 k=111111.1E6 g=83333.3E6 ;E=200 GPa, nu=0.2
change mat=1 range 0.0,0.3 0.0,0.1
change mat=1 range 0.0,0.3 0.2,0.3
change mat=2 range 0.05,0.25 0.1,0.2
joint model cy
set jcondf=cy
joint jkn=100.0E9 jks=100.0E9 jen=0.0 jes=0.0 jfric=30.0 jif=59.3 jr=1.0e-4
; ===apply boundary conditions===
bound stress (0,0,-4.0E6) range 0.0,0.3 -0.0001,0.0001 ;bottom
bound stress (0,0,-4.0E6) range 0.0,0.3 0.2999,0.3001 ;top
bound xvel=0 range 0.0,0.3 -0.0001,0.0001 ;bottom
bound xvel=0 range 0.0,0.3 0.2999,0.3001 ;top
bound xvel=0 range -0.0001,0.0001 0.0,0.3 ;left
bound xvel=0 range 0.2999,0.3001 0.0,0.3 ;right
; ===run the model to equilibrium===
solve
```

; ===record shear stress===

history sstress 0.05,0.20 ;point A

history sstress 0.15,0.20 ;point B

history sstress 0.25,0.20 ;point C

history sstress 0.05,0.10 ;point D

history sstress 0.15,0.10 ;point E

history sstress 0.25,0.10 ;point F

; ===record shear displacement===

history sdis 0.05,0.20 ;point A

history sdis 0.15,0.20 ;point B

history sdis 0.25,0.20 ;point C

history sdis 0.05,0.10 ;point D

history sdis 0.15,0.10 ;point E

history sdis 0.25,0.10 ;point F

; ===record normal stress===

history nstress 0.05,0.20 ; point A

history nstress 0.15,0.20 ; point B

history nstress 0.25,0.20 ; point C

history nstress 0.05,0.10 ; point D

history nstress 0.15,0.10 ; point E

history nstress 0.25,0.10 ; point F

; ===record maximum unbalanced force===

hist unbalanced

; ===apply shear load by imposing x-velocity over the left side of the rock specimen===

bou xvel=0.001 range 0.049,0.051 0.09,0.21

; ===record energy components in the model===

set energy on hist energy

; ===run the model===

step 800000

Normal stress = 8 MPa

Replace the commands in normal stress = 4 MPa case "bound stress (0, 0, -4.0E6) range 0.0, 0.3 -0.0001, 0.0001; bound stress (0, 0, -4.0E6) range 0.0, 0.3 0.2999, 0.3001" with "bound stress (0, 0, -8.0E6) range 0.0, 0.3 -0.0001, 0.0001; bound stress (0, 0, -8.0E6) range 0.0, 0.3 0.2999, 0.3001".

Replace the command in normal stress = 4 MPa case "step 800000" with "step 1500000".

Normal stress = 12 MPa

Replace the commands in normal stress = 4 MPa case "bound stress (0, 0, -4.0E6) range 0.0, 0.3 -0.0001, 0.0001; bound stress (0, 0, -4.0E6) range 0.0, 0.3 0.2999, 0.3001" with "bound stress (0, 0, -12.0E6) range 0.0, 0.3 -0.0001, 0.0001; bound stress (0, 0, -12.0E6) range 0.0, 0.3 0.2999, 0.3001".

Replace the command in normal stress = 4 MPa case "step 800000" with "step 2000000".

Normal stress = 16 MPa

Replace the commands in normal stress = 4 MPa case "bound stress (0, 0, -4.0E6) range 0.0, 0.3 -0.0001, 0.0001; bound stress (0, 0, -4.0E6) range 0.0, 0.3 0.2999, 0.3001" with "bound stress (0, 0, -16.0E6) range 0.0, 0.3 -0.0001, 0.0001; bound stress (0, 0, -16.0E6) range 0.0, 0.3 0.2999, 0.3001".

Replace the command in normal stress = 4 MPa case "step 800000" with "step 3000000".

Normal stress = 20 MPa

Replace the commands in normal stress = 4 MPa case "bound stress (0, 0, -4.0E6) range 0.0, 0.3 -0.0001, 0.0001; bound stress (0, 0, -4.0E6) range 0.0, 0.3 0.2999, 0.3001" with "bound stress (0, 0, -20.0E6) range 0.0, 0.3 -0.0001, 0.0001; bound stress (0, 0, -20.0E6) range 0.0, 0.3 0.2999, 0.3001".

Replace the command in normal stress = 4 MPa case "step 800000" with "step 3500000".

Normal stress = 24 MPa

Replace the commands in normal stress = 4 MPa case “bound stress (0, 0, -4.0E6) range 0.0, 0.3 -0.0001, 0.0001; bound stress (0, 0, -4.0E6) range 0.0, 0.3 0.2999, 0.3001” with “bound stress (0, 0, -24.0E6) range 0.0, 0.3 -0.0001, 0.0001; bound stress (0, 0, -24.0E6) range 0.0, 0.3 0.2999, 0.3001”.

Replace the command in normal stress = 4 MPa case “step 800000” with “step 5500000”.

Normal stress = 28 MPa

Replace the commands in normal stress = 4 MPa case “bound stress (0, 0, -4.0E6) range 0.0, 0.3 -0.0001, 0.0001; bound stress (0, 0, -4.0E6) range 0.0, 0.3 0.2999, 0.3001” with “bound stress (0, 0, -28.0E6) range 0.0, 0.3 -0.0001, 0.0001; bound stress (0, 0, -28.0E6) range 0.0, 0.3 0.2999, 0.3001”.

Replace the command in normal stress = 4 MPa case “step 800000” with “step 5500000”.

D.5 Determination of Model Boundary

Varying dh

dv=100 m, dh=20 m

config

round 0.1

edge 0.2

set ovtol 0.1

; === model geometry===

block -30.0,-100.0 -30.0,100.0 30.0,100.0 30.0,-100.0

crack -100.0 1.0 100.0 1.0 ;top of rock layer

crack -100.0 -1.0 100.0 -1.0 ;bottom of rock layer

crack -100.0 3.0 100.0 3.0 ;the existing rock discontinuity

crack 10.0 -1.0 10.0 1.0 ;right side of the excavation

crack -10.0 -1.0 -10.0 1.0 ;left side of the excavation

; ===generate finite-difference zones===

gen quad 0.4

```
; ===assign constitutive models and material properties===
;
def _parameter
_E1 = 70.0E9 ;rock
_nu1 = 0.2 ;rock
_k1 = _E1/(3*(1-2*_nu1))
_g1 = _E1/(2*(1+_nu1))
end _parameter
;
prop mat=1 d=2670.0 k=_k1 g=_g1
change mat=1
set jcondf=3
change jcons=3
prop jmat=1 jkn=50.0E9 jks=50.0E9 jen=0.0 jes=0.0 jfric=30.0 jif=59.3 jr=1.0e-4 ;the existing rock discontinuity
change jmat=1 range -101.0 101.0 2.9 3.1
prop jmat=2 jkn=100.0E9 jks=100.0E9 jfric=100.0 jcoh=1.0E20 jdil=100.0 jten=1.0E20 ;fictitious joints
change jmat=2 range -101.0 101.0 -1.1 1.1
; ===apply boundary conditions===
insitu stress -5.25E6 0.0 -17.5E6
bound stress -5.25E6 0.0 -17.5E6
bound xvel=0.0 range 29.9,30.1 -110.0,110.0 ;right
bound xvel=0.0 range -30.1,-29.9 -110.0,110.0 ;left
bound xvel=0.0 range -100.0,100.0 99.9,100.1 ;top
bound yvel=0.0 range -100.0,100.0 99.9,100.1 ;top
bound xvel=0.0 range -100.0,100.0 -100.1,-99.9 ;bottom
```

```
bound yvel=0.0 range -100.0,100.0 -100.1,-99.9 ;bottom
solve
; ===finish the excavation===
delete range -10.0 10.0 -1.0 1.0
solve
;;======================
; pull the point towards left
;;======================
; ===record horizontal displacement===
history xdisplace -4.3449522E-6,2.9948833
; ===record shear stress===
history sxy -0.20002633,3.0619617 ;zone No.1
history sxy -0.066677965,3.1953204 ;zone No.2
history sxy 0.06666922,3.1953204 ;zone No.3
history sxy 0.20001763,3.0619617 ;zone No.4
history sxy 0.2000131,2.9278078 ;zone No.5
history sxy 0.0666803,2.7944427 ;zone No.6
history sxy -0.06665472,2.7944424 ;zone No.7
history sxy -0.19998793,2.9278073 ;zone No.8
; ===apply a horizontal velocity to the point of interest===
bound interior xvel -0.05 range -0.1 0.1 2.9 3.1
cycle 2000
;;======================
; pull the point towards right
;;======================
; ===record horizontal displacement===
history xdisplace -4.3449522E-6,2.9948833
```

; ===record shear stress===

history sxy -0.20002633,3.0619617 ;zone No.1

history sxy -0.066677965,3.1953204 ;zone No.2

history sxy 0.06666922,3.1953204 ;zone No.3

history sxy 0.20001763,3.0619617 ;zone No.4

history sxy 0.2000131,2.9278078 ;zone No.5

history sxy 0.0666803,2.7944427 ;zone No.6

history sxy -0.06665472,2.7944424 ;zone No.7

history sxy -0.19998793,2.9278073 ;zone No.8

; ===apply a horizontal velocity to the point of interest===

bound interior xvel 0.05 range -0.1 0.1 2.9 3.1

cycle 2000

dv=100 m, dh=30 m

config

round 0.1

edge 0.2

set ovtol 0.1

; === model geometry===

block -40.0,-100.0 -40.0,100.0 40.0,100.0 40.0,-100.0

crack -100.0 1.0 100.0 1.0 ;top of rock layer

crack -100.0 -1.0 100.0 -1.0 ;bottom of rock layer

crack -100.0 3.0 100.0 3.0 ;the existing rock discontinuity

crack 10.0 -1.0 10.0 1.0 ;right side of the excavation

crack -10.0 -1.0 -10.0 1.0 ;left side of the excavation

; ===generate finite-difference zones===

gen quad 0.4

; ===assign constitutive models and material properties===

```
;
def _parameter
_E1 = 70.0E9 ;rock
_nu1 = 0.2 ;rock
_k1 = _E1/(3*(1-2*_nu1))
_g1 = _E1/(2*(1+_nu1))
end _parameter
;
prop mat=1 d=2670.0 k=_k1 g=_g1
change mat=1
set jcondf=3
change jcons=3
prop jmat=1 jkn=50.0E9 jks=50.0E9 jen=0.0 jes=0.0 jfric=30.0 jif=59.3 jr=1.0e-4 ;the existing rock discontinuity
change jmat=1 range -101.0 101.0 2.9 3.1
prop jmat=2 jkn=100.0E9 jks=100.0E9 jfric=100.0 jcoh=1.0E20 jdil=100.0 jten=1.0E20 ;fictitious joints
change jmat=2 range -101.0 101.0 -1.1 1.1
; ===apply boundary conditions===
insitu stress -5.25E6 0.0 -17.5E6
bound stress -5.25E6 0.0 -17.5E6
bound xvel=0.0 range 39.9,40.1 -110.0,110.0 ;right
bound xvel=0.0 range -40.1,-39.9 -110.0,110.0 ;left
bound xvel=0.0 range -100.0,100.0 99.9,100.1 ;top
bound yvel=0.0 range -100.0,100.0 99.9,100.1 ;top
bound xvel=0.0 range -100.0,100.0 -100.1,-99.9 ;bottom
bound yvel=0.0 range -100.0,100.0 -100.1,-99.9 ;bottom
```

```
solve
; ===finish the excavation===
delete range -10.0 10.0 -1.0 1.0
solve
;;======================
; pull the point towards left
;;======================
; ===record horizontal displacement===
history xdisplace -4.3449522E-6,2.9948833
; ===record shear stress===
history sxy -0.20002633,3.0619617 ;zone No.1
history sxy -0.066677965,3.1953204 ;zone No.2
history sxy 0.06666922,3.1953204 ;zone No.3
history sxy 0.20001763,3.0619617 ;zone No.4
history sxy 0.2000131,2.9278078 ;zone No.5
history sxy 0.0666803,2.7944427 ;zone No.6
history sxy -0.06665472,2.7944424 ;zone No.7
history sxy -0.19998793,2.9278073 ;zone No.8
; ===apply a horizontal velocity to the point of interest===
bound interior xvel -0.05 range -0.1 0.1 2.9 3.1
cycle 2000
;;======================
; pull the point towards right
;;======================
; ===record horizontal displacement===
history xdisplace -4.3449522E-6,2.9948833
; ===record shear stress===
```

history sxy -0.20002633,3.0619617 ;zone No.1

history sxy -0.066677965,3.1953204 ;zone No.2

history sxy 0.06666922,3.1953204 ;zone No.3

history sxy 0.20001763,3.0619617 ;zone No.4

history sxy 0.2000131,2.9278078 ;zone No.5

history sxy 0.0666803,2.7944427 ;zone No.6

history sxy -0.06665472,2.7944424 ;zone No.7

history sxy -0.19998793,2.9278073 ;zone No.8

; ===apply a horizontal velocity to the point of interest===

bound interior xvel 0.05 range -0.1 0.1 2.9 3.1

cycle 2000

dv=100 m, dh=40 m

config

round 0.1

edge 0.2

set ovtol 0.1

; === model geometry===

block -50.0,-100.0 -50.0,100.0 50.0,100.0 50.0,-100.0

crack -100.0 1.0 100.0 1.0 ;top of rock layer

crack -100.0 -1.0 100.0 -1.0 ;bottom of rock layer

crack -100.0 3.0 100.0 3.0 ;the existing rock discontinuity

crack 10.0 -1.0 10.0 1.0 ;right side of the excavation

crack -10.0 -1.0 -10.0 1.0 ;left side of the excavation

; ===generate finite-difference zones===

gen quad 0.4

; ===assign constitutive models and material properties===

;

```
def _parameter
_E1 = 70.0E9 ;rock
_nu1 = 0.2 ;rock
_k1 = _E1/(3*(1-2*_nu1))
_g1 = _E1/(2*(1+_nu1))
end _parameter
;
prop mat=1 d=2670.0 k=_k1 g=_g1
change mat=1
set jcondf=3
change jcons=3
prop jmat=1 jkn=50.0E9 jks=50.0E9 jen=0.0 jes=0.0 jfric=30.0 jif=59.3 jr=1.0e-4 ;the existing rock discontinuity
change jmat=1 range -101.0 101.0 2.9 3.1
prop jmat=2 jkn=100.0E9 jks=100.0E9 jfric=100.0 jcoh=1.0E20 jdil=100.0 jten=1.0E20 ;fictitious joints
change jmat=2 range -101.0 101.0 -1.1 1.1
; ===apply boundary conditions===
insitu stress -5.25E6 0.0 -17.5E6
bound stress -5.25E6 0.0 -17.5E6
bound xvel=0.0 range 49.9,50.1 -110.0,110.0 ;right
bound xvel=0.0 range -50.1,-49.9 -110.0,110.0 ;left
bound xvel=0.0 range -100.0,100.0 99.9,100.1 ;top
bound yvel=0.0 range -100.0,100.0 99.9,100.1 ;top
bound xvel=0.0 range -100.0,100.0 -100.1,-99.9 ;bottom
bound yvel=0.0 range -100.0,100.0 -100.1,-99.9 ;bottom
solve
```

; ===finish the excavation===

delete range -10.0 10.0 -1.0 1.0

solve

;;======================

; pull the point towards left

;;======================

; ===record horizontal displacement===

history xdisplace -4.3449522E-6,2.9948833

; ===record shear stress===

history sxy -0.20002633,3.0619617 ;zone No.1

history sxy -0.066677965,3.1953204 ;zone No.2

history sxy 0.06666922,3.1953204 ;zone No.3

history sxy 0.20001763,3.0619617 ;zone No.4

history sxy 0.2000131,2.9278078 ;zone No.5

history sxy 0.0666803,2.7944427 ;zone No.6

history sxy -0.06665472,2.7944424 ;zone No.7

history sxy -0.19998793,2.9278073 ;zone No.8

; ===apply a horizontal velocity to the point of interest===

bound interior xvel -0.05 range -0.1 0.1 2.9 3.1

cycle 2000

;;======================

; pull the point towards right

;;======================

; ===record horizontal displacement===

history xdisplace -4.3449522E-6,2.9948833

; ===record shear stress===

history sxy -0.20002633,3.0619617 ;zone No.1

history sxy -0.066677965,3.1953204 ;zone No.2

history sxy 0.06666922,3.1953204 ;zone No.3

history sxy 0.20001763,3.0619617 ;zone No.4

history sxy 0.2000131,2.9278078 ;zone No.5

history sxy 0.0666803,2.7944427 ;zone No.6

history sxy -0.06665472,2.7944424 ;zone No.7

history sxy -0.19998793,2.9278073 ;zone No.8

; ===apply a horizontal velocity to the point of interest===

bound interior xvel 0.05 range -0.1 0.1 2.9 3.1

cycle 2000

dv=100 m, dh=50 m

config

round 0.1

edge 0.2

set ovtol 0.1

; === model geometry===

block -60.0,-100.0 -60.0,100.0 60.0,100.0 60.0,-100.0

crack -100.0 1.0 100.0 1.0 ;top of rock layer

crack -100.0 -1.0 100.0 -1.0 ;bottom of rock layer

crack -100.0 3.0 100.0 3.0 ;the existing rock discontinuity

crack 10.0 -1.0 10.0 1.0 ;right side of the excavation

crack -10.0 -1.0 -10.0 1.0 ;left side of the excavation

; ===generate finite-difference zones===

gen quad 0.4

; ===assign constitutive models and material properties===

;

def _parameter

```
_E1 = 70.0E9 ;rock
_nu1 = 0.2 ;rock
_k1 = _E1/(3*(1-2*_nu1))
_g1 = _E1/(2*(1+_nu1))
end _parameter
;
prop mat=1 d=2670.0 k=_k1 g=_g1
change mat=1
set jcondf=3
change jcons=3
prop jmat=1 jkn=50.0E9 jks=50.0E9 jen=0.0 jes=0.0 jfric=30.0 jif=59.3 jr=1.0e-4 ;the existing rock discontinuity
change jmat=1 range -101.0 101.0 2.9 3.1
prop jmat=2 jkn=100.0E9 jks=100.0E9 jfric=100.0 jcoh=1.0E20 jdil=100.0 jten=1.0E20 ;fictitious joints
change jmat=2 range -101.0 101.0 -1.1 1.1
; ===apply boundary conditions===
insitu stress -5.25E6 0.0 -17.5E6
bound stress -5.25E6 0.0 -17.5E6
bound xvel=0.0 range 59.9,60.1 -110.0,110.0 ;right
bound xvel=0.0 range -60.1,-59.9 -110.0,110.0 ;left
bound xvel=0.0 range -100.0,100.0 99.9,100.1 ;top
bound yvel=0.0 range -100.0,100.0 99.9,100.1 ;top
bound xvel=0.0 range -100.0,100.0 -100.1,-99.9 ;bottom
bound yvel=0.0 range -100.0,100.0 -100.1,-99.9 ;bottom
solve
; ===finish the excavation===
```

```
delete range -10.0 10.0 -1.0 1.0
solve
;;======================
; pull the point towards left
;;======================
; ===record horizontal displacement===
history xdisplace -4.3449522E-6,2.9948833
; ===record shear stress===
history sxy -0.20002633,3.0619617 ;zone No.1
history sxy -0.066677965,3.1953204 ;zone No.2
history sxy 0.06666922,3.1953204 ;zone No.3
history sxy 0.20001763,3.0619617 ;zone No.4
history sxy 0.2000131,2.9278078 ;zone No.5
history sxy 0.0666803,2.7944427 ;zone No.6
history sxy -0.06665472,2.7944424 ;zone No.7
history sxy -0.19998793,2.9278073 ;zone No.8
; ===apply a horizontal velocity to the point of interest===
bound interior xvel -0.05 range -0.1 0.1 2.9 3.1
cycle 2000
;;======================
; pull the point towards right
;;======================
; ===record horizontal displacement===
history xdisplace -4.3449522E-6,2.9948833
; ===record shear stress===
history sxy -0.20002633,3.0619617 ;zone No.1
history sxy -0.066677965,3.1953204 ;zone No.2
```

history sxy 0.06666922,3.1953204 ;zone No.3

history sxy 0.20001763,3.0619617 ;zone No.4

history sxy 0.2000131,2.9278078 ;zone No.5

history sxy 0.0666803,2.7944427 ;zone No.6

history sxy -0.06665472,2.7944424 ;zone No.7

history sxy -0.19998793,2.9278073 ;zone No.8

; ===apply a horizontal velocity to the point of interest===

bound interior xvel 0.05 range -0.1 0.1 2.9 3.1

cycle 2000

dv=100 m, dh=60 m

config

round 0.1

edge 0.2

set ovtol 0.1

; === model geometry===

block -70.0,-100.0 -70.0,100.0 70.0,100.0 70.0,-100.0

crack -100.0 1.0 100.0 1.0 ;top of rock layer

crack -100.0 -1.0 100.0 -1.0 ;bottom of rock layer

crack -100.0 3.0 100.0 3.0 ;the existing rock discontinuity

crack 10.0 -1.0 10.0 1.0 ;right side of the excavation

crack -10.0 -1.0 -10.0 1.0 ;left side of the excavation

; ===generate finite-difference zones===

gen quad 0.4

; ===assign constitutive models and material properties===

;

def _parameter

_E1 = 70.0E9 ;rock

```
_nu1 = 0.2 ;rock
_k1 = _E1/(3*(1-2*_nu1))
_g1 = _E1/(2*(1+_nu1))
end _parameter
;
prop mat=1 d=2670.0 k=_k1 g=_g1
change mat=1
set jcondf=3
change jcons=3
prop jmat=1 jkn=50.0E9 jks=50.0E9 jen=0.0 jes=0.0 jfric=30.0 jif=59.3 jr=1.0e-4 ;the existing rock discontinuity
change jmat=1 range -101.0 101.0 2.9 3.1
prop jmat=2 jkn=100.0E9 jks=100.0E9 jfric=100.0 jcoh=1.0E20 jdil=100.0 jten=1.0E20 ;fictitious joints
change jmat=2 range -101.0 101.0 -1.1 1.1
; ===apply boundary conditions===
insitu stress -5.25E6 0.0 -17.5E6
bound stress -5.25E6 0.0 -17.5E6
bound xvel=0.0 range 69.9,70.1 -110.0,110.0 ;right
bound xvel=0.0 range -70.1,-69.9 -110.0,110.0 ;left
bound xvel=0.0 range -100.0,100.0 99.9,100.1 ;top
bound yvel=0.0 range -100.0,100.0 99.9,100.1 ;top
bound xvel=0.0 range -100.0,100.0 -100.1,-99.9 ;bottom
bound yvel=0.0 range -100.0,100.0 -100.1,-99.9 ;bottom
solve
; ===finish the excavation===
delete range -10.0 10.0 -1.0 1.0
```

```
solve
;;======================
; pull the point towards left
;;======================
; ===record horizontal displacement===
history xdisplace -4.3449522E-6,2.9948833
; ===record shear stress===
history sxy -0.20002633,3.0619617 ;zone No.1
history sxy -0.066677965,3.1953204 ;zone No.2
history sxy 0.06666922,3.1953204 ;zone No.3
history sxy 0.20001763,3.0619617 ;zone No.4
history sxy 0.2000131,2.9278078 ;zone No.5
history sxy 0.0666803,2.7944427 ;zone No.6
history sxy -0.06665472,2.7944424 ;zone No.7
history sxy -0.19998793,2.9278073 ;zone No.8
; ===apply a horizontal velocity to the point of interest===
bound interior xvel -0.05 range -0.1 0.1 2.9 3.1
cycle 2000
;;======================
; pull the point towards right
;;======================
; ===record horizontal displacement===
history xdisplace -4.3449522E-6,2.9948833
; ===record shear stress===
history sxy -0.20002633,3.0619617 ;zone No.1
history sxy -0.066677965,3.1953204 ;zone No.2
history sxy 0.06666922,3.1953204 ;zone No.3
```

history sxy 0.20001763,3.0619617 ;zone No.4

history sxy 0.2000131,2.9278078 ;zone No.5

history sxy 0.0666803,2.7944427 ;zone No.6

history sxy -0.06665472,2.7944424 ;zone No.7

history sxy -0.19998793,2.9278073 ;zone No.8

; ===apply a horizontal velocity to the point of interest===

bound interior xvel 0.05 range -0.1 0.1 2.9 3.1

cycle 2000

dv=100 m, dh=70 m

config

round 0.1

edge 0.2

set ovtol 0.1

; === model geometry===

block -80.0,-100.0 -80.0,100.0 80.0,100.0 80.0,-100.0

crack -100.0 1.0 100.0 1.0 ;top of rock layer

crack -100.0 -1.0 100.0 -1.0 ;bottom of rock layer

crack -100.0 3.0 100.0 3.0 ;the existing rock discontinuity

crack 10.0 -1.0 10.0 1.0 ;right side of the excavation

crack -10.0 -1.0 -10.0 1.0 ;left side of the excavation

; ===generate finite-difference zones===

gen quad 0.4

; ===assign constitutive models and material properties===

;

def _parameter

_E1 = 70.0E9 ;rock

_nu1 = 0.2 ;rock

```
_k1 = _E1/(3*(1-2*_nu1))
_g1 = _E1/(2*(1+_nu1))
end _parameter
;
prop mat=1 d=2670.0 k=_k1 g=_g1
change mat=1
set jcondf=3
change jcons=3
prop jmat=1 jkn=50.0E9 jks=50.0E9 jen=0.0 jes=0.0 jfric=30.0 jif=59.3 jr=1.0e-4 ;the existing rock discontinuity
change jmat=1 range -101.0 101.0 2.9 3.1
prop jmat=2 jkn=100.0E9 jks=100.0E9 jfric=100.0 jcoh=1.0E20 jdil=100.0 jten=1.0E20 ;fictitious joints
change jmat=2 range -101.0 101.0 -1.1 1.1
; ===apply boundary conditions===
insitu stress -5.25E6 0.0 -17.5E6
bound stress -5.25E6 0.0 -17.5E6
bound xvel=0.0 range 79.9,80.1 -110.0,110.0 ;right
bound xvel=0.0 range -80.1,-79.9 -110.0,110.0 ;left
bound xvel=0.0 range -100.0,100.0 99.9,100.1 ;top
bound yvel=0.0 range -100.0,100.0 99.9,100.1 ;top
bound xvel=0.0 range -100.0,100.0 -100.1,-99.9 ;bottom
bound yvel=0.0 range -100.0,100.0 -100.1,-99.9 ;bottom
solve
; ===finish the excavation===
delete range -10.0 10.0 -1.0 1.0
solve
```

```
;;======================
; pull the point towards left
;;======================
; ===record horizontal displacement===
history xdisplace -4.3449522E-6,2.9948833
; ===record shear stress===
history sxy -0.20002633,3.0619617 ;zone No.1
history sxy -0.066677965,3.1953204 ;zone No.2
history sxy 0.06666922,3.1953204 ;zone No.3
history sxy 0.20001763,3.0619617 ;zone No.4
history sxy 0.2000131,2.9278078 ;zone No.5
history sxy 0.0666803,2.7944427 ;zone No.6
history sxy -0.06665472,2.7944424 ;zone No.7
history sxy -0.19998793,2.9278073 ;zone No.8
; ===apply a horizontal velocity to the point of interest===
bound interior xvel -0.05 range -0.1 0.1 2.9 3.1
cycle 2000
;;======================
; pull the point towards right
;;======================
; ===record horizontal displacement===
history xdisplace -4.3449522E-6,2.9948833
; ===record shear stress===
history sxy -0.20002633,3.0619617 ;zone No.1
history sxy -0.066677965,3.1953204 ;zone No.2
history sxy 0.06666922,3.1953204 ;zone No.3
history sxy 0.20001763,3.0619617 ;zone No.4
```

history sxy 0.2000131,2.9278078 ;zone No.5

history sxy 0.0666803,2.7944427 ;zone No.6

history sxy -0.06665472,2.7944424 ;zone No.7

history sxy -0.19998793,2.9278073 ;zone No.8

; ===apply a horizontal velocity to the point of interest===

bound interior xvel 0.05 range -0.1 0.1 2.9 3.1

cycle 2000

Varying dv

dv=30 m, dh=60 m

config

round 0.1

edge 0.2

set ovtol 0.1

; === model geometry===

block -70.0,-31.0 -70.0,31.0 70.0,31.0 70.0,-31.0

crack -100.0 1.0 100.0 1.0 ;top of rock layer

crack -100.0 -1.0 100.0 -1.0 ;bottom of rock layer

crack -100.0 3.0 100.0 3.0 ;the existing rock discontinuity

crack 10.0 -1.0 10.0 1.0 ;right side of the excavation

crack -10.0 -1.0 -10.0 1.0 ;left side of the excavation

; ===generate finite-difference zones===

gen quad 0.4

; ===assign constitutive models and material properties===

;

def _parameter

_E1 = 70.0E9 ;rock

_nu1 = 0.2 ;rock

```
_k1 = _E1/(3*(1-2*_nu1))
_g1 = _E1/(2*(1+_nu1))
end _parameter
;
prop mat=1 d=2670.0 k=_k1 g=_g1
change mat=1
set jcondf=3
change jcons=3
prop jmat=1 jkn=50.0E9 jks=50.0E9 jen=0.0 jes=0.0 jfric=30.0 jif=59.3 jr=1.0e-4 ;the existing rock discontinuity
change jmat=1 range -101.0 101.0 2.9 3.1
prop jmat=2 jkn=100.0E9 jks=100.0E9 jfric=100.0 jcoh=1.0E20 jdil=100.0 jten=1.0E20 ;fictitious joints
change jmat=2 range -101.0 101.0 -1.1 1.1
; ===apply boundary conditions===
insitu stress -5.25E6 0.0 -17.5E6
bound stress -5.25E6 0.0 -17.5E6
bound xvel=0.0 range 69.9,70.1 -110.0,110.0 ;right
bound xvel=0.0 range -70.1,-69.9 -110.0,110.0 ;left
bound xvel=0.0 range -100.0,100.0 30.9,31.1 ;top
bound yvel=0.0 range -100.0,100.0 30.9,31.1 ;top
bound xvel=0.0 range -100.0,100.0 -31.1,-30.9 ;bottom
bound yvel=0.0 range -100.0,100.0 -31.1,-30.9 ;bottom
solve
; ===finish the excavation===
delete range -10.0 10.0 -1.0 1.0
solve
```

```
;;======================
; pull the point towards left
;;======================
; ===record horizontal displacement===
history xdisplace -4.3449522E-6,2.9948833
; ===record shear stress===
history sxy -0.20002633,3.0619617 ;zone No.1
history sxy -0.066677965,3.1953204 ;zone No.2
history sxy 0.06666922,3.1953204 ;zone No.3
history sxy 0.20001763,3.0619617 ;zone No.4
history sxy 0.2000131,2.9278078 ;zone No.5
history sxy 0.0666803,2.7944427 ;zone No.6
history sxy -0.06665472,2.7944424 ;zone No.7
history sxy -0.19998793,2.9278073 ;zone No.8
; ===apply a horizontal velocity to the point of interest===
bound interior xvel -0.05 range -0.1 0.1 2.9 3.1
cycle 2000
;;======================
; pull the point towards right
;;======================
; ===record horizontal displacement===
history xdisplace -4.3449522E-6,2.9948833
; ===record shear stress===
history sxy -0.20002633,3.0619617 ;zone No.1
history sxy -0.066677965,3.1953204 ;zone No.2
history sxy 0.06666922,3.1953204 ;zone No.3
history sxy 0.20001763,3.0619617 ;zone No.4
```

history sxy 0.2000131,2.9278078 ;zone No.5

history sxy 0.0666803,2.7944427 ;zone No.6

history sxy -0.06665472,2.7944424 ;zone No.7

history sxy -0.19998793,2.9278073 ;zone No.8

; ===apply a horizontal velocity to the point of interest===

bound interior xvel 0.05 range -0.1 0.1 2.9 3.1

cycle 2000

dv=40 m, dh=60 m

config

round 0.1

edge 0.2

set ovtol 0.1

; === model geometry===

block -70.0,-41.0 -70.0,41.0 70.0,41.0 70.0,-41.0

crack -100.0 1.0 100.0 1.0 ;top of rock layer

crack -100.0 -1.0 100.0 -1.0 ;bottom of rock layer

crack -100.0 3.0 100.0 3.0 ;the existing rock discontinuity

crack 10.0 -1.0 10.0 1.0 ;right side of the excavation

crack -10.0 -1.0 -10.0 1.0 ;left side of the excavation

; ===generate finite-difference zones===

gen quad 0.4

; ===assign constitutive models and material properties===

;

def _parameter

_E1 = 70.0E9 ;rock

_nu1 = 0.2 ;rock

_k1 = _E1/(3*(1-2*_nu1))

```
_g1 = _E1/(2*(1+_nu1))
end _parameter
;
prop mat=1 d=2670.0 k=_k1 g=_g1
change mat=1
set jcondf=3
change jcons=3
prop jmat=1 jkn=50.0E9 jks=50.0E9 jen=0.0 jes=0.0 jfric=30.0 jif=59.3 jr=1.0e-4 ;the existing rock discontinuity
change jmat=1 range -101.0 101.0 2.9 3.1
prop jmat=2 jkn=100.0E9 jks=100.0E9 jfric=100.0 jcoh=1.0E20 jdil=100.0 jten=1.0E20 ;fictitious joints
change jmat=2 range -101.0 101.0 -1.1 1.1
; ===apply boundary conditions===
insitu stress -5.25E6 0.0 -17.5E6
bound stress -5.25E6 0.0 -17.5E6
bound xvel=0.0 range 69.9,70.1 -110.0,110.0 ;right
bound xvel=0.0 range -70.1,-69.9 -110.0,110.0 ;left
bound xvel=0.0 range -100.0,100.0 40.9,41.1 ;top
bound yvel=0.0 range -100.0,100.0 40.9,41.1 ;top
bound xvel=0.0 range -100.0,100.0 -41.1,-40.9 ;bottom
bound yvel=0.0 range -100.0,100.0 -41.1,-40.9 ;bottom
solve
; ===finish the excavation===
delete range -10.0 10.0 -1.0 1.0
solve
;;=====================
```

; pull the point towards left

;;======================

; ===record horizontal displacement===

history xdisplace -4.3449522E-6,2.9948833

; ===record shear stress===

history sxy -0.20002633,3.0619617 ;zone No.1

history sxy -0.066677965,3.1953204 ;zone No.2

history sxy 0.06666922,3.1953204 ;zone No.3

history sxy 0.20001763,3.0619617 ;zone No.4

history sxy 0.2000131,2.9278078 ;zone No.5

history sxy 0.0666803,2.7944427 ;zone No.6

history sxy -0.06665472,2.7944424 ;zone No.7

history sxy -0.19998793,2.9278073 ;zone No.8

; ===apply a horizontal velocity to the point of interest===

bound interior xvel -0.05 range -0.1 0.1 2.9 3.1

cycle 2000

;;======================

; pull the point towards right

;;======================

; ===record horizontal displacement===

history xdisplace -4.3449522E-6,2.9948833

; ===record shear stress===

history sxy -0.20002633,3.0619617 ;zone No.1

history sxy -0.066677965,3.1953204 ;zone No.2

history sxy 0.06666922,3.1953204 ;zone No.3

history sxy 0.20001763,3.0619617 ;zone No.4

history sxy 0.2000131,2.9278078 ;zone No.5

history sxy 0.0666803,2.7944427 ;zone No.6

history sxy -0.06665472,2.7944424 ;zone No.7

history sxy -0.19998793,2.9278073 ;zone No.8

; ===apply a horizontal velocity to the point of interest===

bound interior xvel 0.05 range -0.1 0.1 2.9 3.1

cycle 2000

dv=50 m, dh=60 m

config

round 0.1

edge 0.2

set ovtol 0.1

; === model geometry===

block -70.0,-51.0 -70.0,51.0 70.0,51.0 70.0,-51.0

crack -100.0 1.0 100.0 1.0 ;top of rock layer

crack -100.0 -1.0 100.0 -1.0 ;bottom of rock layer

crack -100.0 3.0 100.0 3.0 ;the existing rock discontinuity

crack 10.0 -1.0 10.0 1.0 ;right side of the excavation

crack -10.0 -1.0 -10.0 1.0 ;left side of the excavation

; ===generate finite-difference zones===

gen quad 0.4

; ===assign constitutive models and material properties===

;

def _parameter

_E1 = 70.0E9 ;rock

_nu1 = 0.2 ;rock

_k1 = _E1/(3*(1-2*_nu1))

_g1 = _E1/(2*(1+_nu1))

```
end _parameter
;
prop mat=1 d=2670.0 k=_k1 g=_g1
change mat=1
set jcondf=3
change jcons=3
prop jmat=1 jkn=50.0E9 jks=50.0E9 jen=0.0 jes=0.0 jfric=30.0 jif=59.3 jr=1.0e-4 ;the existing rock discontinuity
change jmat=1 range -101.0 101.0 2.9 3.1
prop jmat=2 jkn=100.0E9 jks=100.0E9 jfric=100.0 jcoh=1.0E20 jdil=100.0 jten=1.0E20 ;fictitious joints
change jmat=2 range -101.0 101.0 -1.1 1.1
; ===apply boundary conditions===
insitu stress -5.25E6 0.0 -17.5E6
bound stress -5.25E6 0.0 -17.5E6
bound xvel=0.0 range 69.9,70.1 -110.0,110.0 ;right
bound xvel=0.0 range -70.1,-69.9 -110.0,110.0 ;left
bound xvel=0.0 range -100.0,100.0 50.9,51.1 ;top
bound yvel=0.0 range -100.0,100.0 50.9,51.1 ;top
bound xvel=0.0 range -100.0,100.0 -51.1,-50.9 ;bottom
bound yvel=0.0 range -100.0,100.0 -51.1,-50.9 ;bottom
solve
; ===finish the excavation===
delete range -10.0 10.0 -1.0 1.0
solve
;;=====================
; pull the point towards left
```

```
;;======================
; ===record horizontal displacement===
history xdisplace -4.3449522E-6,2.9948833
; ===record shear stress===
history sxy -0.20002633,3.0619617 ;zone No.1
history sxy -0.066677965,3.1953204 ;zone No.2
history sxy 0.06666922,3.1953204 ;zone No.3
history sxy 0.20001763,3.0619617 ;zone No.4
history sxy 0.2000131,2.9278078 ;zone No.5
history sxy 0.0666803,2.7944427 ;zone No.6
history sxy -0.06665472,2.7944424 ;zone No.7
history sxy -0.19998793,2.9278073 ;zone No.8
; ===apply a horizontal velocity to the point of interest===
bound interior xvel -0.05 range -0.1 0.1 2.9 3.1
cycle 2000
;;======================
; pull the point towards right
;;======================
; ===record horizontal displacement===
history xdisplace -4.3449522E-6,2.9948833
; ===record shear stress===
history sxy -0.20002633,3.0619617 ;zone No.1
history sxy -0.066677965,3.1953204 ;zone No.2
history sxy 0.06666922,3.1953204 ;zone No.3
history sxy 0.20001763,3.0619617 ;zone No.4
history sxy 0.2000131,2.9278078 ;zone No.5
history sxy 0.0666803,2.7944427 ;zone No.6
```

history sxy -0.06665472,2.7944424 ;zone No.7

history sxy -0.19998793,2.9278073 ;zone No.8

; ===apply a horizontal velocity to the point of interest===

bound interior xvel 0.05 range -0.1 0.1 2.9 3.1

cycle 2000

dv=60 m, dh=60 m

config

round 0.1

edge 0.2

set ovtol 0.1

; === model geometry===

block -70.0,-61.0 -70.0,61.0 70.0,61.0 70.0,-61.0

crack -100.0 1.0 100.0 1.0 ;top of rock layer

crack -100.0 -1.0 100.0 -1.0 ;bottom of rock layer

crack -100.0 3.0 100.0 3.0 ;the existing rock discontinuity

crack 10.0 -1.0 10.0 1.0 ;right side of the excavation

crack -10.0 -1.0 -10.0 1.0 ;left side of the excavation

; ===generate finite-difference zones===

gen quad 0.4

; ===assign constitutive models and material properties===

;

def _parameter

_E1 = 70.0E9 ;rock

_nu1 = 0.2 ;rock

_k1 = _E1/(3*(1-2*_nu1))

_g1 = _E1/(2*(1+_nu1))

end _parameter

```
;
prop mat=1 d=2670.0 k=_k1 g=_g1
change mat=1
set jcondf=3
change jcons=3
prop jmat=1 jkn=50.0E9 jks=50.0E9 jen=0.0 jes=0.0 jfric=30.0 jif=59.3 jr=1.0e-4 ;the existing rock discontinuity
change jmat=1 range -101.0 101.0 2.9 3.1
prop jmat=2 jkn=100.0E9 jks=100.0E9 jfric=100.0 jcoh=1.0E20 jdil=100.0 jten=1.0E20 ;fictitious joints
change jmat=2 range -101.0 101.0 -1.1 1.1
; ===apply boundary conditions===
insitu stress -5.25E6 0.0 -17.5E6
bound stress -5.25E6 0.0 -17.5E6
bound xvel=0.0 range 69.9,70.1 -110.0,110.0 ;right
bound xvel=0.0 range -70.1,-69.9 -110.0,110.0 ;left
bound xvel=0.0 range -100.0,100.0 60.9,61.1 ;top
bound yvel=0.0 range -100.0,100.0 60.9,61.1 ;top
bound xvel=0.0 range -100.0,100.0 -61.1,-60.9 ;bottom
bound yvel=0.0 range -100.0,100.0 -61.1,-60.9 ;bottom
solve
; ===finish the excavation===
delete range -10.0 10.0 -1.0 1.0
solve
;;======================
; pull the point towards left
;;======================
```

; ===record horizontal displacement===

history xdisplace -4.3449522E-6,2.9948833

; ===record shear stress===

history sxy -0.20002633,3.0619617 ;zone No.1

history sxy -0.066677965,3.1953204 ;zone No.2

history sxy 0.06666922,3.1953204 ;zone No.3

history sxy 0.20001763,3.0619617 ;zone No.4

history sxy 0.2000131,2.9278078 ;zone No.5

history sxy 0.0666803,2.7944427 ;zone No.6

history sxy -0.06665472,2.7944424 ;zone No.7

history sxy -0.19998793,2.9278073 ;zone No.8

; ===apply a horizontal velocity to the point of interest===

bound interior xvel -0.05 range -0.1 0.1 2.9 3.1

cycle 2000

;;======================

; pull the point towards right

;;======================

; ===record horizontal displacement===

history xdisplace -4.3449522E-6,2.9948833

; ===record shear stress===

history sxy -0.20002633,3.0619617 ;zone No.1

history sxy -0.066677965,3.1953204 ;zone No.2

history sxy 0.06666922,3.1953204 ;zone No.3

history sxy 0.20001763,3.0619617 ;zone No.4

history sxy 0.2000131,2.9278078 ;zone No.5

history sxy 0.0666803,2.7944427 ;zone No.6

history sxy -0.06665472,2.7944424 ;zone No.7

history sxy -0.19998793,2.9278073 ;zone No.8

; ===apply a horizontal velocity to the point of interest===

bound interior xvel 0.05 range -0.1 0.1 2.9 3.1

cycle 2000

dv=70 m, dh=60 m

config

round 0.1

edge 0.2

set ovtol 0.1

; === model geometry===

block -70.0,-71.0 -70.0,71.0 70.0,71.0 70.0,-71.0

crack -100.0 1.0 100.0 1.0 ;top of rock layer

crack -100.0 -1.0 100.0 -1.0 ;bottom of rock layer

crack -100.0 3.0 100.0 3.0 ;the existing rock discontinuity

crack 10.0 -1.0 10.0 1.0 ;right side of the excavation

crack -10.0 -1.0 -10.0 1.0 ;left side of the excavation

; ===generate finite-difference zones===

gen quad 0.4

; ===assign constitutive models and material properties===

;

def _parameter

_E1 = 70.0E9 ;rock

_nu1 = 0.2 ;rock

_k1 = _E1/(3*(1-2*_nu1))

_g1 = _E1/(2*(1+_nu1))

end _parameter

;

```
prop mat=1 d=2670.0 k=_k1 g=_g1
change mat=1
set jcondf=3
change jcons=3
prop jmat=1 jkn=50.0E9 jks=50.0E9 jen=0.0 jes=0.0 jfric=30.0 jif=59.3 jr=1.0e-4 ;the existing rock discontinuity
change jmat=1 range -101.0 101.0 2.9 3.1
prop jmat=2 jkn=100.0E9 jks=100.0E9 jfric=100.0 jcoh=1.0E20 jdil=100.0 jten=1.0E20 ;fictitious joints
change jmat=2 range -101.0 101.0 -1.1 1.1
; ===apply boundary conditions===
insitu stress -5.25E6 0.0 -17.5E6
bound stress -5.25E6 0.0 -17.5E6
bound xvel=0.0 range 69.9,70.1 -110.0,110.0 ;right
bound xvel=0.0 range -70.1,-69.9 -110.0,110.0 ;left
bound xvel=0.0 range -100.0,100.0 70.9,71.1 ;top
bound yvel=0.0 range -100.0,100.0 70.9,71.1 ;top
bound xvel=0.0 range -100.0,100.0 -71.1,-70.9 ;bottom
bound yvel=0.0 range -100.0,100.0 -71.1,-70.9 ;bottom
solve
; ===finish the excavation===
delete range -10.0 10.0 -1.0 1.0
solve
;;=====================
; pull the point towards left
;;=====================
; ===record horizontal displacement===
```

```
history xdisplace -4.3449522E-6,2.9948833
; ===record shear stress===
history sxy -0.20002633,3.0619617 ;zone No.1
history sxy -0.066677965,3.1953204 ;zone No.2
history sxy 0.06666922,3.1953204 ;zone No.3
history sxy 0.20001763,3.0619617 ;zone No.4
history sxy 0.2000131,2.9278078 ;zone No.5
history sxy 0.0666803,2.7944427 ;zone No.6
history sxy -0.06665472,2.7944424 ;zone No.7
history sxy -0.19998793,2.9278073 ;zone No.8
; ===apply a horizontal velocity to the point of interest===
bound interior xvel -0.05 range -0.1 0.1 2.9 3.1
cycle 2000
;;======================
; pull the point towards right
;;======================
; ===record horizontal displacement===
history xdisplace -4.3449522E-6,2.9948833
; ===record shear stress===
history sxy -0.20002633,3.0619617 ;zone No.1
history sxy -0.066677965,3.1953204 ;zone No.2
history sxy 0.06666922,3.1953204 ;zone No.3
history sxy 0.20001763,3.0619617 ;zone No.4
history sxy 0.2000131,2.9278078 ;zone No.5
history sxy 0.0666803,2.7944427 ;zone No.6
history sxy -0.06665472,2.7944424 ;zone No.7
history sxy -0.19998793,2.9278073 ;zone No.8
```

; ===apply a horizontal velocity to the point of interest===

bound interior xvel 0.05 range -0.1 0.1 2.9 3.1

cycle 2000

dv=80 m, dh=60 m

config

round 0.1

edge 0.2

set ovtol 0.1

; === model geometry===

block -70.0,-81.0 -70.0,81.0 70.0,81.0 70.0,-81.0

crack -100.0 1.0 100.0 1.0 ;top of rock layer

crack -100.0 -1.0 100.0 -1.0 ;bottom of rock layer

crack -100.0 3.0 100.0 3.0 ;the existing rock discontinuity

crack 10.0 -1.0 10.0 1.0 ;right side of the excavation

crack -10.0 -1.0 -10.0 1.0 ;left side of the excavation

; ===generate finite-difference zones===

gen quad 0.4

; ===assign constitutive models and material properties===

;

def _parameter

_E1 = 70.0E9 ;rock

_nu1 = 0.2 ;rock

_k1 = _E1/(3*(1-2*_nu1))

_g1 = _E1/(2*(1+_nu1))

end _parameter

;

prop mat=1 d=2670.0 k=_k1 g=_g1

change mat=1

set jcondf=3

change jcons=3

prop jmat=1 jkn=50.0E9 jks=50.0E9 jen=0.0 jes=0.0 jfric=30.0 jif=59.3 jr=1.0e-4 ;the existing rock discontinuity

change jmat=1 range -101.0 101.0 2.9 3.1

prop jmat=2 jkn=100.0E9 jks=100.0E9 jfric=100.0 jcoh=1.0E20 jdil=100.0 jten=1.0E20 ;fictitious joints

change jmat=2 range -101.0 101.0 -1.1 1.1

; ===apply boundary conditions===

insitu stress -5.25E6 0.0 -17.5E6

bound stress -5.25E6 0.0 -17.5E6

bound xvel=0.0 range 69.9,70.1 -110.0,110.0 ;right

bound xvel=0.0 range -70.1,-69.9 -110.0,110.0 ;left

bound xvel=0.0 range -100.0,100.0 80.9,81.1 ;top

bound yvel=0.0 range -100.0,100.0 80.9,81.1 ;top

bound xvel=0.0 range -100.0,100.0 -81.1,-80.9 ;bottom

bound yvel=0.0 range -100.0,100.0 -81.1,-80.9 ;bottom

solve

; ===finish the excavation===

delete range -10.0 10.0 -1.0 1.0

solve

;;======================

; pull the point towards left

;;======================

; ===record horizontal displacement===

history xdisplace -4.3449522E-6,2.9948833

; ===record shear stress===

history sxy -0.20002633,3.0619617 ;zone No.1

history sxy -0.066677965,3.1953204 ;zone No.2

history sxy 0.06666922,3.1953204 ;zone No.3

history sxy 0.20001763,3.0619617 ;zone No.4

history sxy 0.2000131,2.9278078 ;zone No.5

history sxy 0.0666803,2.7944427 ;zone No.6

history sxy -0.06665472,2.7944424 ;zone No.7

history sxy -0.19998793,2.9278073 ;zone No.8

; ===apply a horizontal velocity to the point of interest===

bound interior xvel -0.05 range -0.1 0.1 2.9 3.1

cycle 2000

;;======================

; pull the point towards right

;;======================

; ===record horizontal displacement===

history xdisplace -4.3449522E-6,2.9948833

; ===record shear stress===

history sxy -0.20002633,3.0619617 ;zone No.1

history sxy -0.066677965,3.1953204 ;zone No.2

history sxy 0.06666922,3.1953204 ;zone No.3

history sxy 0.20001763,3.0619617 ;zone No.4

history sxy 0.2000131,2.9278078 ;zone No.5

history sxy 0.0666803,2.7944427 ;zone No.6

history sxy -0.06665472,2.7944424 ;zone No.7

history sxy -0.19998793,2.9278073 ;zone No.8

; ===apply a horizontal velocity to the point of interest===

```
bound interior xvel 0.05 range -0.1 0.1 2.9 3.1
cycle 2000
```
dv=90 m, dh=60 m
```
config
round 0.1
edge 0.2
set ovtol 0.1
; === model geometry===
block -70.0,-91.0 -70.0,91.0 70.0,91.0 70.0,-91.0
crack -100.0 1.0 100.0 1.0 ;top of rock layer
crack -100.0 -1.0 100.0 -1.0 ;bottom of rock layer
crack -100.0 3.0 100.0 3.0 ;the existing rock discontinuity
crack 10.0 -1.0 10.0 1.0 ;right side of the excavation
crack -10.0 -1.0 -10.0 1.0 ;left side of the excavation
; ===generate finite-difference zones===
gen quad 0.4
; ===assign constitutive models and material properties===
;
def _parameter
_E1 = 70.0E9 ;rock
_nu1 = 0.2 ;rock
_k1 = _E1/(3*(1-2*_nu1))
_g1 = _E1/(2*(1+_nu1))
end _parameter
;
prop mat=1 d=2670.0 k=_k1 g=_g1
change mat=1
```

```
set jcondf=3
change jcons=3
prop jmat=1 jkn=50.0E9 jks=50.0E9 jen=0.0 jes=0.0 jfric=30.0 jif=59.3 jr=1.0e-4 ;the existing rock discontinuity
change jmat=1 range -101.0 101.0 2.9 3.1
prop jmat=2 jkn=100.0E9 jks=100.0E9 jfric=100.0 jcoh=1.0E20 jdil=100.0 jten=1.0E20 ;fictitious joints
change jmat=2 range -101.0 101.0 -1.1 1.1
; ===apply boundary conditions===
insitu stress -5.25E6 0.0 -17.5E6
bound stress -5.25E6 0.0 -17.5E6
bound xvel=0.0 range 69.9,70.1 -110.0,110.0 ;right
bound xvel=0.0 range -70.1,-69.9 -110.0,110.0 ;left
bound xvel=0.0 range -100.0,100.0 90.9,91.1 ;top
bound yvel=0.0 range -100.0,100.0 90.9,91.1 ;top
bound xvel=0.0 range -100.0,100.0 -91.1,-90.9 ;bottom
bound yvel=0.0 range -100.0,100.0 -91.1,-90.9 ;bottom
solve
; ===finish the excavation===
delete range -10.0 10.0 -1.0 1.0
solve
;;======================
; pull the point towards left
;;======================
; ===record horizontal displacement===
history xdisplace -4.3449522E-6,2.9948833
; ===record shear stress===
```

history sxy -0.20002633,3.0619617 ;zone No.1

history sxy -0.066677965,3.1953204 ;zone No.2

history sxy 0.06666922,3.1953204 ;zone No.3

history sxy 0.20001763,3.0619617 ;zone No.4

history sxy 0.2000131,2.9278078 ;zone No.5

history sxy 0.0666803,2.7944427 ;zone No.6

history sxy -0.06665472,2.7944424 ;zone No.7

history sxy -0.19998793,2.9278073 ;zone No.8

; ===apply a horizontal velocity to the point of interest===

bound interior xvel -0.05 range -0.1 0.1 2.9 3.1

cycle 2000

;;======================

; pull the point towards right

;;======================

; ===record horizontal displacement===

history xdisplace -4.3449522E-6,2.9948833

; ===record shear stress===

history sxy -0.20002633,3.0619617 ;zone No.1

history sxy -0.066677965,3.1953204 ;zone No.2

history sxy 0.06666922,3.1953204 ;zone No.3

history sxy 0.20001763,3.0619617 ;zone No.4

history sxy 0.2000131,2.9278078 ;zone No.5

history sxy 0.0666803,2.7944427 ;zone No.6

history sxy -0.06665472,2.7944424 ;zone No.7

history sxy -0.19998793,2.9278073 ;zone No.8

; ===apply a horizontal velocity to the point of interest===

bound interior xvel 0.05 range -0.1 0.1 2.9 3.1

```
cycle 2000
dv=100 m, dh=60 m
config
round 0.1
edge 0.2
set ovtol 0.1
; === model geometry===
block -70.0,-101.0 -70.0,101.0 70.0,101.0 70.0,-101.0
crack -100.0 1.0 100.0 1.0 ;top of rock layer
crack -100.0 -1.0 100.0 -1.0 ;bottom of rock layer
crack -100.0 3.0 100.0 3.0 ;the existing rock discontinuity
crack 10.0 -1.0 10.0 1.0 ;right side of the excavation
crack -10.0 -1.0 -10.0 1.0 ;left side of the excavation
; ===generate finite-difference zones===
gen quad 0.4
; ===assign constitutive models and material properties===
;
def _parameter
_E1 = 70.0E9 ;rock
_nu1 = 0.2 ;rock
_k1 = _E1/(3*(1-2*_nu1))
_g1 = _E1/(2*(1+_nu1))
end _parameter
;
prop mat=1 d=2670.0 k=_k1 g=_g1
change mat=1
set jcondf=3
```

change jcons=3

prop jmat=1 jkn=50.0E9 jks=50.0E9 jen=0.0 jes=0.0 jfric=30.0 jif=59.3 jr=1.0e-4 ;the existing rock discontinuity

change jmat=1 range -101.0 101.0 2.9 3.1

prop jmat=2 jkn=100.0E9 jks=100.0E9 jfric=100.0 jcoh=1.0E20 jdil=100.0 jten=1.0E20 ;fictitious joints

change jmat=2 range -101.0 101.0 -1.1 1.1

; ===apply boundary conditions===

insitu stress -5.25E6 0.0 -17.5E6

bound stress -5.25E6 0.0 -17.5E6

bound xvel=0.0 range 69.9,70.1 -110.0,110.0 ;right

bound xvel=0.0 range -70.1,-69.9 -110.0,110.0 ;left

bound xvel=0.0 range -100.0,100.0 100.9,101.1 ;top

bound yvel=0.0 range -100.0,100.0 100.9,101.1 ;top

bound xvel=0.0 range -100.0,100.0 -101.1,-100.9 ;bottom

bound yvel=0.0 range -100.0,100.0 -101.1,-100.9 ;bottom

solve

; ===finish the excavation===

delete range -10.0 10.0 -1.0 1.0

solve

;;======================

; pull the point towards left

;;======================

; ===record horizontal displacement===

history xdisplace -4.3449522E-6,2.9948833

; ===record shear stress===

history sxy -0.20002633,3.0619617 ;zone No.1

history sxy -0.066677965,3.1953204 ;zone No.2

history sxy 0.06666922,3.1953204 ;zone No.3

history sxy 0.20001763,3.0619617 ;zone No.4

history sxy 0.2000131,2.9278078 ;zone No.5

history sxy 0.0666803,2.7944427 ;zone No.6

history sxy -0.06665472,2.7944424 ;zone No.7

history sxy -0.19998793,2.9278073 ;zone No.8

; ===apply a horizontal velocity to the point of interest===

bound interior xvel -0.05 range -0.1 0.1 2.9 3.1

cycle 2000

;;======================

; pull the point towards right

;;======================

; ===record horizontal displacement===

history xdisplace -4.3449522E-6,2.9948833

; ===record shear stress===

history sxy -0.20002633,3.0619617 ;zone No.1

history sxy -0.066677965,3.1953204 ;zone No.2

history sxy 0.06666922,3.1953204 ;zone No.3

history sxy 0.20001763,3.0619617 ;zone No.4

history sxy 0.2000131,2.9278078 ;zone No.5

history sxy 0.0666803,2.7944427 ;zone No.6

history sxy -0.06665472,2.7944424 ;zone No.7

history sxy -0.19998793,2.9278073 ;zone No.8

; ===apply a horizontal velocity to the point of interest===

bound interior xvel 0.05 range -0.1 0.1 2.9 3.1

cycle 2000

D.6 Discontinuity Stability Test

```
config
round 0.1
edge 0.2
set ovtol 0.2
; ===model geometry===
block -70.0,-80.0 -70.0,80.0 70.0,80.0 70.0,-80.0
crack -90.0 -1.0 90.0 -1.0 ;top of rock layer
crack -90.0 1.0 90.0 1.0 ;bottom of rock layer
crack -90.0 3.0 90.0 3.0 ;the existing rock discontinuity
crack 10.0 -1.0 10.0 1.0 ;right side of the excavation
crack -10.0 -1.0 -10.0 1.0 ;left side of the excavation
jset 90.0,0.0 2.5,0.0 0.0,0.0 0.25,0.0 10.0,0.0 range -10.0,10.0 -1.0,1.0
; ===generate finite-difference zones===
gen quad 0.4
; ===assign constitutive models and material properties===
;
def _parameter
_E1 = 70.0E9 ;rock
_nu1 = 0.2 ;rock
_k1 = _E1/(3*(1-2*_nu1))
_g1 = _E1/(2*(1+_nu1))
end _parameter
;
prop mat=1 d=2670.0 k=_k1 g=_g1
change mat=1
set jcondf=3
```

change jcons=3

prop jmat=1 jkn=100.0E9 jks=100.0E9 jen=0.0 jes=0.0 jfric=30.0 jif=59.3 jr=1.0e-4 ;the existing rock discontinuity

change jmat=1 range -101.0 101.0 2.9 3.1

prop jmat=2 jkn=50.0E9 jks=50.0E9 jfric=100.0 jcoh=1.0E20 jdil=100.0 jten=1.0E20 ;fictitious joints

change jmat=2 range -101.0 101.0 -1.1 1.1

; ===apply boundary conditions===

insitu stress -5.25E6 0.0 -17.5E6

bound stress -5.25E6 0.0 -17.5E6

bound xvel=0.0 range 69.9 70.1 -90.0 90.0 ;right

bound xvel=0.0 range -70.1 -69.9 -90.0 90.0 ;left

bound xvel=0.0 range -90.0 90.0 79.9 80.1 ;top

bound yvel=0.0 range -90.0 90.0 79.9 80.1 ;top

bound xvel=0.0 range -90.0 90.0 -80.1 -79.9 ;bottom

bound yvel=0.0 range -90.0 90.0 -80.1 -79.9 ;bottom

solve

history n=10

; ===record shear displacement===

history sdis 5.6000075,2.9998622

history sdis 4.4000063,2.9998589

history sdis 3.200005,2.9998567

history sdis 2.0000033,2.999856

history sdis 0.80000144,2.9998543

history sdis -0.3999995,2.9998536

history sdis -1.600001,2.9998548

history sdis -2.8000028,2.999856

history sdis -4.0000043,2.9998577

history sdis -5.200005,2.9998603

history sdis -6.400006,2.9998648

history sdis -7.6000032,2.9998732

history sdis -8.799997,2.999889

history sdis -9.999991,2.9999173

history sdis -11.200003,2.999949

; ===record shear stress===

history sst 5.6000075,2.9998622

history sst 4.4000063,2.9998589

history sst 3.200005,2.9998567

history sst 2.0000033,2.999856

history sst 0.80000144,2.9998543

history sst -0.3999995,2.9998536

history sst -1.600001,2.9998548

history sst -2.8000028,2.999856

history sst -4.0000043,2.9998577

history sst -5.200005,2.9998603

history sst -6.400006,2.9998648

history sst -7.6000032,2.9998732

history sst -8.799997,2.999889

history sst -9.999991,2.9999173

history sst -11.200003,2.999949

; ===record normal stress===

history nst 5.6000075,2.9998622

history nst 4.4000063,2.9998589

history nst 3.200005,2.9998567

history nst 2.0000033,2.999856

history nst 0.80000144,2.9998543

history nst -0.3999995,2.9998536

history nst -1.600001,2.9998548

history nst -2.8000028,2.999856

history nst -4.0000043,2.9998577

history nst -5.200005,2.9998603

history nst -6.400006,2.9998648

history nst -7.6000032,2.9998732

history nst -8.799997,2.999889

history nst -9.999991,2.9999173

history nst -11.200003,2.999949

; ===conduct mining steps===

delete range 9.75 10.0 -1.0 1.0

solve

delete range 9.50 10.0 -1.0 1.0

solve

delete range 9.25 10.0 -1.0 1.0

solve

delete range 9.00 10.0 -1.0 1.0

solve

delete range 8.75 10.0 -1.0 1.0

solve

delete range 8.50 10.0 -1.0 1.0

solve

delete range 8.25 10.0 -1.0 1.0

solve

delete range 8.00 10.0 -1.0 1.0

solve

delete range 7.75 10.0 -1.0 1.0

solve

delete range 7.50 10.0 -1.0 1.0

solve

delete range 7.25 10.0 -1.0 1.0

solve

delete range 7.00 10.0 -1.0 1.0

solve

delete range 6.75 10.0 -1.0 1.0

solve

delete range 6.50 10.0 -1.0 1.0

solve

delete range 6.25 10.0 -1.0 1.0

solve

delete range 6.00 10.0 -1.0 1.0

solve

delete range 5.75 10.0 -1.0 1.0

solve

delete range 5.50 10.0 -1.0 1.0

solve

delete range 5.25 10.0 -1.0 1.0

solve

delete range 5.00 10.0 -1.0 1.0

solve

delete range 4.75 10.0 -1.0 1.0

```
solve
delete range 4.50 10.0 -1.0 1.0
solve
delete range 4.25 10.0 -1.0 1.0
solve
delete range 4.00 10.0 -1.0 1.0
solve
delete range 3.75 10.0 -1.0 1.0
solve
delete range 3.50 10.0 -1.0 1.0
solve
delete range 3.25 10.0 -1.0 1.0
solve
delete range 3.00 10.0 -1.0 1.0
solve
delete range 2.75 10.0 -1.0 1.0
solve
delete range 2.50 10.0 -1.0 1.0
solve
delete range 2.25 10.0 -1.0 1.0
solve
delete range 2.00 10.0 -1.0 1.0
solve
delete range 1.75 10.0 -1.0 1.0
solve
delete range 1.50 10.0 -1.0 1.0
solve
```

delete range 1.25 10.0 -1.0 1.0

solve

delete range 1.00 10.0 -1.0 1.0

solve

delete range 0.75 10.0 -1.0 1.0

solve

delete range 0.50 10.0 -1.0 1.0

solve

delete range 0.25 10.0 -1.0 1.0

solve

delete range 0.00 10.0 -1.0 1.0

solve

delete range -0.25 10.0 -1.0 1.0

solve

delete range -0.50 10.0 -1.0 1.0

solve

delete range -0.75 10.0 -1.0 1.0

solve

delete range -1.00 10.0 -1.0 1.0

solve

delete range -1.25 10.0 -1.0 1.0

solve

delete range -1.50 10.0 -1.0 1.0

solve

delete range -1.75 10.0 -1.0 1.0

solve

delete range -2.00 10.0 -1.0 1.0

```
solve
delete range -2.25 10.0 -1.0 1.0
solve
delete range -2.50 10.0 -1.0 1.0
solve
delete range -2.75 10.0 -1.0 1.0
solve
delete range -3.00 10.0 -1.0 1.0
solve
delete range -3.25 10.0 -1.0 1.0
solve
delete range -3.50 10.0 -1.0 1.0
solve
delete range -3.75 10.0 -1.0 1.0
solve
delete range -4.00 10.0 -1.0 1.0
solve
delete range -4.25 10.0 -1.0 1.0
solve
delete range -4.50 10.0 -1.0 1.0
solve
delete range -4.75 10.0 -1.0 1.0
solve
delete range -5.00 10.0 -1.0 1.0
solve
delete range -5.25 10.0 -1.0 1.0
solve
```

delete range -5.50 10.0 -1.0 1.0

solve

delete range -5.75 10.0 -1.0 1.0

solve

delete range -6.00 10.0 -1.0 1.0

solve

delete range -6.25 10.0 -1.0 1.0

solve

delete range -6.50 10.0 -1.0 1.0

solve

delete range -6.75 10.0 -1.0 1.0

solve

delete range -7.00 10.0 -1.0 1.0

solve

delete range -7.25 10.0 -1.0 1.0

solve

delete range -7.50 10.0 -1.0 1.0

solve

delete range -7.75 10.0 -1.0 1.0

solve

delete range -8.00 10.0 -1.0 1.0

solve

delete range -8.25 10.0 -1.0 1.0

solve

delete range -8.50 10.0 -1.0 1.0

solve

delete range -8.75 10.0 -1.0 1.0

solve

delete range -9.00 10.0 -1.0 1.0

solve

delete range -9.25 10.0 -1.0 1.0

solve

delete range -9.50 10.0 -1.0 1.0

solve

delete range -9.75 10.0 -1.0 1.0

solve

delete range -10.00 10.0 -1.0 1.0

solve

D.7 Analyses of Loading Stiffness

Effect of Excavation Extent

d = 0 m

config

round 0.1

edge 0.2

set ovtol 0.2

; ===model geometry===

block -70.0,-80.0 -70.0,80.0 70.0,80.0 70.0,-80.0

crack -90.0 -1.0 90.0 -1.0 ;floor of rock layer

crack -90.0 1.0 90.0 1.0 ;roof of rock layer

crack -90.0 3.0 90.0 3.0 ;the existing rock discontinuity

crack 10.0 -1.0 10.0 1.0 ;right side of the excavation

crack -10.0 -1.0 -10.0 1.0 ;left side of the excavation

jset 90.0,0.0 2.5,0.0 0.0,0.0 0.25,0.0 10.0,0.0 range -10.0,10.0 -1.0,1.0

; ===generate finite-difference zones===

```
gen quad 0.4
; ===assign constitutive models and material properties===
;
def _parameter
_E1 = 70.0E9 ;rock
_nu1 = 0.2 ;rock
_k1 = _E1/(3*(1-2*_nu1))
_g1 = _E1/(2*(1+_nu1))
end _parameter
;
prop mat=1 d=2670.0 k=_k1 g=_g1
change mat=1
set jcondf=3
change jcons=3
prop jmat=1 jkn=100.0E9 jks=100.0E9 jen=0.0 jes=0.0 jfric=30.0 jif=59.3 jr=1.0e-4
;the existing rock discontinuity
change jmat=1 range -101.0 101.0 2.9 3.1
prop jmat=2 jkn=25.0E9 jks=25.0E9 jfric=100.0 jcoh=1.0E20 jdil=100.0 jten=1.0E20 ;
fictitious joints
change jmat=2 range -101.0 101.0 -1.1 1.1
; ===apply boundary conditions===
insitu stress -5.25E6 0.0 -17.5E6
bound stress -5.25E6 0.0 -17.5E6
bound xvel=0.0 range 69.9 70.1 -90.0 90.0 ;right
bound xvel=0.0 range -70.1 -69.9 -90.0 90.0 ;left
bound xvel=0.0 range -90.0 90.0 79.9 80.1 ;top
bound yvel=0.0 range -90.0 90.0 79.9 80.1 ;top
```

```
bound xvel=0.0 range -90.0 90.0 -80.1 -79.9 ;bottom
bound yvel=0.0 range -90.0 90.0 -80.1 -79.9 ;bottom
solve
;;======================
; pull the point towards right
;;======================
; ===record horizontal displacement===
history xdisplace -9.999768,2.999804
; ===record shear stress===
history sxy -10.199771,3.066309 ;zone No.1
history sxy -10.066433,3.1992908 ;zone No.2
history sxy -9.933098,3.199285 ;zone No.3
history sxy -9.799765,3.0662909 ;zone No.4
history sxy -9.799759,2.9331243 ;zone No.5
history sxy -9.933098,2.7997978 ;zone No.6
history sxy -10.066433,2.7998056 ;zone No.7
history sxy -10.199764,2.9331465 ;zone No.8
; ===apply a horizontal velocity at the point to pull the point towards right===
boundary interior xvel=0.01 range -10.2,-9.8 2.9,3.1
cycle 5000
;;======================
; pull the point towards left
;;======================
; ===record horizontal displacement===
history xdisplace -9.999768,2.999804
; ===record shear stress===
history sxy -10.199771,3.066309 ;zone No.1
```

history sxy -10.066433,3.1992908 ;zone No.2

history sxy -9.933098,3.199285 ;zone No.3

history sxy -9.799765,3.0662909 ;zone No.4

history sxy -9.799759,2.9331243 ;zone No.5

history sxy -9.933098,2.7997978 ;zone No.6

history sxy -10.066433,2.7998056 ;zone No.7

history sxy -10.199764,2.9331465 ;zone No.8

; ===apply a horizontal velocity at the point to pull the point towards left===

boundary interior xvel=-0.01 range -10.2,-9.8 2.9,3.1

cycle 5000

d = 4 m

config

round 0.1

edge 0.2

set ovtol 0.2

; ===model geometry===

block -70.0,-80.0 -70.0,80.0 70.0,80.0 70.0,-80.0

crack -90.0 -1.0 90.0 -1.0 ;floor of rock layer

crack -90.0 1.0 90.0 1.0 ;roof of rock layer

crack -90.0 3.0 90.0 3.0 ;the existing rock discontinuity

crack 10.0 -1.0 10.0 1.0 ;right side of the excavation

crack -10.0 -1.0 -10.0 1.0 ;left side of the excavation

jset 90.0,0.0 2.5,0.0 0.0,0.0 0.25,0.0 10.0,0.0 range -10.0,10.0 -1.0,1.0

; ===generate finite-difference zones===

gen quad 0.4

; ===assign constitutive models and material properties===

;

```
def _parameter
_E1 = 70.0E9 ;rock
_nu1 = 0.2 ;rock
_k1 = _E1/(3*(1-2*_nu1))
_g1 = _E1/(2*(1+_nu1))
end _parameter
;
prop mat=1 d=2670.0 k=_k1 g=_g1
change mat=1
set jcondf=3
change jcons=3
prop jmat=1 jkn=100.0E9 jks=100.0E9 jen=0.0 jes=0.0 jfric=30.0 jif=59.3 jr=1.0e-4
;the existing rock discontinuity
change jmat=1 range -101.0 101.0 2.9 3.1
prop jmat=2 jkn=25.0E9 jks=25.0E9 jfric=100.0 jcoh=1.0E20 jdil=100.0 jten=1.0E20 ;
fictitious joints
change jmat=2 range -101.0 101.0 -1.1 1.1
; ===apply boundary conditions===
insitu stress -5.25E6 0.0 -17.5E6
bound stress -5.25E6 0.0 -17.5E6
bound xvel=0.0 range 69.9 70.1 -90.0 90.0 ;right
bound xvel=0.0 range -70.1 -69.9 -90.0 90.0 ;left
bound xvel=0.0 range -90.0 90.0 79.9 80.1 ;top
bound yvel=0.0 range -90.0 90.0 79.9 80.1 ;top
bound xvel=0.0 range -90.0 90.0 -80.1 -79.9 ;bottom
bound yvel=0.0 range -90.0 90.0 -80.1 -79.9 ;bottom
solve
```

; ===excavate 4 m===

delete range 6.0,10.0 -1.0,1.0

solve

;;=====================

; pull the point towards right

;;=====================

; ===record horizontal displacement===

history xdisplace -9.999768,2.999804

; ===record shear stress===

history sxy -10.199771,3.066309 ;zone No.1

history sxy -10.066433,3.1992908 ;zone No.2

history sxy -9.933098,3.199285 ;zone No.3

history sxy -9.799765,3.0662909 ;zone No.4

history sxy -9.799759,2.9331243 ;zone No.5

history sxy -9.933098,2.7997978 ;zone No.6

history sxy -10.066433,2.7998056 ;zone No.7

history sxy -10.199764,2.9331465 ;zone No.8

; ===apply a horizontal velocity at the point to pull the point towards right===

boundary interior xvel=0.01 range -10.2,-9.8 2.9,3.1

cycle 5000

;;=====================

; pull the point towards left

;;=====================

; ===record horizontal displacement===

history xdisplace -9.999768,2.999804

; ===record shear stress===

history sxy -10.199771,3.066309 ;zone No.1

history sxy -10.066433,3.1992908 ;zone No.2

history sxy -9.933098,3.199285 ;zone No.3

history sxy -9.799765,3.0662909 ;zone No.4

history sxy -9.799759,2.9331243 ;zone No.5

history sxy -9.933098,2.7997978 ;zone No.6

history sxy -10.066433,2.7998056 ;zone No.7

history sxy -10.199764,2.9331465 ;zone No.8

; ===apply a horizontal velocity at the point to pull the point towards left===

boundary interior xvel=-0.01 range -10.2,-9.8 2.9,3.1

cycle 5000

d = 8 m

config

round 0.1

edge 0.2

set ovtol 0.2

; ===model geometry===

block -70.0,-80.0 -70.0,80.0 70.0,80.0 70.0,-80.0

crack -90.0 -1.0 90.0 -1.0 ;floor of rock layer

crack -90.0 1.0 90.0 1.0 ;roof of rock layer

crack -90.0 3.0 90.0 3.0 ;the existing rock discontinuity

crack 10.0 -1.0 10.0 1.0 ;right side of the excavation

crack -10.0 -1.0 -10.0 1.0 ;left side of the excavation

jset 90.0,0.0 2.5,0.0 0.0,0.0 0.25,0.0 10.0,0.0 range -10.0,10.0 -1.0,1.0

; ===generate finite-difference zones===

gen quad 0.4

; ===assign constitutive models and material properties===

;

```
def _parameter
_E1 = 70.0E9 ;rock
_nu1 = 0.2 ;rock
_k1 = _E1/(3*(1-2*_nu1))
_g1 = _E1/(2*(1+_nu1))
end _parameter
;
prop mat=1 d=2670.0 k=_k1 g=_g1
change mat=1
set jcondf=3
change jcons=3
prop jmat=1 jkn=100.0E9 jks=100.0E9 jen=0.0 jes=0.0 jfric=30.0 jif=59.3 jr=1.0e-4
;the existing rock discontinuity
change jmat=1 range -101.0 101.0 2.9 3.1
prop jmat=2 jkn=25.0E9 jks=25.0E9 jfric=100.0 jcoh=1.0E20 jdil=100.0 jten=1.0E20 ;
fictitious joints
change jmat=2 range -101.0 101.0 -1.1 1.1
; ===apply boundary conditions===
insitu stress -5.25E6 0.0 -17.5E6
bound stress -5.25E6 0.0 -17.5E6
bound xvel=0.0 range 69.9 70.1 -90.0 90.0 ;right
bound xvel=0.0 range -70.1 -69.9 -90.0 90.0 ;left
bound xvel=0.0 range -90.0 90.0 79.9 80.1 ;top
bound yvel=0.0 range -90.0 90.0 79.9 80.1 ;top
bound xvel=0.0 range -90.0 90.0 -80.1 -79.9 ;bottom
bound yvel=0.0 range -90.0 90.0 -80.1 -79.9 ;bottom
solve
```

; ===excavate 8 m===

delete range 2.0,10.0 -1.0,1.0

solve

;;======================

; pull the point towards right

;;======================

; ===record horizontal displacement===

history xdisplace -9.999768,2.999804

; ===record shear stress===

history sxy -10.199771,3.066309 ;zone No.1

history sxy -10.066433,3.1992908 ;zone No.2

history sxy -9.933098,3.199285 ;zone No.3

history sxy -9.799765,3.0662909 ;zone No.4

history sxy -9.799759,2.9331243 ;zone No.5

history sxy -9.933098,2.7997978 ;zone No.6

history sxy -10.066433,2.7998056 ;zone No.7

history sxy -10.199764,2.9331465 ;zone No.8

; ===apply a horizontal velocity at the point to pull the point towards right===

boundary interior xvel=0.01 range -10.2,-9.8 2.9,3.1

cycle 5000

;;======================

; pull the point towards left

;;======================

; ===record horizontal displacement===

history xdisplace -9.999768,2.999804

; ===record shear stress===

history sxy -10.199771,3.066309 ;zone No.1

history sxy -10.066433,3.1992908 ;zone No.2

history sxy -9.933098,3.199285 ;zone No.3

history sxy -9.799765,3.0662909 ;zone No.4

history sxy -9.799759,2.9331243 ;zone No.5

history sxy -9.933098,2.7997978 ;zone No.6

history sxy -10.066433,2.7998056 ;zone No.7

history sxy -10.199764,2.9331465 ;zone No.8

; ===apply a horizontal velocity at the point to pull the point towards left===

boundary interior xvel=-0.01 range -10.2,-9.8 2.9,3.1

cycle 5000

d = 12 m

config

round 0.1

edge 0.2

set ovtol 0.2

; ===model geometry===

block -70.0,-80.0 -70.0,80.0 70.0,80.0 70.0,-80.0

crack -90.0 -1.0 90.0 -1.0 ;floor of rock layer

crack -90.0 1.0 90.0 1.0 ;roof of rock layer

crack -90.0 3.0 90.0 3.0 ;the existing rock discontinuity

crack 10.0 -1.0 10.0 1.0 ;right side of the excavation

crack -10.0 -1.0 -10.0 1.0 ;left side of the excavation

jset 90.0,0.0 2.5,0.0 0.0,0.0 0.25,0.0 10.0,0.0 range -10.0,10.0 -1.0,1.0

; ===generate finite-difference zones===

gen quad 0.4

; ===assign constitutive models and material properties===

;

```
def _parameter
_E1 = 70.0E9 ;rock
_nu1 = 0.2 ;rock
_k1 = _E1/(3*(1-2*_nu1))
_g1 = _E1/(2*(1+_nu1))
end _parameter
;
prop mat=1 d=2670.0 k=_k1 g=_g1
change mat=1
set jcondf=3
change jcons=3
prop jmat=1 jkn=100.0E9 jks=100.0E9 jen=0.0 jes=0.0 jfric=30.0 jif=59.3 jr=1.0e-4
;the existing rock discontinuity
change jmat=1 range -101.0 101.0 2.9 3.1
prop jmat=2 jkn=25.0E9 jks=25.0E9 jfric=100.0 jcoh=1.0E20 jdil=100.0 jten=1.0E20 ;
fictitious joints
change jmat=2 range -101.0 101.0 -1.1 1.1
; ===apply boundary conditions===
insitu stress -5.25E6 0.0 -17.5E6
bound stress -5.25E6 0.0 -17.5E6
bound xvel=0.0 range 69.9 70.1 -90.0 90.0 ;right
bound xvel=0.0 range -70.1 -69.9 -90.0 90.0 ;left
bound xvel=0.0 range -90.0 90.0 79.9 80.1 ;top
bound yvel=0.0 range -90.0 90.0 79.9 80.1 ;top
bound xvel=0.0 range -90.0 90.0 -80.1 -79.9 ;bottom
bound yvel=0.0 range -90.0 90.0 -80.1 -79.9 ;bottom
solve
```

; ===excavate 12 m===

delete range -2.0,10.0 -1.0,1.0

solve

;;=====================

; pull the point towards right

;;=====================

; ===record horizontal displacement===

history xdisplace -9.999768,2.999804

; ===record shear stress===

history sxy -10.199771,3.066309 ;zone No.1

history sxy -10.066433,3.1992908 ;zone No.2

history sxy -9.933098,3.199285 ;zone No.3

history sxy -9.799765,3.0662909 ;zone No.4

history sxy -9.799759,2.9331243 ;zone No.5

history sxy -9.933098,2.7997978 ;zone No.6

history sxy -10.066433,2.7998056 ;zone No.7

history sxy -10.199764,2.9331465 ;zone No.8

; ===apply a horizontal velocity at the point to pull the point towards right===

boundary interior xvel=0.01 range -10.2,-9.8 2.9,3.1

cycle 5000

;;=====================

; pull the point towards left

;;=====================

; ===record horizontal displacement===

history xdisplace -9.999768,2.999804

; ===record shear stress===

history sxy -10.199771,3.066309 ;zone No.1

history sxy -10.066433,3.1992908 ;zone No.2

history sxy -9.933098,3.199285 ;zone No.3

history sxy -9.799765,3.0662909 ;zone No.4

history sxy -9.799759,2.9331243 ;zone No.5

history sxy -9.933098,2.7997978 ;zone No.6

history sxy -10.066433,2.7998056 ;zone No.7

history sxy -10.199764,2.9331465 ;zone No.8

; ===apply a horizontal velocity at the point to pull the point towards left===

boundary interior xvel=-0.01 range -10.2,-9.8 2.9,3.1

cycle 5000

d = 16 m

config

round 0.1

edge 0.2

set ovtol 0.2

; ===model geometry===

block -70.0,-80.0 -70.0,80.0 70.0,80.0 70.0,-80.0

crack -90.0 -1.0 90.0 -1.0 ;floor of rock layer

crack -90.0 1.0 90.0 1.0 ;roof of rock layer

crack -90.0 3.0 90.0 3.0 ;the existing rock discontinuity

crack 10.0 -1.0 10.0 1.0 ;right side of the excavation

crack -10.0 -1.0 -10.0 1.0 ;left side of the excavation

jset 90.0,0.0 2.5,0.0 0.0,0.0 0.25,0.0 10.0,0.0 range -10.0,10.0 -1.0,1.0

; ===generate finite-difference zones===

gen quad 0.4

; ===assign constitutive models and material properties===

;

```
def _parameter
_E1 = 70.0E9 ;rock
_nu1 = 0.2 ;rock
_k1 = _E1/(3*(1-2*_nu1))
_g1 = _E1/(2*(1+_nu1))
end _parameter
;
prop mat=1 d=2670.0 k=_k1 g=_g1
change mat=1
set jcondf=3
change jcons=3
prop jmat=1 jkn=100.0E9 jks=100.0E9 jen=0.0 jes=0.0 jfric=30.0 jif=59.3 jr=1.0e-4
;the existing rock discontinuity
change jmat=1 range -101.0 101.0 2.9 3.1
prop jmat=2 jkn=25.0E9 jks=25.0E9 jfric=100.0 jcoh=1.0E20 jdil=100.0 jten=1.0E20 ;
fictitious joints
change jmat=2 range -101.0 101.0 -1.1 1.1
; ===apply boundary conditions===
insitu stress -5.25E6 0.0 -17.5E6
bound stress -5.25E6 0.0 -17.5E6
bound xvel=0.0 range 69.9 70.1 -90.0 90.0 ;right
bound xvel=0.0 range -70.1 -69.9 -90.0 90.0 ;left
bound xvel=0.0 range -90.0 90.0 79.9 80.1 ;top
bound yvel=0.0 range -90.0 90.0 79.9 80.1 ;top
bound xvel=0.0 range -90.0 90.0 -80.1 -79.9 ;bottom
bound yvel=0.0 range -90.0 90.0 -80.1 -79.9 ;bottom
solve
```

; ===excavate 16 m===

delete range -6.0,10.0 -1.0,1.0

solve

;;=====================

; pull the point towards right

;;=====================

; ===record horizontal displacement===

history xdisplace -9.999768,2.999804

; ===record shear stress===

history sxy -10.199771,3.066309 ;zone No.1

history sxy -10.066433,3.1992908 ;zone No.2

history sxy -9.933098,3.199285 ;zone No.3

history sxy -9.799765,3.0662909 ;zone No.4

history sxy -9.799759,2.9331243 ;zone No.5

history sxy -9.933098,2.7997978 ;zone No.6

history sxy -10.066433,2.7998056 ;zone No.7

history sxy -10.199764,2.9331465 ;zone No.8

; ===apply a horizontal velocity at the point to pull the point towards right===

boundary interior xvel=0.01 range -10.2,-9.8 2.9,3.1

cycle 5000

;;=====================

; pull the point towards left

;;=====================

; ===record horizontal displacement===

history xdisplace -9.999768,2.999804

; ===record shear stress===

history sxy -10.199771,3.066309 ;zone No.1

history sxy -10.066433,3.1992908 ;zone No.2

history sxy -9.933098,3.199285 ;zone No.3

history sxy -9.799765,3.0662909 ;zone No.4

history sxy -9.799759,2.9331243 ;zone No.5

history sxy -9.933098,2.7997978 ;zone No.6

history sxy -10.066433,2.7998056 ;zone No.7

history sxy -10.199764,2.9331465 ;zone No.8

; ===apply a horizontal velocity at the point to pull the point towards left===

boundary interior xvel=-0.01 range -10.2,-9.8 2.9,3.1

cycle 5000

d = 20 m

config

round 0.1

edge 0.2

set ovtol 0.2

; ===model geometry===

block -70.0,-80.0 -70.0,80.0 70.0,80.0 70.0,-80.0

crack -90.0 -1.0 90.0 -1.0 ;floor of rock layer

crack -90.0 1.0 90.0 1.0 ;roof of rock layer

crack -90.0 3.0 90.0 3.0 ;the existing rock discontinuity

crack 10.0 -1.0 10.0 1.0 ;right side of the excavation

crack -10.0 -1.0 -10.0 1.0 ;left side of the excavation

jset 90.0,0.0 2.5,0.0 0.0,0.0 0.25,0.0 10.0,0.0 range -10.0,10.0 -1.0,1.0

; ===generate finite-difference zones===

gen quad 0.4

; ===assign constitutive models and material properties===

;

```
def _parameter
_E1 = 70.0E9 ;rock
_nu1 = 0.2 ;rock
_k1 = _E1/(3*(1-2*_nu1))
_g1 = _E1/(2*(1+_nu1))
end _parameter
;
prop mat=1 d=2670.0 k=_k1 g=_g1
change mat=1
set jcondf=3
change jcons=3
prop jmat=1 jkn=100.0E9 jks=100.0E9 jen=0.0 jes=0.0 jfric=30.0 jif=59.3 jr=1.0e-4
;the existing rock discontinuity
change jmat=1 range -101.0 101.0 2.9 3.1
prop jmat=2 jkn=25.0E9 jks=25.0E9 jfric=100.0 jcoh=1.0E20 jdil=100.0 jten=1.0E20 ;
fictitious joints
change jmat=2 range -101.0 101.0 -1.1 1.1
; ===apply boundary conditions===
insitu stress -5.25E6 0.0 -17.5E6
bound stress -5.25E6 0.0 -17.5E6
bound xvel=0.0 range 69.9 70.1 -90.0 90.0 ;right
bound xvel=0.0 range -70.1 -69.9 -90.0 90.0 ;left
bound xvel=0.0 range -90.0 90.0 79.9 80.1 ;top
bound yvel=0.0 range -90.0 90.0 79.9 80.1 ;top
bound xvel=0.0 range -90.0 90.0 -80.1 -79.9 ;bottom
bound yvel=0.0 range -90.0 90.0 -80.1 -79.9 ;bottom
solve
```

; ===excavate 20 m===

delete range -10.0,10.0 -1.0,1.0

solve

;;=======================

; pull the point towards right

;;=======================

; ===record horizontal displacement===

history xdisplace -9.999768,2.999804

; ===record shear stress===

history sxy -10.199771,3.066309 ;zone No.1

history sxy -10.066433,3.1992908 ;zone No.2

history sxy -9.933098,3.199285 ;zone No.3

history sxy -9.799765,3.0662909 ;zone No.4

history sxy -9.799759,2.9331243 ;zone No.5

history sxy -9.933098,2.7997978 ;zone No.6

history sxy -10.066433,2.7998056 ;zone No.7

history sxy -10.199764,2.9331465 ;zone No.8

; ===apply a horizontal velocity at the point to pull the point towards right===

boundary interior xvel=0.01 range -10.2,-9.8 2.9,3.1

cycle 5000

;;=======================

; pull the point towards left

;;=======================

; ===record horizontal displacement===

history xdisplace -9.999768,2.999804

; ===record shear stress===

history sxy -10.199771,3.066309 ;zone No.1

history sxy -10.066433,3.1992908 ;zone No.2

history sxy -9.933098,3.199285 ;zone No.3

history sxy -9.799765,3.0662909 ;zone No.4

history sxy -9.799759,2.9331243 ;zone No.5

history sxy -9.933098,2.7997978 ;zone No.6

history sxy -10.066433,2.7998056 ;zone No.7

history sxy -10.199764,2.9331465 ;zone No.8

; ===apply a horizontal velocity at the point to pull the point towards left===

boundary interior xvel=-0.01 range -10.2,-9.8 2.9,3.1

cycle 5000

Effect of Discontinuity Plane Location

h = 1 m

config

round 0.1

edge 0.2

set ovtol 0.2

; ===model geometry===

block -70.0,-80.0 -70.0,80.0 70.0,80.0 70.0,-80.0

crack -90.0 -1.0 90.0 -1.0 ;floor of rock layer

crack -90.0 1.0 90.0 1.0 ;roof of rock layer

crack -90.0 2.0 90.0 2.0 ;the existing rock discontinuity

crack 10.0 -1.0 10.0 1.0 ;right side of the excavation

crack -10.0 -1.0 -10.0 1.0 ;left side of the excavation

jset 90.0,0.0 2.5,0.0 0.0,0.0 0.25,0.0 10.0,0.0 range -10.0,10.0 -1.0,1.0

; ===generate finite-difference zones===

gen quad 0.4

; ===assign constitutive models and material properties===

```
;
def _parameter
_E1 = 70.0E9 ;rock
_nu1 = 0.2 ;rock
_k1 = _E1/(3*(1-2*_nu1))
_g1 = _E1/(2*(1+_nu1))
end _parameter
;
prop mat=1 d=2670.0 k=_k1 g=_g1
change mat=1
set jcondf=3
change jcons=3
prop jmat=1 jkn=100.0E9 jks=100.0E9 jen=0.0 jes=0.0 jfric=30.0 jif=59.3 jr=1.0e-4
;the existing rock discontinuity
change jmat=1 range -101.0 101.0 1.9 2.1
prop jmat=2 jkn=25.0E9 jks=25.0E9 jfric=100.0 jcoh=1.0E20 jdil=100.0 jten=1.0E20 ;
fictitious joints
change jmat=2 range -101.0 101.0 -1.1 1.1
; ===apply boundary conditions===
insitu stress -5.25E6 0.0 -17.5E6
bound stress -5.25E6 0.0 -17.5E6
bound xvel=0.0 range 69.9 70.1 -90.0 90.0 ;right
bound xvel=0.0 range -70.1 -69.9 -90.0 90.0 ;left
bound xvel=0.0 range -90.0 90.0 79.9 80.1 ;top
bound yvel=0.0 range -90.0 90.0 79.9 80.1 ;top
bound xvel=0.0 range -90.0 90.0 -80.1 -79.9 ;bottom
bound yvel=0.0 range -90.0 90.0 -80.1 -79.9 ;bottom
```

```
solve
; ===excavate 20 m===
delete range -10.0,10.0 -1.0,1.0
solve
;;======================
; pull the point towards right
;;======================
; ===record horizontal displacement===
history xdisplace -1.7342132E-6,1.994329
; ===record shear stress===
history sxy -0.20002797,2.0617309
history sxy -0.06667686,2.1950889
history sxy 0.06667311,2.1950889
history sxy 0.20002422,2.0617309
history sxy 0.20000845,1.9380435
history sxy 0.066669025,1.8269067
history sxy -0.066672444,1.8269067
history sxy -0.2000119,1.9380434
; ===apply a horizontal velocity at the point to pull the point towards right===
boundary interior xvel=0.01 range -0.2,0.2 1.9,2.1
cycle 5000
;;======================
; pull the point towards left
;;======================
; ===record horizontal displacement===
history xdisplace -1.7342132E-6,1.994329
; ===record shear stress===
```

history sxy -0.20002797,2.0617309

history sxy -0.06667686,2.1950889

history sxy 0.06667311,2.1950889

history sxy 0.20002422,2.0617309

history sxy 0.20000845,1.9380435

history sxy 0.066669025,1.8269067

history sxy -0.066672444,1.8269067

history sxy -0.2000119,1.9380434

; ===apply a horizontal velocity at the point to pull the point towards left===

boundary interior xvel=-0.01 range -0.2,0.2 1.9,2.1

cycle 5000

h = 2 m

config

round 0.1

edge 0.2

set ovtol 0.2

; ===model geometry===

block -70.0,-80.0 -70.0,80.0 70.0,80.0 70.0,-80.0

crack -90.0 -1.0 90.0 -1.0 ;floor of rock layer

crack -90.0 1.0 90.0 1.0 ;roof of rock layer

crack -90.0 3.0 90.0 3.0 ;the existing rock discontinuity

crack 10.0 -1.0 10.0 1.0 ;right side of the excavation

crack -10.0 -1.0 -10.0 1.0 ;left side of the excavation

jset 90.0,0.0 2.5,0.0 0.0,0.0 0.25,0.0 10.0,0.0 range -10.0,10.0 -1.0,1.0

; ===generate finite-difference zones===

gen quad 0.4

; ===assign constitutive models and material properties===

```
;
def _parameter
_E1 = 70.0E9 ;rock
_nu1 = 0.2 ;rock
_k1 = _E1/(3*(1-2*_nu1))
_g1 = _E1/(2*(1+_nu1))
end _parameter
;
prop mat=1 d=2670.0 k=_k1 g=_g1
change mat=1
set jcondf=3
change jcons=3
prop jmat=1 jkn=100.0E9 jks=100.0E9 jen=0.0 jes=0.0 jfric=30.0 jif=59.3 jr=1.0e-4
;the existing rock discontinuity
change jmat=1 range -101.0 101.0 2.9 3.1
prop jmat=2 jkn=25.0E9 jks=25.0E9 jfric=100.0 jcoh=1.0E20 jdil=100.0 jten=1.0E20 ;
fictitious joints
change jmat=2 range -101.0 101.0 -1.1 1.1
; ===apply boundary conditions===
insitu stress -5.25E6 0.0 -17.5E6
bound stress -5.25E6 0.0 -17.5E6
bound xvel=0.0 range 69.9 70.1 -90.0 90.0 ;right
bound xvel=0.0 range -70.1 -69.9 -90.0 90.0 ;left
bound xvel=0.0 range -90.0 90.0 79.9 80.1 ;top
bound yvel=0.0 range -90.0 90.0 79.9 80.1 ;top
bound xvel=0.0 range -90.0 90.0 -80.1 -79.9 ;bottom
bound yvel=0.0 range -90.0 90.0 -80.1 -79.9 ;bottom
```

```
solve
; ===excavate 20 m===
delete range -10.0,10.0 -1.0,1.0
solve
;;======================
; pull the point towards right
;;======================
; ===record horizontal displacement===
history xdisplace -9.999768,2.999804
; ===record shear stress===
history sxy -10.199771,3.066309
history sxy -10.066433,3.1992908
history sxy -9.933098,3.199285
history sxy -9.799765,3.0662909
history sxy -9.799759,2.9331243
history sxy -9.933098,2.7997978
history sxy -10.066433,2.7998056
history sxy -10.199764,2.9331465
; ===apply a horizontal velocity at the point to pull the point towards right===
boundary interior xvel=0.01 range -10.2,-9.8 2.9,3.1
cycle 5000
;;======================
; pull the point towards left
;;======================
; ===record horizontal displacement===
history xdisplace -9.999768,2.999804
; ===record shear stress===
```

history sxy -10.199771,3.066309

history sxy -10.066433,3.1992908

history sxy -9.933098,3.199285

history sxy -9.799765,3.0662909

history sxy -9.799759,2.9331243

history sxy -9.933098,2.7997978

history sxy -10.066433,2.7998056

history sxy -10.199764,2.9331465

; ===apply a horizontal velocity at the point to pull the point towards left===

boundary interior xvel=-0.01 range -10.2,-9.8 2.9,3.1

cycle 5000

h = 3 m

config

round 0.1

edge 0.2

set ovtol 0.2

; ===model geometry===

block -70.0,-80.0 -70.0,80.0 70.0,80.0 70.0,-80.0

crack -90.0 -1.0 90.0 -1.0 ;floor of rock layer

crack -90.0 1.0 90.0 1.0 ;roof of rock layer

crack -90.0 4.0 90.0 4.0 ;the existing rock discontinuity

crack 10.0 -1.0 10.0 1.0 ;right side of the excavation

crack -10.0 -1.0 -10.0 1.0 ;left side of the excavation

jset 90.0,0.0 2.5,0.0 0.0,0.0 0.25,0.0 10.0,0.0 range -10.0,10.0 -1.0,1.0

; ===generate finite-difference zones===

gen quad 0.4

; ===assign constitutive models and material properties===

```
;
def _parameter
_E1 = 70.0E9 ;rock
_nu1 = 0.2 ;rock
_k1 = _E1/(3*(1-2*_nu1))
_g1 = _E1/(2*(1+_nu1))
end _parameter
;
prop mat=1 d=2670.0 k=_k1 g=_g1
change mat=1
set jcondf=3
change jcons=3
prop jmat=1 jkn=100.0E9 jks=100.0E9 jen=0.0 jes=0.0 jfric=30.0 jif=59.3 jr=1.0e-4
;the existing rock discontinuity
change jmat=1 range -101.0 101.0 3.9 4.1
prop jmat=2 jkn=25.0E9 jks=25.0E9 jfric=100.0 jcoh=1.0E20 jdil=100.0 jten=1.0E20 ;
fictitious joints
change jmat=2 range -101.0 101.0 -1.1 1.1
; ===apply boundary conditions===
insitu stress -5.25E6 0.0 -17.5E6
bound stress -5.25E6 0.0 -17.5E6
bound xvel=0.0 range 69.9 70.1 -90.0 90.0 ;right
bound xvel=0.0 range -70.1 -69.9 -90.0 90.0 ;left
bound xvel=0.0 range -90.0 90.0 79.9 80.1 ;top
bound yvel=0.0 range -90.0 90.0 79.9 80.1 ;top
bound xvel=0.0 range -90.0 90.0 -80.1 -79.9 ;bottom
bound yvel=0.0 range -90.0 90.0 -80.1 -79.9 ;bottom
```

```
solve
; ===excavate 20 m===
delete range -10.0,10.0 -1.0,1.0
solve
;;======================
; pull the point towards right
;;======================
; ===record horizontal displacement===
history xdisplace 2.2231418E-6,3.9952674
; ===record shear stress===
history sxy -0.2000154,4.062078
history sxy -0.06666981,4.1954374
history sxy 0.066674545,4.1954374
history sxy 0.20002016,4.0620785
history sxy 0.19999853,3.932626
history sxy 0.06666815,3.8075962
history sxy -0.06666368,3.807596
history sxy -0.19999407,3.9326258
; ===apply a horizontal velocity at the point to pull the point towards right===
boundary interior xvel=0.01 range -0.2,0.2 3.9,4.1
cycle 5000
;;======================
; pull the point towards left
;;======================
; ===record horizontal displacement===
history xdisplace 2.2231418E-6,3.9952674
; ===record shear stress===
```

history sxy -0.2000154,4.062078

history sxy -0.06666981,4.1954374

history sxy 0.066674545,4.1954374

history sxy 0.20002016,4.0620785

history sxy 0.19999853,3.932626

history sxy 0.06666815,3.8075962

history sxy -0.06666368,3.807596

history sxy -0.19999407,3.9326258

; ===apply a horizontal velocity at the point to pull the point towards left===

boundary interior xvel=-0.01 range -0.2,0.2 3.9,4.1

cycle 5000

h = 4 m

config

round 0.1

edge 0.2

set ovtol 0.2

; ===model geometry===

block -70.0,-80.0 -70.0,80.0 70.0,80.0 70.0,-80.0

crack -90.0 -1.0 90.0 -1.0 ;floor of rock layer

crack -90.0 1.0 90.0 1.0 ;roof of rock layer

crack -90.0 5.0 90.0 5.0 ;the existing rock discontinuity

crack 10.0 -1.0 10.0 1.0 ;right side of the excavation

crack -10.0 -1.0 -10.0 1.0 ;left side of the excavation

jset 90.0,0.0 2.5,0.0 0.0,0.0 0.25,0.0 10.0,0.0 range -10.0,10.0 -1.0,1.0

; ===generate finite-difference zones===

gen quad 0.4

; ===assign constitutive models and material properties===

```
;
def _parameter
_E1 = 70.0E9 ;rock
_nu1 = 0.2 ;rock
_k1 = _E1/(3*(1-2*_nu1))
_g1 = _E1/(2*(1+_nu1))
end _parameter
;
prop mat=1 d=2670.0 k=_k1 g=_g1
change mat=1
set jcondf=3
change jcons=3
prop jmat=1 jkn=100.0E9 jks=100.0E9 jen=0.0 jes=0.0 jfric=30.0 jif=59.3 jr=1.0e-4
;the existing rock discontinuity
change jmat=1 range -101.0 101.0 4.9 5.1
prop jmat=2 jkn=25.0E9 jks=25.0E9 jfric=100.0 jcoh=1.0E20 jdil=100.0 jten=1.0E20 ;
fictitious joints
change jmat=2 range -101.0 101.0 -1.1 1.1
; ===apply boundary conditions===
insitu stress -5.25E6 0.0 -17.5E6
bound stress -5.25E6 0.0 -17.5E6
bound xvel=0.0 range 69.9 70.1 -90.0 90.0 ;right
bound xvel=0.0 range -70.1 -69.9 -90.0 90.0 ;left
bound xvel=0.0 range -90.0 90.0 79.9 80.1 ;top
bound yvel=0.0 range -90.0 90.0 79.9 80.1 ;top
bound xvel=0.0 range -90.0 90.0 -80.1 -79.9 ;bottom
bound yvel=0.0 range -90.0 90.0 -80.1 -79.9 ;bottom
```

```
solve
; ===excavate 20 m===
delete range -10.0,10.0 -1.0,1.0
solve
;;======================
; pull the point towards right
;;======================
; ===record horizontal displacement===
history xdisplace 1.2810391E-6,4.9956617
; ===record shear stress===
history sxy -0.20000112,5.06225
history sxy -0.06666598,5.1952558
history sxy 0.06666853,5.195256
history sxy 0.2000037,5.06225
history sxy 0.20000327,4.9288993
history sxy 0.06666885,4.795536
history sxy -0.06666628,4.795536
history sxy -0.20000069,4.928899
; ===apply a horizontal velocity at the point to pull the point towards right===
boundary interior xvel=0.01 range -0.2,0.2 4.9,5.1
cycle 5000
;;======================
; pull the point towards left
;;======================
; ===record horizontal displacement===
history xdisplace 1.2810391E-6,4.9956617
; ===record shear stress===
```

history sxy -0.20000112,5.06225

history sxy -0.06666598,5.1952558

history sxy 0.06666853,5.195256

history sxy 0.2000037,5.06225

history sxy 0.20000327,4.9288993

history sxy 0.06666885,4.795536

history sxy -0.06666628,4.795536

history sxy -0.20000069,4.928899

; ===apply a horizontal velocity at the point to pull the point towards left===

boundary interior xvel=-0.01 range -0.2,0.2 4.9,5.1

cycle 5000

h = 5 m

config

round 0.1

edge 0.2

set ovtol 0.2

; ===model geometry===

block -70.0,-80.0 -70.0,80.0 70.0,80.0 70.0,-80.0

crack -90.0 -1.0 90.0 -1.0 ;floor of rock layer

crack -90.0 1.0 90.0 1.0 ;roof of rock layer

crack -90.0 6.0 90.0 6.0 ;the existing rock discontinuity

crack 10.0 -1.0 10.0 1.0 ;right side of the excavation

crack -10.0 -1.0 -10.0 1.0 ;left side of the excavation

jset 90.0,0.0 2.5,0.0 0.0,0.0 0.25,0.0 10.0,0.0 range -10.0,10.0 -1.0,1.0

; ===generate finite-difference zones===

gen quad 0.4

; ===assign constitutive models and material properties===

;

def _parameter

_E1 = 70.0E9 ;rock

_nu1 = 0.2 ;rock

_k1 = _E1/(3*(1-2*_nu1))

_g1 = _E1/(2*(1+_nu1))

end _parameter

;

prop mat=1 d=2670.0 k=_k1 g=_g1

change mat=1

set jcondf=3

change jcons=3

prop jmat=1 jkn=100.0E9 jks=100.0E9 jen=0.0 jes=0.0 jfric=30.0 jif=59.3 jr=1.0e-4 ;the existing rock discontinuity

change jmat=1 range -101.0 101.0 5.9 6.1

prop jmat=2 jkn=25.0E9 jks=25.0E9 jfric=100.0 jcoh=1.0E20 jdil=100.0 jten=1.0E20 ; fictitious joints

change jmat=2 range -101.0 101.0 -1.1 1.1

; ===apply boundary conditions===

insitu stress -5.25E6 0.0 -17.5E6

bound stress -5.25E6 0.0 -17.5E6

bound xvel=0.0 range 69.9 70.1 -90.0 90.0 ;right

bound xvel=0.0 range -70.1 -69.9 -90.0 90.0 ;left

bound xvel=0.0 range -90.0 90.0 79.9 80.1 ;top

bound yvel=0.0 range -90.0 90.0 79.9 80.1 ;top

bound xvel=0.0 range -90.0 90.0 -80.1 -79.9 ;bottom

bound yvel=0.0 range -90.0 90.0 -80.1 -79.9 ;bottom

```
solve
; ===excavate 20 m===
delete range -10.0,10.0 -1.0,1.0
solve
;;======================
; pull the point towards right
;;======================
; ===record horizontal displacement===
history xdisplace 2.2333586E-6,5.9958773
; ===record shear stress===
history sxy -0.19999576,6.0626397
history sxy -0.0666636,6.1959996
history sxy 0.06666806,6.1959996
history sxy 0.20000021,6.0626397
history sxy 0.19999932,5.9316826
history sxy 0.0666681,5.8034496
history sxy -0.06666367,5.8034496
history sxy -0.19999486,5.9316826
; ===apply a horizontal velocity at the point to pull the point towards right===
boundary interior xvel=0.01 range -0.2,0.2 5.9,6.1
cycle 5000
;;======================
; pull the point towards left
;;======================
; ===record horizontal displacement===
history xdisplace 2.2333586E-6,5.9958773
; ===record shear stress===
```

history sxy -0.19999576,6.0626397

history sxy -0.0666636,6.1959996

history sxy 0.06666806,6.1959996

history sxy 0.20000021,6.0626397

history sxy 0.19999932,5.9316826

history sxy 0.0666681,5.8034496

history sxy -0.06666367,5.8034496

history sxy -0.19999486,5.9316826

; ===apply a horizontal velocity at the point to pull the point towards left===

boundary interior xvel=-0.01 range -0.2,0.2 5.9,6.1

cycle 5000

h = 6 m

config

round 0.1

edge 0.2

set ovtol 0.2

; ===model geometry===

block -70.0,-80.0 -70.0,80.0 70.0,80.0 70.0,-80.0

crack -90.0 -1.0 90.0 -1.0 ;floor of rock layer

crack -90.0 1.0 90.0 1.0 ;roof of rock layer

crack -90.0 7.0 90.0 7.0 ;the existing rock discontinuity

crack 10.0 -1.0 10.0 1.0 ;right side of the excavation

crack -10.0 -1.0 -10.0 1.0 ;left side of the excavation

jset 90.0,0.0 2.5,0.0 0.0,0.0 0.25,0.0 10.0,0.0 range -10.0,10.0 -1.0,1.0

; ===generate finite-difference zones===

gen quad 0.4

; ===assign constitutive models and material properties===

```
;
def _parameter
_E1 = 70.0E9 ;rock
_nu1 = 0.2 ;rock
_k1 = _E1/(3*(1-2*_nu1))
_g1 = _E1/(2*(1+_nu1))
end _parameter
;
prop mat=1 d=2670.0 k=_k1 g=_g1
change mat=1
set jcondf=3
change jcons=3
prop jmat=1 jkn=100.0E9 jks=100.0E9 jen=0.0 jes=0.0 jfric=30.0 jif=59.3 jr=1.0e-4
;the existing rock discontinuity
change jmat=1 range -101.0 101.0 6.9 7.1
prop jmat=2 jkn=25.0E9 jks=25.0E9 jfric=100.0 jcoh=1.0E20 jdil=100.0 jten=1.0E20 ;
fictitious joints
change jmat=2 range -101.0 101.0 -1.1 1.1
; ===apply boundary conditions===
insitu stress -5.25E6 0.0 -17.5E6
bound stress -5.25E6 0.0 -17.5E6
bound xvel=0.0 range 69.9 70.1 -90.0 90.0 ;right
bound xvel=0.0 range -70.1 -69.9 -90.0 90.0 ;left
bound xvel=0.0 range -90.0 90.0 79.9 80.1 ;top
bound yvel=0.0 range -90.0 90.0 79.9 80.1 ;top
bound xvel=0.0 range -90.0 90.0 -80.1 -79.9 ;bottom
bound yvel=0.0 range -90.0 90.0 -80.1 -79.9 ;bottom
```

```
solve
; ===excavate 20 m===
delete range -10.0,10.0 -1.0,1.0
solve
;;======================
; pull the point towards right
;;======================
; ===record horizontal displacement===
history xdisplace 2.5790657E-6,6.9960976
; ===record shear stress===
history sxy -0.19999215,7.0626736
history sxy -0.066662215,7.195668
history sxy 0.06666738,7.195668
history sxy 0.1999973,7.0626736
history sxy 0.19999608,6.9293423
history sxy 0.066667214,6.7959805
history sxy -0.066662095,6.7959805
history sxy -0.19999097,6.9293427
; ===apply a horizontal velocity at the point to pull the point towards right===
boundary interior xvel=0.01 range -0.2,0.2 6.9,7.1
cycle 5000
;;======================
; pull the point towards left
;;======================
; ===record horizontal displacement===
history xdisplace 2.5790657E-6,6.9960976
; ===record shear stress===
```

history sxy -0.19999215,7.0626736

history sxy -0.066662215,7.195668

history sxy 0.06666738,7.195668

history sxy 0.1999973,7.0626736

history sxy 0.19999608,6.9293423

history sxy 0.066667214,6.7959805

history sxy -0.066662095,6.7959805

history sxy -0.19999097,6.9293427

; ===apply a horizontal velocity at the point to pull the point towards left===

boundary interior xvel=-0.01 range -0.2,0.2 6.9,7.1

cycle 5000

h = 7 m

config

round 0.1

edge 0.2

set ovtol 0.2

; ===model geometry===

block -70.0,-80.0 -70.0,80.0 70.0,80.0 70.0,-80.0

crack -90.0 -1.0 90.0 -1.0 ;floor of rock layer

crack -90.0 1.0 90.0 1.0 ;roof of rock layer

crack -90.0 8.0 90.0 8.0 ;the existing rock discontinuity

crack 10.0 -1.0 10.0 1.0 ;right side of the excavation

crack -10.0 -1.0 -10.0 1.0 ;left side of the excavation

jset 90.0,0.0 2.5,0.0 0.0,0.0 0.25,0.0 10.0,0.0 range -10.0,10.0 -1.0,1.0

; ===generate finite-difference zones===

gen quad 0.4

; ===assign constitutive models and material properties===

```
;
def _parameter
_E1 = 70.0E9 ;rock
_nu1 = 0.2 ;rock
_k1 = _E1/(3*(1-2*_nu1))
_g1 = _E1/(2*(1+_nu1))
end _parameter
;
prop mat=1 d=2670.0 k=_k1 g=_g1
change mat=1
set jcondf=3
change jcons=3
prop jmat=1 jkn=100.0E9 jks=100.0E9 jen=0.0 jes=0.0 jfric=30.0 jif=59.3 jr=1.0e-4
;the existing rock discontinuity
change jmat=1 range -101.0 101.0 7.9 8.1
prop jmat=2 jkn=25.0E9 jks=25.0E9 jfric=100.0 jcoh=1.0E20 jdil=100.0 jten=1.0E20 ;
fictitious joints
change jmat=2 range -101.0 101.0 -1.1 1.1
; ===apply boundary conditions===
insitu stress -5.25E6 0.0 -17.5E6
bound stress -5.25E6 0.0 -17.5E6
bound xvel=0.0 range 69.9 70.1 -90.0 90.0 ;right
bound xvel=0.0 range -70.1 -69.9 -90.0 90.0 ;left
bound xvel=0.0 range -90.0 90.0 79.9 80.1 ;top
bound yvel=0.0 range -90.0 90.0 79.9 80.1 ;top
bound xvel=0.0 range -90.0 90.0 -80.1 -79.9 ;bottom
bound yvel=0.0 range -90.0 90.0 -80.1 -79.9 ;bottom
```

```
solve
; ===excavate 20 m===
delete range -10.0,10.0 -1.0,1.0
solve
;;======================
; pull the point towards right
;;======================
; ===record horizontal displacement===
history xdisplace 2.8876182E-6,7.996313
; ===record shear stress===
history sxy -0.19998959,8.0630665
history sxy -0.06666119,8.196424
history sxy 0.066666976,8.196424
history sxy 0.19999538,8.063066
history sxy 0.19999391,7.931415
history sxy 0.066666655,7.801759
history sxy -0.0666609,7.801759
history sxy -0.19998814,7.931415
; ===apply a horizontal velocity at the point to pull the point towards right===
boundary interior xvel=0.01 range -0.2,0.2 7.9,8.1
cycle 5000
;;======================
; pull the point towards left
;;======================
; ===record horizontal displacement===
history xdisplace 2.8876182E-6,7.996313
; ===record shear stress===
```

history sxy -0.19998959,8.0630665

history sxy -0.06666119,8.196424

history sxy 0.066666976,8.196424

history sxy 0.19999538,8.063066

history sxy 0.19999391,7.931415

history sxy 0.066666655,7.801759

history sxy -0.0666609,7.801759

history sxy -0.19998814,7.931415

; ===apply a horizontal velocity at the point to pull the point towards left===

boundary interior xvel=-0.01 range -0.2,0.2 7.9,8.1

cycle 5000

h = 8 m

config

round 0.1

edge 0.2

set ovtol 0.2

; ===model geometry===

block -70.0,-80.0 -70.0,80.0 70.0,80.0 70.0,-80.0

crack -90.0 -1.0 90.0 -1.0 ;floor of rock layer

crack -90.0 1.0 90.0 1.0 ;roof of rock layer

crack -90.0 9.0 90.0 9.0 ;the existing rock discontinuity

crack 10.0 -1.0 10.0 1.0 ;right side of the excavation

crack -10.0 -1.0 -10.0 1.0 ;left side of the excavation

jset 90.0,0.0 2.5,0.0 0.0,0.0 0.25,0.0 10.0,0.0 range -10.0,10.0 -1.0,1.0

; ===generate finite-difference zones===

gen quad 0.4

; ===assign constitutive models and material properties===

```
;
def _parameter
_E1 = 70.0E9 ;rock
_nu1 = 0.2 ;rock
_k1 = _E1/(3*(1-2*_nu1))
_g1 = _E1/(2*(1+_nu1))
end _parameter
;
prop mat=1 d=2670.0 k=_k1 g=_g1
change mat=1
set jcondf=3
change jcons=3
prop jmat=1 jkn=100.0E9 jks=100.0E9 jen=0.0 jes=0.0 jfric=30.0 jif=59.3 jr=1.0e-4
;the existing rock discontinuity
change jmat=1 range -101.0 101.0 8.9 9.1
prop jmat=2 jkn=25.0E9 jks=25.0E9 jfric=100.0 jcoh=1.0E20 jdil=100.0 jten=1.0E20 ;
fictitious joints
change jmat=2 range -101.0 101.0 -1.1 1.1
; ===apply boundary conditions===
insitu stress -5.25E6 0.0 -17.5E6
bound stress -5.25E6 0.0 -17.5E6
bound xvel=0.0 range 69.9 70.1 -90.0 90.0 ;right
bound xvel=0.0 range -70.1 -69.9 -90.0 90.0 ;left
bound xvel=0.0 range -90.0 90.0 79.9 80.1 ;top
bound yvel=0.0 range -90.0 90.0 79.9 80.1 ;top
bound xvel=0.0 range -90.0 90.0 -80.1 -79.9 ;bottom
bound yvel=0.0 range -90.0 90.0 -80.1 -79.9 ;bottom
```

```
solve
; ===excavate 20 m===
delete range -10.0,10.0 -1.0,1.0
solve
;;======================
; pull the point towards right
;;======================
; ===record horizontal displacement===
history xdisplace 2.3707496E-6,8.996509
; ===record shear stress===
history sxy -0.1999886,9.06307
history sxy -0.06666122,9.196052
history sxy 0.06666602,9.196052
history sxy 0.1999934,9.06307
history sxy 0.1999918,8.929764
history sxy 0.06666559,8.796404
history sxy -0.06666085,8.796404
history sxy -0.19998707,8.929764
; ===apply a horizontal velocity at the point to pull the point towards right===
boundary interior xvel=0.01 range -0.2,0.2 8.9,9.1
cycle 5000
;;======================
; pull the point towards left
;;======================
; ===record horizontal displacement===
history xdisplace 2.3707496E-6,8.996509
; ===record shear stress===
```

history sxy -0.1999886,9.06307

history sxy -0.06666122,9.196052

history sxy 0.06666602,9.196052

history sxy 0.1999934,9.06307

history sxy 0.1999918,8.929764

history sxy 0.06666559,8.796404

history sxy -0.06666085,8.796404

history sxy -0.19998707,8.929764

; ===apply a horizontal velocity at the point to pull the point towards left===

boundary interior xvel=-0.01 range -0.2,0.2 8.9,9.1

cycle 5000

Effect Of Rock Elastic Modulus (E=50 GPa)

Replace the command in discontinuity stability test "_E1 = 70.0E9" with "_E1 = 50.0E9".

D.8 Modeled UCS Test

E=400 GPa

config

round 0.01

edge 0.02

set ovtol 0.2

; ===model geometry===

block -0.50,-2.0 -0.50,2.0 0.50,2.0 0.50,-2.0

crack -0.5,-1.0 0.5,-1.0 crack -0.5,1.0 0.5,1.0

jset 90.0,0.0 5.0,0.0 0.0,0.0 0.25,0.0 0.0,0.0 range -30.0,70.0 -1.0,1.0

; ===generate finite-difference zones===

gen quad 0.2

; ===assign constitutive models and material properties===

;

```
def _parameter
_E1 = 400.0E9 ;rock
_nu1 = 0.2 ;rock
_E2 = 4.0E9 ;coal
_nu2 = 0.135 ;coal
_k1 = _E1/(3*(1-2*_nu1))
_g1 = _E1/(2*(1+_nu1))
_k2 = _E2/(3*(1-2*_nu2))
_g2 = _E2/(2*(1+_nu2))
end _parameter
;
table 1 0.0,2.2e6 0.00005 2.2E6 0.037,2.0e5 ;cohesion ;MCSS table
table 2 0.0,23.0 0.00002,30.0 0.0078,30.0 ;friction angle ;MCSS table
table 3 0.0,15.0 0.0005,15.0 0.001,5.0 0.0015,5.0 ;dilation ;MCSS table
;
zone model ss density 1313.0 bulk _k2 shear _g2 friction 23.0 cohesion 2200000.0 dilation
15.0 ftable 2.0 ctable 1.0 dtable 3.0 range -0.5,0.5 -1.0,1.0
prop mat=1 d=2670.0 k=_k1 g=_g1
change mat=1 range -0.5,0.5 -2.0,-1.0
change mat=1 range -0.5,0.5 1.0,2.0
prop jmat=1 jkn=50.0E9 jks=50.0E9 jen=0.0 jes=0.0 jfric=20.0 jif=50.0 jr=1.0e-4
change jmat=1 range -0.5,0.5 0.999,1.001 change jmat=1 range -0.5,0.5 -1.001,-0.999
prop jmat=2 jkn=50.0E9 jks=50.0E9 jfric=90.0 jcoh=1.0E20 jdil=90.0 jten=1.0E20
change jmat=2 range -0.5,0.5 -0.999,0.999
; ===apply boundary conditions===
bound yvel=-0.0005 range -1.0 1.0 1.99 2.01 ;top
bound yvel=0.0005 range -1.0 1.0 -2.01 -1.99 ;bottom
```

```
; ===define FISH functions===
def fcall_toks
; Tokens for FishCall numbers ...
FC_CYC_MOT = 0
FC_CONT_CREATE = 1
FC_CONT_DEL = 2
end
fcall_toks
;
def _stress
_sumstress = 0.0
loop n (1,11)
a =-0.6 + n*0.1
zi=z_near(a,0.0)
_sumstress = _sumstress+z_syy(zi)
endloop
end
;
def _averstress
_averstress = -1.0*_sumstress/11.0
end
;
def _dis
_sumdis = 0.0
_sumdis_sys = 0.0
loop m (1,11)
b=-0.6+m*0.1
```

```
gi_top=gp_near(b,1.0) ;top of the rock sample
gi_bot=gp_near(b,-1.0) ;bottom of the rock sample
_sumdis=_sumdis+gp_ydis(gi_bot)-gp_ydis(gi_top)
;
gi_top_sys=gp_near(b,2.0) ;top of the system
gi_bot_sys=gp_near(b,-2.0) ;bottom of the system
_sumdis_sys=_sumdis_sys+gp_ydis(gi_bot_sys)-gp_ydis(gi_top_sys)
endloop
gi1=gp_near(-0.5,0.0) ; left side of rock sample
gi2=gp_near(0.5,0.0) ; right side of rock sample
gi3=gp_near(0.0,1.0) ; top middle
gi4=gp_near(0.0,-1.0) ; bottom middle
_xdis1=gp_xdis(gi1)
_xdis2=gp_xdis(gi2)
_ydis_1=gp_ydis(gi3)
_ydis_2=gp_ydis(gi4)
end
;
def _ystrain
_ystrain=_sumdis/22.0
end
;
def _ystrain_sys
_ystrain_sys=_sumdis_sys/44.0
end
;
def _xstrain
```

```
_xstrain=(-1.0*_xdis1+1.0*_xdis2)/1.0
end
;
def _ystrain_middle
_ystrain_middle=(_ydis_2-_ydis_1)/2.0
end
;
hist n=10
hist unbal
hist _averstress
hist _ystrain
hist _xstrain
hist _ystrain_middle
hist _ystrain_sys
;
set fishcall FC_CYC_MOT _stress
set fishcall FC_CYC_MOT _dis
set fishcall FC_CYC_MOT _ystrain
set fishcall FC_CYC_MOT _xstrain
set fishcall FC_CYC_MOT _averstress
set fishcall FC_CYC_MOT _ystrain_middle
set fishcall FC_CYC_MOT _ystrain_sys
set energy on
hist energy
cycle 3800000
```

E=50 GPa

Replace the command in E=400 GPa simulation "_E1 = 400.0E9" with "_E1 = 50.0E9".

Replace the command in E=400 GPa simulation “cycle 3800000” with “cycle 2800000”.

E=1 GPa

Replace the command in E=400 GPa simulation “_E1 = 400.0E9” with “_E1 = 1.0E9”.

Replace the command in E=400 GPa simulation “cycle 3800000” with “cycle 5000000”.

D.9 Unstable Failure of Sidewall due to Unstable Shear Failure at Interface – CY Model

```
config
round 0.02
edge 0.04
set ovtol 0.2
; ===model geometry===
block -70.0,-80.0 -70.0,80.0 0.0,80.0 0.0,-80.0
crack -80.0 1.0 10.0 1.0
crack -80.0 -1.0 10.0 -1.0
jset 90.0,0.0 5.0,0.0 0.0,0.0 0.25,0.0 20.0,0.0 range -70.0,10.0 -1.0,1.0
; ===generate finite-element zones===
gen quad 0.4 range -70.0,10.0 -80.0,-1.0
gen quad 0.4 range -70.0,10.0 1.0,80.0
gen quad 0.2 range -70.0,10.0 -1.0,1.0
; ===assign constitutive models and material properties===
def _parameter
_E1 = 70.0E9 ;rock
_nu1 = 0.2 ;rock
_E2 = 4.0E9 ;coal
_nu2 = 0.135 ;coal
_k1 = _E1/(3*(1-2*_nu1))
_g1 = _E1/(2*(1+_nu1))
```

_k2 = _E2/(3*(1-2*_nu2))

_g2 = _E2/(2*(1+_nu2))

end

_parameter

;

table 1 0.0,2.2e6 0.00005 2.2E6 0.037,2.0e5 ;cohesion

table 2 0.0,23.0 0.00002,30.0 0.0078,30.0 ;friction angle

table 3 0.0,15.0 0.0005,15.0 0.001,5.0 0.0015,5.0 ;dilation

;

zone model ss density 1313.0 bulk _k2 shear _g2 friction 23.0 cohesion 2200000.0 dilation 15.0 ftable 2.0 ctable 1.0 dtable 3.0 range -80.0,10.0 -1.0,1.0

zone model elas density 2670.0 bulk _k1 shear _g1 range -80.0,10.0 1.0,100.0

zone model elas density 2670.0 bulk _k1 shear _g1 range -80.0,10.0 -100.0,-1.0 ;

;

set jcondf=3

change jcons=3 prop jmat=1 jkn=50.0E9 jks=50.0E9 jen=0.0 jes=0.0 jfric=20.0 jif=50.0 jr=1.0e-4

change jmat=1 range -80.0,10.0 0.999,1.001

change jmat=1 range -80.0,10.0 -1.001,-0.999

prop jmat=2 jkn=50.0E9 jks=50.0E9 jfric=90.0 jcoh=1.0E20 jdil=90.0 jten=1.0E20

change jmat=2 range -80.0,10.0 -0.999,0.999

; ===apply boundary conditions===

insitu stress -3.0E6 0.0 -10.0E6

bound stress -3.0E6 0.0 -10.0E6

bound xvel=0.0 range -0.1 0.1 -81.0 81.0 ;right

bound xvel=0.0 range -70.1 -69.9 -81.0 81.0 ;left

bound xvel=0.0 range -80.0 10.0 79.9 80.1 ;top

```
bound yvel=0.0 range -80.0 10.0 79.9 80.1 ;top
bound xvel=0.0 range -80.0 10.0 -80.1 -79.9 ;bottom
bound yvel=0.0 range -80.0 10.0 -80.1 -79.9 ;bottom
;
solve
; === shear displacement at the upper contact at left (10) ===
history sdisplace -10.124997,0.9998622 ;1
history sdisplace -10.624997,0.99986255 ;2
history sdisplace -11.124997,0.99986094 ;3
history sdisplace -11.624997,0.9998621 ;4
history sdisplace -12.124997,0.9998625 ;5
history sdisplace -12.624997,0.99986285 ;6
history sdisplace -13.124996,0.99986124 ;7
history sdisplace -13.624997,0.9998624 ;8
history sdisplace -14.124996,0.99986273 ;9
history sdisplace -14.624997,0.99986315 ;10
; === shear stress at the upper contact at left (10) ===
history sst -10.124997,0.9998622 ;1
history sst -10.624997,0.99986255 ;2
history sst -11.124997,0.99986094 ;3
history sst -11.624997,0.9998621 ;4
history sst -12.124997,0.9998625 ;5
history sst -12.624997,0.99986285 ;6
history sst -13.124996,0.99986124 ;7
history sst -13.624997,0.9998624 ;8
history sst -14.124996,0.99986273 ;9
history sst -14.624997,0.99986315 ;10
```

```
; === normal stress at the upper contact at left (10) ===
history nst -10.124997,0.9998622 ;1
history nst -10.624997,0.99986255 ;2
history nst -11.124997,0.99986094 ;3
history nst -11.624997,0.9998621 ;4
history nst -12.124997,0.9998625 ;5
history nst -12.624997,0.99986285 ;6
history nst -13.124996,0.99986124 ;7
history nst -13.624997,0.9998624 ;8
history nst -14.124996,0.99986273 ;9
history nst -14.624997,0.99986315 ;10
;
def fcall_toks
;Tokens for FishCall numbers ...
FC_CYC_MOT = 0
FC_CONT_CREATE = 1
FC_CONT_DEL = 2
end
fcall_toks
; ===W=0.5m (1) left-1 (-10.5 m to -10.0 m)===
def _stress1
_sumstress1 = 0.0
loop n1 (1,6)
a1 =-9.9 - n1*0.1
zi1=z_near(a1,0.0)
_sumstress1 = _sumstress1+z_syy(zi1)
endloop
```

```
end
;
def _averstress1
_averstress1 = -1.0*_sumstress1/6.0
end
;
def _dis1
_sumdis1 = 0.0
loop m1 (1,6)
b1=-9.9-m1*0.1
gi_top1=gp_near(b1,1.01) ;top of the coal layer
gi_bot1=gp_near(b1,-1.01) ;bottom of the coal layer
_sumdis1=_sumdis1+gp_ydis(gi_bot1)-gp_ydis(gi_top1)
endloop
end
;
def _ystrain1
_ystrain1=_sumdis1/12.0
end
;================================
;===W=1.0m (2)===
def _stress2
_sumstress2 = 0.0
loop n2 (1,6)
a2 =-9.8 - n2*0.2
zi2=z_near(a2,0.0)
_sumstress2 = _sumstress2+z_syy(zi2)
```

```
endloop
end
;
def _averstress2
_averstress2 = -1.0*_sumstress2/6.0
end
;
def _dis2
_sumdis2 = 0.0
loop m2 (1,6)
b2=-9.8-m2*0.2
gi_top2=gp_near(b2,1.01) ;top of the coal layer
gi_bot2=gp_near(b2,-1.01) ;bottom of the coal layer
_sumdis2=_sumdis2+gp_ydis(gi_bot2)-gp_ydis(gi_top2)
endloop
end
;
def _ystrain2
_ystrain2=_sumdis2/12.0
end
;================================
;===W=1.5m (3)===
def _stress3
_sumstress3 = 0.0
loop n3 (1,6)
a3 =-9.7 - n3*0.3
zi3=z_near(a3,0.0)
```

```
_sumstress3 = _sumstress3+z_syy(zi3)
endloop
end
;
def _averstress3
_averstress3 = -1.0*_sumstress3/6.0
end
;
def _dis3
_sumdis3 = 0.0
loop m3 (1,6)
b3=-9.7-m3*0.3
gi_top3=gp_near(b3,1.01) ;top of the coal layer
gi_bot3=gp_near(b3,-1.01) ;bottom of the coal layer
_sumdis3=_sumdis3+gp_ydis(gi_bot3)-gp_ydis(gi_top3)
endloop
end
;
def _ystrain3
_ystrain3=_sumdis3/12.0
end
;==================================
;===W=2.0m (4)===
_sumstress4 = 0.0
loop n4 (1,11)
a4 =-9.8 - n4*0.2
zi4=z_near(a4,0.0)
```

```
_sumstress4 = _sumstress4+z_syy(zi4)
endloop
end
;
def _averstress4
_averstress4 = -1.0*_sumstress4/11.0
end
;
def _dis4
_sumdis4 = 0.0
loop m4 (1,11)
b4=-9.8-m4*0.2
gi_top4=gp_near(b4,1.01) ;top of the coal layer
gi_bot4=gp_near(b4,-1.01) ;bottom of the coal layer
_sumdis4=_sumdis4+gp_ydis(gi_bot4)-gp_ydis(gi_top4)
endloop
end
;
def _ystrain4
_ystrain4=_sumdis4/22.0
end
;==================================
;===W=2.5m (5)===
def _stress5
_sumstress5 = 0.0
loop n5 (1,11)
a5 =-9.75 - n5*0.25
```

```
zi5=z_near(a5,0.0)
_sumstress5 = _sumstress5+z_syy(zi5)
endloop
end
;
def _averstress5
_averstress5 = -1.0*_sumstress5/11.0
end
;
def _dis5
_sumdis5 = 0.0
loop m5 (1,11)
b5=-9.75-m5*0.25
gi_top5=gp_near(b5,1.01) ;top of the coal layer
gi_bot5=gp_near(b5,-1.01) ;bottom of the coal layer
_sumdis5=_sumdis5+gp_ydis(gi_bot5)-gp_ydis(gi_top5)
endloop
end
;
def _ystrain5
_ystrain5=_sumdis5/22.0
end
;==================================
;===W=3.0m (6)===
def _stress6
_sumstress6 = 0.0
loop n6 (1,11)
```

```
a6 =-9.7 - n6*0.3
zi6=z_near(a6,0.0)
_sumstress6 = _sumstress6+z_syy(zi6)
endloop
end
;
def _averstress6
_averstress6 = -1.0*_sumstress6/11.0
end
;
def _dis6
_sumdis6 = 0.0
loop m6 (1,11)
b6=-9.7-m6*0.3
gi_top6=gp_near(b6,1.01) ;top of the coal layer
gi_bot6=gp_near(b6,-1.01) ;bottom of the coal layer
_sumdis6=_sumdis6+gp_ydis(gi_bot6)-gp_ydis(gi_top6)
endloop
end
;
def _ystrain6
_ystrain6=_sumdis6/22.0
end
;==============================
;===W=0.5m, left-2 (-11.0 m to -10.5 m)===
def _stress7
_sumstress7 = 0.0
```

```
loop n7 (1,6)
a7 =-10.4 - n7*0.1
zi7=z_near(a7,0.0)
_sumstress7 = _sumstress7+z_syy(zi7)
endloop
end
;
def _averstress7
_averstress7 = -1.0*_sumstress7/6.0
end
;
def _dis7
_sumdis7 = 0.0
loop m7 (1,6)
b7=-10.4-m7*0.1
gi_top7=gp_near(b7,1.01) ;top of the coal layer
gi_bot7=gp_near(b7,-1.01) ;bottom of the coal layer
_sumdis7=_sumdis7+gp_ydis(gi_bot7)-gp_ydis(gi_top7)
endloop end
;
def _ystrain7
_ystrain7=_sumdis7/12.0
end
;==============================
;===W=0.5m, left-3 (-11.5 m to -11.0 m)===
def _stress8
_sumstress8 = 0.0
```

```
loop n8 (1,6)
a8 =-10.9 - n8*0.1
zi8=z_near(a8,0.0)
_sumstress8 = _sumstress8+z_syy(zi8)
endloop
end
;
def _averstress8
_averstress8 = -1.0*_sumstress8/6.0
end
;
def _dis8
_sumdis8 = 0.0
loop m8 (1,6)
b8=-10.9-m8*0.1
gi_top8=gp_near(b8,1.01) ;top of the coal layer
gi_bot8=gp_near(b8,-1.01) ;bottom of the coal layer
_sumdis8=_sumdis8+gp_ydis(gi_bot8)-gp_ydis(gi_top8)
endloop
end
;
def _ystrain8
_ystrain8=_sumdis8/12.0
end
;==============================
;===W=0.5m, left-4 (-12.0 m to -11.5 m)===
def _stress9
```

```
_sumstress9 = 0.0
loop n9 (1,6)
a9 =-11.4 - n9*0.1
zi9=z_near(a9,0.0)
_sumstress9 = _sumstress9+z_syy(zi9)
endloop
end
;
def _averstress9
_averstress9 = -1.0*_sumstress9/6.0
end
;
def _dis9
_sumdis9 = 0.0
loop m9 (1,6)
b9=-11.4-m9*0.1
gi_top9=gp_near(b9,1.01) ;top of the coal layer
gi_bot9=gp_near(b9,-1.01) ;bottom of the coal layer
_sumdis9=_sumdis9+gp_ydis(gi_bot9)-gp_ydis(gi_top9)
endloop
end
;
def _ystrain9
_ystrain9=_sumdis9/12.0
end
;================================
;===W=0.5m, left-5 (-12.5 m to -12.0 m)===
```

```
def _stress10
_sumstress10 = 0.0
loop n10 (1,6)
a10 =-11.9 - n10*0.1
zi10=z_near(a10,0.0)
_sumstress10 = _sumstress10+z_syy(zi10)
endloop
end
;
def _averstress10
_averstress10 = -1.0*_sumstress10/6.0
end
;
def _dis10
_sumdis10 = 0.0
loop m10 (1,6)
b10=-11.9-m10*0.1
gi_top10=gp_near(b10,1.01) ;top of the coal layer
gi_bot10=gp_near(b10,-1.01) ;bottom of the coal layer
_sumdis10=_sumdis10+gp_ydis(gi_bot10)-gp_ydis(gi_top10)
endloop
end
;
def _ystrain10
_ystrain10=_sumdis10/12.0
end
;================================
```

```
;===W=0.5m, left-6 (-13.0 m to -12.5 m)===
def _stress11
_sumstress11 = 0.0
loop n11 (1,6)
a11 =-12.4 - n11*0.1
zi11=z_near(a11,0.0)
_sumstress11 = _sumstress11+z_syy(zi11)
endloop
end
;
def _averstress11
_averstress11 = -1.0*_sumstress11/6.0
end
;
def _dis11
_sumdis11 = 0.0
loop m11 (1,6)
b11=-12.4-m11*0.1
gi_top11=gp_near(b11,1.01) ;top of the coal layer
gi_bot11=gp_near(b11,-1.01) ;bottom of the coal layer
_sumdis11=_sumdis11+gp_ydis(gi_bot11)-gp_ydis(gi_top11)
endloop
end
;
def _ystrain11
_ystrain11=_sumdis11/12.0
end
```

;

hist unbal

hist _averstress1

hist _ystrain1

hist _averstress2

hist _ystrain2

hist _averstress3

hist _ystrain3

hist _averstress4

hist _ystrain4

hist _averstress5

hist _ystrain5

hist _averstress6

hist _ystrain6

hist _averstress7

hist _ystrain7

hist _averstress8

hist _ystrain8

hist _averstress9

hist _ystrain9

hist _averstress10

hist _ystrain10

hist _averstress11

hist _ystrain11

;

set fishcall FC_CYC_MOT _stress1

set fishcall FC_CYC_MOT _dis1

```
set fishcall FC_CYC_MOT _ystrain1
set fishcall FC_CYC_MOT _averstress1
;
set fishcall FC_CYC_MOT _stress2
set fishcall FC_CYC_MOT _dis2
set fishcall FC_CYC_MOT _ystrain2
set fishcall FC_CYC_MOT _averstress2
;
set fishcall FC_CYC_MOT _stress3
set fishcall FC_CYC_MOT _dis3
set fishcall FC_CYC_MOT _ystrain3
set fishcall FC_CYC_MOT _averstress3
;
set fishcall FC_CYC_MOT _stress4
set fishcall FC_CYC_MOT _dis4
set fishcall FC_CYC_MOT _ystrain4
set fishcall FC_CYC_MOT _averstress4
;
set fishcall FC_CYC_MOT _stress5
set fishcall FC_CYC_MOT _dis5
set fishcall FC_CYC_MOT _ystrain5
set fishcall FC_CYC_MOT _averstress5
;
set fishcall FC_CYC_MOT _stress6
set fishcall FC_CYC_MOT _dis6
set fishcall FC_CYC_MOT _ystrain6
set fishcall FC_CYC_MOT _averstress6
```

;

set fishcall FC_CYC_MOT _stress7

set fishcall FC_CYC_MOT _dis7

set fishcall FC_CYC_MOT _ystrain7

set fishcall FC_CYC_MOT _averstress7

;

set fishcall FC_CYC_MOT _stress8

set fishcall FC_CYC_MOT _dis8

set fishcall FC_CYC_MOT _ystrain8

set fishcall FC_CYC_MOT _averstress8

;

set fishcall FC_CYC_MOT _stress9

set fishcall FC_CYC_MOT _dis9

set fishcall FC_CYC_MOT _ystrain9

set fishcall FC_CYC_MOT _averstress9

;

set fishcall FC_CYC_MOT _stress10

set fishcall FC_CYC_MOT _dis10

set fishcall FC_CYC_MOT _ystrain10

set fishcall FC_CYC_MOT _averstress10

;

set fishcall FC_CYC_MOT _stress11

set fishcall FC_CYC_MOT _dis11

set fishcall FC_CYC_MOT _ystrain11

set fishcall FC_CYC_MOT _averstress11

;

delete range -0.25 0.0 -1.0 1.0

```
solve
delete range -0.50 0.0 -1.0 1.0
solve
delete range -0.75 0.0 -1.0 1.0
solve
delete range -1.00 0.0 -1.0 1.0
solve
delete range -1.25 0.0 -1.0 1.0
solve
delete range -1.50 0.0 -1.0 1.0
solve
delete range -1.75 0.0 -1.0 1.0
solve
delete range -2.00 0.0 -1.0 1.0
solve
delete range -2.25 0.0 -1.0 1.0
solve
delete range -2.50 0.0 -1.0 1.0
solve
delete range -2.75 0.0 -1.0 1.0
solve
delete range -3.00 0.0 -1.0 1.0
solve
delete range -3.25 0.0 -1.0 1.0
solve
delete range -3.50 0.0 -1.0 1.0
solve
```

delete range -3.75 0.0 -1.0 1.0

solve

delete range -4.00 0.0 -1.0 1.0

solve

delete range -4.25 0.0 -1.0 1.0

solve

delete range -4.50 0.0 -1.0 1.0

solve

delete range -4.75 0.0 -1.0 1.0

solve

delete range -5.00 0.0 -1.0 1.0

solve

delete range -5.25 0.0 -1.0 1.0

solve

delete range -5.50 0.0 -1.0 1.0

solve

delete range -5.75 0.0 -1.0 1.0

solve

delete range -6.00 0.0 -1.0 1.0

solve

delete range -6.25 0.0 -1.0 1.0

solve

delete range -6.50 0.0 -1.0 1.0

solve

delete range -6.75 0.0 -1.0 1.0

solve

delete range -7.00 0.0 -1.0 1.0

```
solve
delete range -7.25 0.0 -1.0 1.0
solve
delete range -7.50 0.0 -1.0 1.0
solve
delete range -7.75 0.0 -1.0 1.0
solve
delete range -8.00 0.0 -1.0 1.0
solve
delete range -8.25 0.0 -1.0 1.0
solve
delete range -8.50 0.0 -1.0 1.0
solve
delete range -8.75 0.0 -1.0 1.0
solve
delete range -9.00 0.0 -1.0 1.0
solve
delete range -9.25 0.0 -1.0 1.0
solve
delete range -9.50 0.0 -1.0 1.0
solve
delete range -9.75 0.0 -1.0 1.0
solve
delete range -10.00 0.0 -1.0 1.0
solve
bound yvel=-0.02 range -80.0 10.0 79.9 80.1 ;top
bound yvel=0.02 range -80.0 10.0 -80.1 -79.9 ;bottom
```

;

cycle 40000

D.10 Unstable Failure of Sidewall due to Unstable Shear Failure at Interface – MC Model

Raplace the commands in CY simulation "set jcondf=3; change jcons=3 prop jmat=1 jkn=50.0E9 jks=50.0E9 jen=0.0 jes=0.0 jfric=20.0 jif=50.0 jr=1.0e-4; change jmat=1 range -80.0,10.0 0.999,1.001; change jmat=1 range -80.0,10.0 -1.001,-0.999" with "prop jmat=1 jkn=50.0E9 jks=50.0E9 jfric=20.0 jcoh=2.5E6; change jmat=1 range -80.0,10.0 0.999,1.001; change jmat=1 range -80.0,10.0 -1.001,-0.999 ".

D.11 Unstable Compressive Failure of Mining Face and Sidewall due to Weak Region at Interface – Varying w_{wr}

w_{wr}= 0.0 m

Same as USF-CY simulation

w_{wr}= 0.5 m

config

round 0.02

edge 0.04

set ovtol 0.2

; ===model geometry===

block -70.0,-80.0 -70.0,80.0 0.0,80.0 0.0,-80.0

crack -80.0 1.0 10.0 1.0

crack -80.0 -1.0 10.0 -1.0

jset 90.0,0.0 5.0,0.0 0.0,0.0 0.25,0.0 20.0,0.0 range -70.0,10.0 -1.0,1.0

; ===generate finite-element zones===

gen quad 0.4 range -70.0,10.0 -80.0,-1.0

gen quad 0.4 range -70.0,10.0 1.0,80.0

gen quad 0.2 range -70.0,10.0 -1.0,1.0

```
; ===assign constitutive models and material properties===
def _parameter
_E1 = 70.0E9 ;rock
_nu1 = 0.2 ;rock
_E2 = 4.0E9 ;coal
_nu2 = 0.135 ;coal
_k1 = _E1/(3*(1-2*_nu1))
_g1 = _E1/(2*(1+_nu1))
_k2 = _E2/(3*(1-2*_nu2))
_g2 = _E2/(2*(1+_nu2))
end
_parameter
;
table 1 0.0,2.2e6 0.00005 2.2E6 0.037,2.0e5 ;cohesion
table 2 0.0,23.0 0.00002,30.0 0.0078,30.0 ;friction angle
table 3 0.0,15.0 0.0005,15.0 0.001,5.0 0.0015,5.0 ;dilation
;
zone model ss density 1313.0 bulk _k2 shear _g2 friction 23.0 cohesion 2200000.0 dilation
15.0 ftable 2.0 ctable 1.0 dtable 3.0 range -80.0,10.0 -1.0,1.0
zone model elas density 2670.0 bulk _k1 shear _g1 range -80.0,10.0 1.0,100.0
zone model elas density 2670.0 bulk _k1 shear _g1 range -80.0,10.0 -100.0,-1.0 ;
;
set jcondf=3
change jcons=3 prop jmat=1 jkn=50.0E9 jks=50.0E9 jen=0.0 jes=0.0 jfric=20.0 jif=50.0
jr=1.0e-4
change jmat=1 range -80.0,10.0 0.999,1.001
change jmat=1 range -80.0,10.0 -1.001,-0.999
```

```
prop jmat=2 jkn=50.0E9 jks=50.0E9 jfric=90.0 jcoh=1.0E20 jdil=90.0 jten=1.0E20
change jmat=2 range -80.0,10.0 -0.999,0.999
prop jmat=3 jkn=50.0E9 jks=50.0E9 jfric=0.0 jcoh=0.0 jdil=0.0 jten=0.0
change jmat=3 range -11.0,-10.5 0.999,1.001
change jmat=3 range -11.0,-10.5 -1.001,-0.999
; ===apply boundary conditions===
insitu stress -3.0E6 0.0 -10.0E6
bound stress -3.0E6 0.0 -10.0E6
bound xvel=0.0 range -0.1 0.1 -81.0 81.0 ;right
bound xvel=0.0 range -70.1 -69.9 -81.0 81.0 ;left
bound xvel=0.0 range -80.0 10.0 79.9 80.1 ;top
bound yvel=0.0 range -80.0 10.0 79.9 80.1 ;top
bound xvel=0.0 range -80.0 10.0 -80.1 -79.9 ;bottom
bound yvel=0.0 range -80.0 10.0 -80.1 -79.9 ;bottom
;
solve
; === shear displacement at the upper contact at left (10) ===
history sdisplace -10.124997,0.9998622 ;1
history sdisplace -10.624997,0.99986255 ;2
history sdisplace -11.124997,0.99986094 ;3
history sdisplace -11.624997,0.9998621 ;4
history sdisplace -12.124997,0.9998625 ;5
history sdisplace -12.624997,0.99986285 ;6
history sdisplace -13.124996,0.99986124 ;7
history sdisplace -13.624997,0.9998624 ;8
history sdisplace -14.124996,0.99986273 ;9
history sdisplace -14.624997,0.99986315 ;10
```

; === shear stress at the upper contact at left (10) ===

history sst -10.124997,0.9998622 ;1

history sst -10.624997,0.99986255 ;2

history sst -11.124997,0.99986094 ;3

history sst -11.624997,0.9998621 ;4

history sst -12.124997,0.9998625 ;5

history sst -12.624997,0.99986285 ;6

history sst -13.124996,0.99986124 ;7

history sst -13.624997,0.9998624 ;8

history sst -14.124996,0.99986273 ;9

history sst -14.624997,0.99986315 ;10

; === normal stress at the upper contact at left (10) ===

history nst -10.124997,0.9998622 ;1

history nst -10.624997,0.99986255 ;2

history nst -11.124997,0.99986094 ;3

history nst -11.624997,0.9998621 ;4

history nst -12.124997,0.9998625 ;5

history nst -12.624997,0.99986285 ;6

history nst -13.124996,0.99986124 ;7

history nst -13.624997,0.9998624 ;8

history nst -14.124996,0.99986273 ;9

history nst -14.624997,0.99986315 ;10

;

def fcall_toks

;Tokens for FishCall numbers ...

FC_CYC_MOT = 0

FC_CONT_CREATE = 1

```
FC_CONT_DEL = 2
end
fcall_toks
; ===W=0.5m (1) left-1 (-10.5 m to -10.0 m)===
def _stress1
_sumstress1 = 0.0
loop n1 (1,6)
a1 =-9.9 - n1*0.1
zi1=z_near(a1,0.0)
_sumstress1 = _sumstress1+z_syy(zi1)
endloop
end
;
def _averstress1
_averstress1 = -1.0*_sumstress1/6.0
end
;
def _dis1
_sumdis1 = 0.0
loop m1 (1,6)
b1=-9.9-m1*0.1
gi_top1=gp_near(b1,1.01) ;top of the coal layer
gi_bot1=gp_near(b1,-1.01) ;bottom of the coal layer
_sumdis1=_sumdis1+gp_ydis(gi_bot1)-gp_ydis(gi_top1)
endloop
end
;
```

```
def _ystrain1
_ystrain1=_sumdis1/12.0
end
;==================================
;===W=1.0m (2)===
def _stress2
_sumstress2 = 0.0
loop n2 (1,6)
a2 =-9.8 - n2*0.2
zi2=z_near(a2,0.0)
_sumstress2 = _sumstress2+z_syy(zi2)
endloop
end
;
def _averstress2
_averstress2 = -1.0*_sumstress2/6.0
end
;
def _dis2
_sumdis2 = 0.0
loop m2 (1,6)
b2=-9.8-m2*0.2
gi_top2=gp_near(b2,1.01) ;top of the coal layer
gi_bot2=gp_near(b2,-1.01) ;bottom of the coal layer
_sumdis2=_sumdis2+gp_ydis(gi_bot2)-gp_ydis(gi_top2)
endloop
end
```

```
;
def _ystrain2
_ystrain2=_sumdis2/12.0
end
;==================================
;===W=1.5m (3)===
def _stress3
_sumstress3 = 0.0
loop n3 (1,6)
a3 =-9.7 - n3*0.3
zi3=z_near(a3,0.0)
_sumstress3 = _sumstress3+z_syy(zi3)
endloop
end
;
def _averstress3
_averstress3 = -1.0*_sumstress3/6.0
end
;
def _dis3
_sumdis3 = 0.0
loop m3 (1,6)
b3=-9.7-m3*0.3
gi_top3=gp_near(b3,1.01) ;top of the coal layer
gi_bot3=gp_near(b3,-1.01) ;bottom of the coal layer
_sumdis3=_sumdis3+gp_ydis(gi_bot3)-gp_ydis(gi_top3)
endloop
```

```
end
;
def _ystrain3
_ystrain3=_sumdis3/12.0
end
;==============================
;===W=2.0m (4)===
def _stress4
_sumstress4 = 0.0
loop n4 (1,11)
a4 =-9.8 - n4*0.2
zi4=z_near(a4,0.0)
_sumstress4 = _sumstress4+z_syy(zi4)
endloop
end
;
def _averstress4
_averstress4 = -1.0*_sumstress4/11.0
end
;
def _dis4
_sumdis4 = 0.0
loop m4 (1,11)
b4=-9.8-m4*0.2
gi_top4=gp_near(b4,1.01) ;top of the coal layer
gi_bot4=gp_near(b4,-1.01) ;bottom of the coal layer
_sumdis4=_sumdis4+gp_ydis(gi_bot4)-gp_ydis(gi_top4)
```

```
endloop
end
;
def _ystrain4
_ystrain4=_sumdis4/22.0
end
;==================================
;===W=2.5m (5)===
def _stress5
_sumstress5 = 0.0
loop n5 (1,11)
a5 =-9.75 - n5*0.25
zi5=z_near(a5,0.0)
_sumstress5 = _sumstress5+z_syy(zi5)
endloop
end
;
def _averstress5
_averstress5 = -1.0*_sumstress5/11.0
end
;
def _dis5
_sumdis5 = 0.0
loop m5 (1,11)
b5=-9.75-m5*0.25
gi_top5=gp_near(b5,1.01) ;top of the coal layer
gi_bot5=gp_near(b5,-1.01) ;bottom of the coal layer
```

```
_sumdis5=_sumdis5+gp_ydis(gi_bot5)-gp_ydis(gi_top5)
endloop
end
;
def _ystrain5
_ystrain5=_sumdis5/22.0
end
;==============================
;===W=3.0m (6)===
def _stress6
_sumstress6 = 0.0
loop n6 (1,11)
a6 =-9.7 - n6*0.3
zi6=z_near(a6,0.0)
_sumstress6 = _sumstress6+z_syy(zi6)
endloop
end
;
def _averstress6
_averstress6 = -1.0*_sumstress6/11.0
end
;
def _dis6
_sumdis6 = 0.0
loop m6 (1,11)
b6=-9.7-m6*0.3
gi_top6=gp_near(b6,1.01) ;top of the coal layer
```

```
gi_bot6=gp_near(b6,-1.01) ;bottom of the coal layer
_sumdis6=_sumdis6+gp_ydis(gi_bot6)-gp_ydis(gi_top6)
endloop
end
;
def _ystrain6
_ystrain6=_sumdis6/22.0
end
;================================
;===W=0.5m, left-2 (-11.0 m to -10.5 m)===
def _stress7
_sumstress7 = 0.0
loop n7 (1,6)
a7 =-10.4 - n7*0.1
zi7=z_near(a7,0.0)
_sumstress7 = _sumstress7+z_syy(zi7)
endloop
end
;
def _averstress7
_averstress7 = -1.0*_sumstress7/6.0
end
;
def _dis7
_sumdis7 = 0.0
loop m7 (1,6)
b7=-10.4-m7*0.1
```

```
gi_top7=gp_near(b7,1.01) ;top of the coal layer
gi_bot7=gp_near(b7,-1.01) ;bottom of the coal layer
_sumdis7=_sumdis7+gp_ydis(gi_bot7)-gp_ydis(gi_top7)
endloop end
;
def _ystrain7
_ystrain7=_sumdis7/12.0
end
;================================
;===W=0.5m, left-3 (-11.5 m to -11.0 m)===
def _stress8
_sumstress8 = 0.0
loop n8 (1,6)
a8 =-10.9 - n8*0.1
zi8=z_near(a8,0.0)
_sumstress8 = _sumstress8+z_syy(zi8)
endloop
end
;
def _averstress8
_averstress8 = -1.0*_sumstress8/6.0
end
;
def _dis8
_sumdis8 = 0.0
loop m8 (1,6)
b8=-10.9-m8*0.1
```

```
gi_top8=gp_near(b8,1.01) ;top of the coal layer
gi_bot8=gp_near(b8,-1.01) ;bottom of the coal layer
_sumdis8=_sumdis8+gp_ydis(gi_bot8)-gp_ydis(gi_top8)
endloop
end
;
def _ystrain8
_ystrain8=_sumdis8/12.0
end
;==============================
;===W=0.5m, left-4 (-12.0 m to -11.5 m)===
def _stress9
_sumstress9 = 0.0
loop n9 (1,6)
a9 =-11.4 - n9*0.1
zi9=z_near(a9,0.0)
_sumstress9 = _sumstress9+z_syy(zi9)
endloop
end
;
def _averstress9
_averstress9 = -1.0*_sumstress9/6.0
end
;
def _dis9
_sumdis9 = 0.0
loop m9 (1,6)
```

```
b9=-11.4-m9*0.1
gi_top9=gp_near(b9,1.01) ;top of the coal layer
gi_bot9=gp_near(b9,-1.01) ;bottom of the coal layer
_sumdis9=_sumdis9+gp_ydis(gi_bot9)-gp_ydis(gi_top9)
endloop
end
;
def _ystrain9
_ystrain9=_sumdis9/12.0
end
;==============================
;===W=0.5m, left-5 (-12.5 m to -12.0 m)===
def _stress10
_sumstress10 = 0.0
loop n10 (1,6)
a10 =-11.9 - n10*0.1
zi10=z_near(a10,0.0)
_sumstress10 = _sumstress10+z_syy(zi10)
endloop
end
;
def _averstress10
_averstress10 = -1.0*_sumstress10/6.0
end
;
def _dis10
_sumdis10 = 0.0
```

```
loop m10 (1,6)
b10=-11.9-m10*0.1
gi_top10=gp_near(b10,1.01) ;top of the coal layer
gi_bot10=gp_near(b10,-1.01) ;bottom of the coal layer
_sumdis10=_sumdis10+gp_ydis(gi_bot10)-gp_ydis(gi_top10)
endloop
end
;
def _ystrain10
_ystrain10=_sumdis10/12.0
end
;==================================
;===W=0.5m, left-6 (-13.0 m to -12.5 m)===
def _stress11
_sumstress11 = 0.0
loop n11 (1,6)
a11 =-12.4 - n11*0.1
zi11=z_near(a11,0.0)
_sumstress11 = _sumstress11+z_syy(zi11)
endloop
end
;
def _averstress11
_averstress11 = -1.0*_sumstress11/6.0
end
;
def _dis11
```

```
_sumdis11 = 0.0
loop m11 (1,6)
b11=-12.4-m11*0.1
gi_top11=gp_near(b11,1.01) ;top of the coal layer
gi_bot11=gp_near(b11,-1.01) ;bottom of the coal layer
_sumdis11=_sumdis11+gp_ydis(gi_bot11)-gp_ydis(gi_top11)
endloop
end
;
def _ystrain11
_ystrain11=_sumdis11/12.0
end
;
hist unbal
hist _averstress1
hist _ystrain1
hist _averstress2
hist _ystrain2
hist _averstress3
hist _ystrain3
hist _averstress4
hist _ystrain4
hist _averstress5
hist _ystrain5
hist _averstress6
hist _ystrain6
hist _averstress7
```

hist _ystrain7

hist _averstress8

hist _ystrain8

hist _averstress9

hist _ystrain9

hist _averstress10

hist _ystrain10

hist _averstress11

hist _ystrain11

;

set fishcall FC_CYC_MOT _stress1

set fishcall FC_CYC_MOT _dis1

set fishcall FC_CYC_MOT _ystrain1

set fishcall FC_CYC_MOT _averstress1

;

set fishcall FC_CYC_MOT _stress2

set fishcall FC_CYC_MOT _dis2

set fishcall FC_CYC_MOT _ystrain2

set fishcall FC_CYC_MOT _averstress2

;

set fishcall FC_CYC_MOT _stress3

set fishcall FC_CYC_MOT _dis3

set fishcall FC_CYC_MOT _ystrain3

set fishcall FC_CYC_MOT _averstress3

;

set fishcall FC_CYC_MOT _stress4

set fishcall FC_CYC_MOT _dis4

```
set fishcall FC_CYC_MOT _ystrain4
set fishcall FC_CYC_MOT _averstress4
;
set fishcall FC_CYC_MOT _stress5
set fishcall FC_CYC_MOT _dis5
set fishcall FC_CYC_MOT _ystrain5
set fishcall FC_CYC_MOT _averstress5
;
set fishcall FC_CYC_MOT _stress6
set fishcall FC_CYC_MOT _dis6
set fishcall FC_CYC_MOT _ystrain6
set fishcall FC_CYC_MOT _averstress6
;
set fishcall FC_CYC_MOT _stress7
set fishcall FC_CYC_MOT _dis7
set fishcall FC_CYC_MOT _ystrain7
set fishcall FC_CYC_MOT _averstress7
;
set fishcall FC_CYC_MOT _stress8
set fishcall FC_CYC_MOT _dis8
set fishcall FC_CYC_MOT _ystrain8
set fishcall FC_CYC_MOT _averstress8
;
set fishcall FC_CYC_MOT _stress9
set fishcall FC_CYC_MOT _dis9
set fishcall FC_CYC_MOT _ystrain9
set fishcall FC_CYC_MOT _averstress9
```

;

set fishcall FC_CYC_MOT _stress10

set fishcall FC_CYC_MOT _dis10

set fishcall FC_CYC_MOT _ystrain10

set fishcall FC_CYC_MOT _averstress10

;

set fishcall FC_CYC_MOT _stress11

set fishcall FC_CYC_MOT _dis11

set fishcall FC_CYC_MOT _ystrain11

set fishcall FC_CYC_MOT _averstress11

;

delete range -0.25 0.0 -1.0 1.0

solve

delete range -0.50 0.0 -1.0 1.0

solve

delete range -0.75 0.0 -1.0 1.0

solve

delete range -1.00 0.0 -1.0 1.0

solve

delete range -1.25 0.0 -1.0 1.0

solve

delete range -1.50 0.0 -1.0 1.0

solve

delete range -1.75 0.0 -1.0 1.0

solve

delete range -2.00 0.0 -1.0 1.0

solve

delete range -2.25 0.0 -1.0 1.0

solve

delete range -2.50 0.0 -1.0 1.0

solve

delete range -2.75 0.0 -1.0 1.0

solve

delete range -3.00 0.0 -1.0 1.0

solve

delete range -3.25 0.0 -1.0 1.0

solve

delete range -3.50 0.0 -1.0 1.0

solve

delete range -3.75 0.0 -1.0 1.0

solve

delete range -4.00 0.0 -1.0 1.0

solve

delete range -4.25 0.0 -1.0 1.0

solve

delete range -4.50 0.0 -1.0 1.0

solve

delete range -4.75 0.0 -1.0 1.0

solve

delete range -5.00 0.0 -1.0 1.0

solve

delete range -5.25 0.0 -1.0 1.0

solve

delete range -5.50 0.0 -1.0 1.0

```
solve
delete range -5.75 0.0 -1.0 1.0
solve
delete range -6.00 0.0 -1.0 1.0
solve
delete range -6.25 0.0 -1.0 1.0
solve
delete range -6.50 0.0 -1.0 1.0
solve
delete range -6.75 0.0 -1.0 1.0
solve
delete range -7.00 0.0 -1.0 1.0
solve
delete range -7.25 0.0 -1.0 1.0
solve
delete range -7.50 0.0 -1.0 1.0
solve
delete range -7.75 0.0 -1.0 1.0
solve
delete range -8.00 0.0 -1.0 1.0
solve
delete range -8.25 0.0 -1.0 1.0
solve
delete range -8.50 0.0 -1.0 1.0
solve
delete range -8.75 0.0 -1.0 1.0
solve
```

delete range -9.00 0.0 -1.0 1.0

solve

delete range -9.25 0.0 -1.0 1.0

solve

delete range -9.50 0.0 -1.0 1.0

solve

delete range -9.75 0.0 -1.0 1.0

solve

delete range -10.00 0.0 -1.0 1.0

solve

bound yvel=-0.02 range -80.0 10.0 79.9 80.1 ;top

bound yvel=0.02 range -80.0 10.0 -80.1 -79.9 ;bottom

;

cycle 40000

w_{wr}= 1.0 m

Replacement commands in **w_{wr}= 0.5 m** "change jmat=3 range -11.0, -10.5 0.999, 1.001; change jmat=3 range -11.0, -10.5 -1.001, -0.999" with "change jmat=3 range -11.5, -10.5 0.999, 1.001; change jmat=3 range -11.5, -10.5 -1.001, -0.999".

w_{wr}= 1.5 m

Replacement commands in **w_{wr}= 0.5 m** "change jmat=3 range -11.0, -10.5 0.999, 1.001; change jmat=3 range -11.0, -10.5 -1.001, -0.999" with "change jmat=3 range -12.0, -10.5 0.999, 1.001; change jmat=3 range -12.0, -10.5 -1.001, -0.999".

w_{wr}= 2.0 m

Replacement commands in **w_{wr}= 0.5 m** "change jmat=3 range -11.0, -10.5 0.999, 1.001; change jmat=3 range -11.0, -10.5 -1.001, -0.999" with "change jmat=3 range -12.5, -10.5 0.999, 1.001; change jmat=3 range -12.5, -10.5 -1.001, -0.999".

D.12 Unstable Compressive Failure of Mining Face and Sidewall due to Weak Region at Interface – Varying w_b

w_b= 0.0 m

```
config
round 0.02
edge 0.04
set ovtol 0.2
; ===model geometry===
block -70.0,-80.0 -70.0,80.0 0.0,80.0 0.0,-80.0
crack -80.0 1.0 10.0 1.0
crack -80.0 -1.0 10.0 -1.0
jset 90.0,0.0 5.0,0.0 0.0,0.0 0.25,0.0 20.0,0.0 range -70.0,10.0 -1.0,1.0
; ===generate finite-element zones===
gen quad 0.4 range -70.0,10.0 -80.0,-1.0
gen quad 0.4 range -70.0,10.0 1.0,80.0
gen quad 0.2 range -70.0,10.0 -1.0,1.0
; ===assign constitutive models and material properties===
def _parameter
_E1 = 70.0E9 ;rock
_nu1 = 0.2 ;rock
_E2 = 4.0E9 ;coal
_nu2 = 0.135 ;coal
_k1 = _E1/(3*(1-2*_nu1))
_g1 = _E1/(2*(1+_nu1))
_k2 = _E2/(3*(1-2*_nu2))
_g2 = _E2/(2*(1+_nu2))
end
```

_parameter

;

table 1 0.0,2.2e6 0.00005 2.2E6 0.037,2.0e5 ;cohesion

table 2 0.0,23.0 0.00002,30.0 0.0078,30.0 ;friction angle

table 3 0.0,15.0 0.0005,15.0 0.001,5.0 0.0015,5.0 ;dilation

;

zone model ss density 1313.0 bulk _k2 shear _g2 friction 23.0 cohesion 2200000.0 dilation 15.0 ftable 2.0 ctable 1.0 dtable 3.0 range -80.0,10.0 -1.0,1.0

zone model elas density 2670.0 bulk _k1 shear _g1 range -80.0,10.0 1.0,100.0

zone model elas density 2670.0 bulk _k1 shear _g1 range -80.0,10.0 -100.0,-1.0 ;

;

set jcondf=3

change jcons=3 prop jmat=1 jkn=50.0E9 jks=50.0E9 jen=0.0 jes=0.0 jfric=20.0 jif=50.0 jr=1.0e-4

change jmat=1 range -80.0,10.0 0.999,1.001

change jmat=1 range -80.0,10.0 -1.001,-0.999

prop jmat=2 jkn=50.0E9 jks=50.0E9 jfric=90.0 jcoh=1.0E20 jdil=90.0 jten=1.0E20

change jmat=2 range -80.0,10.0 -0.999,0.999

prop jmat=3 jkn=50.0E9 jks=50.0E9 jfric=0.0 jcoh=0.0 jdil=0.0 jten=0.0

change jmat=3 range -12.0,-10.0 0.999,1.001

change jmat=3 range -12.0,-10.0 -1.001,-0.999

; ===apply boundary conditions===

insitu stress -3.0E6 0.0 -10.0E6

bound stress -3.0E6 0.0 -10.0E6

bound xvel=0.0 range -0.1 0.1 -81.0 81.0 ;right

bound xvel=0.0 range -70.1 -69.9 -81.0 81.0 ;left

bound xvel=0.0 range -80.0 10.0 79.9 80.1 ;top

bound yvel=0.0 range -80.0 10.0 79.9 80.1 ;top

bound xvel=0.0 range -80.0 10.0 -80.1 -79.9 ;bottom

bound yvel=0.0 range -80.0 10.0 -80.1 -79.9 ;bottom

;

solve

; === shear displacement at the upper contact at left (10) ===

history sdisplace -10.124997,0.9998622 ;1

history sdisplace -10.624997,0.99986255 ;2

history sdisplace -11.124997,0.99986094 ;3

history sdisplace -11.624997,0.9998621 ;4

history sdisplace -12.124997,0.9998625 ;5

history sdisplace -12.624997,0.99986285 ;6

history sdisplace -13.124996,0.99986124 ;7

history sdisplace -13.624997,0.9998624 ;8

history sdisplace -14.124996,0.99986273 ;9

history sdisplace -14.624997,0.99986315 ;10

; === shear stress at the upper contact at left (10) ===

history sst -10.124997,0.9998622 ;1

history sst -10.624997,0.99986255 ;2

history sst -11.124997,0.99986094 ;3

history sst -11.624997,0.9998621 ;4

history sst -12.124997,0.9998625 ;5

history sst -12.624997,0.99986285 ;6

history sst -13.124996,0.99986124 ;7

history sst -13.624997,0.9998624 ;8

history sst -14.124996,0.99986273 ;9

history sst -14.624997,0.99986315 ;10

```
; === normal stress at the upper contact at left (10) ===
history nst -10.124997,0.9998622 ;1
history nst -10.624997,0.99986255 ;2
history nst -11.124997,0.99986094 ;3
history nst -11.624997,0.9998621 ;4
history nst -12.124997,0.9998625 ;5
history nst -12.624997,0.99986285 ;6
history nst -13.124996,0.99986124 ;7
history nst -13.624997,0.9998624 ;8
history nst -14.124996,0.99986273 ;9
history nst -14.624997,0.99986315 ;10
;
def fcall_toks
;Tokens for FishCall numbers ...
FC_CYC_MOT = 0
FC_CONT_CREATE = 1
FC_CONT_DEL = 2
end
;===W=0.5m (1) left-1 (-10.5 m to -10.0 m)===
def _stress1
_sumstress1 = 0.0
loop n1 (1,6)
a1 =-9.9 - n1*0.1
zi1=z_near(a1,0.0)
_sumstress1 = _sumstress1+z_syy(zi1)
endloop end
;
```

```
def _averstress1
_averstress1 = -1.0*_sumstress1/6.0
end
;
def _dis1
_sumdis1 = 0.0
loop m1 (1,6)
b1=-9.9-m1*0.1
gi_top1=gp_near(b1,1.01) ;top of the coal layer
gi_bot1=gp_near(b1,-1.01) ;bottom of the coal layer
_sumdis1=_sumdis1+gp_ydis(gi_bot1)-gp_ydis(gi_top1)
endloop
end
;
def _ystrain1
_ystrain1=_sumdis1/12.0
end
;================================
;===W=1.0m (2)===
def _stress2
_sumstress2 = 0.0
loop n2 (1,6)
a2 =-9.8 - n2*0.2
zi2=z_near(a2,0.0)
_sumstress2 = _sumstress2+z_syy(zi2)
endloop
end
```

```
;
def _averstress2
_averstress2 = -1.0*_sumstress2/6.0
end
;
def _dis2
_sumdis2 = 0.0
loop m2 (1,6)
b2=-9.8-m2*0.2
gi_top2=gp_near(b2,1.01) ;top of the coal layer
gi_bot2=gp_near(b2,-1.01) ;bottom of the coal layer
_sumdis2=_sumdis2+gp_ydis(gi_bot2)-gp_ydis(gi_top2)
endloop
end
;
def _ystrain2
_ystrain2=_sumdis2/12.0
end
;================================
;===W=1.5m (3)===
def _stress3
_sumstress3 = 0.0
loop n3 (1,6)
a3 =-9.7 - n3*0.3
zi3=z_near(a3,0.0)
_sumstress3 = _sumstress3+z_syy(zi3)
endloop
```

```
end
;
def _averstress3
_averstress3 = -1.0*_sumstress3/6.0
end
;
def _dis3
_sumdis3 = 0.0
loop m3 (1,6)
b3=-9.7-m3*0.3
gi_top3=gp_near(b3,1.01) ;top of the coal layer
gi_bot3=gp_near(b3,-1.01) ;bottom of the coal layer
_sumdis3=_sumdis3+gp_ydis(gi_bot3)-gp_ydis(gi_top3)
endloop
end
;
def _ystrain3
_ystrain3=_sumdis3/12.0
end
;==================================
;===W=2.0m (4)===
def _stress4
_sumstress4 = 0.0
loop n4 (1,11)
a4 =-9.8 - n4*0.2
zi4=z_near(a4,0.0)
_sumstress4 = _sumstress4+z_syy(zi4)
```

```
endloop
end
;
def _averstress4
_averstress4 = -1.0*_sumstress4/11.0
end
;
def _dis4
_sumdis4 = 0.0
loop m4 (1,11)
b4=-9.8-m4*0.2
gi_top4=gp_near(b4,1.01) ;top of the coal layer
gi_bot4=gp_near(b4,-1.01) ;bottom of the coal layer
_sumdis4=_sumdis4+gp_ydis(gi_bot4)-gp_ydis(gi_top4)
endloop
end
;
def _ystrain4
_ystrain4=_sumdis4/22.0
end
;================================
;===W=2.5m (5)===
def _stress5
_sumstress5 = 0.0
loop n5 (1,11)
a5 =-9.75 - n5*0.25
zi5=z_near(a5,0.0)
```

```
_sumstress5 = _sumstress5+z_syy(zi5)
endloop
end
;
def _averstress5
_averstress5 = -1.0*_sumstress5/11.0
end
;
def _dis5
_sumdis5 = 0.0
loop m5 (1,11)
b5=-9.75-m5*0.25
gi_top5=gp_near(b5,1.01) ;top of the coal layer
gi_bot5=gp_near(b5,-1.01) ;bottom of the coal layer
_sumdis5=_sumdis5+gp_ydis(gi_bot5)-gp_ydis(gi_top5)
endloop
end
;
def _ystrain5
_ystrain5=_sumdis5/22.0
end
;================================
;===W=3.0m (6)===
def _stress6
_sumstress6 = 0.0
loop n6 (1,11)
a6 =-9.7 - n6*0.3
```

```
zi6=z_near(a6,0.0)
_sumstress6 = _sumstress6+z_syy(zi6)
endloop
end
;
def _averstress6
_averstress6 = -1.0*_sumstress6/11.0
end
;
def _dis6
_sumdis6 = 0.0
loop m6 (1,11)
b6=-9.7-m6*0.3
gi_top6=gp_near(b6,1.01) ;top of the coal layer
gi_bot6=gp_near(b6,-1.01) ;bottom of the coal layer
_sumdis6=_sumdis6+gp_ydis(gi_bot6)-gp_ydis(gi_top6)
endloop
end
;
def _ystrain6
_ystrain6=_sumdis6/22.0
end
;==================================
;===W=0.5m, left-2 (-11.0 m to -10.5 m)===
def _stress7
_sumstress7 = 0.0
loop n7 (1,6)
```

```
a7 =-10.4 - n7*0.1
zi7=z_near(a7,0.0)
_sumstress7 = _sumstress7+z_syy(zi7)
endloop
end
;
def _averstress7
_averstress7 = -1.0*_sumstress7/6.0
end
;
def _dis7
_sumdis7 = 0.0
loop m7 (1,6)
b7=-10.4-m7*0.1
gi_top7=gp_near(b7,1.01) ;top of the coal layer
gi_bot7=gp_near(b7,-1.01) ;bottom of the coal layer
_sumdis7=_sumdis7+gp_ydis(gi_bot7)-gp_ydis(gi_top7)
endloop end
;
def _ystrain7
_ystrain7=_sumdis7/12.0
end
;================================
;===W=0.5m, left-3 (-11.5 m to -11.0 m)===
def _stress8
_sumstress8 = 0.0
loop n8 (1,6)
```

```
a8 =-10.9 - n8*0.1
zi8=z_near(a8,0.0)
_sumstress8 = _sumstress8+z_syy(zi8)
endloop
end
;
def _averstress8
_averstress8 = -1.0*_sumstress8/6.0
end
;
def _dis8
_sumdis8 = 0.0
loop m8 (1,6)
b8=-10.9-m8*0.1
gi_top8=gp_near(b8,1.01) ;top of the coal layer
gi_bot8=gp_near(b8,-1.01) ;bottom of the coal layer
_sumdis8=_sumdis8+gp_ydis(gi_bot8)-gp_ydis(gi_top8)
endloop
end
;
def _ystrain8
_ystrain8=_sumdis8/12.0
end
;==============================
;===W=0.5m, left-4 (-12.0 m to -11.5 m)===
def _stress9
_sumstress9 = 0.0
```

```
loop n9 (1,6)
a9 =-11.4 - n9*0.1
zi9=z_near(a9,0.0)
_sumstress9 = _sumstress9+z_syy(zi9)
endloop
end
;
def _averstress9
_averstress9 = -1.0*_sumstress9/6.0
end
;
def _dis9
_sumdis9 = 0.0
loop m9 (1,6)
b9=-11.4-m9*0.1
gi_top9=gp_near(b9,1.01) ;top of the coal layer
gi_bot9=gp_near(b9,-1.01) ;bottom of the coal layer
_sumdis9=_sumdis9+gp_ydis(gi_bot9)-gp_ydis(gi_top9)
endloop
end
;
def _ystrain9
_ystrain9=_sumdis9/12.0
end
;==============================
;===W=0.5m, left-5 (-12.5 m to -12.0 m)===
def _stress10
```

```
_sumstress10 = 0.0
loop n10 (1,6)
a10 =-11.9 - n10*0.1
zi10=z_near(a10,0.0)
_sumstress10 = _sumstress10+z_syy(zi10)
endloop
end
;
def _averstress10
_averstress10 = -1.0*_sumstress10/6.0
end
;
def _dis10
_sumdis10 = 0.0
loop m10 (1,6)
b10=-11.9-m10*0.1
gi_top10=gp_near(b10,1.01) ;top of the coal layer
gi_bot10=gp_near(b10,-1.01) ;bottom of the coal layer
_sumdis10=_sumdis10+gp_ydis(gi_bot10)-gp_ydis(gi_top10)
endloop
end
;
def _ystrain10
_ystrain10=_sumdis10/12.0
end
;================================
;===W=0.5m, left-6 (-13.0 m to -12.5 m)===
```

```
def _stress11
_sumstress11 = 0.0
loop n11 (1,6)
a11 =-12.4 - n11*0.1
zi11=z_near(a11,0.0)
_sumstress11 = _sumstress11+z_syy(zi11)
endloop end
;
def _averstress11
_averstress11 = -1.0*_sumstress11/6.0
end
;
def _dis11
_sumdis11 = 0.0
loop m11 (1,6)
b11=-12.4-m11*0.1
gi_top11=gp_near(b11,1.01) ;top of the coal layer
gi_bot11=gp_near(b11,-1.01) ;bottom of the coal layer
_sumdis11=_sumdis11+gp_ydis(gi_bot11)-gp_ydis(gi_top11)
endloop
end
;
def _ystrain11
_ystrain11=_sumdis11/12.0
end
;================================
;===W=0.5m, left-7 (-13.5 m to -13.0 m)===
```

```
def _stress12
_sumstress12 = 0.0
loop n12 (1,6)
a12 =-12.9 - n12*0.1
zi12=z_near(a12,0.0)
_sumstress12 = _sumstress12+z_syy(zi12)
endloop
end
;
def _averstress12
_averstress12 = -1.0*_sumstress12/6.0
end
;
def _dis12
_sumdis12 = 0.0
loop m12 (1,6)
b12=-12.9-m12*0.1
gi_top12=gp_near(b12,1.01) ;top of the coal layer
gi_bot12=gp_near(b12,-1.01) ;bottom of the coal layer
_sumdis12=_sumdis12+gp_ydis(gi_bot12)-gp_ydis(gi_top12)
endloop
end
;
def _ystrain12
_ystrain12=_sumdis12/12.0
end
;================================
```

```
;===W=0.5m, left-8 (-14.0 m to -13.5 m)===
def _stress13
_sumstress13 = 0.0
loop n13 (1,6)
a13 =-13.4 - n13*0.1
zi13=z_near(a13,0.0)
_sumstress13 = _sumstress13+z_syy(zi13)
endloop
end
;
def _averstress13
_averstress13 = -1.0*_sumstress13/6.0
end
;
def _dis13
_sumdis13 = 0.0
loop m13 (1,6)
b13=-13.4-m13*0.1
gi_top13=gp_near(b13,1.01) ;top of the coal layer
gi_bot13=gp_near(b13,-1.01) ;bottom of the coal layer
_sumdis13=_sumdis13+gp_ydis(gi_bot13)-gp_ydis(gi_top13)
endloop
end
;
def _ystrain13
_ystrain13=_sumdis13/12.0
end
```

```
;================================
;===W=0.5m, left-9 (-14.5 m to -14.0 m)===
def _stress14
_sumstress14 = 0.0
loop n14 (1,6)
a14 =-13.9 - n14*0.1
zi14=z_near(a14,0.0)
_sumstress14 = _sumstress14+z_syy(zi14)
endloop
end
;
def _averstress14
_averstress14 = -1.0*_sumstress14/6.0
end
;
def _dis14
_sumdis14 = 0.0
loop m14 (1,6)
b14=-13.9-m14*0.1
gi_top14=gp_near(b14,1.01) ;top of the coal layer
gi_bot14=gp_near(b14,-1.01) ;bottom of the coal layer
_sumdis14=_sumdis14+gp_ydis(gi_bot14)-gp_ydis(gi_top14)
endloop
end
;
def _ystrain14
_ystrain14=_sumdis14/12.0
```

```
end
;==================================
;===W=3.5m (7)===
def _stress15
_sumstress15 = 0.0
loop n15 (1,11)
a15 =-9.65 - n15*0.35
zi15=z_near(a15,0.0)
_sumstress15 = _sumstress15+z_syy(zi15)
endloop
end
;
def _averstress15
_averstress15 = -1.0*_sumstress15/11.0
end
;
def _dis15
_sumdis15 = 0.0
loop m15 (1,11)
b15=-9.65-m15*0.35
gi_top15=gp_near(b15,1.01) ;top of the coal layer
gi_bot15=gp_near(b15,-1.01) ;bottom of the coal layer
_sumdis15=_sumdis15+gp_ydis(gi_bot15)-gp_ydis(gi_top15)
endloop
end
;
def _ystrain15
```

```
_ystrain15=_sumdis15/22.0
end
;==============================
;===W=4.0m (8)===
def _stress16
_sumstress16 = 0.0
loop n16 (1,11)
a16 =-9.6 - n16*0.4
zi16=z_near(a16,0.0)
_sumstress16 = _sumstress16+z_syy(zi16)
endloop
end
;
def _averstress16
_averstress16 = -1.0*_sumstress16/11.0
end
;
def _dis16
_sumdis16 = 0.0
loop m16 (1,11)
b16=-9.6-m16*0.4
gi_top16=gp_near(b16,1.01) ;top of the coal layer
gi_bot16=gp_near(b16,-1.01) ;bottom of the coal layer
_sumdis16=_sumdis16+gp_ydis(gi_bot16)-gp_ydis(gi_top16)
endloop
end
;
```

```
def _ystrain16
_ystrain16=_sumdis16/22.0
end
;==================================
;===W=4.5m (9)===
def _stress17
_sumstress17 = 0.0
loop n17 (1,11)
a17 =-9.55 - n17*0.45
zi17=z_near(a17,0.0)
_sumstress17 = _sumstress17+z_syy(zi17)
endloop
end
;
def _averstress17
_averstress17 = -1.0*_sumstress17/11.0
end
;
def _dis17
_sumdis17 = 0.0
loop m17 (1,11)
b17=-9.55-m17*0.45
gi_top17=gp_near(b17,1.01) ;top of the coal layer
gi_bot17=gp_near(b17,-1.01) ;bottom of the coal layer
_sumdis17=_sumdis17+gp_ydis(gi_bot17)-gp_ydis(gi_top17)
endloop
end
```

;

def _ystrain17

_ystrain17=_sumdis17/22.0

end

;

hist unbal

hist _averstress1

hist _ystrain1

hist _averstress2

hist _ystrain2

hist _averstress3

hist _ystrain3

hist _averstress4

hist _ystrain4

hist _averstress5

hist _ystrain5

hist _averstress6

hist _ystrain6

hist _averstress7

hist _ystrain7

hist _averstress8

hist _ystrain8

hist _averstress9

hist _ystrain9

hist _averstress10

hist _ystrain10

hist _averstress11

hist _ystrain11

hist _averstress12

hist _ystrain12

hist _averstress13

hist _ystrain13

hist _averstress14

hist _ystrain14

hist _averstress15

hist _ystrain15

hist _averstress16

hist _ystrain16

hist _averstress17

hist _ystrain17

;

set fishcall FC_CYC_MOT _stress1

set fishcall FC_CYC_MOT _dis1

set fishcall FC_CYC_MOT _ystrain1

set fishcall FC_CYC_MOT _averstress1

;

set fishcall FC_CYC_MOT _stress2

set fishcall FC_CYC_MOT _dis2

set fishcall FC_CYC_MOT _ystrain2

set fishcall FC_CYC_MOT _averstress2

;

set fishcall FC_CYC_MOT _stress3

set fishcall FC_CYC_MOT _dis3

set fishcall FC_CYC_MOT _ystrain3

set fishcall FC_CYC_MOT _averstress3

;

set fishcall FC_CYC_MOT _stress4

set fishcall FC_CYC_MOT _dis4

set fishcall FC_CYC_MOT _ystrain4

set fishcall FC_CYC_MOT _averstress4

;

set fishcall FC_CYC_MOT _stress5

set fishcall FC_CYC_MOT _dis5

set fishcall FC_CYC_MOT _ystrain5

set fishcall FC_CYC_MOT _averstress5

;

set fishcall FC_CYC_MOT _stress6

set fishcall FC_CYC_MOT _dis6

set fishcall FC_CYC_MOT _ystrain6

set fishcall FC_CYC_MOT _averstress6

;

set fishcall FC_CYC_MOT _stress7

set fishcall FC_CYC_MOT _dis7

set fishcall FC_CYC_MOT _ystrain7

set fishcall FC_CYC_MOT _averstress7

;

set fishcall FC_CYC_MOT _stress8

set fishcall FC_CYC_MOT _dis8

set fishcall FC_CYC_MOT _ystrain8

set fishcall FC_CYC_MOT _averstress8

;

set fishcall FC_CYC_MOT _stress9

set fishcall FC_CYC_MOT _dis9

set fishcall FC_CYC_MOT _ystrain9

set fishcall FC_CYC_MOT _averstress9

;

set fishcall FC_CYC_MOT _stress10

set fishcall FC_CYC_MOT _dis10

set fishcall FC_CYC_MOT _ystrain10

set fishcall FC_CYC_MOT _averstress10

;

set fishcall FC_CYC_MOT _stress11

set fishcall FC_CYC_MOT _dis11

set fishcall FC_CYC_MOT _ystrain11

set fishcall FC_CYC_MOT _averstress11

;

set fishcall FC_CYC_MOT _stress12

set fishcall FC_CYC_MOT _dis12

set fishcall FC_CYC_MOT _ystrain12

set fishcall FC_CYC_MOT _averstress12

;

set fishcall FC_CYC_MOT _stress13

set fishcall FC_CYC_MOT _dis13

set fishcall FC_CYC_MOT _ystrain13

set fishcall FC_CYC_MOT _averstress13

;

set fishcall FC_CYC_MOT _stress14

set fishcall FC_CYC_MOT _dis14

```
set fishcall FC_CYC_MOT _ystrain14
set fishcall FC_CYC_MOT _averstress14
;
set fishcall FC_CYC_MOT _stress15
set fishcall FC_CYC_MOT _dis15
set fishcall FC_CYC_MOT _ystrain15
set fishcall FC_CYC_MOT _averstress15
;
set fishcall FC_CYC_MOT _stress16
set fishcall FC_CYC_MOT _dis16
set fishcall FC_CYC_MOT _ystrain16
set fishcall FC_CYC_MOT _averstress16
;
set fishcall FC_CYC_MOT _stress17
set fishcall FC_CYC_MOT _dis17
set fishcall FC_CYC_MOT _ystrain17
set fishcall FC_CYC_MOT _averstress17
;
delete range -0.25 0.0 -1.0 1.0
solve
delete range -0.50 0.0 -1.0 1.0
solve
delete range -0.75 0.0 -1.0 1.0
solve
delete range -1.00 0.0 -1.0 1.0
solve
delete range -1.25 0.0 -1.0 1.0
```

```
solve
delete range -1.50 0.0 -1.0 1.0
solve
delete range -1.75 0.0 -1.0 1.0
solve
delete range -2.00 0.0 -1.0 1.0
solve
delete range -2.25 0.0 -1.0 1.0
solve
delete range -2.50 0.0 -1.0 1.0
solve
delete range -2.75 0.0 -1.0 1.0
solve
delete range -3.00 0.0 -1.0 1.0
solve
delete range -3.25 0.0 -1.0 1.0
solve
delete range -3.50 0.0 -1.0 1.0
solve
delete range -3.75 0.0 -1.0 1.0
solve
delete range -4.00 0.0 -1.0 1.0
solve
delete range -4.25 0.0 -1.0 1.0
solve
delete range -4.50 0.0 -1.0 1.0
solve
```

delete range -4.75 0.0 -1.0 1.0

solve

delete range -5.00 0.0 -1.0 1.0

solve

delete range -5.25 0.0 -1.0 1.0

solve

delete range -5.50 0.0 -1.0 1.0

solve

delete range -5.75 0.0 -1.0 1.0

solve

delete range -6.00 0.0 -1.0 1.0

solve

delete range -6.25 0.0 -1.0 1.0

solve

delete range -6.50 0.0 -1.0 1.0

solve

delete range -6.75 0.0 -1.0 1.0

solve

delete range -7.00 0.0 -1.0 1.0

solve

delete range -7.25 0.0 -1.0 1.0

solve

delete range -7.50 0.0 -1.0 1.0

solve

delete range -7.75 0.0 -1.0 1.0

solve

delete range -8.00 0.0 -1.0 1.0

solve

delete range -8.25 0.0 -1.0 1.0

solve

delete range -8.50 0.0 -1.0 1.0

solve

delete range -8.75 0.0 -1.0 1.0

solve

delete range -9.00 0.0 -1.0 1.0

solve

delete range -9.25 0.0 -1.0 1.0

solve

delete range -9.50 0.0 -1.0 1.0

solve

delete range -9.75 0.0 -1.0 1.0

solve

delete range -10.00 0.0 -1.0 1.0

solve

bound yvel=-0.02 range -80.0 10.0 79.9 80.1 ;top

bound yvel=0.02 range -80.0 10.0 -80.1 -79.9 ;bottom

;

cycle 40000

w_b= 0.5 m

Same as **w_{wr}= 2.0 m in Section D.11**

w_b= 1.0 m

Replace the commands in **w_b= 0.0 m** "change jmat=3 range -12.0, -10.0 0.999, 1.001; change jmat=3 range -12.0, -10.0 -1.001, -0.999" with "change jmat=3 range -13.0, -11.0 0.999, 1.001; change jmat=3 range -13.0, -11.0 -1.001, -0.999"

w_b= 1.5 m

Replace the commands in **w_b= 0.0 m** "change jmat=3 range -12.0, -10.0 0.999, 1.001; change jmat=3 range -12.0, -10.0 -1.001, -0.999" with "change jmat=3 range -13.5, -11.5 0.999, 1.001; change jmat=3 range -13.5, -11.5 -1.001, -0.999".

w_b= 2.0 m

Replace the commands in **w_b= 0.0 m** "change jmat=3 range -12.0, -10.0 0.999, 1.001; change jmat=3 range -12.0, -10.0 -1.001, -0.999" with "change jmat=3 range -14.0, -12.0 0.999, 1.001; change jmat=3 range -14.0, -12.0 -1.001, -0.999".